Imperial College London

Nonlinear Modal Analysis for Blisks with Friction Dampers

YEKAI SUN

Department of Mechanical Engineering
Imperial College London

Submitted in part fulfilment of the requirements for the degree of
Doctor of Philosophy of Imperial College London
and the Diploma of Imperial College London

March 2021

This thesis was completed during the worldwide pandemic of COVID-19 in 2020. I would like to dedicate this thesis to all doctors, nurses, and other medical professionals and staff, who have been working on the front line in the fight against Coronavirus all over the world.

Declaration

Originality

I hereby declare that except where specific reference is made to the work of others, the contents of this dissertation are original and have not been submitted in whole or in part for consideration for any other degree or qualification in this, or any other university. This dissertation is my own work which has been done after registration for the degree of *Doctor of Philosophy* at Imperial College London, and contains nothing which is the outcome of work done in collaboration with others, except as specified in the text and Acknowledgements. This dissertation contains fewer than 100,000 words including footnotes, but excluding appendices and bibliography.

Copyright

The copyright of this thesis rests with the author. Unless otherwise indicated, its contents are licensed under a Creative Commons Attribution-Non Commercial 4.0 International Licence (CC BY-NC). Under this licence, you may copy and redistribute the material in any medium or format. You may also create and distribute modified versions of the work. This is on the condition that: you credit the author and do not use it, or any derivative works, for a commercial purpose. When reusing or sharing this work, ensure you make the licence terms clear to others by naming the licence and linking to the licence text. Where a work has been adapted, you should indicate that the work has been changed and describe those changes. Please seek permission from the copyright holder for uses of this work that are not included in this licence or permitted under UK Copyright Law.

YEKAI SUN
March 2021

Acknowledgements

This doctoral thesis is the final result of a three-year research at the Dynamics Research Group, Imperial College London and would have been unachievable without the involvement of a number of people and my sponsorship.

Above all, the present thesis would not have been possible without the financial support from the China Scholarship Council (File NO. 201708060239).

I sincerely address my thanks to my supervisor Dr Loïc Salles for facilitating a favourable environment for independent research and development of novel ideas and approaches. His great enthusiasm, unlimited support and careful guidance always encouraged me. Thanks to his insight of nonlinear dynamics and inspiring ideas, that I could achieve my doctoral degree within three years.

I would like to say thanks to Professor Norbert Hoffmann for enrolling me as a research postgraduate in Imperial College London. I am pleased to acknowledge Professor David Nowell, Dr Christoph Schwingshackl and Mr Peter Higgs for hosting the daily routine of the Dynamics Research Group. I also want to thank all current and previous members of the Dynamics Research Group for the friendly working environment.

I express my gratitude to Dr Jie Yuan, Dr Enora Denimal and Dr Luca Pesaresi for their co-supervision and their comments on the present thesis. Moreover, I also thank to Dr Fadi el Haddad, Dr Filipe Fontanela, Alessandra Vizzaccaro, Shuqing Lian, Jiří Blahoš and Mertol Tüfekci for numerous useful discussions and exchanging ideas.

I am very grateful to all my friends who always made my time in UK enjoyable and unforgettable. It is difficult to list down all the names here. Just to name a few groups: those we met from A-Level, friends from University of Bristol, Hammersmith kuakua group, GAMEMCEM group and so on.

A very special thanks is for my families, including my cousins Guanxiong Sun and Ye Zheng for their company. My deepest thanks go to my father Ruisong Sun and my mother Tao Liu that I want to end these acknowledgements. Without their supports, patience and encouragements, I could have never gotten this and other important milestones in my life.

Abstract

Dynamic analyses of nonlinear systems have become an important topic in the field of turbomachinery. In industrial turbomachinery, the friction damping is regarded as the major damping source compared to the aerodynamic damping and material damping. Contact with friction is a type of common non-conservative and non-smooth nonlinearities. The existence of various friction joints in industrial turbomachinery makes the dynamic analysis complicated. The definition of the damped Nonlinear Normal Modes (dNNMs) and various numerical approaches facilitate the infrastructure of nonlinear modal analysis for structures with friction dampers. However, the relations between dNNMs and resonant solutions in forced responses cannot be directly addressed. In this context, the purpose of the present thesis is (i) to evaluate the performance of the existing numerical approaches for computing the dNNMs of systems with non-conservative nonlinearities; (ii) to develop a new method to directly relate the dNNMs to the resonant solutions in forced response for such system; and (iii) to study the geometric influence of the friction ring dampers on their dynamic responses and damping performances.

The first contribution of the present thesis is to provide a comprehensive comparison of the existing numerical approaches, including Complex Nonlinear Mode (CNM) and Extended Periodic Motion Concept (EPMC). EPMC with artificial hysteretic damping is firstly attempted and compared with the original EPMC and CNM. The advantages and limitations of each method are critically discussed.

The second contribution is the development of the Extended Energy Balance Method (E-EBM), which is a numerical method used to efficiently predict the resonances using the dNNMs of a non-conservative nonlinear system. This E-EBM can be simply applied to both CNM and EPMC approaches.

The third contribution is the investigation the damping performance of friction ring dampers for blisk structures, especially the geometric effects of the ring dampers. The geometric design of the ring dampers is achieved by using kriging meta-modelling to predict the dNNMs. Useful advice is proposed for the future design of friction ring dampers.

Table of contents

List of figures **15**

List of tables **19**

1 Introduction **21**
1.1 Jet Engine 21
1.1.1 Gas turbine engine 22
1.2 Vibration in Turbomachinery 25
1.2.1 Bladed disk and blisk 25
1.2.2 High cycle fatigue 26
1.2.3 Vibration mechanism 27
1.2.4 Vibration reduction mechanism 29
1.2.5 Overview of vibration of blisk 29
1.3 Nonlinear Vibration 30
1.4 Thesis Objectives and Outlines 31

2 State of Knowledge **33**
2.1 Fundamental Dynamics of Blisk 33
2.1.1 Periodicity of mode 33
2.1.2 Engine order excitation 35
2.1.3 Relation between engine order and nodal diameter 36
2.2 Friction Damping in Turbomachinery 39
2.2.1 Various friction damping for assembled bladed disks 39
2.2.2 Friction ring dampers for blisks 40
2.2.3 Geometric optimization of friction dampers 47
2.3 Constitutive Models for Friction 48
2.3.1 Dry friction models 48

2.3.2 Dynamic friction models . . . 50
2.3.3 Macroslip models . . . 50
2.3.4 Microslip models . . . 55
2.3.5 Identification of contact parameters . . . 55
2.3.6 Uncertainties involved in contact parameters . . . 55
2.4 Numerical Methods for Nonlinear Dynamics . . . 56
2.4.1 Time domain methods . . . 56
2.4.2 Spectral methods . . . 58
2.4.3 Continuation method . . . 60
2.5 Model Reduction . . . 61
2.5.1 Component mode synthesis . . . 61
2.5.2 Cyclic symmetric reduction . . . 62
2.5.3 Cyclic interface reduction . . . 63
2.5.4 Model reduction for tuned blisks with friction dampers . . . 63
2.6 Nonlinear Normal Mode . . . 63
2.6.1 Rosenberg's definition . . . 64
2.6.2 Shaw and Pierre's definition . . . 64
2.6.3 Computation of nonlinear modes . . . 65
2.7 Relating Nonlinear Mode to Forced Response . . . 66
2.7.1 Energy balance method . . . 66
2.7.2 Nonlinear modal synthesis . . . 67
2.8 Concluding Remarks . . . 67

3 Numerical Methods for Nonlinear Modal Analysis 69
3.1 Harmonic Balance Method . . . 69
3.1.1 Fourier-Galerkin procedure . . . 69
3.1.2 Alternating frequency/time method . . . 71
3.2 Continuation Method . . . 72
3.2.1 Prediction . . . 73
3.2.2 Correction . . . 74
3.3 Damped Nonlinear Normal Mode . . . 75
3.3.1 Complex nonlinear mode . . . 75
3.3.2 Extended periodic motion concept . . . 76
3.3.3 Energy dependency and normalisation . . . 78
3.3.4 Summary for two numerical approaches . . . 79

3.4 Extended Energy Balance Method . . . 79
3.4.1 Assumptions . . . 79
3.4.2 Numerical formulations . . . 80
3.5 Numerical Examples . . . 83
3.5.1 One DoF system with frictional contact . . . 84
3.5.2 One DoF system with quadratic nonlinear damping . . . 88
3.5.3 Duffing oscillator . . . 92
3.5.4 Summary . . . 95
3.6 Concluding Remarks . . . 96

4 Numerical Validation and Parametric Study of Frictional Dampers 97
4.1 Validation of Numerical Methods . . . 98
4.1.1 Experimental setup for validation . . . 98
4.1.2 Mechanical model for validation . . . 98
4.1.3 Numerical results and experimental results . . . 100
4.1.4 Summary . . . 101
4.2 Parametric Study of Frictional Dampers . . . 101
4.2.1 Model description . . . 101
4.2.2 Numerical results . . . 104
4.2.3 Uncertainty quantification . . . 109
4.3 Concluding Remarks . . . 113

5 Application of Nonlinear Modal Analysis to Blisks with Ring Dampers 115
5.1 Lumped parameter model . . . 115
5.1.1 Natural frequency against nodal diameter . . . 117
5.1.2 Effect of nodal diameter on damping performance . . . 118
5.1.3 Effect of damper mass on damping performance . . . 119
5.1.4 Summary . . . 120
5.2 Full-scale Blisk with Friction Ring Damper . . . 121
5.2.1 Finite element model . . . 121
5.2.2 Methodology for pre-processing . . . 122
5.2.3 Nonlinear vibration solver . . . 125
5.2.4 Nonlinear modal analysis . . . 132
5.2.5 Summary . . . 136
5.3 Concluding Remarks . . . 137

6 Geometric Study of a Frictional Ring Damper in a Blisk **139**
6.1 Damper Geometry Parametrisation 139
6.2 Nonlinear Modal Analysis 144
6.3 Kriging Meta-Modelling 146
6.4 Construction and Validation of the Meta-models 147
6.5 Design Space Exploration and Discussion 149
6.5.1 Influences of each design parameter 149
6.5.2 All design space exploration 153
6.6 Variance Based Sensitivity Analysis 156
6.6.1 Sobol indices 156
6.6.2 Sensitivity analysis 157
6.7 Concluding Remarks 160

7 Conclusions and Future Work **161**
7.1 Conclusions of the Research Work 161
7.1.1 Conclusions on nonlinear modal analysis 161
7.1.2 Conclusions on existing numerical approaches 162
7.1.3 Conclusions on the extended energy balance method 163
7.1.4 Conclusions on friction ring dampers 163
7.2 Scientific Contribution 165
7.3 Future Work 165
7.4 Publications 166
7.4.1 Journal publications 166
7.4.2 Conference publications 167

References **169**

Appendix A Numerical Formulations for Contact Models **183**
A.1 One Dimensional Contact Element 183
A.2 Two Dimensional Contact Element 184
A.3 Three Dimensional Contact Element 185

List of figures

1.1 An example of the jet engine 22
1.2 Typical gas turbines 23
1.3 Bladed disk and blisk 25
1.4 Example Goodman diagram 26
1.5 Example Campbell diagram 28

2.1 Structure with cyclic symmetry and one repeated sector 34
2.2 An example of Campbell diagram 36
2.3 Examples of zig-zag diagram 38
2.4 Various types of friction damping 39
2.5 Dampers used for fan blades in an aircraft engine CFM56-5A 40
2.6 Ring dampers in labyrinth air seals by Niemotka and Ziegert 41
2.7 Ring dampers in gears 42
2.8 Ring dampers for blisks from Laboratoire de Tribologie et Dynamique des Systemes at École Centrale de Lyon 43
2.9 Main results from the experimental testrig for a rotating blisk with a friction ring damper 44
2.10 Ring dampers for blisk from University of Michigan 46
2.11 Static friction models 49
2.12 Three contact elements 51
2.13 Examples of friction forces and hysteresis loops for the one dimensional contact element 52
2.14 Examples of friction forces and hysteresis loops for the two dimensional contact element 53
2.15 Examples of friction forces for the three dimensional contact element . . . 54
2.16 One predictor-corrector step of the continuation method 61

2.17 An example of a linear mode and a nonlinear mode in a two-dimensional phase space 65

3.1 Demonstration of alternating frequency/time method 71
3.2 Demonstration of predictors in a continuation step 73
3.3 Demonstration of correctors in a continuation step 74
3.4 Demonstration of resonant shared solution between damped nonlinear normal mode and nonlinear forced response 80
3.5 The energy transferred by the damping terms for a fixed modal amplitude and the energy transferred by the forcing term for different excitation levels with respect to the forcing phase 82
3.6 One DoF system with frictional contact 84
3.7 Numerical results from the damped nonlinear normal mode within a range of modal amplitude for the one DoF system with frictional contact 85
3.8 Invariant manifolds for the one DoF system with frictional contact 86
3.9 Solutions of the damped nonlinear normal modes for the one DoF system with frictional contact 87
3.10 Using nonlinear forced response to validate the frequency-amplitude plot and the force-amplitude plot for the one DoF system with frictional contact 87
3.11 Numerical results from the damped nonlinear normal mode within a range of modal amplitude for the one DoF system with quadratic nonlinear damping 89
3.12 Invariant manifolds for the one DoF system with quadratic nonlinear damping 90
3.13 Solutions of the damped nonlinear normal mode for the one DoF system with quadratic nonlinear damping 91
3.14 Using nonlinear forced response to validate the frequency-amplitude plot and the force-amplitude plot for the one DoF system with quadratic nonlinear damping 92
3.15 Numerical results from the damped nonlinear normal mode within a range of modal amplitude for the Duffing oscillator 93
3.16 Invariant manifolds for the Duffing oscillator 94
3.17 Using nonlinear forced response to validate the frequency-amplitude plot and the force-amplitude plot for the Duffing oscillator 94

4.1 Experimental setups 98
4.2 Reference mechanical model 99
4.3 Experimental results and numerical results 100

4.4 Mechanical model . . . 102
4.5 Two dimensional contact model . . . 103
4.6 Linear mode shape for beam model . . . 104
4.7 Modal characteristics against kinetic energy . . . 105
4.8 Normalised hysteresis loops . . . 106
4.9 Three design objectives . . . 107
4.10 Hysteresis loop for different contact angles . . . 108
4.11 Natural frequency sensitivity . . . 109
4.12 Uncertainty quantification . . . 110
4.13 Monte Carlo Simulation: Stochastic modal characteristics against kinetic energy . . . 111
4.14 Monte Carlo Simulation: Three design objectives . . . 112

5.1 Demonstration of lumped parameter model . . . 116
5.2 Natural frequency against nodal diameter for lumped parameter model . . . 118
5.3 Mode shape of second modal family . . . 118
5.4 Modal damping ratio against the vibration amplitude for different nodal diameters . . . 119
5.5 Modal damping ratio against vibration amplitude for different values of damper mass . . . 120
5.6 A three-dimensional blisk with ring damper . . . 121
5.7 Flow chart for pre-processing . . . 122
5.8 Normalised natural frequency against nodal diameter . . . 123
5.9 Mode shapes of the first four modes with nodal diameter three . . . 124
5.10 Campbell diagram . . . 125
5.11 Contact status from the nonlinear static analysis . . . 125
5.12 Flow chart for nonlinear vibration solver . . . 126
5.13 Demonstration of the partition for DoFs of a generic isolated sector . . . 127
5.14 Convergence study for the number of modes used in the model reduction porcess . . . 131
5.15 Numerical results from the damped nonlinear normal mode within a range of modal amplitude for the blisk with ring damper . . . 133
5.16 Normalised energy dissipated distribution for the four cases . . . 134
5.17 Using nonlinear forced responses with different excitation forcing values to validate the predicted excitation forcing for the blisk with ring damper . . . 135

5.18 Comparison of the energy dissipated distributions under resonance 136

6.1 A three dimensional blisk with ring damper 140
6.2 Demonstration of damper geometry parametrisation 141
6.3 Different geometries of a sector of ring damper 143
6.4 Damped nonlinear normal mode and force amplitude plot for all seven geometries 145
6.5 Meta-models validation 148
6.6 Effect of the first design parameter on the damped nonlinear normal mode . 150
6.7 Effect of the second design parameter on the damped nonlinear normal mode 151
6.8 Effect of the third design parameter on the damped nonlinear normal mode . 152
6.9 Design space exploration of the damped nonlinear normal mode 154
6.10 The optimal geometry 155
6.11 Sobol indices for different levels of the vibrational amplitude within the whole design space 159

A.1 Three contact elements 184

List of tables

2.1 Examples of the relation between engine order and nodal diameter 38

4.1 Uncertain Parameters 110

5.1 Lumped Model Parameter 116
5.2 Number of DoFs for each model reduction step 132
5.3 Comparison of computational time among three methods 136
5.4 Comparison of computational time for nonlinear forced responses 136

6.1 Parameters that describe the damper geometry 142
6.2 Comparison of maximum modal damping using surrogate models 155

Chapter 1

Introduction

In the first chapter, basic knowledge about gas turbine engines is provided. Then, the fundamental basis of the vibration problems within the turbomachinery are introduced, including: differences between bladed disks and blisks; high cycle fatigue issue; various sources of vibration; different vibration reduction mechanisms. Furthermore, two emerging research directions in the field of the vibration of turbomachinery (mistuning analyses and nonlinear dynamic analyses) are summarised. Then, the research motivations and objectives of the present thesis are discussed in detail. The present thesis aims to develop an efficient numerical tool to investigate the nonlinear dynamic responses of structures with friction joints. Finally, the organisation of the present thesis is outlined.

1.1 Jet Engine

Jet engines are propulsive devices that can provide thrust by discharging a high-speed stream of air. Jet engines can be considered a well-known application of the Newton's third law, stating that "for every reaction, there is an equal and opposite reaction". Jet engines provide propulsive thrust by propelling air backwards with a certain speed. The atmospheric air is forced to accelerate backwards by engines, and there is a force with an equal magnitude and opposite direction applied on the body that generates the accelerating force on the atmospheric air. The total thrust T generated by a jet engine can be calculated using Eqn.(1.1), and as demonstrated in Fig.1.1. The velocity, pressure, cross section area and mass flow rate are defined as V, p, A and $\dot{m}$, the subscript $*_0$ represents the intake air stream and subscript $*_e$ for the exhausted jet. According to Eqn.(1.1), a jet engine can provide large thrust by either propelling a large amount of air at a low speed or a small amount of air at a high speed.

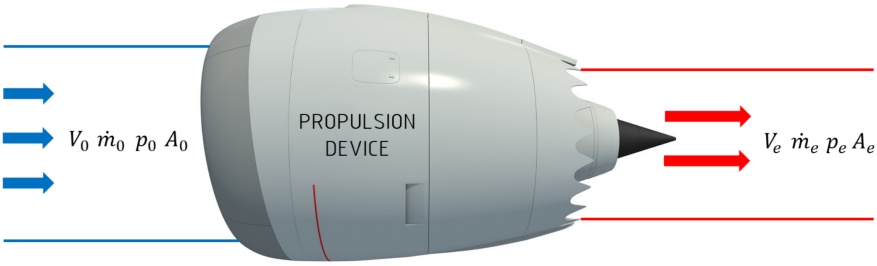


Fig. 1.1 An example of the jet engine [48]

$$T = \dot{m}_e V_e - \dot{m}_0 V_0 + p_e A_e - p_0 A_0 \tag{1.1}$$

1.1.1 Gas turbine engine

Based on different propulsive mechanisms, jet engines can be classified into several categories: gas turbine engines, ram jets, rockets and so on. Gas turbine engines are used in most civil and military aircrafts. The core components for a gas turbine engine consist of compressors, combustion chambers and turbines. For different aircraft, gas turbine engines can be further classified into: turbojet, turbofan, turboprop and turboshaft engines, as shown in Fig.1.2. These important components within a gas turbine engine are described below:

- *Air inlet*: All gas turbine engines have an air inlet to take the free stream air into engines. Air inlets usually have a divergent shape to decelerate the intake air flow. For a supersonic aircraft, the air inlet is a crucial component to ensure that the intake air has been decelerated to subsonic speed before it reaches the compressors.

- *Ducted fan*: Ducted fans are only used on turbofan engines, and are located after the air inlets and before the compressors. The intake air is slightly compressed by a rotating fan. The air past the fan is divided into two separated air flows. A small amount of air flow goes through the engine core, and it is exhausted through a nozzle at a high speed with high temperature, also known as the hot flow. A larger volume of air is directly ejected into the atmosphere through the bypass at a low speed with low temperature (cold flow). The mass ratio between the cold flow and the hot flow of the jet air is defined as the bypass ratio.

- *Propeller*: A turboprop engine usually has a propeller to provide most of its thrust. The propeller is also used in a helicopter to provide lift and is driven by a shaft within

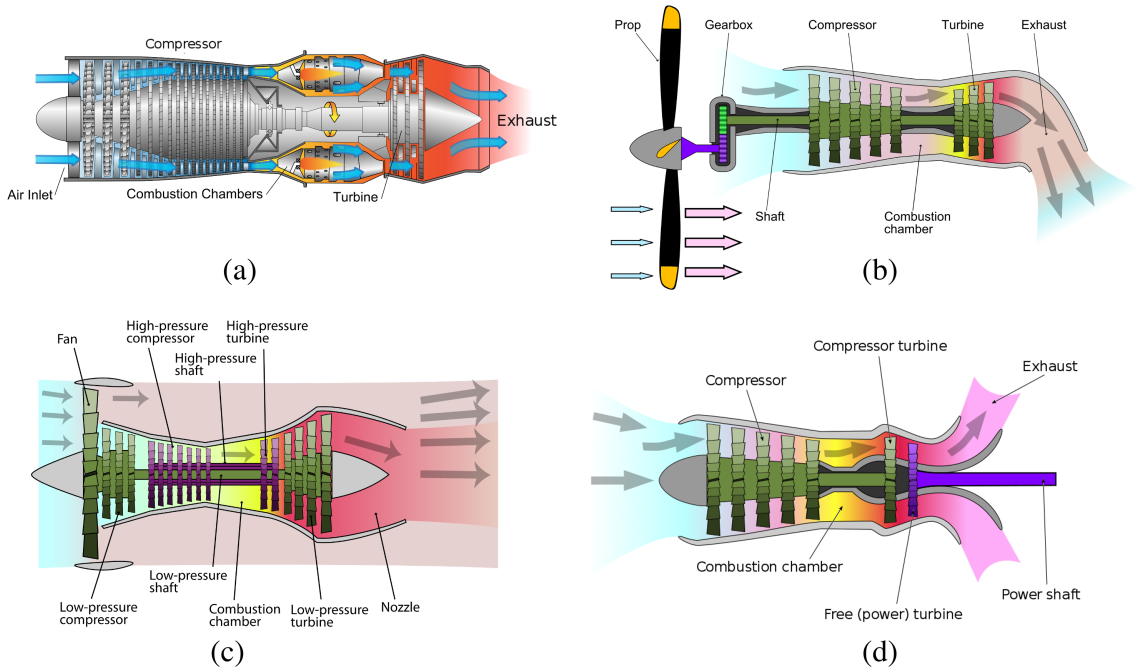


Fig. 1.2 Typical gas turbines (from Wikipedia): (a) A turbojet engine; (b) A turboprop engine; (c) A turbofan engine; (d) A turboshaft engine

turboshaft engines. A propeller usually consists of a hub and several individual blades. These blades have similar cross sections as aerofoils with a certain twist angle. The rotation of the blade generates a lift in the upstream direction and provide a propulsive force for turboprop engines.

- *Compressor*: Compressors are used to compress the air stream and transfer the mechanical energy into the thermal energy of the air stream. Compressors in gas turbine engines can be classified into two types: centrifugal compressors and axial compressors. The axial compressors are commonly used in the gas turbine engines and usually consist of several stages of bladed disks or blisks. Most gas turbine engines have two stages of compressors: a low pressure compressor and a high pressure compressor. Turbofan engines designed by Rolls-Royce plc. typically have an extra middle pressure compressor. The compressors are usually driven by the different shafts with a different speed, i.e. the low pressure shaft is connected to the low pressure compressor.

- *Combustion chamber*: In combustion chambers, the aviation fuel is injected and burnt to release the chemical energy into the thermal energy of the compressed gas. The maximum temperature of the compressed air is within the range of 1100 K to 1900 K.

- *Turbine*: The main function of a turbine is providing the mechanical energy to the rotating components through different shafts, like the compressors, ducted fan in turbofan engines and the propellers in turboprop engines. There are usually several stages of turbines, each turbine stage consists of a rotor and stator. The rotors use a blisk or bladed disk type structure, whereas the stators are fixed to the casings. The cross sections of a rotor and stator are designed to expand the gas stream and reduce the pressure. The high temperature, high speed gas drives the rotor to provide the power through different shafts. For example, the high pressure compressor is driven by a shaft connected with the first few stages of the turbine.
- *Nozzle*: The exhaust gas is usually ejected through a nozzle in a specific direction. The nozzle is usually designed in a convergent shape.

Turbojet engine

In turbojet engines, the thrust is generated by discharging of the high speed, high temperature exhaust gas into the atmosphere through a nozzle. The inlet air is directly compressed by compressors. Turbojet engines have a low efficiency at low cruise speeds. Therefore, turbojet engines are mainly used in supersonic aircrafts.

Turboprop engine

Thrust in turboprop engines mainly comes from the propeller which is driven by the turbines. Turboprop engines have a higher efficiency at a low cruise speed and a low cruise altitude. Military transport and maritime patrol aircraft, and aircraft used in general aviation usually use turboprop engines.

Turbofan engine

Turbofan engines have a ducted fan in front of the compressor. Most modern civil and military aircraft use turbofan engines due to their higher efficiency. In turbofan engines, a larger bypass ratio leads to a higher propulsive efficiency. However, a turbofan engine with a larger bypass ratio usually has large fan diameter, resulting in a lower ground clearance of the aircraft engine. Consequently, a long landing gear are required for the engine with a larger bypass ratio. However, for military aircraft, a long landing gear increases the total weight of the aircraft leading to a poor maneuverability. Therefore, turbofan engines with a low bypass ratio are usually preferred for military aircrafts. Whereas, for commercial flights,



Fig. 1.3 Bladed disk (left); Blisk (right) [86]

the fuel efficiency is one of the most important design considerations. Thus, engines used in commercial flights usually have a high bypass ratio.

Turboshaft engine

Turboshaft engines usually have two major parts: the gas generator and the power section. A gas generator consists of a compressor, a combustion chamber and one or more stages of turbines. The power section consists of a power turbine and a power shaft. Depending on the actual design, gearboxes can be used. A high speed, high temperature jet is generated by the gas generator and to drive the power turbine to provide the mechanical power through a power shaft. Turboshaft engines are mainly used in helicopters.

1.2 Vibration in Turbomachinery

1.2.1 Bladed disk and blisk

Turbomachinery is considered as one of the most important structural components within modern gas turbine engines. The bladed disk is the fundamental, critical and vulnerable structure in industrial turbomachinery. In traditional manufacturing, the bladed disks are assembled structures by a disk and several individual blades. Compared to the classic bladed disks, the integrally bladed disk (or blisk) is designed as a single piece of structure, as shown in Fig.1.3. Usually, blisks have a lighter structure than the classic bladed disks. The use

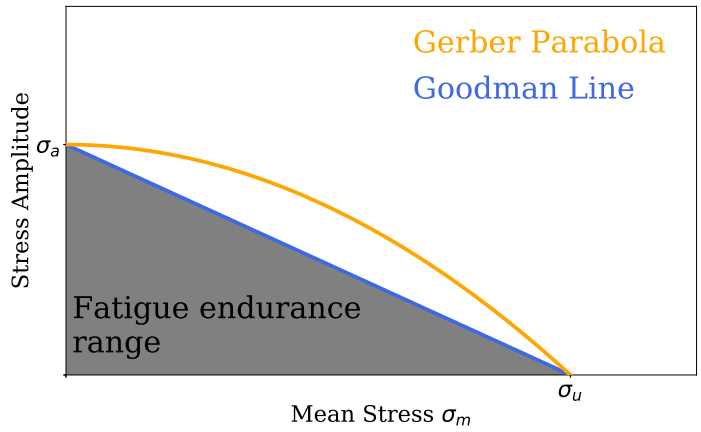


Fig. 1.4 Example Goodman diagram: Goodman line (blue); Gerber parabola (orange); σ_u Tensile strength; σ_a Alternating fatigue limit.

of blisks can improve the aerodynamic efficiency. Therefore, industries have given their priorities to blisks rather than bladed disks.

For an ideal multi-stage blisk system, there are two basic assumptions for most research in the literature. The first assumption is a rotationally spatial consistency (cyclic symmetry assumption). The cyclic symmetry assumption governs a tuned blisk system, which has several identical blades and disk sectors. When the cyclic symmetry is broken, the blisk is defined as a mistuned blisk. The second assumption is an axially spatial consistency (identical blisk for each stage). Based on these assumptions, a complicated multi-stage blisk or bladed disk system can be simply decomposed by analysing a single sector within one stage.

1.2.2 High cycle fatigue

In real aircraft engine, turbomachinery is usually working under high temperatures and at a high rotational speed. It undergoes a complicated operational environment with thermal loads, static fluid pressures and rotation-induced centrifugal loads. Various types of vibration sources might cause a large vibration amplitude leading to the High Cycle Fatigue (HCF). Consequently, HCF is regarded as the major reason for failures in gas turbine engines.

HCF is a type of fatigue with a small stress under a large number of loading cycles. The total stress comes from the combination of a mean stress and an alternating stress. The mean stress refers to the residual stress, whereas the alternating stress comes from the thermal or dynamic stress at a certain frequency. In the case of the blisk failure, the mean stress is caused by the assembled loading and thermal stress, whereas the vibration of blisk contributes to

the alternating stress. Alternating stresses are lower than the yield strength of the material. Goodman relation is a useful tool to govern the relation between the mean stress and the alternating stress, and to predict the fatigue endurance. An example Goodman diagram is shown in Fig.1.4 to demonstrate the fatigue endurance range.

1.2.3 Vibration mechanism

There are basically three types of vibration mechanisms for a blisk: forced responses, aeroelastic flutter and mechanical induced vibrations [161]. The first two are of the aeroelastic nature, whereas the third one relates to its mechanical nature.

Synchronous forced vibration

In turbomachinery, the forced response occurs when the circumferentially inhomogeneous air flow passes through a rotating blisk. The inhomogeneities of the air flow are mainly caused by non-uniform inflow conditions and blade row interactions [83], for example, from the upstream obstacles such as the casing ovality, struts or other structures. As for blade row interactions, the air flow from the stator vanes can be considered as a perfect example. From the stationary perspective, the inhomogeneous air flow shows invariance in time. Whereas, by considering the rotating blisk, the air flow is in the form of a travelling wave at the blisk's rotational speed. This type of excitation is named as "engine order excitation" (or synchronous excitation). The excitation frequency equals a multiple of an integer and the rotational speed. The resonances are usually identified using the Campbell diagram, which will be described in detail in Section 2.1. An example Campbell diagram is shown as Fig.1.5 and resonances are highlighted.

Aeroelastic flutter

Aeroelastic flutter is a phenomenon caused by a unstable aeroelastic interaction between a blisk and their surrounding air flow. In the case of flutter, the energy is injected into a blisk from the surrounding air flow leading to the vibration of blisks under a self-excited mechanism. Aeroelastic flutter is an important risk for blisks, resulting in the HCF issue. The frequency of flutter is usually close to the natural frequency of the excited mode, because the mass ratio between the surrounding air and the blisk is very small.

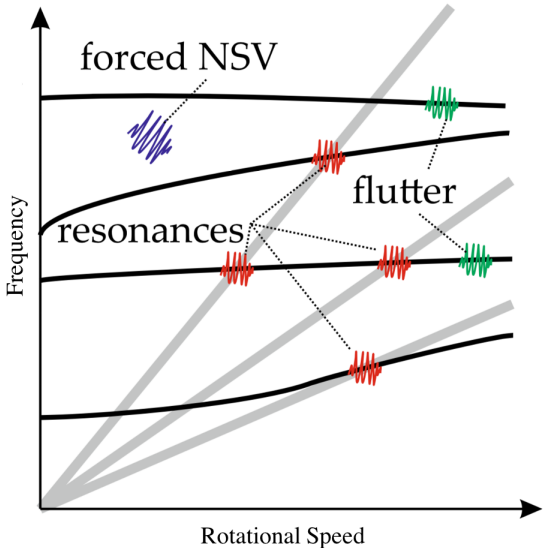


Fig. 1.5 Example Campbell diagram [83]: Grey oblique lines: synchronous excitation; Black curves: change of natural frequency against rotational speed; Red marker: Resonances excited by synchronous excitation; Green markers: flutter; Blue markers: non-synchronous vibration

Mechanical induced vibration

Mechanical induced vibration refers to the vibration excited by a mechanical interaction between the structural components within gas turbine engines. The rotational motion and the planar motion of a rotor shaft can excite the vibration of a blisk. Besides that, friction induced vibration can be also considered as an example of mechanical induced vibration. This phenomenon usually happens, when the oscillations of the tangential friction force are caused by the oscillations of the normal force. The friction force acts as a structural coupling force to make two modes of an undamped system closer to each other, until these two modes merge and become a pair of an unstable mode and a stable mode [63]. In turbomachinery, the friction induced vibration can be caused by the interaction between the tip of blade and casing. When a radial mode of a blade is excited leading a contact behaviour with the casing, resulting in an excitation of another flexural mode. In addition, the ingestion of foreign or domestic objects is seen as an accidental event of the mechanical induced vibration, such as birds (foreign) or debris from the damaged structures (domestic).

1.2.4 Vibration reduction mechanism

Vibration of blisks is expected to be avoided and mitigated to reduce the risk of HCF. There are many different strategies to achieve that. One of the most important way is to avoid the excitation of resonances, aeroelastic instabilities and mechanical interactions. This can be done in the design stage by adjusting design parameters to change the natural frequencies. However, most industrial blisks have a high modal density and a wide range of operating speed makes it almost impossible to avoid all critical resonances. Therefore, it is vital to reduce the resonant amplitude within a tolerable level. The total damping for blisks mainly comes from three sources: the aerodynamic damping, the material damping and the friction damping. Material damping in metals or alloys may comes from the internal friction in a microscope view, i.e. point defect damping, dislocation damping, grain-boundary damping and interface damping [196]. Thanks to the existence of material damping, the elastic strain energy can be dissipated when the structure is under mechanical vibration. Aerodynamic damping can be both positive (dissipative) and negative. In the case of aeroelastic flutter, the aerodynamic damping can be negative and the energy is transferred from the surrounding air flow into the blisk. During operation, the material damping and aerodynamic damping do not contribute significantly. Thus, a proper design of friction joints is considered as the major means to reduce the vibration amplitude of industrial blisks [83].

1.2.5 Overview of vibration of blisk

The dynamic analyses of bladed disks or blisks have a great practical importance to avoid the structural failures. From 1960 to 1980, many pioneering researchers paid their attention to the study of the vibration of blisks. Plenty of research have been done in that period by Whitehead [186], Wagner [183], Dye and Henry [36], Ewins [37–40] and Srinivasan [160]. From these pioneering works, the dynamic nature of such complicated mechanical systems has been disclosed. After 1980s, the mistuning effects and nonlinear effects are considered as two emerging research directions for the dynamic analyses of blisks.

Mistuning effect

For a perfectly tuned bladed disk or blisk, the full annulus can be considered as a cyclic symmetric structure. Each sector of a blisk is identical. In reality, it is very difficult to ensure the cyclic symmetry of blisks because of many uncertain factors, such as manufacturing tolerances, material imperfections, operational wearing and damages. These can break the cyclic symmetry of blisks leading to a variation of their natural frequencies and mode shapes

from their designed one [21]. This effect is named as the mistuning effect. In the worst scenario, the mistuning effect can lead to mode localization phenomena, the modal energy is transferred and confined to a certain set of blades [193]. The vibration amplitude of this set of blades can be slightly greater than the expectation. Consequently, the mistuning effect can reduce the durability of blades resulting in a lower HCF endurance.

Nonlinear effect

The dynamic responses of blisks with various nonlinear characteristics have become an important research field that is able to improve the design of future turbomachinery. Three of the most important nonlinearities of blisks are from: material nonlinearities, geometric nonlinearities and friction joints. For fan blades, composite materials have become a popular choice in industries. One source of material nonlinearities relates to the viscoelastic behaviour in polymeric matrices or the plasticity in metal matrices [4]. Geometric nonlinearities are another non-negligible nonlinearity under the presence of a large deformation. This usually happens to the blade rather than the disk, since the latter one is too stiff and large deformation is almost impossible. Contact with friction for friction joints exhibits a strong non-smooth nonlinearity. These nonlinear characteristics caused by friction behaviour have a significant effect on the global dynamic behaviour of blisks, such as a shift of the resonant frequency. Therefore, the nonlinear dynamic analysis for blisks is seen as a very crucial modelling strategy to capture the accurate dynamic response of blisks with various nonlinearities.

1.3 Nonlinear Vibration

In a nonlinear system, the dynamic responses are very complicated and there are many phenomena, i.e. stiffening and softening effects [60, 120], modal interactions [135], internal resonances [111] and bifurcations [42, 144]. Therefore, using a linear dynamic analysis cannot capture the main features of such a nonlinear system. In turbomachinery industry, experimental testing can provide convincing results. However, it is time consuming and expensive to set up an experimental test rig in every step of the design process. The validated numerical tools can be considered as an efficient way to obtain credible results with a lower cost.

There are two numerical modelling strategies to investigate the dynamic response of a nonlinear system, which are forced response analyses [120, 126, 195, 198], and nonlinear modal analyses [77, 79, 92, 111, 117, 135, 154]. In forced response analyses, the structure is

excited by a harmonic force with a range of excitation frequency. Through that, the resonances can be identified and frequency response of such nonlinear system can be obtained. The structure can be tested by different values of the excitation forcing level to show the evolution of resonances with respect to the excitation forcing level. Apart from forced response analysis, nonlinear modal analysis has become a useful tool to investigate the resonances using nonlinear modes and other model properties. Nonlinear modes can be seen as a collection of resonant solutions in forced responses. The mode shape, the resonant frequency and the modal damping ratio of a nonlinear mode change with energy level of the system according to its energy-dependence. In nonlinear modal analysis, the evolution of the mode shape, the resonant frequency and the modal damping ratio with respect to the energy can be directly computed. Using nonlinear modal analysis can significantly improve the modelling efficiency and reduce the computation costs than using the forced response analysis.

1.4 Thesis Objectives and Outlines

The overall objective of this thesis is to develop a numerical methodology to analyse the nonlinear dynamic response of structures with friction damping. This numerical methodology is based on the nonlinear modal analysis. An academic blisk with a friction ring damper is considered as the application of this numerical methodology.

In nonlinear modal analysis, the nonlinear modes, the resonant frequency and the modal damping ratio can be efficiently calculated for a nonlinear structure. The resonant responses can be directly represented by nonlinear modes and the computation of full forced responses is not necessarily required. Using nonlinear modes can significantly improve the modelling efficiency and reduce the computational cost. Therefore, the first objective of the present thesis is to compare the existing numerical methods used for nonlinear modal analysis of structures with non-conservative nonlinearities.

However, it is difficult to directly relate each solution in nonlinear modes to resonant solutions in forced responses. The use of nonlinear modal analysis is highly limited by this disadvantage in engineering applications. The second objective of the present thesis is to develop a numerical method that can provide a direct relation between nonlinear modes and resonant solutions in the forced response. This numerical method is named as extended energy balance method.

Friction ring dampers are one of the emerging damping techniques for blisks. In the literature, most research about friction ring dampers are considered as proof-of-concept works. Therefore, the third objective of this thesis is using the developed numerical methods

to investigate the dynamic response, damping performance and geometric effects of friction ring dampers.

The present thesis is organized as following:

Chapter 2 introduces the fundamental dynamics of blisks. Besides that, the state of knowledge about various friction damping, different friction models and existing numerical methods used for nonlinear vibration are also provided. Furthermore, the model reduction methods in the literature are reviewed. Finally, the past works related to nonlinear modes are described.

Chapter 3 provides the detailed numerical formulations for existing numerical approaches to compute nonlinear modes for structures with friction joints. In addition, the formulations of extended energy balance method are derived for different existing approaches. After that, three illustrative testcases are tested using the described numerical methods to identify the benefits and limitations of each approach.

Chapter 4 shows the validation of the numerical methods used in the present thesis. The experimental setup and the model used for validation are described. The results from the numerical methods are compared with the existed experimental results from the literature. Then, a parametric study is provided to investigate the influence of contact angle and platform vertical position for underplatfrorm damper. Furthermore, Monte Carlo simulation is applied to investigate the effect caused by the uncertain parameters involved within the contact interface.

Chapter 5 demonstrates the nonlinear dynamic response of blisks with friction ring dampers using nonlinear modal analysis. An illustrative lumped parameter model is used to provide a qualitative understanding of dynamics of the blisk with ring damper. Then, a full-scale finite element model is used to represent the blisk with ring damper. A linear modal analysis, rotor dynamic analysis and nonlinear static analysis are applied in the first place. Then, the nonlinear modes and other modal properties are computed and used to study the damping performance and the dynamic responses of the blisk with friction ring damper.

Chapter 6 illustrates the geometric effects of the friction ring damper using the nonlinear modal analysis by exploring three design parameters. To reduce the computational costs, Kriging meta-models are used to explore the whole design space. The sensitivity of each design parameters is investigated using Sobol indices. The importance of designing damper geometry and some design guidelines are provided.

Chapter 2

State of Knowledge

2.1 Fundamental Dynamics of Blisk

2.1.1 Periodicity of mode

Bladed disks or blisks fall into a class of structure with a rotational periodicity or cyclic symmetry. This type of structure usually consists of a finite number of identical repeated substructures or sectors as shown in Fig.2.1, where S_{n_s} represents the n_s^{th} sector of a cyclic symmetric structure. Cyclic symmetric structures exhibit the same set of vibration modes. Based on this fact, the full annulus of such cyclic symmetric structures can be represented by one repeated sector with cyclic symmetric boundaries. In static or dynamic analyses, the modelling efficiency can be significantly improved by only using one sector.

For a perfect cyclic symmetric structure, the sector angle is defined as $2\pi/N_s$, where N_s is the total number of the repeated sectors. Thomas [174] provides a comprehensive explanation for the dynamics of structures exhibiting cyclic symmetry. In a modal analysis of cyclic structures, most vibration modes appear in a pair of modes with a same natural frequency and orthogonal mode shapes. All possible modes can be considered as the same mode shape among identical sectors with a phase shift ϕ_p between adjacent sectors, ϕ_p is defined in Eqn.(2.1), where p is the periodicity of the mode and also known as Nodal Diameter (ND). ND is defined as the number of diameters with zero displacements in a cyclic symmetric structure. The displacements between adjacent blades are defined in Eqn.(2.2), $\underline{u}_{r,n_s}$ and $\underline{u}_{l,n_s}$ are the Degrees of Freedoms (DoFs) in the right and left frontier of n_s sector and $\underline{u}_i$ represents the internal DoFs. Generally, the DoFs associating to the right frontier at n_s sector $\underline{u}_{r,n_s}$ is considered to be identical to the DoFs of the left frontier at the n_s+1 sector $\underline{u}_{l,n_s+1}$. The force applied to the adjacent left and right sector can be expressed as Eqn.(2.3).

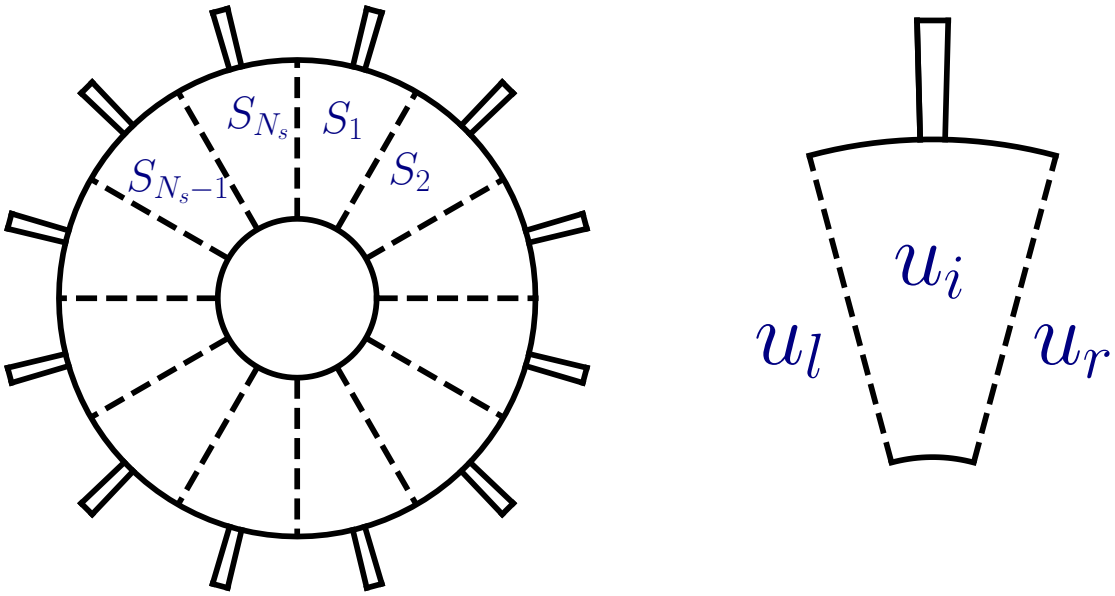


Fig. 2.1 Structure with cyclic symmetry and one repeated sector

Eqn.(2.3).

$$\phi_p = \frac{2\pi p}{N_s} \tag{2.1}$$

$$\underline{u}_{l,n_s+1} = \underline{u}_{r,n_s} = \underline{u}_{l,n_s} e^{i\phi_p} \tag{2.2}$$

$$\underline{F}_{l,n_s+1} = \underline{F}_{r,n_s} = \underline{F}_{l,n_s} e^{i\phi_p} \tag{2.3}$$

The general Equation of Motion (EoM) of a sector can be repartitioned into a form among the left DoFs, the internal DoFs and the right DoFs, as shown in Eqn.(2.4). Then, applying Eqn.(2.1-2.3) into Eqn.(2.4), the right DoFs can be expressed by the left DoFs.

$$\begin{bmatrix} \underline{\underline{\mathbf{M}}}_{ii} & \underline{\underline{\mathbf{M}}}_{il} & \underline{\underline{\mathbf{M}}}_{ir} \\ \underline{\underline{\mathbf{M}}}_{li} & \underline{\underline{\mathbf{M}}}_{ll} & \underline{\underline{\mathbf{M}}}_{lr} \\ \underline{\underline{\mathbf{M}}}_{ri} & \underline{\underline{\mathbf{M}}}_{rl} & \underline{\underline{\mathbf{M}}}_{rr} \end{bmatrix} \begin{bmatrix} \ddot{\underline{u}}_i \\ \ddot{\underline{u}}_l \\ \ddot{\underline{u}}_r \end{bmatrix} + \begin{bmatrix} \underline{\underline{\mathbf{K}}}_{ii} & \underline{\underline{\mathbf{K}}}_{il} & \underline{\underline{\mathbf{K}}}_{ir} \\ \underline{\underline{\mathbf{K}}}_{li} & \underline{\underline{\mathbf{K}}}_{ll} & \underline{\underline{\mathbf{K}}}_{lr} \\ \underline{\underline{\mathbf{K}}}_{ri} & \underline{\underline{\mathbf{K}}}_{rl} & \underline{\underline{\mathbf{K}}}_{rr} \end{bmatrix} \begin{bmatrix} \underline{u}_i \\ \underline{u}_l \\ \underline{u}_r \end{bmatrix} = \begin{bmatrix} \underline{0} \\ \underline{0} \\ \underline{0} \end{bmatrix} \tag{2.4}$$

$$\underline{\underline{\mathbf{M}}}_{cyc,p} = \begin{bmatrix} \underline{\underline{\mathbf{M}}}_{ii} & \underline{\underline{\mathbf{M}}}_{il} + e^{-i\phi_p}\underline{\underline{\mathbf{M}}}_{ir} \\ \underline{\underline{\mathbf{M}}}_{li} + e^{i\phi_p}\underline{\underline{\mathbf{M}}}_{ri} & \underline{\underline{\mathbf{M}}}_{ll} + \underline{\underline{\mathbf{M}}}_{rr} + \underline{\underline{\mathbf{M}}}_{rl} + e^{i\phi_p}\underline{\underline{\mathbf{M}}}_{lr} + e^{-i\phi_p}\underline{\underline{\mathbf{M}}}_{rl} \end{bmatrix} \tag{2.5}$$

$$\underline{\underline{\mathbf{K}}}_{cyc,p} = \begin{bmatrix} \underline{\underline{\mathbf{K}}}_{ii} & \underline{\underline{\mathbf{K}}}_{il} + e^{-i\phi_p}\underline{\underline{\mathbf{K}}}_{ir} \\ \underline{\underline{\mathbf{K}}}_{li} + e^{i\phi_p}\underline{\underline{\mathbf{K}}}_{ri} & \underline{\underline{\mathbf{K}}}_{ll} + \underline{\underline{\mathbf{K}}}_{rr} + \underline{\underline{\mathbf{K}}}_{rl} + e^{i\phi_p}\underline{\underline{\mathbf{K}}}_{lr} + e^{-i\phi_p}\underline{\underline{\mathbf{K}}}_{rl} \end{bmatrix} \tag{2.6}$$

$$\underline{\underline{\mathbf{M}}}_{cyc,p}\begin{bmatrix}\underline{\ddot{u}}_i\\ \underline{\ddot{u}}_l\end{bmatrix}+\underline{\underline{\mathbf{K}}}_{cyc,p}\begin{bmatrix}\underline{u}_i\\ \underline{u}_l\end{bmatrix}=\begin{bmatrix}\underline{0}\\ \underline{0}\end{bmatrix} \tag{2.7}$$

Then, the eigenfrequencies and the mode shapes can be computed using an isolated sector with a known periodicity of mode p using Eqn.(2.8). If ϕ_p equals zero, in this case, each sector has the same mode shape and vibrate in phase with its neighbouring sector, where $\underline{u}_{r,n_s}=\underline{u}_{l,n_s}=\underline{u}_{r,n_s+1}$ and n_s is the number of sectors $n_s=1,2,3,\cdots,N_s$. This mode is a standing wave mode with only single eigenfrequency and mode shape and is also known as the mode with ND 0. Whereas if ϕ_p equals to π, each sector has the same mode shape as its neighbours but it vibrates in anti-phase, leading to $\underline{u}_{r,n_s}=-\underline{u}_{l,n_s}=-\underline{u}_{r,n_s+1}$. These modes are known as the mode with ND $N_s/2$ and only if the total number of sectors N_s is even.

$$(\underline{\underline{\mathbf{K}}}_{cyc,p}-\omega^2\underline{\underline{\mathbf{M}}}_{cyc,p})\begin{bmatrix}\underline{u}_i\\ \underline{u}_r\end{bmatrix}=\begin{bmatrix}\underline{0}\\ \underline{0}\end{bmatrix} \tag{2.8}$$

2.1.2 Engine order excitation

In an industrial turbomachinery, the Engine Order (EO) excitation is a common source of excitation for rotating structures. EO excitation force is based on the fact that the rotors are rotating in a steady flow with a non-uniformity around the full annulus. The non-uniformity of the flow is generally caused by the non-uniformity of the intake, like the presence of vanes and the rotating bladed disks. Therefore, the gas stream exerts a non-uniform pressure and flow intensity around the full annulus of the blisk. This type of excitation force has a frequency, which relates the engine order *eo* and its rotational speed. *eo* is an integer to represent the non-uniformity of the spatial variation around the full annulus. The spatial variation of flow can be decomposed by applying a Fourier transformation into spatial harmonics. The excitation with a specific harmonic can only excite the mode with the same periodicity [83].

Campbell diagram is an efficient way to show the characteristics of EO excitations in forced responses. In Fig.2.2, an example Campbell diagram is given: black oblique lines represent excited EO excitations; grey oblique lines for unexcited EO excitations; red curves for the change of natural frequencies against the rotational speed; the resonances caused by EO excitation force are shown by blue markers. The excitation frequency Ω_e equals the product of *eo* and the rotational speed Ω, $\Omega_e = eo\times\Omega$. The natural frequencies can change with the rotational speed due to the stiffening effect, while a rotating structure experience a centrifugal force. From the Campbell diagram, they are plenty of crossing points between the black oblique lines and the red curves. But only a few of them represents the resonances

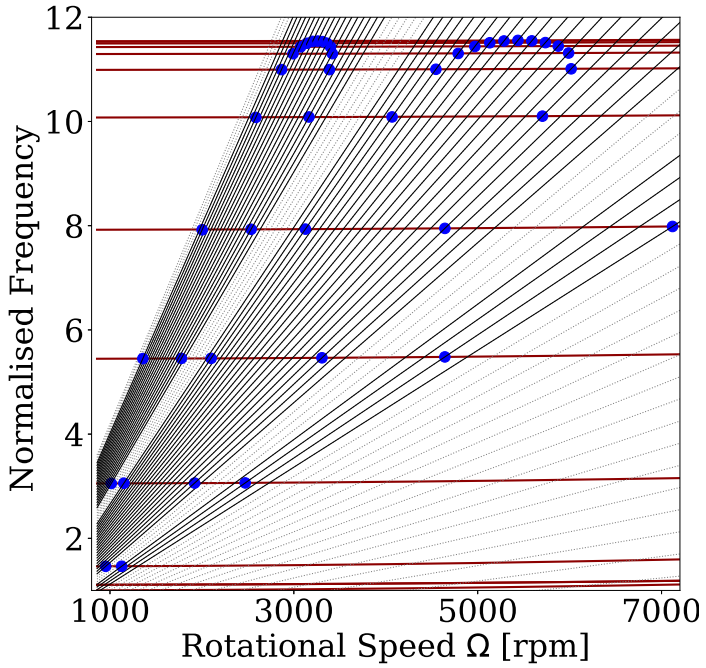


Fig. 2.2 An example of Campbell diagram: black lines: excited engine order excitation force; grey lines: unexcited engine order excitation force; red curves: natural frequency; blue markers: resonance caused by engine order excitation force.

excited by EO excitations. The resonance occurs when excitation frequency with a specific harmonic coincides with natural frequency with same ND. The relation between ND and EO excitation will be derived and discussed later in this section.

2.1.3 Relation between engine order and nodal diameter

The mode with a specific ND p can be only excited by the EO excitation with a certain order eo. A typical zig-zag diagram is usually used to represent the relation between eo and p. If the EO excitation force is considered in the form of harmonics with an order of n_h. N_h is the maximum order of harmonics used. Ω is the engine rotational speed. N_s is the total number of sectors. Then, the general excitation force for a reference sector can be written as Eqn.(2.9). For n_s^{th} sector, the excitation force can be represented as Eqn.(2.10).

$$F_{ref}(t) = \sum_{n_h=1}^{N_h} f^{c,n_h} \cos(n_h \cdot eo \times \Omega t) - f^{s,n_h} \sin(n_h \cdot eo \times \Omega t) \tag{2.9}$$

$$F_{n_s}(t) = \sum_{n_h=1}^{N_h} f^{c,n_h} \cos[n_h \cdot eo(\Omega t - \frac{2\pi(n_s-1)}{N_s})] - f^{s,n_h} \sin[n_h \cdot eo(\Omega t - \frac{2\pi(n_s-1)}{N_s})] \tag{2.10}$$

The Fourier transformation is applied to Eqn.(2.10), and we can arrive at Eqn.(2.11). After a simplification of right-hand-side of Eqn.(2.11), Eqn.(2.12-2.13) are obtained. j represents the imaginary part.

$$\tilde{F}_p^{n_h,A} - j\tilde{F}_p^{n_h,B} = \frac{2}{N_s} \sum_{n_s=1}^{N_s} f^{c,n_h} \cos[n_h \cdot eo(\Omega t - \frac{2\pi(n_s-1)}{N_s})] - f^{s,n_h} \sin[n_h \cdot eo(\Omega t - \frac{2\pi(n_s-1)}{N_s})] e^{-j2\pi \cdot p \cdot (n_s-1)/N_s} \tag{2.11}$$

$$\tilde{F}_p^{n_h,A} = \frac{f^{c,n_h}}{N_s} [e^{-j \cdot n_h \cdot p \cdot \Omega t} \sum_{n_s=1}^{N_s} e^{j2\pi(n_h \cdot eo - p)(n_s-1)/N_s} + e^{j n_h p \Omega t} \sum_{n_s=1}^{N_s} e^{-j2\pi(n_h \cdot eo + p)(n_s-1)/N_s}] \tag{2.12}$$

$$\tilde{F}_p^{n_h,B} = \frac{f^{s,n_h}}{N_s} [e^{-j \cdot n_h \cdot p \cdot \Omega t} \sum_{n_s=1}^{N_s} e^{j2\pi(n_h \cdot eo - p)(n_s-1)/N_s} - e^{j \cdot n_h \cdot p \cdot \Omega t} \sum_{n_s=1}^{N_s} e^{-j2\pi(n_h \cdot eo + p)(n_s-1)/N_s}] \tag{2.13}$$

In the case of $n_h \cdot eo + p = z \cdot N_s$, where z is a positive integer:

$$\tilde{F}_p^{n_h,A} - i\tilde{F}_p^{n_h,B} = (f^{c,n_h} + if^{s,n_h}) e^{j \cdot n_h \cdot eo \cdot \Omega t} \tag{2.14}$$

Whereas in the case of $n_h \cdot eo - p = z \cdot N_s$:

$$\tilde{F}_p^{n_h,A} - i\tilde{F}_p^{n_h,B} = (f^{c,n_h} - if^{s,n_h}) e^{-j \cdot n_h \cdot eo \cdot \Omega t} \tag{2.15}$$

In other cases, the coefficients $\tilde{F}_p^{n_h,A}$ and $\tilde{F}_p^{n_h,B}$ are zero. From the derivation of equations, EO excitation with an order eo and a harmonic n_h can only excite the mode with ND p, that satisfies the following relations:

$$n_h \cdot eo \pm p = z \cdot N_s \tag{2.16}$$

The maximum ND can be achieved is $N_s/2$ if N_s is an even number or $(N_s-1)/2$ if N_s is an odd number. A zig-zag diagram is used to demonstrate the relation between EO and ND, as shown in Fig.2.3. Figure 2.3(a) shows the relation of ND and EO in the case of the total number of sectors is even, whereas the other case (odd) is provided in Fig.2.3(b). Several

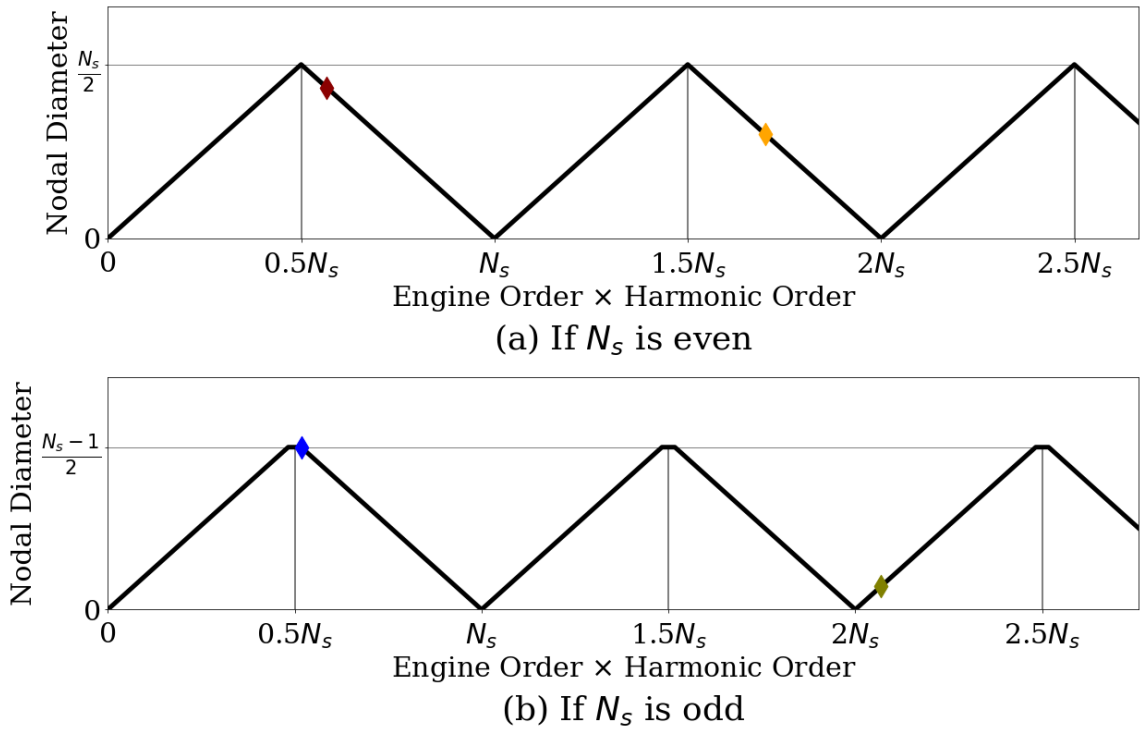


Fig. 2.3 Examples of zig-zag diagram

examples are provided in Tab. 2.1 and highlighted in Fig.2.3. There are four examples provided in the table, two of them for a cyclic symmetric structure with an even N_s; the others for an odd N_s. By looking at the Example 1, if the EO is 17 with the first order of harmonic, the mode with ND 13 is excited as shown by the red diamond in Fig.2.3(a). Whereas the mode with ND 9 is excited if the third order harmonic is considered (yellow diamond in Fig.2.3(a)). When considering the Example 3 and Example 4, the total number of sectors is 29, therefore the maximum ND is $(N_s - 1)/2 = 14$. The EO 15 with the first harmonic will excite the mode with ND 14 and the third harmonic for ND 2, as shown in Fig.2.3(b).

Table 2.1 Examples of the relation between engine order and nodal diameter

	Example 1	Example 2	Example 3	Example 4
Number of sectors N_s	30	30	29	29
Engine order eo	17	17	15	15
Harmonic order n_h	1	3	1	4
Nodal diameter p	13	9	14	2

2.2 Friction Damping in Turbomachinery

2.2.1 Various friction damping for assembled bladed disks

Most friction damping mechanisms come from the contact interfaces within the mechanical joints, that are either inherent to the bladed disks or additionally introduced. Various types of friction damping mechanisms have been studied in the literature and are shown in Fig.2.4: root joints [6, 127, 151, 198], tip shrouds [55, 157, 171] and UnderPlatform Dampers (UPDs) [7, 43, 45, 114, 115, 120, 118, 147]. Root joints and tip shrouds can be considered as the damping mechanism inherent to assembly of the bladed disks, whereas UPDs are regarded as the most popular way to add additional damping. Effectiveness of such friction damping techniques have been demonstrated using both numerical simulations and experimental testing [169, 83, 147].

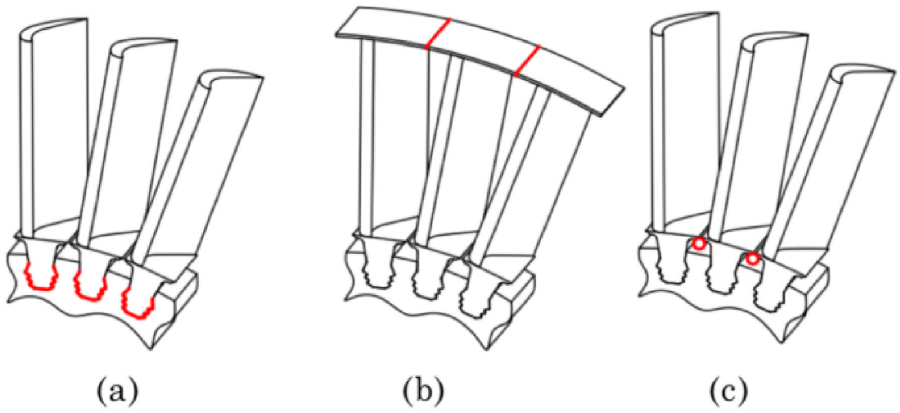


Fig. 2.4 Various types of friction damping [83]: (a) Root joints; (b) Tip shrouds; (c) Underplatform dampers

An appropriate design of mechanical joints can lead to a considerable dissipation of the vibration energy and a significant reduction in the resonant amplitude. Thus, the reliability of bladed disk structures can be significantly improved and the costs related to the fatigue issues can be effectively reduced. Furthermore, the bladed disks with a higher reliability can enhance the potential blade design and extend the range of tolerable working condition leading to a significant improvement on the efficiency of industrial turbomachinery. An example of friction dampers used for fan blades in a commercial aircraft engine CFM56-5A is provided in Fig.2.5 [99].

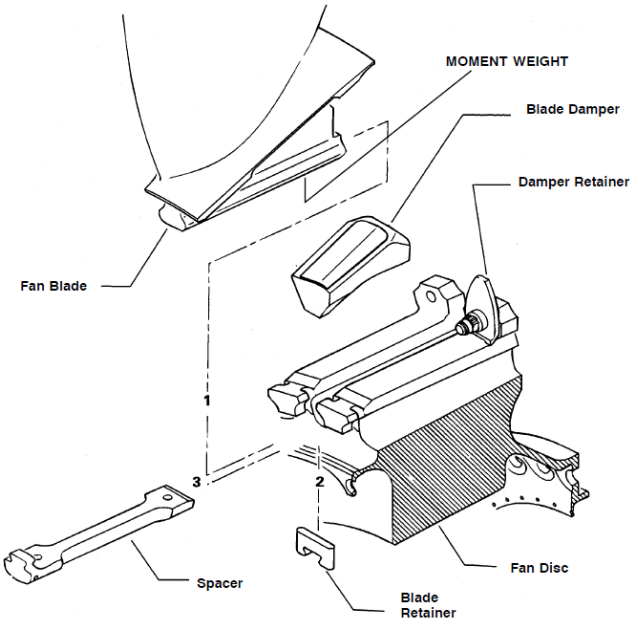


Fig. 2.5 Dampers used for fan blades in an aircraft engine CFM56-5A [99]

2.2.2 Friction ring dampers for blisks

The use of blisks instead of the traditional bladed disks is very popular in turbomachinery industries nowadays. The classic assembled bladed disks consist of a disk with several individual blades and assembled using root joints. The contact interfaces within the root joints can provide friction damping to dissipate the vibration energy. Whereas in blisks, the disk and blades are manufactured in a single piece component leading to a reduction of mass and a better aerodynamic performance. But the absence of contact interfaces in root joints gives a low internal damping. Therefore, an alternative damping source is introduced for blisks to add an external friction interface for extra damping. An emerging technique is the use of friction ring dampers. This friction ring damper is located in the groove of the blisk and is held against the disk by centrifugal forces. The friction ring has a small open gap which is used to apply the preload.

Ring dampers in labyrinth air seals

Friction ring damper was first used in labyrinth air seals by Niemotka and Ziegert [113] in 1995. In their work, the damping performance of an open ring was investigated and optimized for labyrinth air seals, as shown in Fig.2.6(a). The ring damper can have either a circular cross section or a rectangular cross section. To model the damping performance, only elastic

deformation was considered and the energy dissipation per vibration cycle was calculated to represent the damping ability. Then, based on this modelling strategy, the ring damper was optimized for five design parameters including: the damper diameter D, the interface radius R_F, the axial location along the seal L, the friction coefficient μ and the damper aspect ratio h/W (if a rectangular cross section is considered). From the optimization, both the optimum circular and rectangular dampers were found at the minimum interface radius R_F and the maximum friction coefficient μ. For a ring damper with a circular cross section, the optimal design has the largest diameter and is located at the far end of the seal. Whereas for a rectangular damper, the optimum damper was found to have a height of 6.75 *mm* and width 7.5 *mm*. The energy dissipation with respect to the modal amplitude were calculated and shown in their work. In Niemotka and Ziegert's work [113], the effectiveness of friction ring dampers was first studied and some useful design guidelines were also provided. In addition, the importance of normal load applied on the damper was identified as well.

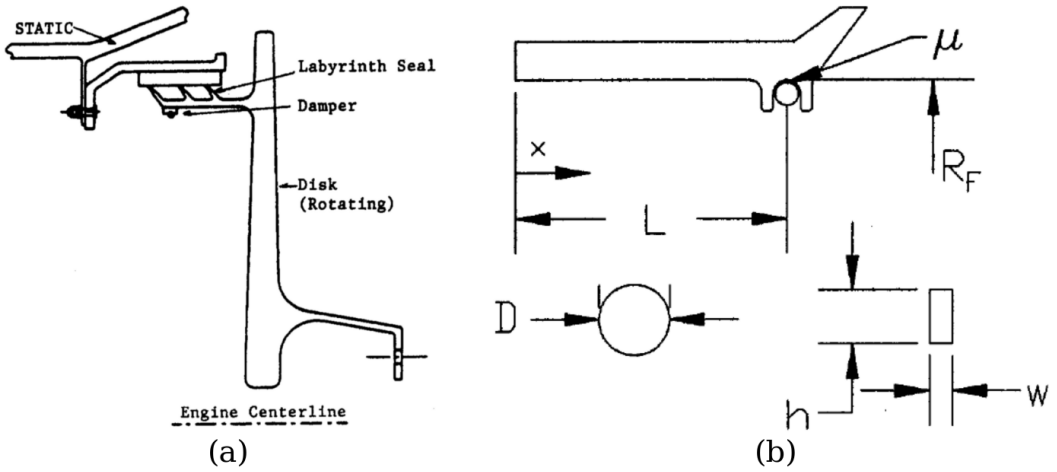


Fig. 2.6 Ring dampers in labyrinth air seals by Niemotka and Ziegert [113]: (a) An overview of ring damper in labyrinth air seal; (b) Design parameters in the optimization process

Ring dampers in gears

In aviation gears, friction ring dampers are also known as an efficient damping technique [197, 184]. An example of a Finite Element (FE) model for a gear with friction ring damper is provided in Fig.2.7(a) [184]; the mode shape of a gear with ring damper is also provided in Fig.2.7(b) [197].

Zucca *et al* [197] demonstrated a method to design the friction ring damper for industrial gears using the classic forced response analysis. A full-scale FE model was used to represent a sector of gear and ring damper, the friction forces within the contact interface were simulated using classic 3D contact elements. The numerical methods used for nonlinear vibration analyses were used to obtain the nonlinear forced response. From [197], they found out the optimal damper mass and friction coefficient. The increase in the damper mass and friction coefficient can lead to a situation that the ring damper is fully stuck to the gear and no energy is dissipated. Furthermore, by varying the torque applied to the gear and damper, one can achieve a robust design of ring damper, in that case, the damping ability is insensitive to the torque level.

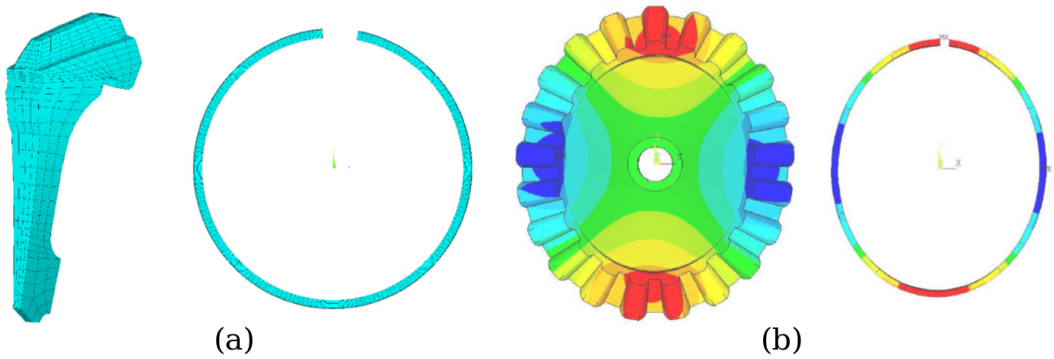


Fig. 2.7 Ring dampers in gears: (a) Finite element model of the ring damper in a gear by Wang *et al* [184]; (b) Mode shape of the targeting mode for the gear and ring damper by Zucca *et al* [197]

Wang *et al* [184] described another method to evaluate the damping performance using the linear mode shape without the computation of nonlinear dynamic responses. An open ring damper and full annulus of the gear were studied in their work. Then, an equation that governs the bending strain of the damper, and the strain caused by friction was used to identify the sliding and sticking regions within the full annulus of the gear and damper. Then, the energy dissipation was calculated by integrating the friction force and the relative displacement based on the sticking/sliding regions. Using such a method, the curves representing the relation between the energy dissipation and the vibration amplitude can be obtained. The influences of many design factors were investigated and discussed, including the gear rotational speed, the working temperature, the damper density and the friction coefficient.

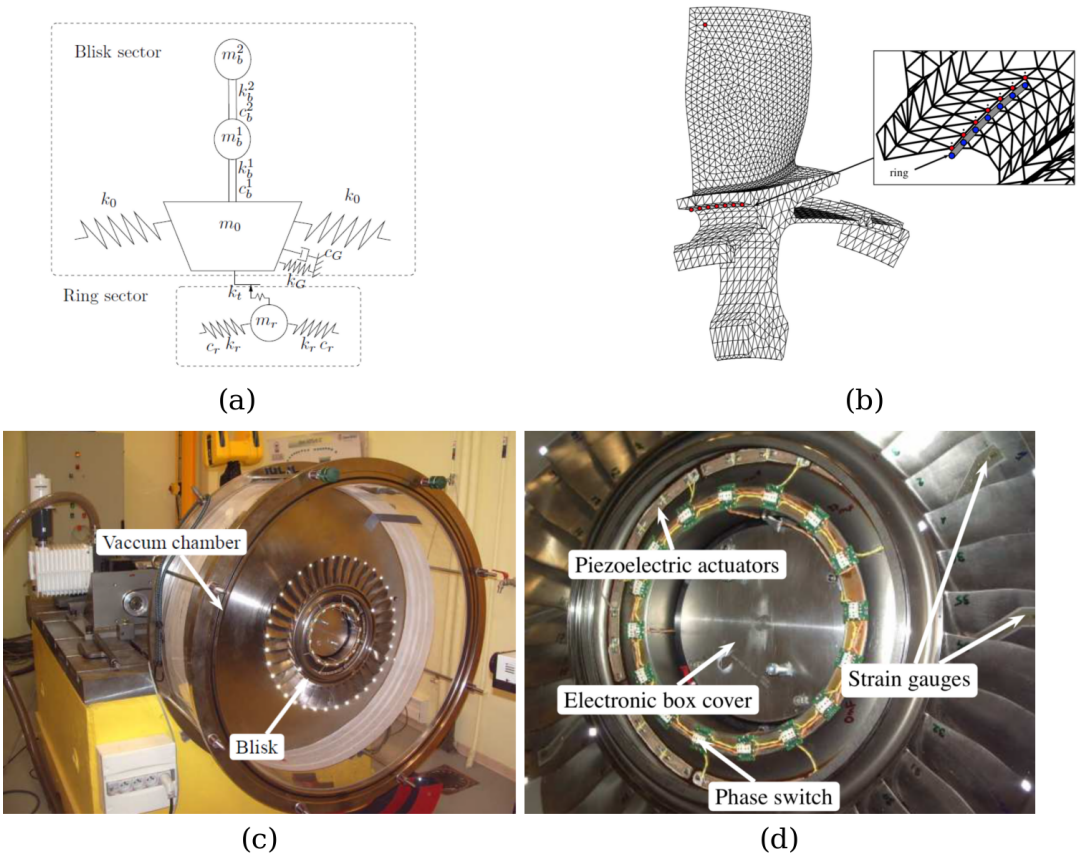


Fig. 2.8 Ring dampers for blisks from Laboratoire de Tribologie et Dynamique des Systemes at École Centrale de Lyon: (a) Lumped parameter model [94]; (b) FE model [90, 91, 93]; (c-d) Experimental test rig [90]

Ring dampers in blisks: Research from École Centrale de Lyon

At École Centrale de Lyon, several researchers have been attempted to investigate the friction ring dampers for blisks in different ways. The first qualitative study of friction ring dampers for blisks was attempted by Laxalde *et al.* [94]. In their work, the blisk with friction ring damper was modelled using a lumped parameter model (see Fig.2.8(a)), with three DoFs for a sector of blisk and another one for a sector of ring. A nonlinear forced response analysis was applied on such an illustrative model to compare the damping ability for different modes (a blade dominated mode and a disk dominated mode). The effects of the damper mass and the normal load were also investigated. Furthermore, a mistuning effect caused by the open ring damper was also demonstrated. In summary, the friction ring damper has been proven to be an efficient damping technique only for disk dominated modes. The existence of open gap in ring damper cannot significantly affect the damping performance.

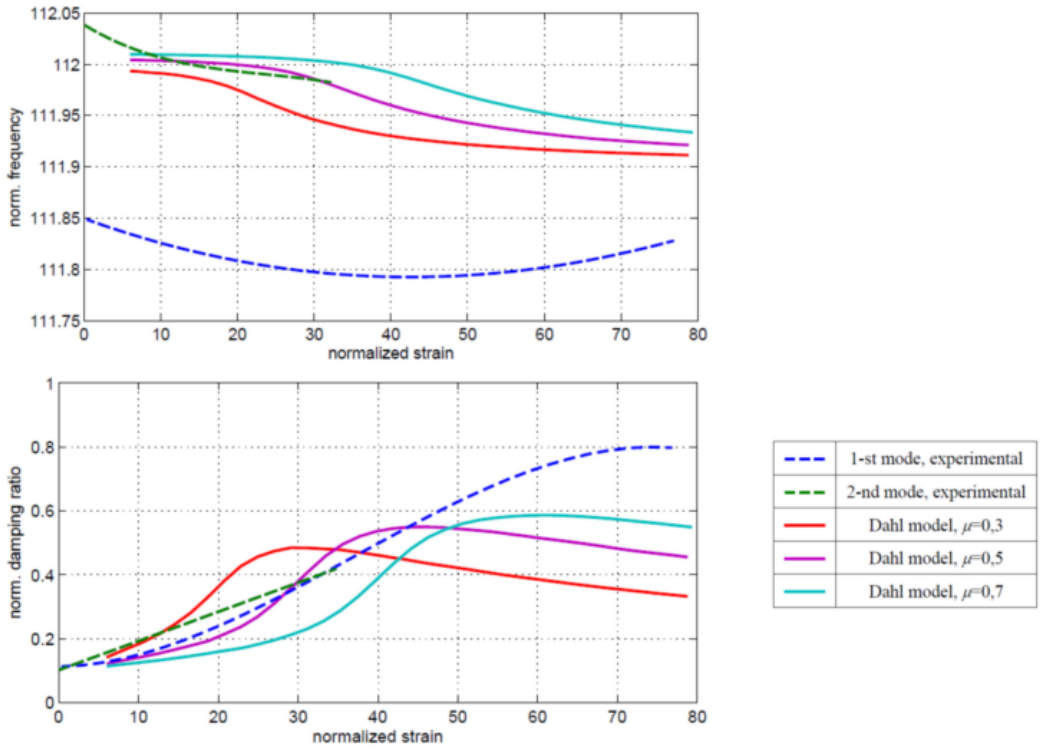


Fig. 2.9 Main results from the experimental testrig for a rotating blisk with a friction ring damper [90]

The nonlinear dynamic analysis of a full-scale blisk with a friction ring damper was attempted, as shown in Fig.2.8(b) [90, 91, 93]. The FE model used for the blisk consists of 36 sectors. The ring damper was assumed to have a constant circular cross section around the circumferential direction. The open gap within the friction ring damper was ignored. Then, the full annulus of the blisk and ring damper was modelled by a sector with cyclic symmetric boundaries conditions. A nonlinear modal analysis was achieved by Laxalde *et al.* [91]. Using nonlinear modal analyses, the evolution of modal damping ratio against the vibration amplitude can be directly computed by solving the nonlinear autonomous dynamic equation. The nonlinear modal analysis was firstly attempted for a full-scale structure with friction damper in [91]. Then, the nonlinear forced response analysis was completed by Laxalde *et al.* [93]. In this work, they found that most energy dissipated usually happened when the motion of the contact interfaces features an alternating stick and sliding contact condition.

The first experimental testrig for a blisk and a friction ring damper was achieved by Laxalde *et al.* [90]. The overview of experimental setup is shown in Fig.2.8(c). The test

structure is a high pressure compressor blisk with 36 blades and driven by an electric motor with a rotational speed upto 5000 rpm. The excitation was achieved by using 24 piezoelectric plates divided into 8 groups to obtain a better control of the mode excited (Fig.2.8(d)). The vibration amplitude of the rotating blisk was measured by 12 semiconductor strain gauges: 8 of them were attached to the suction side of the blades and the other 4 are on the disk. Using such experimental setup, the forced response of the rotating blisk was measured for different rotational speeds. The evolution of the resonant frequency and modal damping ratio with respect to the vibration strain (frequency-strain curves and damping-strain curves) was extracted from the experimental measured forced responses using a nonlinear modal identification technique. The nonlinear modal analysis was also applied to obtain the frequency-strain curves and damping-strain curves. The main results are provided in Fig.2.9. From the comparison between the experimental and numerical results, they pointed out that the addition efforts were expected to improve the numerical simulation.

Ring dampers in blisks: Research from University of Michigan

The dynamic analyses for blisks with friction ring dampers have been investigated by several researchers in University of Michigan [9, 100, 101, 172, 173]. Baek and Epureanu [9] described a Reduced Order Modelling (ROM) method for blisks with friction ring dampers. The FE model studied in this work is shown in Fig.2.10(a). In their work, the contact forces within the contact interface were modelled by assuming an elastic body and calculated by means of quasi-static analysis. An equivalent structural damping was used to model the dissipative effect of the contact interfaces, whereas the equivalent stiffness was used to model the elastic behaviour in stick contact conditions. After that, instead of the direct applying the friction law in the dynamic equation, this equivalent structural damping and stiffness were used to build the reduced order model, based on one sector with cyclic symmetric boundaries conditions. The results from the reduced model were compared with the full model. This reduced model can provide accurate steady-state response with a significant reduction in computational time.

Tang and Epureanu [172] described a ROM method named as the method of coherent ring damper, or CoRiD. A full annulus of the blisk with friction ring damper was studied in this work as shown in Fig.2.10(a). In this method, they pointed out that the all possible dynamic responses are considered as an intermediate state between the full stick case and full sliding case. This statement is based on the fact that the ring damper is small enough that the ring damper can only have limited effects on the dynamic responses of the blisk. Using this method can significantly reduce the number of DoFs within the contact interface. Then, the

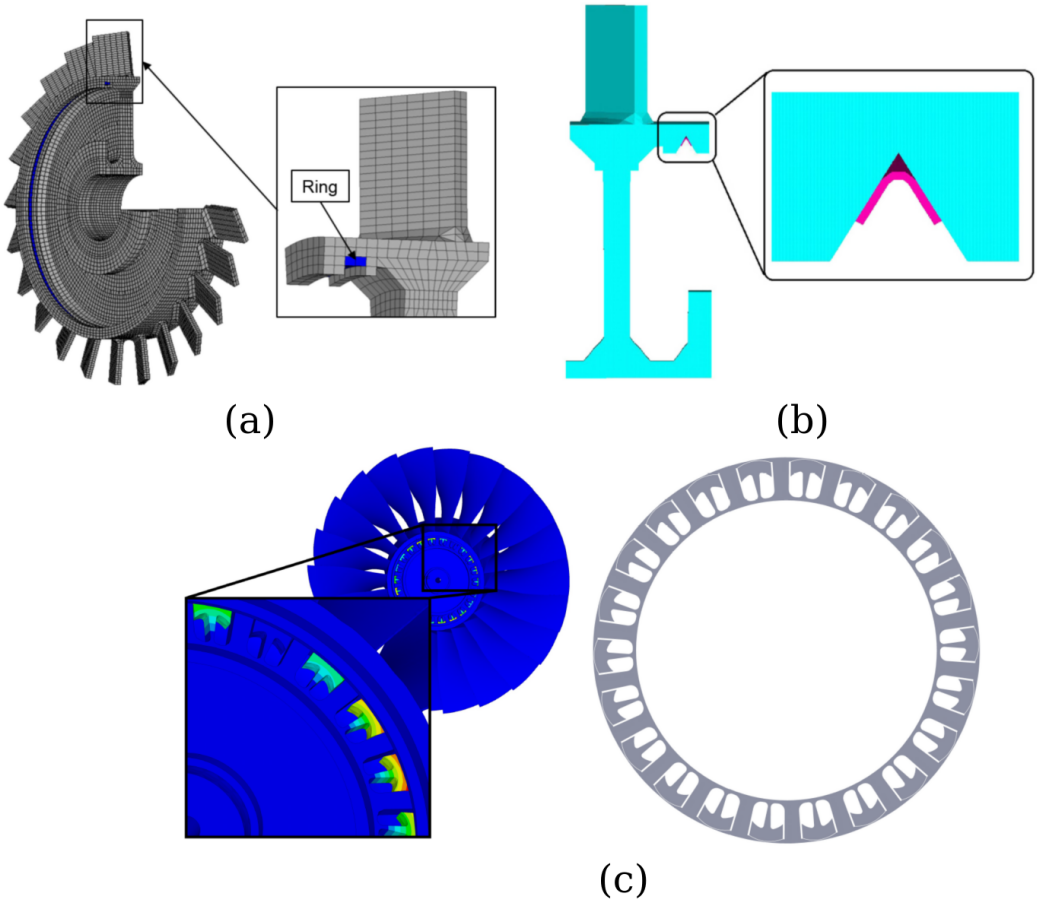


Fig. 2.10 Ring dampers for blisks from University of Michigan : (a) FE model [9, 101, 172]; (b) FE model [173]; (c) FE model [100]

influences of the random blade mistuning patterns were investigated using classic nonlinear forced response analyses. From their work, they found that the tuned blisk system shows the lowest amplitude reduction ratio 37.9% by comparing with 100 mistuning patterns. The maximum amplitude reduction ratio of 100 mistuning patterns is 40.0%. In conclusion, an optimal damper designed for a tuned blisk shown a significant damping ability for a blisk with small mistuning patterns. A geometric design of the cross section for friction ring dampers was also done by Tang and Epureanu [173]. Using the CoRiD method made the geometric design possible. In the first part of [173], they found that variation of a V-shaped damper (Fig.2.10(b)) cannot improve the damping performance. Then, several different cross sections of the ring damper were designed, i.e. a cone-shaped damper, double-cone shaped damper so on. From [173], the effect of the cross section of the ring damper was

firstly attempted and the importance of the designing the cross section of the ring damper was highlighted.

Lupini and Epureanu [100, 101] proposed an idea that treating the friction ring damper as a tuned vibration damper. To achieve that, it is necessary to tune the damper ensuring that one of its natural frequencies matches the blisk's natural frequency of the target mode. Then, the vibration energy of the blisk can be transferred to the ring damper, and the relative displacements between the blisk and ring damper are enlarged to achieve a better damping performance. In [100], a friction ring damper with oscillator beams were designed, as shown in Fig.2.10(c). The presence of the oscillator beam made the tuning of the damper much easier by simply changing the head mass. In addition, the blisk can be kept as its original condition and avoided the wearing effect caused by the rubbing motion of the ring damper.

Ring dampers with piezoelectric material

Friction ring dampers coupled with piezoelectric materials are an emerging research direction in the turbomachinery field. Liu *et al.* [96] compared the dynamic responses of a blisk with a ring damper and a piezoelectric synchronized switch damper using a lumped parameter model. Compared with the friction ring damper, this piezoelectric synchronized switch damper shown a smaller variation in its resonant frequencies. The damping ratio is less sensitive to the excitation forcing level. Furthermore, Wu *et al.* [190] designed a dry friction and piezoelectric hybrid ring damper for a blisk using a lumped parameter model and a full-scale structure through a nonlinear modal analysis. However, the use of piezoelectric materials in the aircraft engine compressors or turbines is still an open question. It is difficult to ensure the durability and strength of the piezoelectric materials under extreme working conditions.

2.2.3 Geometric optimization of friction dampers

Several researchers have been involved in working on the dynamic analysis of blisks with various friction dampers through numerical simulations and experimental tests [90, 118, 120]. The use of friction damper has been proven to be an efficient way to reduce the vibration amplitude of blisk structures. The accuracy of numerical simulations is also proved in the literature [118, 120]. Therefore, academia was started to work on the optimization of friction dampers using validated numerical methods.

Most of optimization studies of friction dampers are on the basis of a parametric simulation method of nonlinear forced responses through a finite number of evaluations of

the design parameters. Design of UPDs have been attempted by several researchers [43–45, 114, 115, 195]. In [195], Yuan *et al.* carried out a geometric optimization of UPDs using a surrogate model. For friction ring dampers, only a few researchers tried to study the geometric effects of friction ring dampers. As mentioned in Section 2.2.2, Tang and Epureanu [173] investigated the effectiveness of a ring damper with different cross sections through a parametric study. The geometric effects of friction ring dampers are still of interest and need to be further studied.

2.3 Constitutive Models for Friction

Current friction models can be simply classified into two main groups: dry friction models (also known as velocity-based friction models) and dynamic friction models [17, 46]. Dry friction models explicitly provide the insight of the relation between the velocity and friction force. Whereas, the dynamic friction models are used in dynamic analyses, where the friction forces are calculated based on loading histories.

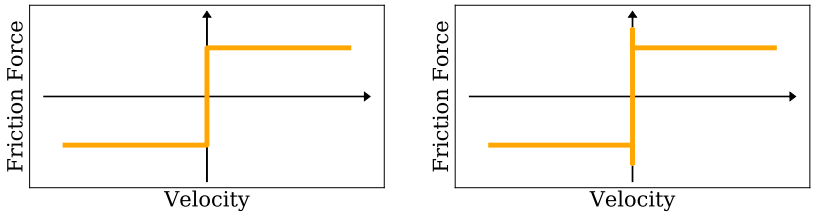
2.3.1 Dry friction models

There are four different dry friction models: Coulomb friction, stiction, viscous friction and Stribeck friction. The demonstration of each friction models is provided in Fig.2.11.

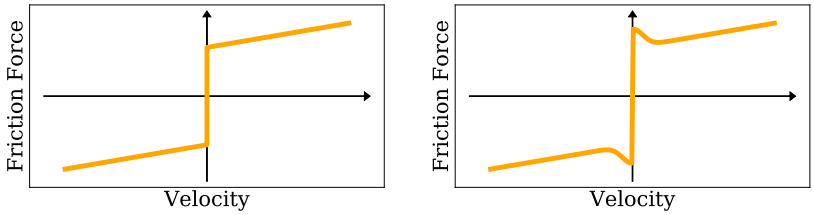
Coulomb friction

Guillaume Amontons [5] defined the laws of friction in the 17^{th} century, stating that friction force is independent of the apparent area of the contact interfaces and it is proportional to the normal force applied on the contact interfaces. After that, Charles-Augustin de Coulomb [27] stated that friction force is independent of the sliding velocity in the 18^{th} century. The first friction model is defined as Amontons-Coulomb friction or Coulomb friction model [129]. In the Coulomb friction model, the friction force F is defined as product of the normal load N_0 and the friction coefficient μ in the opposite direction of the sliding relative velocity V, as shown in Eqn.(2.17) and Fig.2.11(a). If the applied force is smaller than the Coulomb friction, the friction force equals the force applied F_{app}. In this situation, the velocity is zero.

$$F = \begin{cases} \mu N_0 \cdot \text{sign}(V) & \text{if} \quad V \neq 0 \\ F_{app} & \text{if} \quad V = 0 \quad \text{and} \quad F_{app} < \mu N_0 \end{cases} \tag{2.17}$$



(a) Coulomb Friction (b) Stiction



(c) Viscous Friction (d) Stribeck Friction

Fig. 2.11 Static friction models: (a) Coulomb friction; (b) Stiction; (c) Viscous friction; (d) Stribeck friction

Stiction

Morin [109] found out that the friction force at zero velocity is greater than the Coulomb friction. The stiction friction model includes the Morin's findings and considers the differences between the static friction coefficient μ_s and the dynamic friction coefficient μ_k, as shown in Eqn.(2.18) and Fig.2.11(b).

$$F = \begin{cases} \mu_k N_0 \cdot \text{sign}(V) & \text{if} \quad V \neq 0 \\ F_{app} & \text{if} \quad V = 0 \quad \text{and} \quad F_{app} < \mu_s N_0 \end{cases} \tag{2.18}$$

Viscous friction

Reynolds defined the viscous friction which is associated with the lubrication by combining the viscous effect and the Coulomb friction. As shown in Eqn.(2.19) and Fig.2.11(c), k_v is the viscous coefficient.

$$F = \begin{cases} \mu N_0 \cdot \text{sign}(v) + k_v V & \text{if} \quad v \neq 0 \\ F_{app} & \text{if} \quad V = 0 \quad \text{and} \quad F_{app} < \mu N_0 \end{cases} \tag{2.19}$$

Stribeck friction

In 1902, Stribeck [162] found a fact that the friction force decreases with the relative velocity from the static friction to the Coulomb friction through an experimental work. This effect is

named as Stribeck effect. Stribeck friction is considered as a dry friction model that includes the Coulomb friction, the viscous effect, and the Stribeck effect. As shown in Eqn.(2.20) and Fig.2.11(d), V_c is the critical velocity.

$$F = (\mu_k N_0 + (\mu_s - \mu_k) N_0 e^{-(V/V_c)^j}) \text{sign}(V) + k_v V \tag{2.20}$$

2.3.2 Dynamic friction models

Dynamic friction models are the contact elements used in dynamic simulations. Contact elements defined the friction behaviour between two nodes. The use of these contact elements makes the accurate prediction of energy dissipation within the contact interface possible. A contact element can be applied by means of node-to-node or between a portion of contact interface represented by a single master node. The latter one is also known as patch-to-patch contact element. All existing dynamic friction models can be generally classified into two main groups: macroslip models and microslip models. The mircoslip effect is defined that parts of contact interface are fully sliding whereas other parts are stuck.

2.3.3 Macroslip models

Macroslip models are the contact elements that do not take the microslip effects into account. In this section, only node-to-node contact elements are explained and discussed. For node-to-node contact elements, the contact interface is discretised into a finite number of contact pairs (one of them from body A and the other one from body B). The frictional behaviour in the tangential contact plane shows a strong non-smoothness based on the Coulomb law. The pure non-smooth Coulomb friction in the tangential plane coupled by unilateral normal behaviour can be solved using dynamic Lagrangian mixed frequency–time method [110, 142, 141]. Most of macroslip models use the Jenkins element [71] to simulate the frictional behaviour instead of directly using Coulomb law. The Jenkins element is also known as a friction slider element. In Jenkins elements, the Coulomb friction is connected to an elastic spring (known as tangential contact stiffness) to represent the relation between the friction force and the relative displacement. Although, Jenkins elements cannot capture the microslip effect, it can still represent this phenomenon. If a contact interface is discretised into enough contact node pairs, an independent Jenkins element is assigned to each contact pair. Thus, the microslip effect can be simply replicated, since portions of discretised contact interface can slide whereas other parts can be stuck. Three main node-to-node contact elements (based on Jenkins elements) are available in the literature.

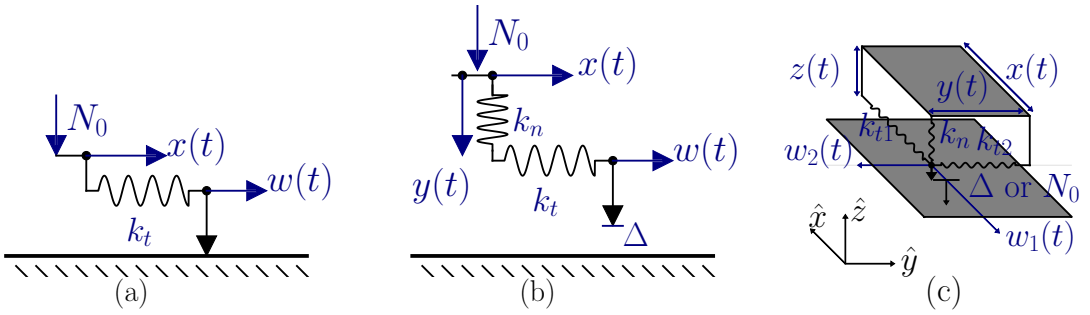


Fig. 2.12 Three contact elements: (a) One dimensional contact element (A Jenkins element in the tangential direction with a constant normal load); (b) Two dimensional contact element (A Jenkins element in the tangential direction with a unilateral spring); (c) Three dimensional contact element (Two Jenkins elements in the tangential plane with a unilateral spring)

1. *One dimensional contact element* This contact element consists of one Jenkins element in one tangential direction with a constant normal load [53], see Fig.2.12(a).

2. *Two dimensional contact element* This contact element consists of one Jenkins element in one tangential direction with a varied normal load [191], see Fig.2.12(b). The displacement in the normal direction is modelled by a unilateral spring with an initial normal load or gap.

3. *Three dimensional contact element* This contact element consists of two Jenkins elements in the tangential plane with a varied normal load [192], see Fig.2.12(c). The displacement in the normal direction is modelled by a unilateral spring with an initial normal load or gap.

The contact element 1 ignores the variation of normal load. This contact element cannot model partial separation during a vibration cycle. Whereas, contact elements 2 and 3 take the normal reaction into consideration. For all contact elements mentioned above, a pre-defined normal load (or an initial gap for contact element 2 and 3) is required to compute the periodic friction forces. This pre-defined normal load or gap usually comes from nonlinear static analyses or quasi-static analyses, which are regarded as a prerequisite work of dynamic analyses.

The three contact elements mentioned above and their numerical formulations will be described in the following section. Some results are provided as an example to demonstrate the main features of the contact element. It should be noticed that these contact elements are used to compute a periodic friction force using a periodic relative displacement.

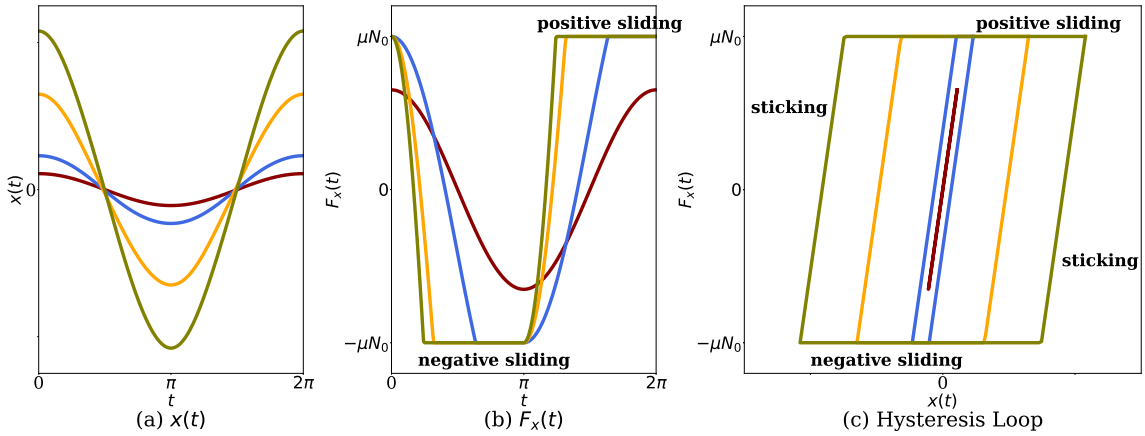


Fig. 2.13 Examples of friction forces and hysteresis loops for the one dimensional contact element: (a)$x(t)$; (b) $F_x(t)$; (c) Hysteresis loops

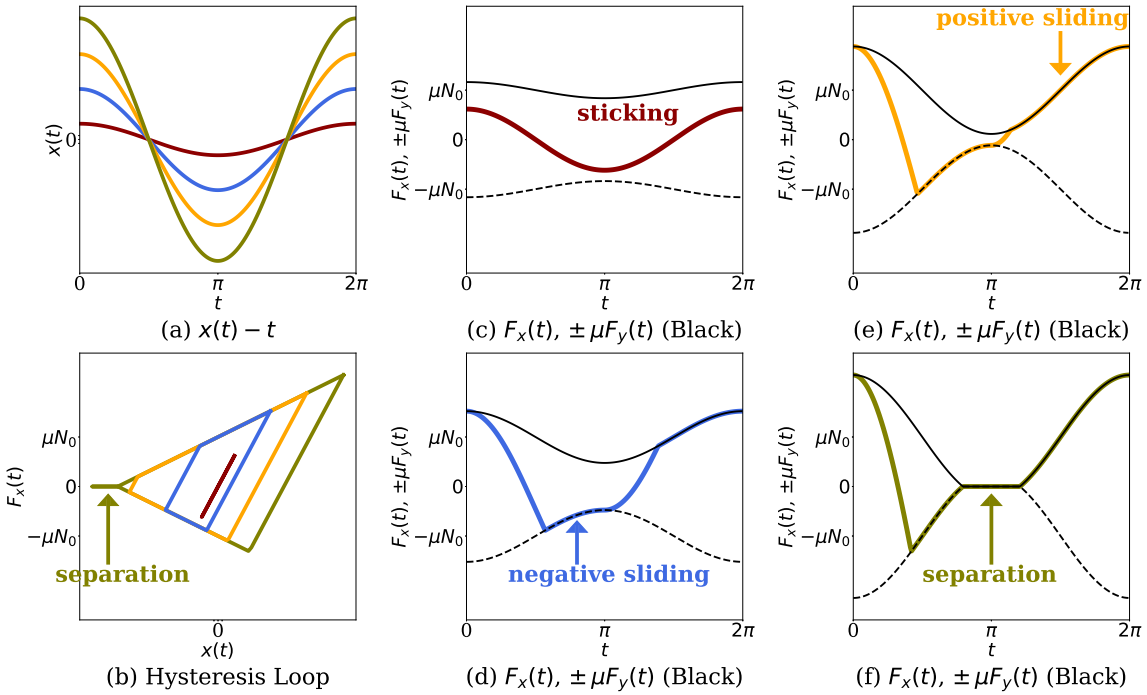
One dimensional contact element

This one dimensional contact element consists of a Jenkins element in the tangential direction with a constant normal load as shown in Fig.2.12(a). N_0 is the constant normal load; k_t is the tangential contact stiffness; μ is the friction coefficient. $x(t)$ is the periodic tangential relative displacement between the contact pairs; $w(t)$ is the relative displacement of the contact point. The tangential friction force $F_x(t)$ can be computed using Eqn.(A.1-A.3) in Appendix A.1.

When the tangential friction force $F_x(t)$ is lower than the critical value μN_0, the contact node is completely sticking as shown by the red curves in Fig.2.13. Then, there is no energy dissipated by the friction force. Whereas, if the tangential friction force exceeds the critical value, the sticking-sliding contact condition happens (blue, orange and green curves in Fig.2.13). The hysteresis loops are given in Fig.2.13(b). The area under hysteresis loop represents the energy dissipated by the friction force.

Two dimensional contact element

This two dimensional contact element consists of a Jenkins element in the tangential direction with a unilateral spring in the normal direction as shown in Fig.2.12(b). N_0 is the constant normal load; Δ is the initial gap; k_t and k_n are the tangential and normal contact stiffness. $x(t)$ and $y(t)$ are the periodic relative displacements between the contact pairs in the tangential and normal direction; $w(t)$ is the relative displacement of contact point. This contact element can model the variation of the normal contact force and the partial separation. If the normal displacement $y(t)$ is zero, then this contact element coincides with the contact element in Fig.2.12(a). If a normal load is applied and contact pairs are initially in-contact, then the



(a) $x(t) - t$ (c) $F_x(t)$, $\pm\mu F_y(t)$ (Black) (e) $F_x(t)$, $\pm\mu F_y(t)$ (Black)

(b) Hysteresis Loop (d) $F_x(t)$, $\pm\mu F_y(t)$ (Black) (f) $F_x(t)$, $\pm\mu F_y(t)$ (Black)

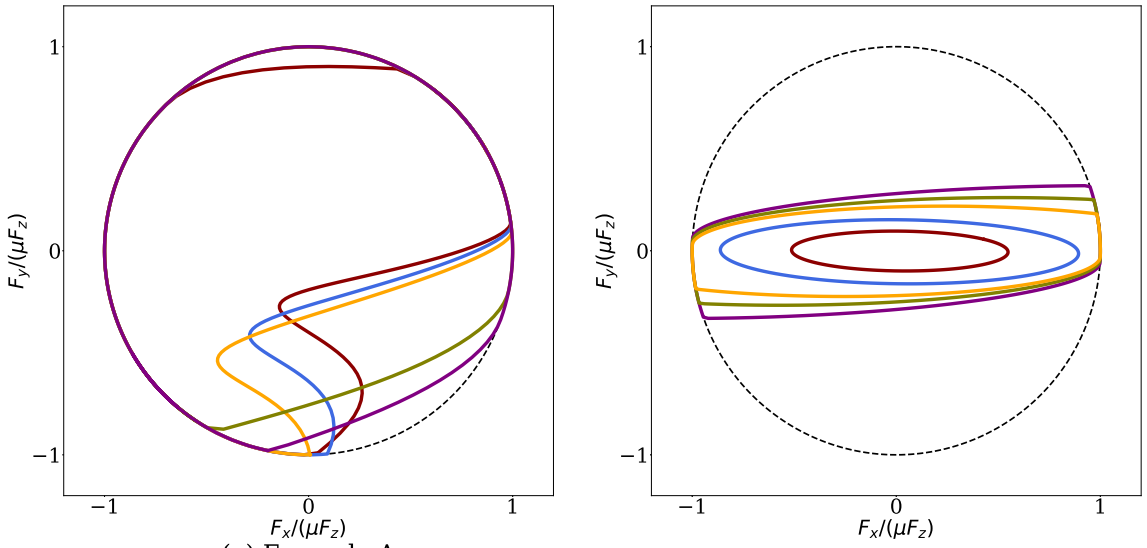
Fig. 2.14 Examples of friction forces and hysteresis loops for the two dimensional contact element: (a) $x(t)$; (b) Hysteresis loops; (c, d, e, f) $F_x(t)$ and $\pm\mu F_y(t)$ (Black)

initial normal force $N = N_0$. Whereas, if the contact pairs are separated with an initial gap Δ in a static equilibrium position, a negative initial normal load is obtained as $N = -k_n\Delta$. The tangential friction force $F_x(t)$ and the normal contact force $F_y(t)$ can be calculated using Eqn.(A.4-A.7) in Appendix A.1.

Figure 2.14 shows several examples of contact forces and hysteresis loops. A sticking contact condition is shown by the red curves in Fig.2.14. As the vibration amplitude increases, the hysteresis loop changes its shape. In the case of sticking-sliding contact condition, the vibration energy is dissipated and the area enclosed by the hysteresis loop is the amount of energy loss (blue and orange curves in Fig.2.14). Further increase in vibration amplitude causes partial-separation and a segment of the tangential contact force equals zero (see green curves in Fig.2.14) leading to a triangular hysteresis loop.

Three dimensional contact element

This three dimensional contact element consists of two Jenkins elements in the tangential plane with a unilateral spring in the normal direction as shown in Fig.2.12(c). N_0 is the constant normal load; Δ is the initial gap; $k_{t,1}$, $k_{t,2}$ and k_n are the tangential and normal contact stiffness. $x(t)$, $y(t)$ and $z(t)$ are the periodic relative displacements between contact



(a) Example A (b) Example B

Fig. 2.15 Examples of friction forces for the three dimensional contact element: (a, b) $F_x/(\mu F_z) - F_y/(\mu F_z)$

pairs in the tangential and normal direction; $w_1(t)$ and $w_2(t)$ are the relative displacement of contact point in the tangential plane. This contact element characterises the friction force in a two dimensional contact plane ($\hat{x} - \hat{y}$ plane). To model the contact stiffness in the contact plane, two tangential springs are assumed along $k_{t,1}$, $k_{t,2}$ two orthogonal directions. If a normal load is applied and the contact pairs are in-contact, then the initial normal force $N = N_0$. Whereas, if the contact pairs are separated with an initial gap Δ, a negative initial normal load is obtained as $N = -k_n\Delta$. Contact force in the three directions can be calculated using Eqn.(A.8-A.14) in Appendix A.1. $F_x(t)$ represents the tangential friction force in the $\hat{x}$ direction; $F_y(t)$ represents the tangential friction force in the $\hat{y}$ direction; $F_z(t)$ represents the normal contact force in the $\hat{z}$ direction.

Figure 2.15 shows two examples of different trajectories of the tangential friction forces. The black dashed circle represents the fully sliding case, which cannot be modelled by contact elements shown in Fig.2.12(a) and Fig.2.12(b). In Example B, the red and blue curves represent the fully sticking contact condition. As the vibration amplitude increases, the sticking-sliding contact condition occurs and parts of the trajectory overlap with the black circle.

2.3.4 Microslip models

Microslip model can describe the microslip regime of the hysteresis loop measured from experiments. A fine discretisation of the contact interface is not necessary for microslip models, since a few patch-to-patch contact elements are used to model friction force. Most parameters in microslip models do not have an explicit physical meaning, and are obtained by tuning the model to experimental results. There are many microslip models existed in the literature, such as Iwan [69, 153], Bouc-Wen [15, 185], Dahl [30], LuGre [19], Preisach [2, 130] and Valanis model [182].

Pesaresi *et al.*[118] developed a novel modelling strategy of contact behaviours within the contact interface for an UPD. This novel modelling strategy is achieved by discretising the contact interface into a dense grid of microslip contact elements, which can reproduce the macroscale contact properties and micromechanical properties. Using such a novel microslip contact model, the numerical simulation can provide a more accurate nonlinear forced response comparing with experimental results. The similar results also can be found in the work of Marquina *et al.* [104].

2.3.5 Identification of contact parameters

Most contact elements can replicate frictional behaviour with proper contact parameters. Therefore, the identification of contact parameters has a great practical importance to improve the accuracy of numerical simulations. Various experimental test rigs have been designed to measure the contact parameters [41, 64, 74, 89, 119]. To make the contact element more predictive and convincing, the input parameters are usually tuned against the experimental results [120, 152, 170]. However, a significant amount of uncertainties existed in the experimental process, i.e. wear effects, manufacturing tolerance, mounting and mistuning. In addition, contact parameters also depend on the material of structure, the temperature, the humidity and the contact area. Measuring the contact parameters is obviously outside the scope of this thesis. The contact parameters from literature [82, 120] are used in this thesis to provide a qualitative dynamic analysis for structures with friction joints.

2.3.6 Uncertainties involved in contact parameters

Contact parameters for any contact model cannot be considered as a deterministic problem. In a real engineering problem, various uncertainties are involved within the contact interface, such as wear effects, manufacturing tolerances, mounting, mistuning and material

imperfections. Therefore, modelling of the contact behaviour is a complicated task and to be more accurate, the uncertainties associated to the contact parameters are also necessary. Uncertainty quantification of dynamic response for a structure with frictional contact is an interesting research direction. Several researchers have investigated the uncertainties involved in dynamic analysis for bladed disk. Petrov [123–125] and Krack *el al.* [80, 84] carried out a sensitivity analysis of dynamic responses for structures with friction damping to those contact parameters. A recent published work by Bhatnagar *el al.* [14] investigated the effects of contact parameters for the UPD using a polynomial chaos expansion and a sobol analysis. From their work, they found that the variation of contact parameters can influence the nonlinear forced responses and the affected situations for different contact parameters are different as well.

2.4 Numerical Methods for Nonlinear Dynamics

The existence of the contact with friction in a structure makes the system nonlinear. Nonlinear dynamic equations have to be solved. For certain nonlinearities, the exact solutions can be obtained analytically or semi-analytically by using a perturbation method [83]. In the case of a structure with friction joints, the non-smooth contact interaction makes the application of such analytical approaches impossible for a multi-degree-of-freedom model. Moreover, these methods have limited applicability. Therefore, researchers always give their priorities to numerical methods for the computation of dynamic response of structures with friction joints. The general EoM used for a nonlinear system is:

$$\underline{\underline{\mathbf{M}}}\,\underline{\ddot{Q}}(t)+\underline{\underline{\mathbf{C}}}\,\underline{\dot{Q}}(t)+\underline{\underline{\mathbf{K}}}\,\underline{Q}(t)+\underline{F}_{nl}(\underline{Q},\underline{\dot{Q}})=\underline{F}_{ex}(t) \tag{2.21}$$

where $\underline{\underline{\mathbf{M}}}$, $\underline{\underline{\mathbf{C}}}$ and $\underline{\underline{\mathbf{K}}}$ are the mass, damping and stiffness matrices of a system. $\underline{Q}(t)$ is the displacement of system; $\underline{F}_{nl}(\underline{Q},\underline{\dot{Q}})$ and $\underline{F}_{ex}(t)$ are the nonlinear force and the excitation force respectively.

2.4.1 Time domain methods

Time integration methods

The most popular techniques to study nonlinear dynamic systems are the numerical integration methods. In these methods, the time evolutions of the coordinates are computed using its differential equations and an initial condition. The responses are calculated step by step

through a discrete time history. Most time integration methods can be generally classified into an explicit and implicit scheme [35]. There are various explicit schemes. Runge-Kutta is a classical explicit scheme, which has been well developed and integrated in ODE45 function in MATLAB. Examples of other explicit methods are: Trujillo's method [178], stiffly stable method [35], Predictor-Corrector method [35], Generalised-α method [24] and matrix exponentiation [65, 20]. In explicit schemes, the current response of the system is calculated based on the previous steps. These explicit schemes have less computational costs per time step and a less storage used, because the matrices are not required to be stored step by step. However, not all explicit methods are conditionally stable and they require small time steps to guarantee a numerical stability [35]. In implicit schemes, the current response is calculated based on both the current step and the previous step. Most implicit schemes are unconditionally stable for linear systems but a larger storage and larger computational efforts are expected. There are several implicit methods developed, Newmark scheme [112, 20], Wilson-θ [35] and Houbolt method [35]. This class of time integration methods can generally provide accurate solutions, but they can introduce numerical errors if the time step is too large.

Shooting method

An arbitrary value is usually given at as an initial solution in time integration methods, and it requires long time to reach a steady state solution. In dynamic analyses, the solutions of structures are usually in a periodic form. To improve the efficiency of numerical methods, the fundamental idea of the class of time integration methods has been reformulated by enforcing a periodic boundary condition. Therefore, the initial value problem is transferred into a boundary value problem. Shooting method is a numerical method to find the initial solutions that satisfy the periodic boundary condition [117]. Within the period, the solutions are still calculated by the idea of time integration. In addition, monodromy matrices are the by-products of the shooting method, which can be used for stability analyses based on the Floquet theory.

Orthogonal collocation method

Orthogonal collocation method is a numerical method to solve boundary value problems of nonlinear ordinary differential equations. The periodic solution is decomposed into mesh intervals, and represented by orthogonal polynomials on each intervals. Methods based on orthogonal collocation have been successfully applied in several softwares: e.g., AUTO [34],

colsys [8], CONTENT [87], Matcont [33] and coco [31]. Orthogonal collocation methods have been seldom attempted for full-scale structure, since the discretisation may need a considerable memory space. Furthermore, orthogonal collocation methods can be efficient with an iterative solver (for example generalized minimal residual method) as it is easy to build an efficient pre-conditioner. This class of methods have been widely used in the field of electronics.

2.4.2 Spectral methods

Spectral methods are a group of methods where the solutions are approximated by a series of periodic base functions and corresponding coefficients. The methods belong to the family of Galerkin methods. These periodic base functions guarantee the periodicity boundary conditions which are considered as the fundamental needs of such problems. There are various spectral methods, such as Fourier Galerkin method [85], Wavelet Galerkin method [1].

Harmonic balance method

Harmonic Balance Method (HBM) is considered as one of the most popular spectral methods in the literature for analysing the periodic solutions of a nonlinear dynamic system. The HBM method is a type of spectral method using harmonic base functions and it is also known as Fourier–Galerkin procedure. The HBM is an application of Galerkin methods with a Fourier basis. The periodic signals are estimated by their Fourier coefficients. The first attempt using harmonic functions to solve nonlinear problems was done by Krylov and Bogoliubov in 1943 [85]. Only the first order harmonic was used in their work to linearise the nonlinear problem and solve it. Then, Urabe [179] demonstrated the procedure using several harmonics to simulate the nonlinear periodic system. In 1990, Cheung [23] used the incremental HBM to work on a cubic nonlinearity and proposed that it provided an enhanced performance for highly nonlinear problems. Cameron [18] introduced the Alternating Frequency/Time (AFT) method in 1989, which exhibited a more accurate approximation of nonlinear forces. In his work, he indicated that the problem can be solved in an iterative scheme, by alternating between frequency and time domain. Different calculations are performed in different domains within the AFT scheme. Guskov *et al.* [56] described a multi-HBM that includes the multi-dimensional fast Fourier transformation in the AFT procedure. Salles [140] proposed a technique to update the number of harmonics depending on the contact condition in his thesis. Grolet and Thouverez [54] developed an adaptive-HBM using a stepwise regression procedure to achieve the selection of harmonics. These variations of HBM can improve

usability, performance, or robustness. Because the direct computation of friction contact forces in the frequency domain is very complicated and inefficient, the multi-HBM with AFT is considered as the most popular numerical method in the modelling of structures with friction joints in the literature.

In HBM, the time domain dynamic variables $\underline{Q}(t)$ are approximated by the Fourier series truncated to the N_h order of harmonics. $\underline{\tilde{Q}}$ is the collection of Fourier coefficients for the n_h^{th} order of harmonics. n_h is the order of harmonics, ω is the frequency. j represents the imaginary parts. HBM methods are expected to be solved iteratively using a Newton-Raphson method or Quasi-Newton method.

$$\underline{Q}(t) = \sum_{n_h=0}^{N_h} \underline{\tilde{Q}}_p e^{jn_h\omega t};\ \underline{\tilde{Q}}_{nh} = \underline{\tilde{Q}}_{nh}^c - j\underline{\tilde{Q}}_{nh}^s \tag{2.22}$$

In a nonlinear system, quasi-periodic solutions are also possible due to the nonlinear effect. The quasi-periodic solution represents the motion with two base frequencies. The quasi-periodic expansion is only valid when the two frequencies are incommensurable, otherwise one of the base frequencies can be seen as a harmonic of the other. Both the shooting method [95] and HBM [150] can be extended to compute such solutions. In a recent published paper, Fontanela *et al.* [42] developed a fully numerical approach to compute quasi-periodic solutions bifurcating from a nonlinear periodic state in structures exhibiting cyclic symmetry using HBM.

Time spectral methods

Time Spectral Method (TSM), sometimes called as High dimensional harmonic balance method, is also referred as the pseudo-spectral method. TSMs are widely used in the research of computation fluid dynamics [50, 156] and have proven to be highly efficient. TSM was developed by Hall *et al.* [58] and investigated by Liu *et al.* [97, 98] and LaBryer [88]. In classic HBM, the solutions are solved in the frequency domain to obtain the Fourier coefficients of displacement. Whereas in TSM, the unknowns are the values of displacements with an equal time step over one vibration period. Thus, the use of TSM can be easily formulated based on an existing time marching solver. TSM has also been tested in the field of nonlinear dynamics [81, 143].

2.4.3 Continuation method

Continuation technique is a numerical method that can be used to track the evolution of a systematic behaviour against one or several of the systematic parameters [3]. There are two major benefits from using continuation techniques. Firstly, the continuation technique is able to distinguish the solutions which are very close to each other. Secondly, they can be used to find the different solutions for a single parameter. In the nonlinear case, more than one solution can coexist for one parameter. A proper continuation method includes two parts: a prediction step and a correction step, as shown in Fig.2.16. The solutions are plotted a $y-\lambda$ space, where y is the collection of the system solutions and λ is the systematic parameter of interest.

In the prediction step, a new solution is predicted using the solutions from previous points. After that, this predicted solution is updated to an accurate solution using a Newton-Raphson method during the correction step. There are various prediction methods and correction methods in the literature. For prediction methods, the following techniques exist: the natural prediction using previous point, the secant method, the tangent method and high-order interpolation based on Lagrange polynomials [149]. The secant method is a simple, cheap and quite accurate method, but it has difficulty in capturing curves with a small radius. Within the tangent method, the tangent vector of y to λ is expected to be calculated for each step. In addition, the sign of the tangent vector is also required. Compared to the secant method, the tangent method requires more computational efforts but provides better convergence at points with a small radius of curvature. There are three common correction methods which are widely used in the literature: arc-length method [29], pseudo arc-length method [136] and Moore-Penrose/pseudo-inverse method [3, 149].

The classical HBM integrated with AFT and a continuation technique is considered as the most suitable numerical method to compute the dynamic response for structures with friction joints and it will be used in this thesis. For nonlinear forced response analyses, the dynamic responses are calculated for a range of excitation frequency. Therefore, the excitation frequency is chosen as the continuation parameter. For the computation of nonlinear modes, the modal amplitude is the continuation parameter.

Asymptotic numerical method

The classical HBM method and a continuation method is a widely used technique to follow the dynamic periodic solutions of nonlinear systems with respect to a specific chasing parameter. Cochelin and Vergez [26] proposed a purely frequency-based technique coupled

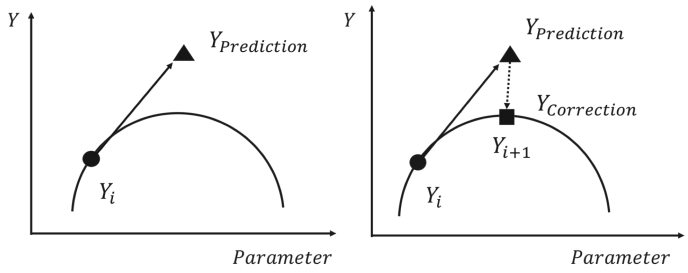


Fig. 2.16 One predictor-corrector step of the continuation method

with a high order nonlinear solver. This continuation method is called asymptotic numerical method and relied on a high-order Taylor expansion of the solution. In order to optimise the computation of the Taylor's terms, a quadratic recast is required beforehand [25]. In detail, the EoM is reformulated into a set of equations with only quadratic terms. Then, the periodic solutions are expanded into a power series based on high-order derivatives of this set of nonlinear functions. This method has the advantage of providing a robust and an efficient continuation of the solutions. However, the quadratic recast can be difficult for non-smooth systems and can lead to inaccurate results for low harmonic order (aliasing issue). Woiwode *et al.* [189] compared the performance between the classic HBM-AFT-continuation method and HBM-asymptotic numerical method. More work is needed to get a clear comparison between the two approaches.

2.5 Model Reduction

2.5.1 Component mode synthesis

Reduced Order Modelling (ROM) has great practical importance for improving the efficiency and reducing the computational cost [194]. ROM has been investigated from the 1960s, since finite element methods appeared [121]. Guyan [57] defined a static condensation method in 1965. Meanwhile, the concept of Component Mode Synthesis (CMS) has been proposed by Hurty [66]. CMS based ROMs can be considered as a group of methods which are used to reduce the model for assembled structures with interfaces [10, 17, 121], e.g. contact interfaces, cyclic symmetric interfaces. In CMS based ROM approaches, each component within the assembly is considered as a substructure. Therefore, the model reduction can be achieved by using linear normal modes and static modes, which are associated to the nodes retained within the interface of each substructures. The reduction basis is built by these linear

normal modes and static modes. Using such a reduction basis, Galerkin projection can be performed and most DoFs can be eliminated. After the reduction, only the DoFs associated to the nodes within the interface are retained. There are many CMS approaches developed in the literature. These CMS approaches use the vibration modes of the substructures based on different boundary conditions applied to the interfaces. Depending on that, CMS approaches can be classified into three main groups: fixed interface methods [28, 67]; free interface methods [49, 62, 138]; hybrid interface methods [103]. The Craig-Bampton method [28] is known as one of the most popular fixed interface CMS approaches, because of its efficiency and ease to implement. For these CMS approaches, the number of retained DoFs is determined by the number of nodes within the interface. For structures with high mesh density within the interface, the computational costs can be unaffordable [12]. This limits the efficiency of these classic CMS approaches. Therefore, to further improve the modelling efficiency, the concept of interface modes has been proposed by Bourquin [16] to reduce the static modes. Instead of using full size of the static modes, a subset of eigenvectors of the system projected by the interface static modes is used.

Several interface reduction techniques have been proposed in the literature, such as the work from Becker and Gaul [12]. In [187], Witteveen proposed another interface reduction approach namely, joints interface mode method, which shows better convergence rate over the common interface reduction method [12]. Witteveen [188] also proposed another approach called trial vector derivative method to improve the convergence rate. This trial vector derivative method is essentially based on the modal derivatives [68], which is obtained by the first-order Taylor expansion to the linear CMS subspace.

2.5.2 Cyclic symmetric reduction

For cyclic symmetric structures, thanks to the periodicity of the modes, the size of systems can be reduced. Several numerical methods have been proposed in the literature. Thomas [174] proposed a method to reduce the mass and stiffness matrices of the full annulus to a single sector corresponding to a phase angle. Similar results can be obtained from Mead's approach [106, 107]. Mead's approach is achieved by applying cyclic boundaries onto a generic isolated sector and projecting the DoFs corresponding to the left cyclic symmetric boundaries onto the DoFs related to the right cyclic symmetric boundaries with a phase angle. Furthermore, Petrov [122] described a numerical method which integrates the cyclic symmetric reduction into the multi-harmonic formulations of EoMs using a generic sector model. In Petrov's work, cyclic symmetric reduction is achieved by reducing the complex

dynamic stiffness matrix instead of the mass and stiffness matrices. Researchers give their priorities to this method because it makes the implementation of the dynamic analysis for cyclic symmetric structures using multi-harmonic formulations less complicated. However, further reduction on cyclic boundaries cannot be simply applied using the method described by Petrov [122].

2.5.3 Cyclic interface reduction

For structures with a cyclic symmetry, a repeated sector with cyclic symmetric boundary conditions is usually studied instead of using the whole annulus. In this case, the nodes within cyclic interfaces (cyclic symmetric boundaries) highly determines the size of the reduced system and the modelling efficiency. Tran [176] described the interface reduction methods which applied to structures with a cyclic symmetry. Using such a method, all interface DoFs are eliminated from a CMS reduced system. However, keeping a part of interface DoFs is sometimes important and desirable. For example, in a structure with some of its contact nodes lying on the cyclic interface, retaining these contact nodes in the reduced system is essential. To overcome that, Tran [177] proposed another method using Partial Interface Mode (PIM). This method can reduce a significant number of interface DoFs and retaining some interface DoFs with important information, like the classic CMS approach. This approach can be considered as applying a second level CMS approach on a Guyan's reduced system.

2.5.4 Model reduction for tuned blisks with friction dampers

For an ideal blisk with a friction damper, the full-scale model can be reduced using a three-step model reduction to achieve an acceptable computational efficiency. This three-step model reduction includes a classic CMS approach, a cyclic reduction and an interface reduction; and has been widely used in the literature and industrial solvers [9]. The detailed numerical derivations of this three-step model reduction are provided in Section 5.2.3.

2.6 Nonlinear Normal Mode

Normal modes usually consist of important modal information for a dynamic system, including its natural frequencies, modal damping and mode shapes. In a linear system, the linear normal modes can be simply obtained through an eigen value problem, which are considered as the solution of the free vibration system. In a nonlinear system, the existence of various

nonlinearities makes the concept of linear normal modes invalid. In detail, unlike the linear normal modes, the nonlinear modes are not orthogonal to each other and cannot be used for the modal superposition. In addition, some important dynamic phenomena such as modal interaction and modal bifurcation cannot be explained by a linear modal theory. Therefore, the theory of nonlinear modes is crucial in the field of nonlinear dynamics.

The foundation of the theory of nonlinear modes can be traced back to the centre theorem from Lyapunov and Poincaré [75, 102]. In the centre theorem, for a finite dimensional Hamiltonian system, different families of periodic motions can be found around several stable equilibrium points. This can be considered as the a nonlinear extension of normal modes underlying a nonlinear system [135].

2.6.1 Rosenberg's definition

Based on that, the first definition of nonlinear modes given by Rosenberg [137] defined the Nonlinear Normal Modes (NNMs) as a vibration unison, where all points in a structure reach their equilibrium positions and their extreme positions simultaneously. All DoFs within the system move at same frequency. There is a constant relation between all coordinates, like in a linear system. Rosenberg's work has been further developed by Rand [132–134] and Szemplinska [167]. Readers are invited to refer to [108, 180] for a comprehensive review of these pioneering works. The restriction of Rosenberg's definition has been pointed out in [117]. The definition proposed by Rosenberg cannot explain the modal interactions, when there are at least two interacting modes.

2.6.2 Shaw and Pierre's definition

However, most works mentioned above considered undamped NNMs with a periodic solution, i.e. a conservative nonlinear system. When a non-conservative nonlinear system is considered, the NNMs are no longer periodic and defined as damped Nonlinear Normal Modes (dNNMs) [148]. Shaw and Pierre [154, 155] proposed an excellent definition of the dNNMs in non-conservative nonlinear systems using the concept of invariant manifold. They defined that the normal modes of a nonlinear autonomous system take place in a two dimensional invariant manifold in a phase space. This manifold must pass through a stable equilibrium point of the system and, it is tangent to the plane of linear normal mode [154]. Shaw and Pierre provided a more general definition of NNMs, since their definition can be applied in both conservative and non-conservative systems. Furthermore, Haller and Ponsioen mathematically proved the existence and uniqueness of dNNMs using the theory of

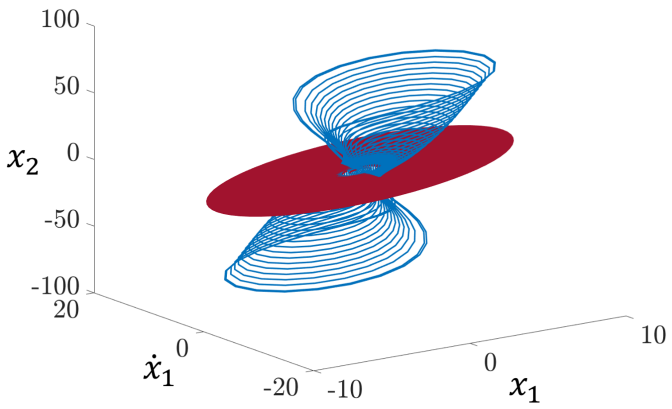


Fig. 2.17 An example of a linear mode and a nonlinear mode in a two-dimensional phase space: Red plane: linear normal mode; Blue hypersurface: nonlinear mode

Spectral SubManifold (SSM) [59]. The use of SSM in the model reduction is also provided in an open source numerical tool, namely SSMtool [128].

An example of invariant manifold is given in Fig.2.17 using a one DoF system with a cubic spring. The linear normal modes are interpreted as an invariant plane in the phase space as shown by the red plane in Fig.2.17, the dNNMs are considered as an invariant manifold, a two-dimensional hypersurface (see blue surface in Fig.2.17). This hypersurface is built using a collection of periodic orbits.

2.6.3 Computation of nonlinear modes

Several analytical and semi-analytical methods have been proposed to derive the NNMs based on the perturbation techniques [47, 111] (e.g. normal form [72, 175], multiple scales [111] and spectral sub-manifold [59]). An analytical analysis of the NNMs unmask the dynamics of nonlinear autonomous systems including NNMs' energy dependence, interactions and bifurcations. Some analytical methods also can be used to compute the dNNMs in a nonlinear damped system with a smooth non-conservative nonlinearity, i.e. Van Der Pol oscillator. However, most analytical methods are restricted to small degree polynomial nonlinearities. For systems with friction joints, because of the non-smoothness of the friction forces, it is difficult to apply these analytical methods, especially for full-scale structures. Therefore, numerical methods for computation of dNNMs are essential.

Laxalde and Thouverez [91] described a numerical method to compute the dNNMs using the extension of Complex Nonlinear Modes (CNM) by solving complex eigenproblems. In their work, the damped solutions are represented by harmonic solutions with an exponential

decay. Thanks to the CNM method, the dNNMs of full-scale structures with friction joints can be efficiently computed. To obtain a periodic based dNNMs, Krack [79] developed a numerical method, namely Extended Periodic Motion Concept (EPMC) where an artificial viscous damping is introduced into the system to compensate for the energy dissipated by the nonlinear forces. These two numerical modelling strategies can be considered as the most popular computational approaches for structures with friction joints.

2.7 Relating Nonlinear Mode to Forced Response

In an engineering perspective, forced responses are always regarded as a crucial design consideration. HCF is usually considered as one of the most frequent reasons for structural failures. To predict the endurance of structural components, an accurate prediction of the resonant stress for forced responses is essential. The use of nonlinear modes in engineering design process can be achieved by relating the nonlinear modes to the nonlinear forced responses. At resonance, the dynamic response has a similar form (solution) as the underlying nonlinear mode at a specific energy level. In fact, the backbone curves are sometimes seen as the collection of resonant solutions for a varying value of the excitation force. In addition, the nonlinear forced responses can be reconstructed using nonlinear modes as well.

2.7.1 Energy balance method

An analytical method named Energy Balance Method (EBM) has been introduced by Hill *er al.* [60] to predict where the resonant solution of a forced response crosses the underlying nonlinear mode. Before this EBM, similar energy transfer analysis has been described in [47, 76, 181]. Grenat used similar energy analysis to calculate the non-conservative NNMs based on the NNMs [52]. The EBM is originally developed for systems with conservative nonlinearities using the theory of NNMs and successfully applied to a two DoFs nonlinear oscillator [60]. EBM is also able to capture the isolas in forced responses and isolated branches of nonlinear modes [61]. The method relies on the fact that, for any steady-state response, the net energy transferred into a system over one period of vibration must be zero [60]. Moreover, the work of Cenedese and Haller [22] used a Melnikov function analysis that defines the mathematical conditions under which the EBM is valid.

2.7.2 Nonlinear modal synthesis

In a linear system, the general forced responses can be simply formulated as a synthesis of all possible solutions from an eigenproblem. Thanks to the superposition principle and orthogonality conditions, using modal synthesis is a very efficient method to reconstruct the forced responses. Unlike in a linear system, these conditions are not valid in a nonlinear system. Therefore, extra assumptions are required to adopt the modal synthesis in such a nonlinear system.

A single nonlinear resonant mode theory [168] was proposed to apply modal synthesis to a nonlinear system. The existence of nonlinear modal interactions is not considered in this situation. This theory based on the fact that the energy is basically concentrated on a single nonlinear mode and the system response is dominated by this single nonlinear mode. Then, the generic forced responses can be synthesised using the single nonlinear mode and linearised counterpart of other modes. This method have been successfully attempted in following work [82].

2.8 Concluding Remarks

In this chapter, the main aspects related to the nonlinear modal analysis for structures with friction joints were reviewed. Friction damping has been proven to be a very efficient damping technique in industrial turbomachinery. The use of friction ring dampers in an industrial blisk has become a popular solution to improve the damping ability. Most works related to friction ring dampers were evaluated. Few researchers attempted to design or optimise the geometry of the ring dampers. To obtain an optimal and robust design of friction ring dampers, geometric study is necessary to investigate the factors that can influence the damping performance.

In the initial design stage, the experimental testing is expensive and time consuming. Thus, the development of numerical methods to model the nonlinear dynamic responses of structures with friction joints is very important. With the help of existing contact models, well-established numerical methods and validated model reduction techniques, the numerical simulations of such structures are achievable. The application of nonlinear modal analysis in such structures is also possible thanks to the development of nonlinear modal theory. However, the limitations of these numerical methods used for the computation of nonlinear modes are still an open question. Furthermore, the relating the nonlinear modes to the forced responses is always the most of interest topic for the engineering industry.

In the next chapter, the existing numerical approaches used for nonlinear modal analysis will be formulated in detail, including complex nonlinear mode and extended periodic motion concept. In addition, different damping assumptions will be tested in the latter case. Then, the proposed extended-energy balance method will be explained and derived, which is used to provide a direct relation between nonlinear modes and resonances for structures with non-conservative nonlinearities. The combination of nonlinear modes and an extended-energy balance method will be the numerical approach used in the present thesis. Three illustrative testcases will be demonstrated in the next chapter as well.

Chapter 3

Numerical Methods for Nonlinear Modal Analysis

In the previous chapter, the general theories of nonlinear modal analyses have been reviewed. The main objective of this chapter is to elaborate two main numerical approaches for the computation of damped nonlinear normal modes (dNNM) in the frequency domain, and to introduce a novel method for forced response interpretation from dNNMs. These two numerical approaches are Complex Nonlinear Mode (CNM) and Extend Periodic Motion Concept (EPMC) respectively. The mathematical formulations of the framework of Harmonic Balance Method (HBM) including Alternating Frequency/Time (AFT) method and continuation techniques are described at the first place. Then, a detailed description of these two numerical approaches are explained followed by the introduction of the novel method, namely Extended Energy Balance Method (E-EBM). To illustrate the differences of presented numerical approaches, three illustrative examples, including a one Degree of Freedom (DoF) system with frictional contact, a one DoF system with a quadratic nonlinear damping and a Duffing oscillator, are given in this chapter. The advantages and limitations of these numerical methods are then discussed through these three examples. Parts of this chapter has already been published in Sun *et al*. [163].

3.1 Harmonic Balance Method

3.1.1 Fourier-Galerkin procedure

The classic HBM integrated with the AFT method is applied to solve the nonlinear dynamic equation in frequency domain. The general Equation of Motion (EoM) for a nonlinear

dynamic problem is given in Eqn.(3.1), where $\underline{\underline{\mathbf{M}}}$ is the mass matrix; $\underline{\underline{\mathbf{C}}}$ is the damping matrix; $\underline{\underline{\mathbf{K}}}$ is the stiffness matrix. $\underline{Q}(t)$ is the periodic solutions of this nonlinear dynamic equation, the underline of the symbol is used to represent the vector and the variable t does not appear explicitly in the following equations in this chapter. $\underline{F}_{nl}(\underline{Q},\dot{\underline{Q}})$ is the periodic nonlinear force and $\underline{F}_{ex}(t)$ is the periodic external excitation force.

$$\underline{\underline{\mathbf{M}}}\ddot{\underline{Q}}(t)+\underline{\underline{\mathbf{C}}}\dot{\underline{Q}}(t)+\underline{\underline{\mathbf{K}}}\underline{Q}(t)+\underline{F}_{nl}(\underline{Q},\dot{\underline{Q}})=\underline{F}_{ex}(t) \tag{3.1}$$

In the framework of HBM, the solutions $\underline{Q}$, the nonlinear force $\underline{F}_{nl}$ and the excitation force $\underline{F}_{ex}$ are in a periodic form with an excitation frequency Ω_e. In this case, the vibration frequency ω equals the excitation frequency Ω_e. The periodic solutions and forces are decomposed by Fourier series truncated up to the N_h order of harmonics, as shown in Eqn.(3.2). n_h is the order of harmonics up to N_h and j represents the imaginary parts.

$$\begin{aligned}
\underline{Q}(t)&=\textstyle\sum_{n_h=0}^{N_h}\underline{\tilde{Q}}_{nh}e^{jn_h\omega t} \qquad & \underline{\tilde{Q}}_{nh}&=\underline{\tilde{Q}}^{c}_{nh}-j\underline{\tilde{Q}}^{s}_{nh}\\
\underline{F}_{nl}(t)&=\textstyle\sum_{n_h=0}^{N_h}\underline{\tilde{F}}_{nl,nh}e^{jn_h\omega t} & \underline{\tilde{F}}_{nl,nh}&=\underline{\tilde{F}}^{c}_{nl,nh}-j\underline{\tilde{F}}^{s}_{nl,nh}\\
\underline{F}_{ex}(t)&=\textstyle\sum_{n_h=0}^{N_h}\underline{\tilde{F}}_{ex,nh}e^{jn_h\omega t} & \underline{\tilde{F}}_{ex,nh}&=\underline{\tilde{F}}^{c}_{ex,nh}-j\underline{\tilde{F}}^{s}_{ex,nh}
\end{aligned} \tag{3.2}$$

Substituting Eqn.(3.2) into Eqn.(3.1) and balancing the harmonic terms with a Galerkin projection. Then, this nonlinear dynamic equation is transformed into the frequency domain, where $\underline{\tilde{Q}}$ is a collection of Fourier coefficients: $\underline{\tilde{Q}}=[\underline{\tilde{Q}}_{nh=0},\underline{\tilde{Q}}_{nh=1},\cdots,\underline{\tilde{Q}}_{nh=N_h}]^{\mathrm{T}}$. $\underline{\tilde{F}}_{nl}$ and $\underline{\tilde{F}}_{ex}$ have the similar form with $\underline{\tilde{Q}}$. $\underline{\tilde{Q}}_{nh}$ has the dimension of N_{DoF}, where N_{DoF} is the number of DoFs within the whole system. Then, $\underline{\tilde{Q}}$ has the dimension of $[N_{DoF}(N_h+1)\times 1]$.

$$\underline{\underline{\mathbf{Z}}}(\omega)\,\underline{\tilde{Q}}+\underline{\tilde{F}}_{nl}(\underline{\tilde{Q}})=\underline{\tilde{F}}_{ex} \tag{3.3}$$

$$\underline{\underline{\mathbf{Z}}}=\begin{bmatrix}\underline{\underline{\mathbf{Z}}}_0 & \underline{\underline{\mathbf{0}}} & \cdots & \underline{\underline{\mathbf{0}}}\\ \underline{\underline{\mathbf{0}}} & \underline{\underline{\mathbf{Z}}}_1 & \cdots & \underline{\underline{\mathbf{0}}}\\ \vdots & \vdots & \ddots & \vdots\\ \underline{\underline{\mathbf{0}}} & \underline{\underline{\mathbf{0}}} & \cdots & \underline{\underline{\mathbf{Z}}}_{N_h}\end{bmatrix} \tag{3.4}$$

$$\underline{\underline{\mathbf{Z}}}_{nh}=\underline{\underline{\mathbf{K}}}-n_h^2\omega^2\underline{\underline{\mathbf{M}}}+j2n_h\omega\underline{\underline{\mathbf{C}}} \tag{3.5}$$

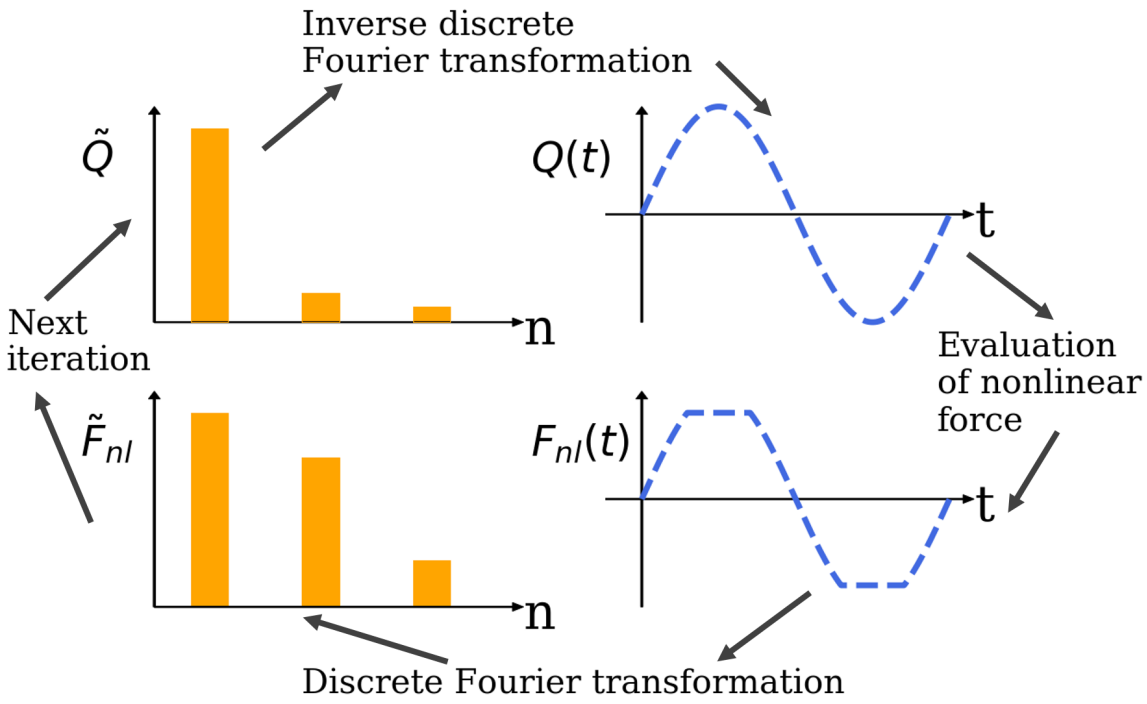


Fig. 3.1 Demonstration of alternating frequency/time method

3.1.2 Alternating frequency/time method

The classic HBM is used to solve the dynamic equations in the frequency domain referring to Eqn.(3.3-3.5). The nonlinear forces in the frequency domain are represented by $\underline{\tilde{F}}_{nl}(\underline{\tilde{Q}})$. It is complicated and expensive to directly obtain the nonlinear force in the frequency domain, especially for friction forces. Therefore, instead of a direct computation of the nonlinear forces in the frequency domain, the classic AFT method [18] is used to calculate $\underline{\tilde{F}}_{nl}(\underline{\tilde{Q}})$. In AFT method, $\underline{\tilde{F}}_{nl}(\underline{\tilde{Q}})$ is calculated in an iterative scheme, alternating between the frequency and time domain, as demonstrated in Fig.3.1. Different calculations are performed in different domains within the AFT scheme. AFT method can be only applied based on the fact that the solutions $\underline{Q}(t)$ and the nonlinear force $\underline{F}_{nl}(t)$ are periodic.

In general, the Inverse Discrete Fourier Transformation (IDFT) is achieved by a linear operator $\underline{\underline{\Xi}}(\omega)$. First, one period of oscillation is discretised by a number of N_t time samples $(t_1, t_2, \cdots, t_N)$. As such, the periodic solutions or forces in the time domain can be represented in the form as Eqn.(3.6). $\underline{Q}_1(t_1)$ has the dimension of N_{DoF}, where N_{DoF} is the number of

DoFs within the whole system. There, $\hat{\underline{Q}}$ has the dimension of $[N_{DoF}\,N_t \times 1]$.

$$\begin{aligned}
\hat{\underline{Q}} &= [\underline{Q}_1(t_1), \underline{Q}_2(t_2), \cdots, \underline{Q}_N(t_N)]^{\mathrm{T}} \\
\hat{\underline{F}}_{nl} &= [\underline{F}_{nl,1}(t_1), \underline{F}_{nl,2}(t_2), \cdots, \underline{F}_{nl,N}(t_N)]^{\mathrm{T}} \\
\hat{\underline{F}}_{ex} &= [\underline{F}_{ex,1}(t_1), \underline{F}_{ex,2}(t_2), \cdots, \underline{F}_{ex,N}(t_N)]^{\mathrm{T}}
\end{aligned} \tag{3.6}$$

Then, in IDFT, the periodic oscillations in the time domain can be obtained using Eqn.(3.7). The linear operator of IDFT $\underline{\underline{\Xi}}(\omega)$ has the shape of $[N_{DoF}\,N_t \times N_{DoF}(N_h+1)]$. The computation of $\underline{\underline{\Xi}}(\omega)$ is given in Eqn.(3.8), where $\bigotimes$ represents the Kronecker product. In Discrete Fourier Transformation (DFT) process, the $\tilde{\underline{Q}}$ can be computed by using $\underline{\underline{\Xi}}^{\mathrm{H}}(\omega)$, where the superscript $*^{\mathrm{H}}$ stands for the Hermitian transpose process.

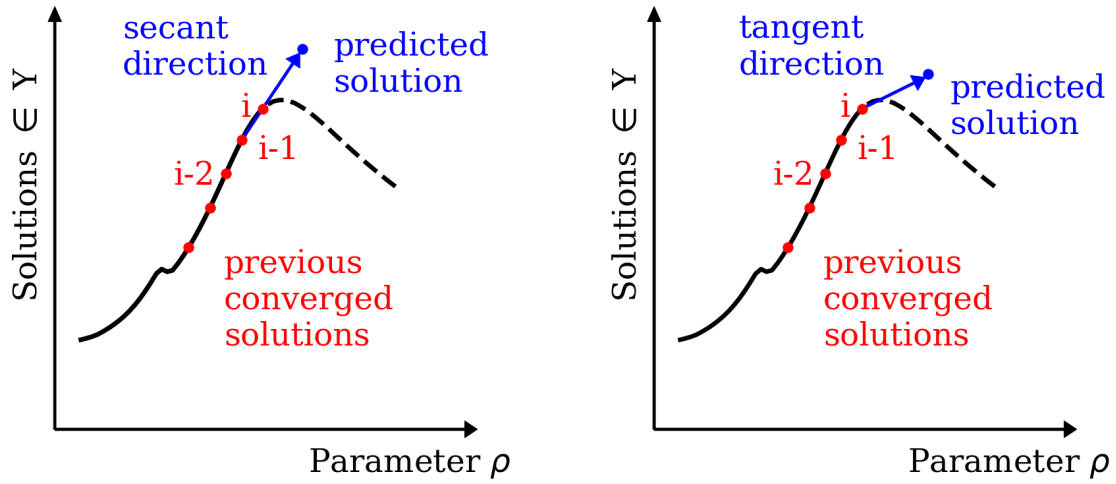
$$\hat{\underline{Q}} = \underline{\underline{\Xi}}(\omega) * \tilde{\underline{Q}};\ \hat{\underline{F}}_{nl} = \underline{\underline{\Xi}}(\omega) * \tilde{\underline{F}}_{nl};\ \hat{\underline{F}}_{ex} = \underline{\underline{\Xi}}(\omega) * \tilde{\underline{F}}_{ex} \tag{3.7}$$

$$\underline{\underline{\Xi}}(\omega) = \begin{bmatrix} \underline{\underline{\mathbf{I}}}_{N_{DoF}} \bigotimes \begin{bmatrix} 1 \\ 1 \\ \vdots \\ 1 \end{bmatrix} & \underline{\underline{\mathbf{I}}}_{N_{DoF}} \bigotimes \begin{bmatrix} e^{j\omega t_1} \\ e^{j\omega t_2} \\ \vdots \\ e^{j\omega t_N} \end{bmatrix} & \underline{\underline{\mathbf{I}}}_{N_{DoF}} \bigotimes \begin{bmatrix} e^{j2\omega t_1} \\ e^{j2\omega t_2} \\ \vdots \\ e^{j2\omega t_N} \end{bmatrix} & \cdots & \underline{\underline{\mathbf{I}}}_{N_{DoF}} \bigotimes \begin{bmatrix} e^{jN_h\omega t_1} \\ e^{jN_h\omega t_2} \\ \vdots \\ e^{jN_h\omega t_N} \end{bmatrix} \end{bmatrix} \tag{3.8}$$

3.2 Continuation Method

To obtain an evolution nonlinear dynamic response against a certain chasing parameter, the classic continuation method is applied [3]. It is a useful numerical method to track the evolution of systemic behaviour with respect to a specific parameter, especially in the field of nonlinear dynamics. For example, in the computation of nonlinear forced responses, the solutions are expected to be computed for a range of excitation frequency. Therefore, in this case, the excitation frequency is considered as the chasing parameter and the evolution of dynamic response against excitation frequency can be accurately calculated using the continuation method.

In a classic continuation process, each step consists of two parts: a predictor and a corrector. In the predictor, the initial solutions are predicted based on a certain algorithm. Then, these predicted solutions are iteratively converged to the actual solutions following a correction constrains using the classic Newton-Raphson solver.



(a) Secant Predictor (b) Tangent Predictor

Fig. 3.2 Demonstration of predictors in a continuation step: (a) Secant predictor; (b) Tangent Predictor

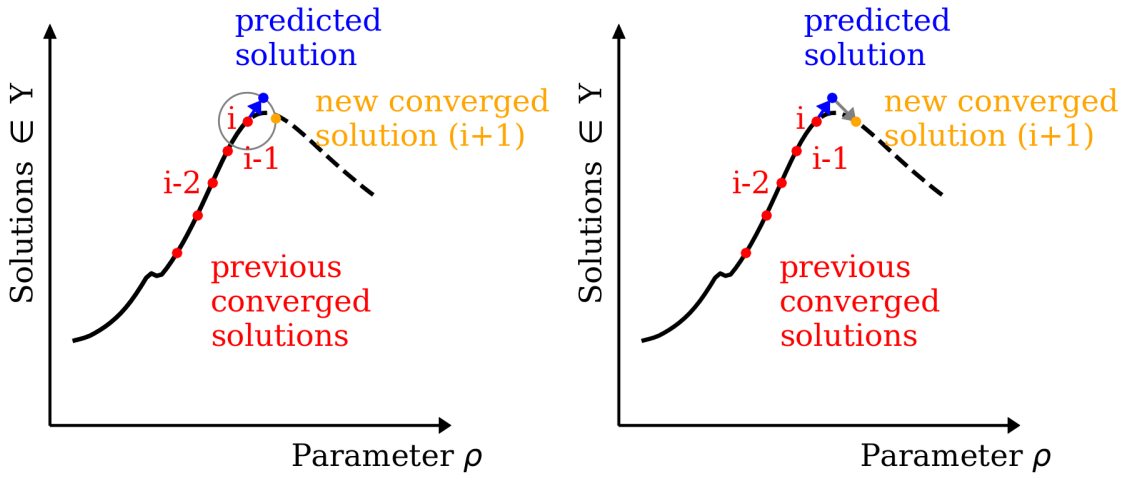
3.2.1 Prediction

In each iteration, the solutions $\underline{Y}$ are predicted in the first place using a certain principle. There are many types of predictors in the literature, i.e. the secant method, the tangent method and the Lagrange polynomial [3]. In Fig.3.2, the demonstration of a secant predictor and a tangent predictor is provided.

Secant method is a simple and cheap method, but it is difficult to capture the curve with a small radius. The solutions in the next iteration $\underline{Y}_{i+1}$ is predicted in the secant direction. If the converged solutions and parameter at the current step is defined as $\underline{Y}_i$ and λ_i, the step size is defined as δs, then the predicted solutions $\underline{Y}_{pre}$ and λ_{pre} can be defined using Eqn.(3.9).

$$\begin{aligned} \lambda_{pre} &= \lambda_i + \delta s \\ \underline{Y}_{pre} &= \underline{Y}_i + \delta s \cdot (\underline{Y}_i - \underline{Y}_{i-1})/(\lambda_i - \lambda_{i-1}) \end{aligned} \tag{3.9}$$

The use of tangent predictor is another popular method. The tangent vector is required to be computed in advance. Then, the solutions in the next iteration are predicted following the tangent direction. Compared to the secant method, the tangent method requires more computational efforts and can provide better convergence at curve with a small radius. The



(a) Arc-length Corrector (b) Pseudo Arc-length Corrector

Fig. 3.3 Demonstration of correctors in a continuation step: (a) Arc-length corrector; (b) Pseudo arc-length corrector

equations are shown in Eqn.(3.10), where $\delta \underline{Y}$ is the tangent vector.

$$\begin{aligned} \lambda_{pre} &= \lambda_i + \delta s \\ \underline{Y}_{pre} &= \underline{Y}_i + \delta s \cdot \delta \underline{Y} \end{aligned} \tag{3.10}$$

Determination of the step size δs is also important to achieve a better prediction. Usually, there is self-updated process for an automatically change in the step size. The step size is decided based on the speed of convergence in the previous step (number of Newton's iterations to converge). For example, in the region with less nonlinear phenomena, only a small number of steps are required to converge a solution in the Newton-Raphson solver. Therefore, the step size δs is automatically enlarged. This is achieved by setting up a criterion, i.e. if only one Newton iteration is required in the previous step, then the step size δs increases 10%. Whereas, in the region with a turning point, the step size δs is expected to be small enough to capture the real solution.

3.2.2 Correction

In the correction process, the predicted solution is considered as an initial solution and the actual solution in the next step is converged through a Newton-Raphson process. The general idea of a correction method is that an extra constraint is augmented to HBM equations. In the literature, there are many different correctors, i.e. the arc-length corrector [29] and the

pseudo arc-length corrector [136]. Figure 3.3 provides a detailed description of these two correctors.

In an arc-length correction process, a constant radius constraint is applied. The equation used to govern this constraint is provided as Eqn.(3.11). Where in a pseudo arc-length method, an orthogonal constraint is applied as shown in Eqn.(3.12).

$$\sqrt{(\underline{Y}_{pre}-\underline{Y}_i)^2+(\lambda_{pre}-\lambda_i)^2}=\sqrt{(\underline{Y}_{i+1}-\underline{Y}_i)^2+(\lambda_{i+1}-\lambda_i)^2} \tag{3.11}$$

$$(\underline{Y}_{pre}-\underline{Y}_i)/(\lambda_{pre}-\lambda_i)\cdot(\underline{Y}_{pre}-\underline{Y}_{i+1})/(\lambda_{pre}-\lambda_{i+1})=-1 \tag{3.12}$$

3.3 Damped Nonlinear Normal Mode

In this section, two different numerical approaches used to compute the dNNMs will be described, which are CNM approach, EPMC approach. The general EoM for the computation of dNNMs is given in Eqn.(3.13). The dNNMs are usually considered as the solutions of an autonomous system with non-conservative nonlinearities, where the linear damping (either viscous and structural) and the external excitation force are not taken into account.

$$\underline{\underline{\mathbf{M}}}\,\underline{\ddot{Q}}+\underline{\underline{\mathbf{K}}}\,\underline{Q}+\underline{F}_{nl}(\underline{Q},\underline{\dot{Q}})=0 \tag{3.13}$$

3.3.1 Complex nonlinear mode

In a system with a non-conservative nonlinear force, solutions are not periodic anymore. Therefore, the idea of CNM [92] is that, instead of using an undamped periodic solution for conservative systems, a damped solution is assumed for Eqn.(3.13) and approximated using Fourier series with an exponential decay as shown in Eqn.(3.14):

$$\underline{Q}(t)=\sum_{n_h=0}^{N_h}\underline{\tilde{Q}}_{nh}e^{n_h(j\omega_d-\beta)t};\ \underline{\tilde{Q}}_{nh}=\underline{\tilde{Q}}^c_{nh}-j\underline{\tilde{Q}}^s_{nh} \tag{3.14}$$

Where n_h is the order of harmonics up to N_h and j represents imaginary part. ω_d is the damped resonant frequency and β is the decay factor, where $\omega_d=\omega_0\sqrt{1-\zeta^2}$ and $\beta=\zeta\omega_0$. ω_0 is the resonant frequency and ζ is the modal damping ratio. In CNM approach, the damping ratio of the damped solution is assumed to be identical for each order of harmonics. Substitute the solution in Eqn.(3.14) into Eqn.(3.13), and the EoM can be rewritten as Eqn.(3.15):

$$(jn_h\omega_d - n_h\beta)^2\underline{\underline{\mathbf{M}}}\,\underline{\tilde{Q}}_{nh} + \underline{\underline{\mathbf{K}}}\,\underline{\tilde{Q}}_{nh} + \underline{\tilde{F}}_{nl,nh}(\underline{\tilde{Q}}_{nh}) = 0 \tag{3.15}$$

$$\underline{\underline{\mathbf{Z}}}^{cnm}\,\underline{\tilde{Q}} + \underline{\tilde{F}}_{nl}(\underline{\tilde{Q}}) = 0 \tag{3.16}$$

$$\underline{\underline{\mathbf{Z}}}^{cnm}_{nh} = \underline{\underline{\mathbf{K}}} - n_h^2\omega_d^2\underline{\underline{\mathbf{M}}} + n_h^2\beta^2\underline{\underline{\mathbf{M}}} - j2\beta\omega_d n_h^2\underline{\underline{\mathbf{M}}} \tag{3.17}$$

$$\underline{\underline{\mathbf{Z}}}^{cnm}_{nh} = \underline{\underline{\mathbf{K}}} - n_h^2\omega_0^2\underline{\underline{\mathbf{M}}} + 2n_h^2\zeta^2\omega_0^2\underline{\underline{\mathbf{M}}} - j2\zeta n_h^2\omega_0^2\sqrt{1-\zeta^2}\underline{\underline{\mathbf{M}}} \tag{3.18}$$

Where $\underline{\tilde{F}}_{nl,nh}$ is the nonlinear force in the frequency domain calculated using AFT method. Then, EoM in the frequency domain is given in Eqn.(3.15), where $\underline{\underline{\mathbf{Z}}}^{cnm}$ is the complex dynamic stiffness for CNM approach with a similar form as Eqn.(3.4). $\underline{\underline{\mathbf{Z}}}^{cnm}_{nh}$ is given as Eqn.(3.18).

3.3.2 Extended periodic motion concept

In the EPMC approach, a periodic concept of the dNNMs is described by introducing an artificial damping to balance the energy exchanged and make the solutions periodic [79]. In EPMC, a linear artificial damping is used to represent the nonlinear damping effect caused by the non-conservative nonlinear force. Thanks to this artificial damping, the energy loss or gained is compensated leading to a periodic solution. For example, in a system with friction damping, the energy dissipated because of the rubbing motion between the contact interfaces leads to a negative artificial damping. Then, the energy dissipated by the frictional contact is made up by this negative artificial damping resulting in a periodic solution of dNNMs.

Two different types of artificial damping are considered in this thesis: one is the viscous damping originally proposed by Krack in [79] and the other one is hysteretic damping which is firstly attempted in the present thesis. Thanks to the artificial damping term, a periodic solution can be assumed for Eqn.(3.13) and solved by the classic HBM and AFT method.

$$\underline{Q}(t) = \sum_{n_h=0}^{N_h} \underline{\tilde{Q}}_{nh} e^{j\cdot n_h\omega_0 t};\ \underline{\tilde{Q}}_{nh} = \underline{\tilde{Q}}^c_{nh} - j\underline{\tilde{Q}}^s_{nh} \tag{3.19}$$

Viscous damping vs hysteretic damping

In practice, the damping mechanisms within mechanical structures are complicated. There are two types of common damping mechanisms in both physical and mathematical concepts: viscous damping and hysteretic (structural damping). Viscous damping mechanism usually denotes the fact that, in microscopic view, the energy dissipation caused by the resistive force

while molecules of fluid are rubbing together. This resistive force opposes the velocity of molecules within the fluid. Mathematically, viscous damping refers to a velocity proportional force in the form of $\underline{\underline{\mathbf{C}}}\underline{\dot{Q}}$, where $\underline{\underline{\mathbf{C}}}$ is a general damping matrix. Whereas the hysteretic damping can be considered as the friction force between the molecular layers within solids. Thus, the hysteretic damping force is proportional to the displacement from its equilibrium position. The hysteretic damping effect is mathematically achieved by using an imaginary stiffness, which guarantees a 90-degree phase shift relative to its original stiffness component. The hysteretic damping force is usually represented as: $j\zeta\underline{\underline{\mathbf{K}}}\underline{Q}$, where $\underline{\underline{\mathbf{K}}}$ is the stiffness matrix and ζ is the damping ratio. Compared to the viscous damping, the hysteretic damping is independent of the vibration frequency. Both types of damping can be used in EPMC approach as an artificial damping term to balance the energy exchanged caused by the non-conservative nonlinear force. From the author's knowledge, it still is an open question in the literature which damping mechanism is preferred in EPMC approach. Therefore, the formulations for both types of artificial damping are described when they are used in the computation of dNNMs and E-EBM in this work. For the sake of clarity, EPMC method with a viscous artificial damping proposed by Krack [79] is called as EPMC-V and the one with a hysteretic damping is named as EPMC-H.

Artificial viscous damping (EPMC-V)

A negative artificial viscous damping is introduced into Eqn.(3.13) and the EoM becomes Eqn.(3.20). ζ is the modal damping ratio. By substituting Eqn.(3.19) into Eqn.(3.20) for each order of harmonics and applying Fourier-Galerkin procedure, the EoM in the frequency domain is obtained. $\underline{\underline{\mathbf{Z}}}^{ev}$ is the complex dynamic stiffness matrix for the EPMC approach with a viscous damping and the diagonal matrices of $\underline{\underline{\mathbf{Z}}}^{ev}$ are given in Eqn.(3.23). The superscript ^{ev} represents the EPMC-V.

$$\underline{\underline{\mathbf{M}}}\underline{\ddot{Q}} - 2\zeta\omega_0\underline{\underline{\mathbf{M}}}\underline{\dot{Q}} + \underline{\underline{\mathbf{K}}}\underline{Q} + \underline{F}_{nl}(\underline{Q}) = 0 \tag{3.20}$$

$$(jn_h\omega_0)^2\underline{\underline{\mathbf{M}}}\underline{\tilde{Q}}_{nh} - j2n_h\zeta\omega_0^2\underline{\underline{\mathbf{M}}}\underline{\tilde{Q}}_{nh} + \underline{\underline{\mathbf{K}}}\underline{\tilde{Q}}_{nh} + \underline{\tilde{F}}_{nl,nh}(\underline{\tilde{Q}}_{nh}) = 0 \tag{3.21}$$

$$\underline{\underline{\mathbf{Z}}}^{ev}\underline{\tilde{Q}} + \underline{\tilde{F}}_{nl}(\underline{\tilde{Q}}) = 0 \tag{3.22}$$

$$\underline{\underline{\mathbf{Z}}}^{ev}_{nh} = \underline{\underline{\mathbf{K}}} - n_h^2\omega_0^2\underline{\underline{\mathbf{M}}} - j2n_h\zeta\omega_0^2\underline{\underline{\mathbf{M}}} \tag{3.23}$$

Artificial hysteretic damping (EPMC-H)

A negative artificial hysteretic damping is introduced into Eqn.(3.13) and a new EoM is shown in Eqn.(3.24). The hysteretic damping is related to its linear stiffness. After a similar derivation, the EoM in the frequency domain is shown in Eqn.(3.26-3.27). The superscript ^{eh} represents the EPMC-H.

$$\underline{\underline{\mathbf{M}}}\,\underline{\ddot{Q}} + \underline{\underline{\mathbf{K}}}\,\underline{Q} - j2\zeta\,\underline{\underline{\mathbf{K}}}\,\underline{Q} + \underline{F}_{nl}(\underline{Q}) = 0 \tag{3.24}$$

$$(jn_h\omega_0)^2\underline{\underline{\mathbf{M}}}\,\underline{\tilde{Q}}_{nh} + (\underline{\underline{\mathbf{K}}} - j2\zeta\underline{\underline{\mathbf{K}}})\,\underline{\tilde{Q}}_{nh} + \underline{\tilde{F}}_{nl,nh}(\underline{\tilde{Q}}_{nh}) = 0 \tag{3.25}$$

$$\underline{\underline{\mathbf{Z}}}^{eh}\,\underline{\tilde{Q}} + \underline{\tilde{F}}_{nl}(\underline{\tilde{Q}}) = 0 \tag{3.26}$$

$$\underline{\underline{\mathbf{Z}}}^{eh}_{nh} = \underline{\underline{\mathbf{K}}} - n_h^2\omega_0^2\underline{\underline{\mathbf{M}}} - j2\zeta\underline{\underline{\mathbf{K}}} \tag{3.27}$$

3.3.3 Energy dependency and normalisation

Unlike the linear normal modes, the nonlinear modes and other modal properties are highly energy-dependent. The nonlinear mode shape $\underline{Q}$ and the resonant frequency ω_0 vary with the level of energy within the system. To capture this energy-dependence, a new parameter, the modal amplitude α, is introduced into the system to quantify the modal energy. Then, the modal displacement can be expressed as: $\underline{Q} = \alpha \cdot \underline{Q}_{mn}$, where $\underline{Q}_{mn}$ is the mass normalised modal displacement. This modal amplitude α is the chasing parameter used in the continuation method (see Section 3.2) to track the evolution of the dNNMs with respect to the modal energy. Then, the general EoM for the computation of dNNMs in the frequency domain is rewritten as Eqn.(3.28), where $\underline{\underline{\mathbf{Z}}}$ is the general dynamic stiffness matrix (see Eqn.(3.17) for CNM, Eqn.(3.23) for EPMC-V and Eqn.(3.27) for EPMC-H). The mass normalised modal displacement is achieved by applying Eqn.(3.29) as a constraint, where $\underline{\underline{\mathbf{I}}}$ is the identity matrix. In addition, the absolute phase of the dNNMs is arbitrary. Therefore, a phase normalisation is required and shown in Eqn.(3.30). Other types of phase normalisation can be found in [51].

$$\alpha \cdot \underline{\underline{\mathbf{Z}}}\,\underline{\tilde{Q}}_{mn} + \underline{\tilde{F}}_{nl}(\alpha \cdot \underline{\tilde{Q}}_{mn}) = 0 \tag{3.28}$$

$$\underline{\tilde{Q}}^{\mathrm{T}}_{mn} \cdot (\underline{\underline{\mathbf{I}}}_{N_h} \otimes \underline{\underline{\mathbf{M}}}) \cdot \underline{\tilde{Q}}_{mn} = \underline{\underline{\mathbf{I}}} \tag{3.29}$$

$$\mathrm{imag}(\tilde{Q}^1_{mn,n=1}) = 0 \tag{3.30}$$

3.3.4 Summary for two numerical approaches

Two existing numerical approaches used to compute the dNNMs for systems with non-conservative nonlinearities are formulated in this section, which are CNM and EPMC. Because of the presence of non-conservative nonlinearities, the actual solutions of such systems are not periodic. These two numerical approaches used different strategies to handle the aperiodicity. In CNM, the damped solutions are assumed in a harmonic form with an exponential decay. Whereas, in EPMC, an artificial damping term is introduced to balance the energy exchange caused by the non-conservative nonlinearities.

Then, HBM with AFT method is applied in both approaches. However, to adopt AFT method in CNM approach, a very important assumption is made in advance. In the classic AFT process, the exponential decay terms cannot be addressed in the DFT process. Thus, the non-conservative terms cannot be included, while calculating the displacement in the time domain from its Fourier coefficients. Therefore, to adopt the classic AFT method into the CNM approach, the terms that represent the exponential decay are simply eliminated leading to a periodic solution as described in [91]. In [70], a phase correction of the nonlinear force is added to capture the decay term in the CNM approach. Unfortunately, this phase correction can only be applied to single DoF system analytically. In this work, the damped solutions from CNM approaches are assumed to be periodic in AFT procedure, and the decay terms are simply removed.

3.4 Extended Energy Balance Method

The resonant amplitude has a great significance in the determination of high cycle fatigue. The E-EBM is a tool to predict the resonant solution in a forced system with non-conservative nonlinearities using its dNNM. The applications of E-EBM on different numerical methods, including the CNM approach and EPMC approach, are explained in this section.

3.4.1 Assumptions

The prediction of resonances is based on the assumption that the solutions of an autonomous system that bear resemblance with the solutions in the nonlinear forced responses. In detail, the E-EBM assumes that the resonant solution of nonlinear forced responses and that of the dNNMs are similar for a small enough level of damping and forcing. Therefore, these solutions can be assumed to be identical, and have been named as “resonant shared solutions”, as shown in Fig.3.4.

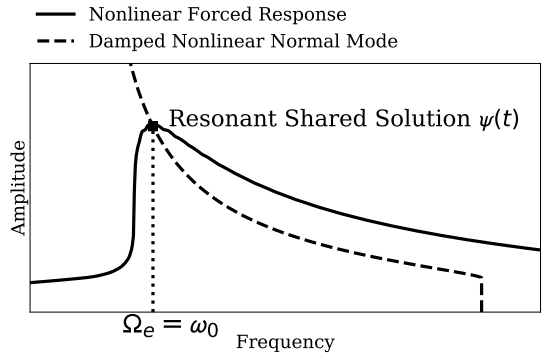


Fig. 3.4 Demonstration of resonant shared solution between damped nonlinear normal mode and nonlinear forced response

In a complicated dynamic system with a high modal density, many shared solutions may coexist in the amplitude-frequency plot. But only the solutions of the dNNMs that show a high similarity with the solutions in the forced responses are defined as "resonant shared solutions" [60]. This similarity indicates that two solutions (one from the dNNMs, the other from the forced responses) have a similar shape with a similar amplitude at the similar frequency.

It is important to emphasize that the mode shape of a dNNM has already included the effects from other modes, because it is calculated from the full stiffness and mass matrices [135]. This concept is different than that in a linear system, since all linear normal modes are orthogonal to each other. For example, in the case of internal resonance, more than one modes can respond at the same frequency. Thus, the dNNMs have a shape which can be seen as a combination of these two modes [163]. Whereas in the forced response, it is difficult to ensure that the solutions of each DoF respond a same shape of the corresponding DoF in dNNMs, which is highly depends on the shape of the excitation forces. Furthermore, for a system with a high order polynomial nonlinearity or with a nonlinear energy sink, the DoFs within such a system may not respond at the same frequency [181]. Therefore, the assumption of the "resonant shared solution" is only valid in a weakly nonlinear system with the absence of the internal resonance [22].

3.4.2 Numerical formulations

The general EoM in a forced system with non-conservative nonlinear forces is given in Eqn.(3.31). $\underline{\underline{\mathbf{C}}}$ is the known damping matrix. $\underline{F}_{ex}$ is the external excitation force, $\underline{\bar{F}}_{ex}$ is the unit vector of excitation force and γ is the excitation forcing level. Ω_e is the excitation frequency; φ is the absolute phase of the excitation force. In this work, the external excitation

force is considered as a simple harmonic excitation and the solutions of system are represented by multi-harmonics. It is easy to extend to the system with a multi-harmonics excitation. After applying the HBM, the EoM can be transferred into the frequency domain as given in Eqn.(3.33)

$$\underline{\underline{\mathbf{M}}}\,\underline{\ddot{Q}}_f + \underline{\underline{\mathbf{C}}}\,\underline{\dot{Q}}_f + \underline{\underline{\mathbf{K}}}\,\underline{Q}_f + \underline{F}_{nl}(\underline{Q}_f, \underline{\dot{Q}}_f) = \underline{F}_{ex}(\gamma, \Omega_e, \varphi, t) \tag{3.31}$$

$$\underline{Q}_f(t) = \sum_{n=0}^{N_h} \underline{\tilde{Q}}_{f,n} e^{jn_h\Omega_e t};\ \underline{F}_e = \gamma \underline{\bar{F}}_e e^{j(\Omega_e t+\varphi)} \tag{3.32}$$

$$(jn_h\Omega_e)^2 \underline{\underline{\mathbf{M}}}\,\underline{\tilde{Q}}_{f,nh} + jn_h\Omega_e \underline{\underline{\mathbf{C}}}\,\underline{\tilde{Q}}_{f,nh} + \underline{\underline{\mathbf{K}}}\,\underline{\tilde{Q}}_{f,nh} + \underline{\tilde{F}}_{nl,nh}(\underline{\tilde{Q}}_{f,nh}) = \begin{cases} \gamma e^{j\varphi}\underline{\bar{F}}_{ex} & \text{if} \quad n_h = 1 \\ \underline{\mathbf{0}} & \text{if} \quad n_h \neq 1 \end{cases} \tag{3.33}$$

$$\underline{\underline{\mathbf{Z}}}^f\,\underline{\tilde{Q}}_f + \underline{\tilde{F}}_{nl}(\underline{\tilde{Q}}_f) = [\underline{\mathbf{0}}, \gamma e^{j\varphi}\underline{\bar{F}}_{ex}, \cdots, \underline{\mathbf{0}}]^{\mathrm{T}} \tag{3.34}$$

$$\underline{\underline{\mathbf{Z}}}^f_{nh} = \underline{\underline{\mathbf{K}}} - n_h^2\Omega_e^2\underline{\underline{\mathbf{M}}} + jn_h\Omega_e\,\underline{\underline{\mathbf{C}}} \tag{3.35}$$

As shown in Eqn.3.36, when the excitation frequency Ω_e equals the resonant frequency ω_0, the resonant shared solution between the forced response and the dNNM can be found and represented by $\underline{\psi}$. Figure 3.4 shows an example of a resonant shared solution. Each solution points along the dNNM can be considered as a resonant shared solution of a nonlinear forced response with a certain excitation forcing level.

$$\underline{\psi} = \underline{Q} \approx \underline{Q}_f \text{ and } \underline{\tilde{\psi}} = \alpha \cdot \underline{\tilde{Q}}_m \approx \underline{\tilde{Q}}_f \text{ when } \omega = \Omega_e = \omega_0 \tag{3.36}$$

For each level of the modal amplitude α, the resonant shared solution $\underline{\psi}$, the resonant frequency ω_0 and the modal damping ratio ζ are calculated using either CNM approach and EPMC approach. The excitation forcing level γ and the phase of excitation force φ can be determined using E-EBM if the damping matrix $\underline{\underline{\mathbf{C}}}$ and the unit vector of the excitation force $\underline{\bar{F}}_{ex}$ are given. Recalling the Eqn.(3.28, 3.34) and assuming that the solution of the nonlinear forced response equals the resonant shared solution $\underline{\psi}$, the subtraction of Eqn.(3.28) to Eqn.(3.34) must hold in its weak form. Then, the energy exchanged caused by the damping terms E^d and the forcing term $E^f(\gamma, \varphi)$ are calculated by integrating the damping force and excitation force times the velocity over one vibrational period $2\pi/\omega$. The calculation of $E^f(\gamma, \varphi)$ is given in Eqn.(3.37, 3.39) and it is the same for both CNM and EPMC. Equations used for calculation of E^d are described Eqn.(3.38-3.39), where $\underline{\underline{\mathbf{C}}}^*\,\underline{\tilde{\psi}}_{nh} e^{jn\omega t}$ represents the

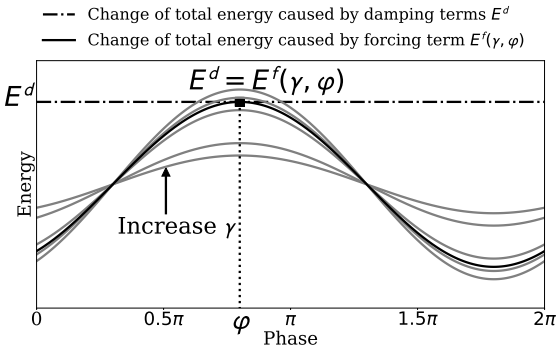


Fig. 3.5 The energy transferred by the damping terms (E^d) for a fixed modal amplitude α and the energy transferred by forcing terms ($E^f(\gamma,\varphi)$) for different excitation levels γ with respect to the forcing phase φ

net non-conservative force, which is different between the CNM and EPMC approaches.

$$E^f_{nh}(\gamma,\varphi) = \int_0^{\frac{2\pi}{n_h\omega}} \gamma e^{j\varphi} \underline{\bar{F}}_{ex} e^{j\omega t} \cdot j n_h \omega \underline{\tilde{\psi}}_{nh} e^{j n_h \omega t} \delta t \tag{3.37}$$

$$E^d_{nh} = \int_0^{\frac{2\pi}{n_h\omega}} \underline{\underline{\mathbf{C}}}^* \underline{\tilde{\psi}}_{nh} e^{j n_h \omega t} \cdot j n_h \omega \underline{\tilde{\psi}}_{nh} e^{j n_h \omega t} \delta t \tag{3.38}$$

$$\begin{aligned} E^f(\gamma,\varphi) &= E^f_{n_h=1}(\gamma,\varphi) \\ E^d &= \textstyle\sum_{n_h=0}^{N_h} E^d_{nh} \end{aligned} \tag{3.39}$$

$$\underline{\underline{\mathbf{C}}}^{cnm} = -2n^2\zeta^2\omega_0^2\underline{\underline{\mathbf{M}}} + jn\omega_0\underline{\underline{\mathbf{C}}} + j2\zeta n^2\omega_0^2\sqrt{1-\zeta^2}\underline{\underline{\mathbf{M}}} \tag{3.40}$$

$$\underline{\underline{\mathbf{C}}}^{ev} = jn\omega_0\underline{\underline{\mathbf{C}}} + j2n\zeta\omega_0^2\underline{\underline{\mathbf{M}}} \tag{3.41}$$

$$\underline{\underline{\mathbf{C}}}^{eh} = jn\omega_0\underline{\underline{\mathbf{C}}} + j2\zeta\underline{\underline{\mathbf{K}}} \tag{3.42}$$

The dNNM, the resonant frequency ω_0 and the modal damping ratio ζ are calculated for a range value of modal amplitude α using the continuation method. For each particular value of α, the dNNM can be seen as the resonant shared solution with a nonlinear forced response with a certain excitation forcing level. The energy exchanged by the damping terms E^d and excitation forcing term E^f are computed for each value of α using Eqn.(3.37-3.42). E^d is constant for a given resonant shared solution, whereas E^f depends on the value of the forcing level γ and the forcing phase φ (see Eqn.3.38). A typical scenario is provided in Fig.3.5 showing the variation of E^d and E^f for a certain value of α. To determine φ and γ is to find the single intersection between the curve of $E^f(\gamma,\varphi)$ and the constant value of E^d that will occur at the maximum (if $E^d > 0$) or the minimum (if $E^d < 0$) of $E_f(\gamma,\varphi)$. A

classic force amplitude curve can be built, if this operation is applied to each value of modal amplitude α. In a system with non-conservative nonlinear forces, the modal damping ratio ζ can be either positive (like systems with nonlinear damping) or negative (systems with self-excited solutions). Based on the value of E^d and ζ, there are four situations in total.

(i) $\zeta > 0$: When the modal damping ratio is positive, the non-conservative nonlinear force in the system provides external damping and the total energy of the autonomous system is dissipated. In this case, the total energy injected by the external excitation force is required to balance the summation of the energy dissipated by viscous damping and external damping generated by the nonlinear force.

(ii) $\zeta < 0$ and $E^d > 0$: The modal damping ratio is negative meaning that the nonlinear force is injecting energy into the system. Although, the energy dissipated by damping terms is higher than the energy injected by nonlinear force leading to a positive E^d. In this case, the external excitation force has to provide energy to the system to balance the difference between the viscous damping and the negative modal damping generated by the nonlinear force.

(iii) $\zeta < 0$ and $E^d = 0$: The modal damping ratio is negative and it perfectly balances the energy dissipated by the viscous damping term, so E_d equals to zero. In this case, self-excited solutions can be found and no external force is required to observe a periodic solution, which coincides with the limit cycle oscillation.

(iv) $\zeta < 0$ and $E^d < 0$: The modal damping ratio is negative and it overcomes the energy dissipated by the viscous damping term, so E_d is negative. In this case, for periodic solution to exist, the external force has to take energy out of the system.

3.5 Numerical Examples

In this section, three illustrative cases are tested using CNM, EPMC-V and EPMC-H methods, including a one DoF system with frictional contact, a one DoF system with quadratic nonlinear damping and a one DoF system with a cubic spring (Duffing oscillator). In each testcase, the dNNMs are computed using all three methods described in Section 3.3. The E-EBM is also applied to show the relevance between the dNNMs and the resonant solutions in forced responses. From three illustrative cases, the advantages and limitations of each methods are discussed in detail.

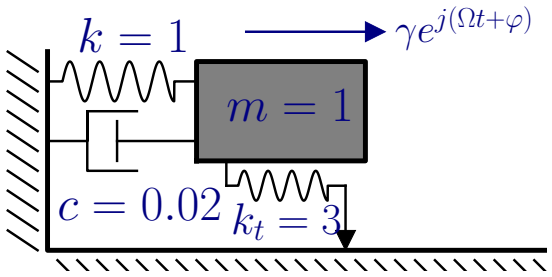


Fig. 3.6 One DoF system with frictional contact

3.5.1 One DoF system with frictional contact

The first considered system consists of a single point mass oscillator with a Jenkins element as shown in Fig.3.6. This one DoF model has also been tested in [70]. The dynamic equation of the forced system is given in Eqn.(3.44), where $\underline{f}_{nl}$ represents the friction forces calculated from the Jenkins element. This Jenkins element is considered as a simplistic model to represent the friction forces with a value of maximum static friction $f_{max} = 1$. The formulations of this Jenkins element are provided in Appendix A.1. There are two contact conditions in this Jenkins element model, which are sticking and sliding. The EoM used for the computation of the dNNM is shown in Eqn.(3.43). The classic force amplitude curve (γ-q_{max} plot) obtained from E-EBM is shown together with dNNM (ω_0-q_{max}, ζ-q_{max} plots) calculated using HBM with the first five harmonics $N_h = 5$. A simple harmonic excitation force is applied to the same system with an excitation forcing level γ. The results calculated from the three different methods (CNM, EPMC-V and EPMC-H) are shown in Fig.3.7. The evolutions of ω_0, ζ and γ are plotted with respect to the vibration amplitude q_{max}.

$$m\underline{\ddot{q}} + k\underline{q} + \underline{f}_{nl}(\underline{q}) = 0 \tag{3.43}$$

The analytical ω_0 at the sticking condition is 2. As shown in Fig.3.7(a) (ω_0-q_{max} plot), the evolution of ω_0 calculated from EPMC approaches exhibits a great agreement (between EPMC-V and EPMC-H). Whereas ω_0 calculated from CNM shows a slight discrepancy between that from EPMC. Results from all three methods show a similar trend: a constant ω_0 is obtained at low amplitude, and an increase in the vibration amplitude leads to a softening effect. The change of ω_0 is a typical phenomenon in a system with frictional contact. As for modal damping ratio ζ, the one calculated from EPMC-H deviates from other two methods. To achieve a better understanding, the normalised energy dissipation caused by the friction force is also shown in Fig.3.7(b) by the red curve. It is worth pointing out that the energy dissipation curves are exactly same among the three methods. The energy dissipation is

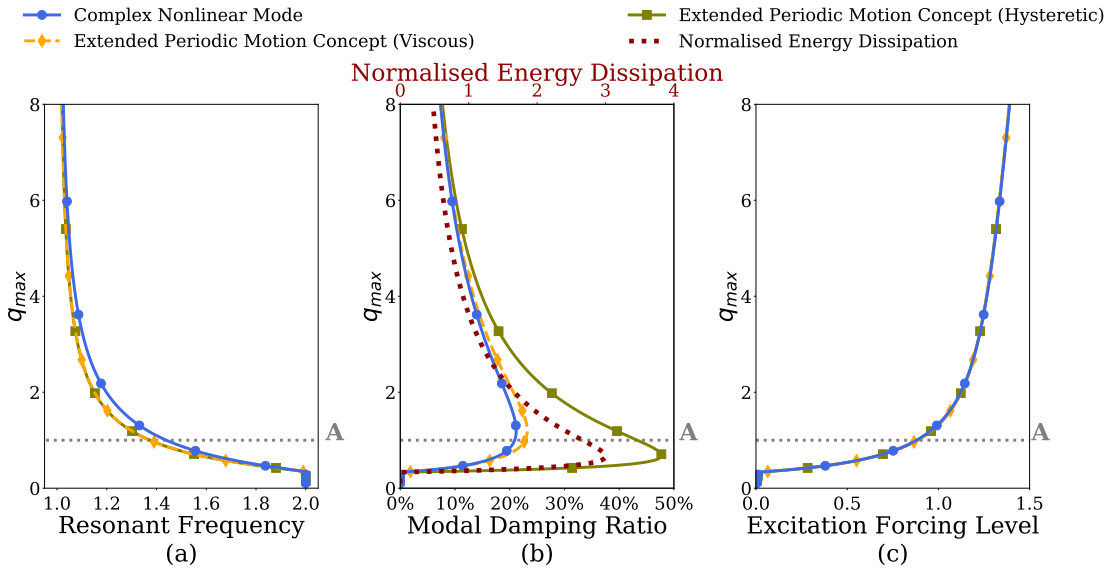
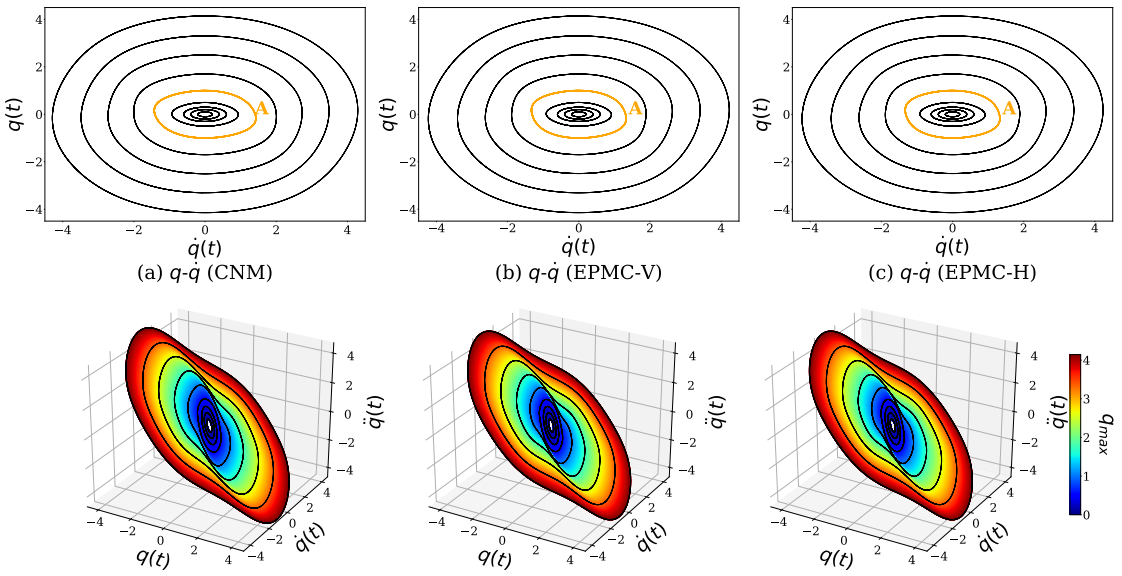


Fig. 3.7 Numerical results from the damped nonlinear normal mode within a range of modal amplitude for the one DoF system with frictional contact: (a) ω_0-q_{max} plot; (b) ζ-q_{max} plot and normalised energy dissipation against q_{max}; plot(c) γ-q_{max} plot using the extended energy balance method

simply calculated by integrating the product of tangential friction force and velocity within one vibrational period $2\pi/\omega_0$. Comparing the ζ-q_{max} plots, the result from EPMC-H shows better agreement with the energy dissipation curve. As the hysteretic damping is independent on resonant frequency ω_0, whereas viscous damping relates to ω_0. Due to existence of the softening effect caused by the frictional contact, a decrease in resonant frequency leads to a smaller viscous damping ratio and an unchanged hysteretic damping ratio. As described in Section 3.3, different assumptions are used in three different methods resulting in a deviation of modal damping ratio ζ. The friction force is computed based on the classic Jenkins element, which is independent on resonant frequency. Therefore, the EPMC-H can provide more accurate representation of the energy dissipation than the EPMC-V method.

Figure 3.7(c) demonstrates the evolutions of γ against the amplitude q_{max} obtained using E-EBM, which is equivalent to classic force amplitude plot and widely used in structural dynamics. As shown in Fig.3.7(c), the predicted excitation forcing level γ from the three methods are very similar. The invariant manifold of this mode is represented by a hypersurface ($\ddot{q}$-q-$\dot{q}$), as shown in Fig.3.8. The undamped solutions from CNM are used to construct the manifold. From the figure, the envelopes are almost indistinguishable between the three methods. The solutions of dNNM with vibration amplitude q_{max} of 1 (Case A in Fig.3.7 and Fig.3.8) are shown in Fig.3.9. The blue and purple solid curves represent the damped and



(a) q-$\dot{q}$ (CNM) (b) q-$\dot{q}$ (EPMC-V) (c) q-$\dot{q}$ (EPMC-H)

(d) Invariant Manifold (CNM) (e) Invariant Manifold (EPMC-V) (f) Invariant Manifold (EPMC-H)

Fig. 3.8 Invariant manifolds for the one DoF system with frictional contact: (a, b, c) $q(t)$-$\dot{q}(t)$ plot; (d, e, f) Invariant Manifolds

undamped solutions calculated from CNM approach; the yellow dotted curve and green solid curve show the periodic solutions obtained from EPMC-H and EPMC-V. The results from EPMC-H and EPMC-V are very similar. By looking at damped and undamped solutions from the CNM approach, it should be noticed that there is a non-negligible discrepancy in resonant frequency in Fig.3.9(b). In Fig.3.9(c), the solutions are plotted in a three dimensional space. Solutions from CNM and EPMC do not lie on a same hypersurface. Therefore, the manifold obtained from CNM approaches shows slight differences to the EPMC approach.

To verify the modal properties obtained from dNNM coupled with E-EBM, several nonlinear force responses of this one DoF system with frictional contact are computed. The EoM used in the computation of forced responses is given as Eqn(3.44). Nonlinear forced responses calculated using five different values of γ (0.2, 0.6, 1, 1.2 and 1.3) are shown in Fig.3.10. For a given value of γ, the resonant frequency ω_0 and vibrational amplitude q_{max} can be predicted using the dNNMs. By looking at Fig.3.10(b) and Fig.3.10(c), the dNNMs computed using EPMC approaches provide very accurate predictions for the resonant frequency ω_0 and vibrational amplitude q_{max}. Whereas in Fig.3.10(a), the resonances predicted using CNM approach slightly deviate from the actual resonances obtained from nonlinear forced response. A zoom-in of the resonant shared solutions is provided in Fig.3.10.

$$m\underline{\ddot{q}} + c\underline{\dot{q}} + k\underline{q} + \underline{f}_{nl}(\underline{q}) = \gamma e^{j(\Omega_e t + \varphi)} \tag{3.44}$$

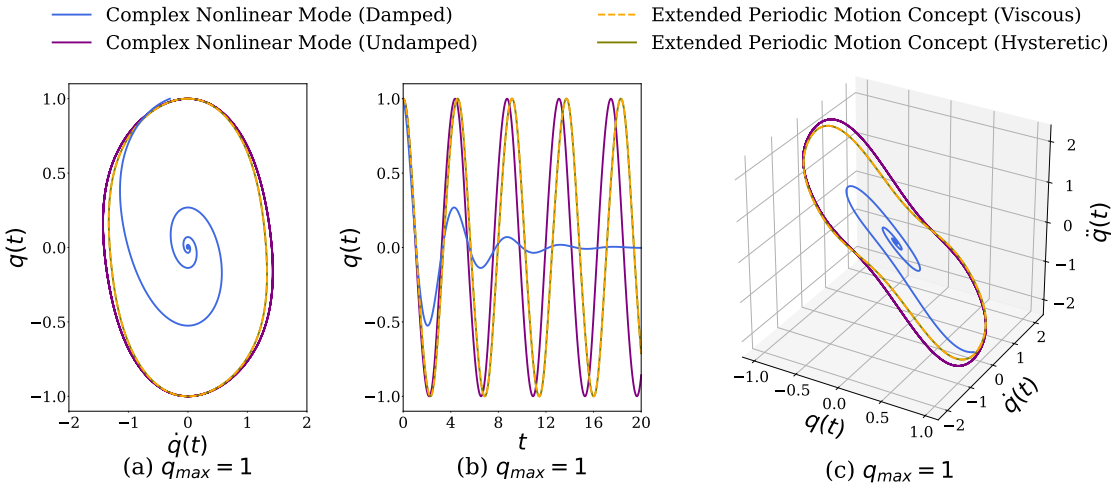


Fig. 3.9 Solutions of the damped nonlinear normal modes with vibration amplitude q_{max} of 1 for the one DoF system with frictional contact (Case A in Fig.3.7 and Fig.3.7): (a) $q(t)$-$\dot{q}(t)$ envelopes; (b) $q(t)$-t plot; (c) $\ddot{q}(t)$-$q(t)$-$\dot{q}(t)$ plot

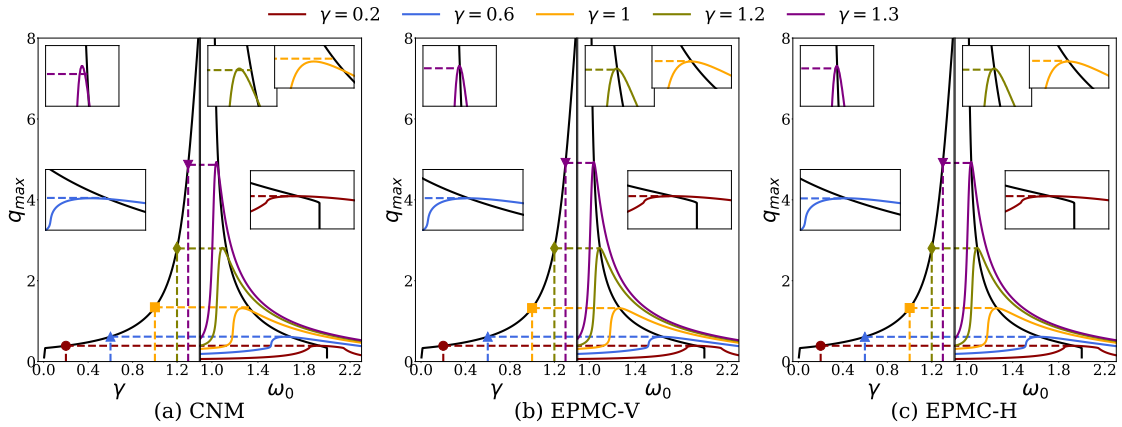


Fig. 3.10 Using nonlinear forced response to validate ω_0-q_{max} plot and γ-q_{max} plot for the one DoF system with frictional contact: (a) Complex Nonlinear Mode; (b) Extended Periodic Motion Concept with Artificial Viscous Damping; (c) Extended Periodic Motion Concept with Artificial Hysteretic Damping; Left: γ-q_{max} plot (Black curve); Right: ω_0-q_{max} (Black curve) and five nonlinear forced response in different colours

The resonances predicted using CNM coupled with E-EBM show a lower accuracy than EPMC approaches when ζ is greater than 15%. In AFT procedure, the damped solution in CNM is assumed to be periodic. The accuracy of CNM approach is lower in the case of larger damping. Whereas, in EPMC approach, the introduction of an artificial damping makes solutions periodic leading to a better performance in the AFT procedure. For this one DoF system with frictional contact, EPMC-H method provides a better representation of the energy dissipation.

3.5.2 One DoF system with quadratic nonlinear damping

A one DoF system with quadratic nonlinear damping is investigated as the second test case in this chapter. This system has been studied in [79]. The EoM for this nonlinear system is shown in Eqn.(3.45). The evolutions of ω_0, ζ and γ against vibrational amplitude q_{max} are given in Fig.3.11. The dNNMs are computed using the first 15 harmonics.

$$\ddot{\underline{q}} + 0.1\,\underline{q}^2\,\dot{\underline{q}} + \underline{q} = 0 \tag{3.45}$$

The reference results are calculated based on the theory of Spectral SubManifold (SSM) using an open source software, SSMtool [128]. SSM is considered as a smooth invariant manifold and is tangent to the linear modal subspace at the origin. An exact mathematical nonlinear reduced model is provided by the SSMtool. This reduced model is obtained through the reduction of full dynamics of studied system to the exactly invariant SSM surfaces, tangent to those subspaces [128]. The reference backbone curve and modal damping ratio curve obtained from SSMtool are provided in Fig.3.11.

The manifolds of this dNNM from the three methods and SSMtool are given in Fig.3.12. The left column shows the results from CNM; the middle left one represents EPMC-V; the middle right one for EPMC-H; the reference results from SSMtool are shown in right column. The $q-\dot{q}$(in first row), $\ddot{q}-\dot{q}$(in second row) and $\ddot{q}-q$(in third row) envelopes are provided. The manifolds are shown in the bottom row. Similar features can be seen from the manifolds. The manifold obtained from CNM shows a significant discrepancy from EPMC approaches. Further, the manifolds from the three methods are also different from the reference one from SSMtool. In addition, the solutions calculated using classic time integration are also provided as grey dotted curves in the figure as exact solutions for such a system. The solutions from time integration matches the manifold from SSMtool. To achieve a further demonstration, solutions with vibrational amplitude of 4 and 6 are shown in Fig.3.13. These two cases are highlighted in Fig.3.11 and Fig.3.12(a-d).

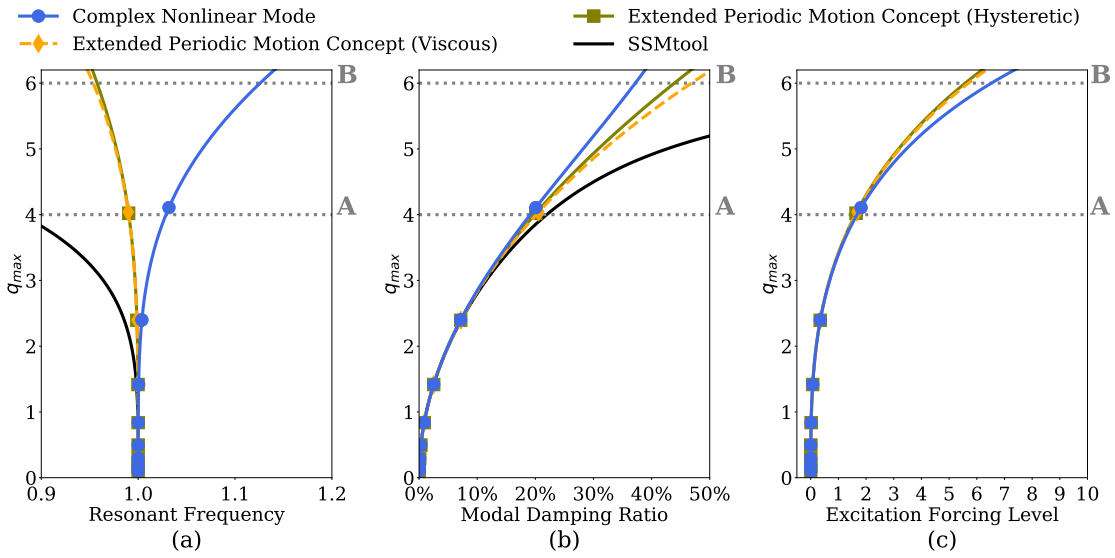


Fig. 3.11 Numerical results from the damped nonlinear normal mode within a range of modal amplitude for the one DoF system with quadratic nonlinear damping: (a) ω_0-q_{max} plot; (b) ζ-q_{max} plot; (c) γ-q_{max} plot using the extended energy balance method

In Fig.3.13, the blue and purple solid curves represent damped and undamped solutions calculated from CNM approach; the yellow dotted curves and green solid curves show the periodic solutions obtained from EPMC-H and EPMC-V; solutions from SSMtool are represented by grey curves. The solutions for Case A are shown in the top row and the bottom row represents the solutions for Case B. By comparing $q(t)$-ωt plot, the solutions computed from all numerical methods exhibit a similarity with the reference one. However, the inaccurate prediction of the resonant frequency leads to a significant discrepancy in $q(t)$-$\dot{q}(t)$ envelope.

$$\ddot{\underline{q}} + 0.1\,\underline{q}^2\,\dot{\underline{q}} + 0.01\,\dot{\underline{q}} + \underline{q} = \gamma e^{j(\Omega_e t+\varphi)} \tag{3.46}$$

To verify the ω_0-q_{max} curve and γ-q_{max} curve obtained from the dNNMs coupled with E-EBM, several nonlinear force responses of this one DoF with nonlinear damping are computed. The EoM used in the computation of the forced response is given as Eqn.(3.46). Nonlinear forced responses calculated using three different values of γ (0.5, 1 and 1.5) are shown in Fig.3.14. The backbone curve calculated from SSMtool is also given in the figure. As described before, from CNM approach, a hardening effect is obtained whereas other results (from EPMC-V, EPMC-H and SSMtool) show a softening effect. It is worth noticing that the backbone curve computed from SSMtool does not match the resonances from forced

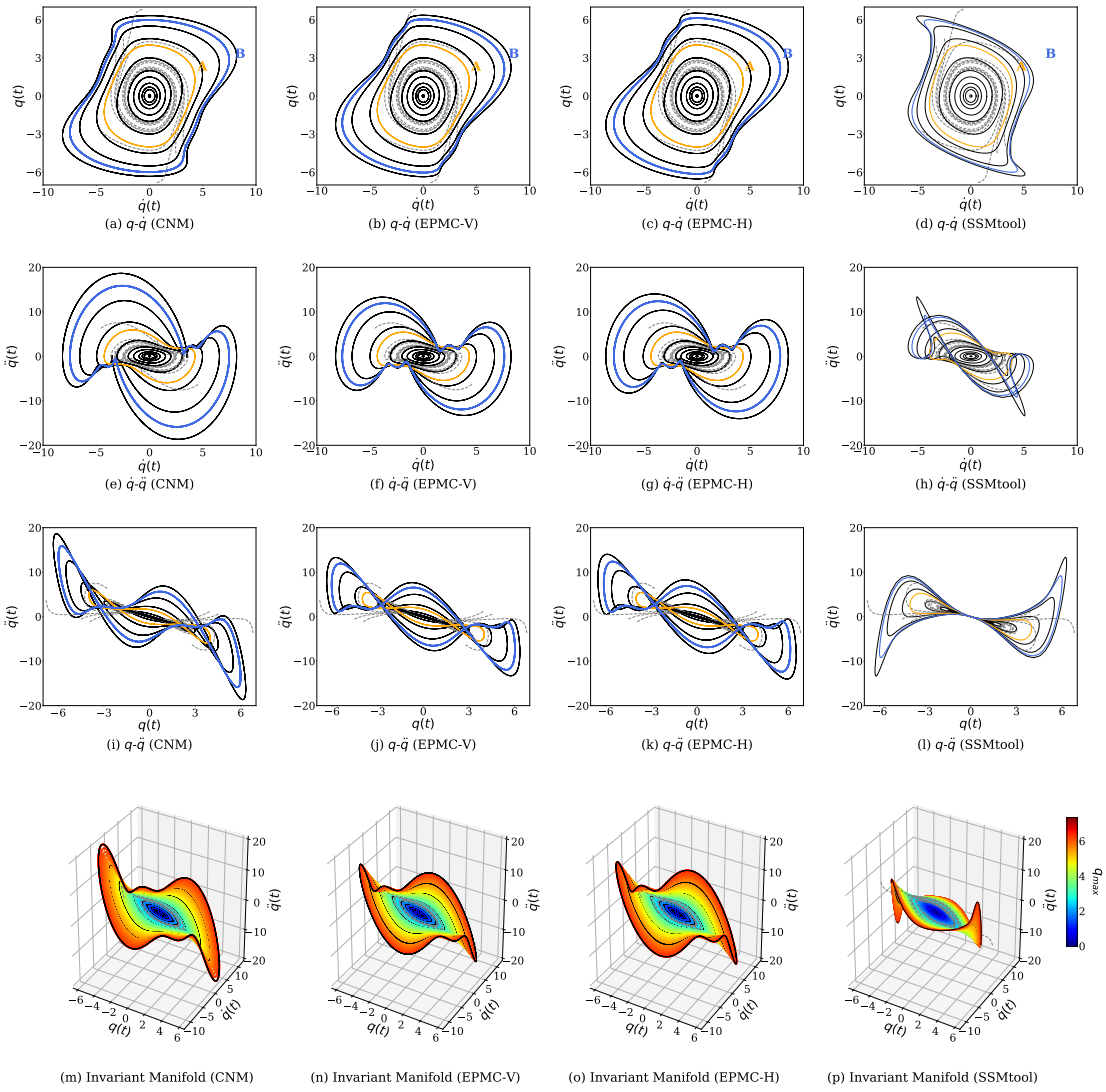


Fig. 3.12 Invariant manifolds for the one DoF system with quadratic nonlinear damping: (a, e, i, m) Results from CNM; (b, f, j, n) Results from EPMC-V; (c, g, k, o) Results from EPMC-H; (d, h, l, p) Results from SSMtool; (a-d) $q(t)$-$\dot{q}(t)$ envelopes; (e-h) $\ddot{q}-\dot{q}$ envelopes; (i-l) $\ddot{q}-q$ envelopes; (m-p) invariant manifolds

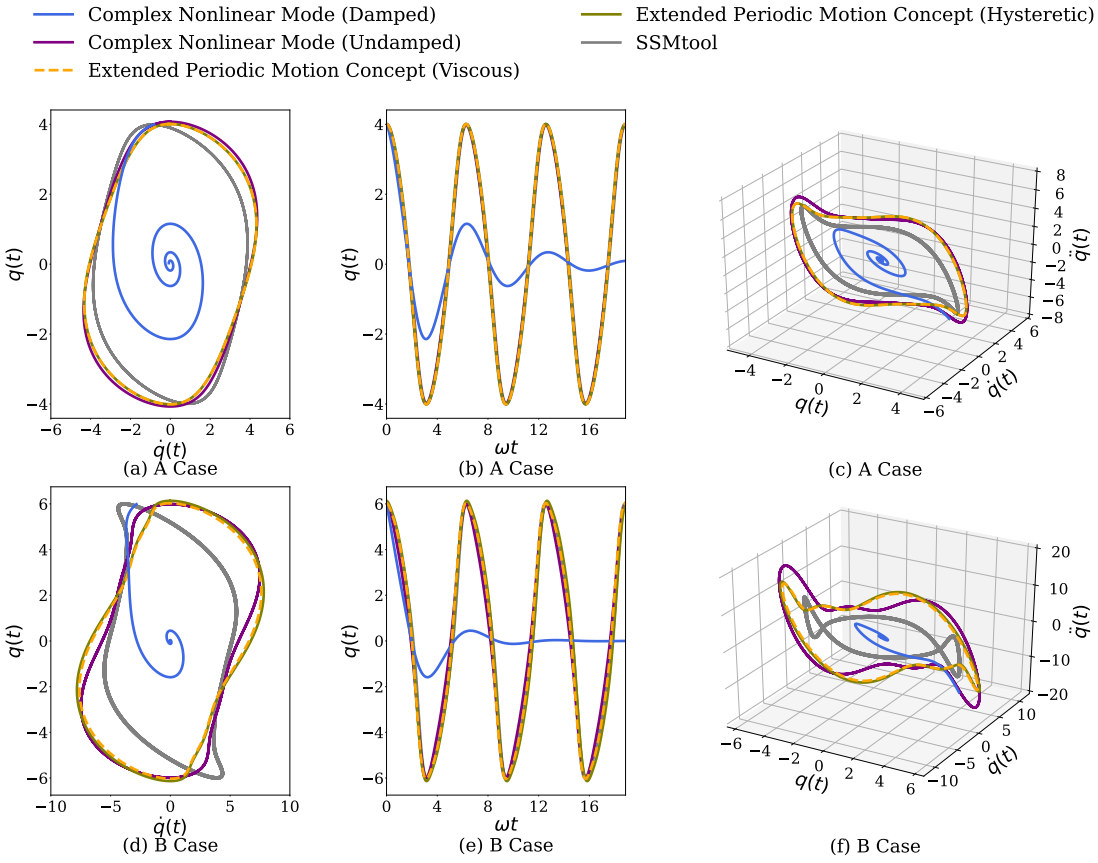


Fig. 3.13 Solutions of the damped nonlinear normal modes for the one DoF system with quadratic nonlinear damping (Case A and B in Fig.3.11 and Fig.3.12): (a, b, c) Case A; (d, e, f) Case B; (a, d) $q(t)$-$\dot{q}(t)$ envelopes; (b, e) $q(t)$-ωt plot; (c, f) $\ddot{q}(t)$-$q(t)$-$\dot{q}(t)$ plot

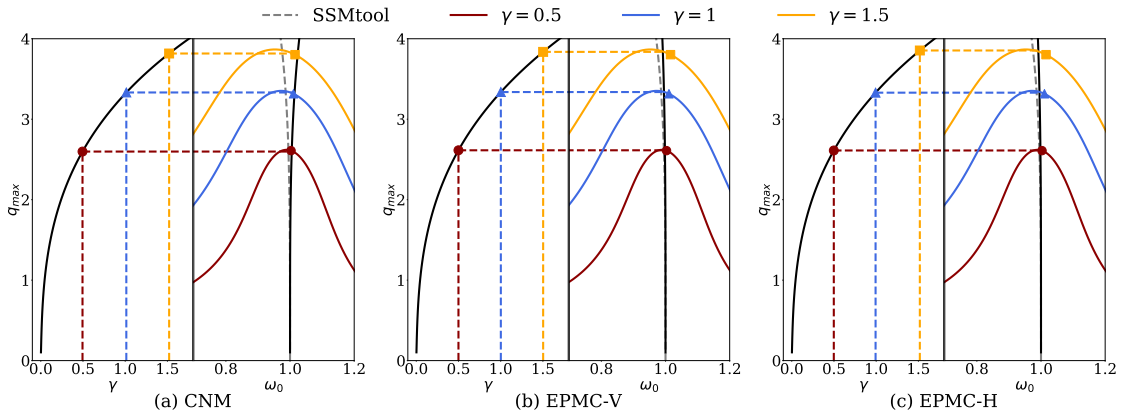


Fig. 3.14 Using nonlinear forced response to validate ω_0-q_{max} plot and γ-q_{max} plot for the one DoF system with quadratic nonlinear damping: (a) Complex Nonlinear Mode; (b) Extended Periodic Motion Concept with Artificial Viscous Damping; (c) Extended Periodic Motion Concept with Artificial Hysteretic Damping; Left: γ-q_{max} plot (Black curve); Right: ω_0-q_{max} (Black curve) and three nonlinear forced response in different colours

response in the case of large damping. It is because the backbone curve can be seen as a collection of resonances under the conditions of small forcing and damping [22].

The one DoF system with quadratic nonlinear damping ($q^2\dot{q}$) is tested using the three numerical and results are compared with SSMtool and time integration. A hardening effect is obtained from CNM, whereas the mathematical backbone (from SSMtool) shows a softening trend. This is caused by periodic assumption in AFT procedure of CNM method as explained in Section 3.5.1. The manifolds computed from three numerical methods show an obvious difference with one from SSMtool.

3.5.3 Duffing oscillator

The third system consists of a single point mass oscillator with a cubic spring, also known as the Duffing oscillator. This system is considered as an example of the system with a conservative nonlinearity. The EoM used for the computation of dNNMs is shown in Eqn.(3.47). The classic force amplitude curve (γ-q_{max} plot) obtained from the E-EBM is shown together with the dNNMs (ω_0-q_{max}, ζ-q_{max} plots) calculated using HBM with the first 5 harmonics. A simple harmonic excitation force is applied to the same system with an excitation forcing level γ. The EoM of the forced system is given in Eqn.(3.48).

$$\ddot{\underline{q}} + \underline{q} + 0.2\underline{q}^3 = 0 \tag{3.47}$$

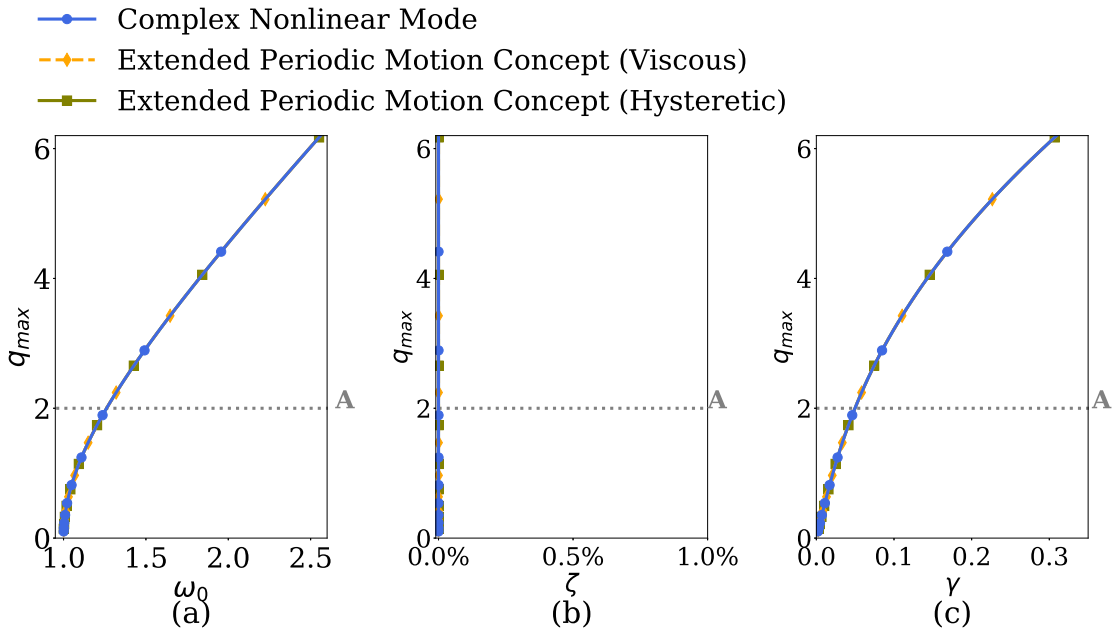
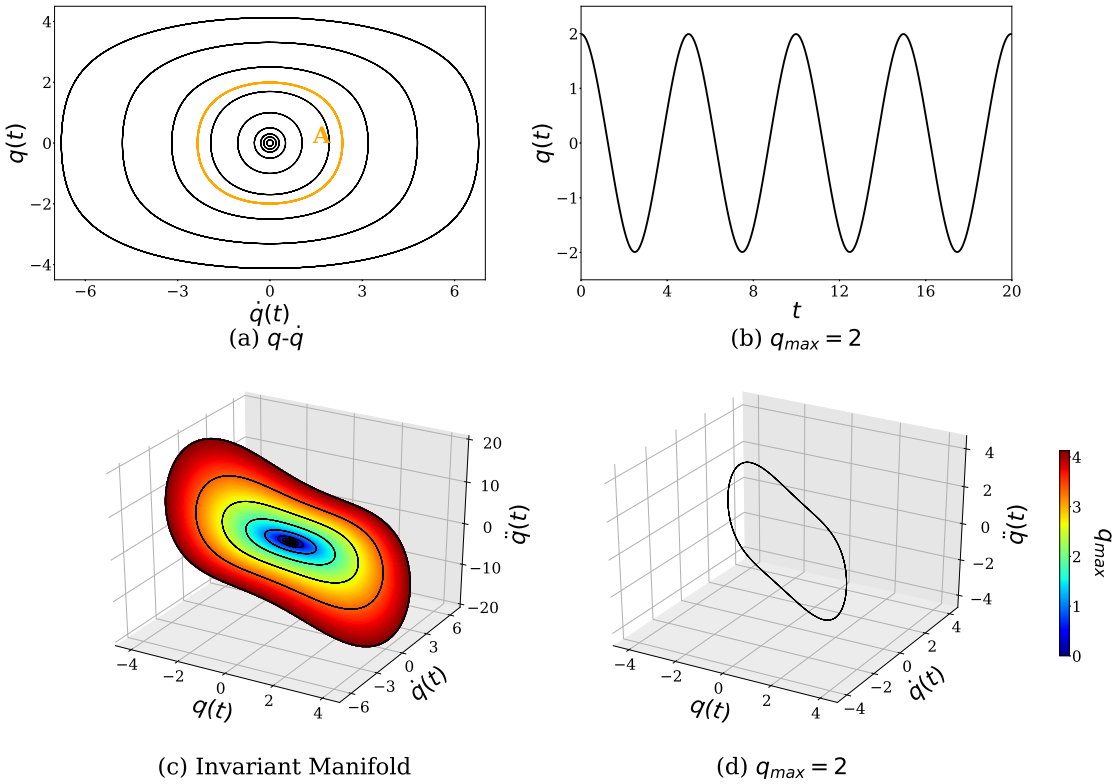


Fig. 3.15 Numerical results from the damped nonlinear normal mode within a range of modal amplitude for the Duffing oscillator: (a) ω_0-q_{max} plot; (b) ζ-q_{max} plot; (c) γ-q_{max} plot using the extended energy balance method

Figure 3.15 shows the evolution of resonant the frequency ω_0, the modal damping ratio ζ and the excitation forcing level γ with respect to the vibration amplitude using the three methods described above. From the figures, the results from all three methods show an excellent agreement. It is because this Duffing oscillator is a conservative system. Therefore, the different damping assumptions used in different numerical methods cannot affect the accuracy of the results. As shown in Fig.3.15(b), the modal damping ratio ζ is always zero. For resonant frequency, a typical hardening trend can be seen. Since these three methods provide the same results, only the results from EPMC-V are shown in the following figures. The invariant manifold of this mode is represented by a hypersurface ($\ddot{q}$-q-$\dot{q}$), as shown in Fig.3.16(c). Figure 3.16(a) shows a two-dimensional envelope (q-$\dot{q}$ plot) of the selected mode. The solutions of the dNNM with vibration amplitude q_{max} of 2 (Case A in Fig.3.15) are shown in Fig.3.16(b, d).

$$\underline{\ddot{q}} + 0.01\,\underline{\dot{q}} + \underline{q} + 0.2\,\underline{q}^3 = \gamma e^{j(\Omega_e t + \varphi)} \tag{3.48}$$

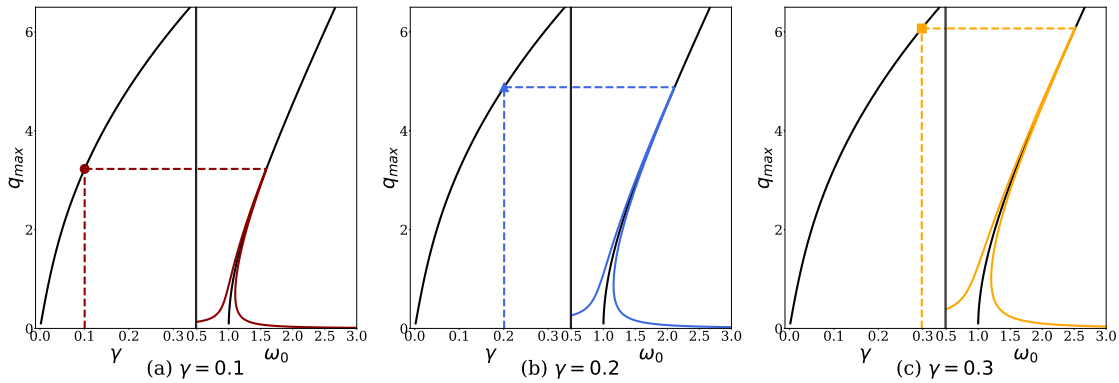
To verify the modal properties obtained from the dNNM coupled with E-EBM, several nonlinear force responses of this Duffing oscillator are computed. The EoM used in the computation of the forced response is given as Eqn.(3.48). Nonlinear forced responses



(a) q-$\dot{q}$ (b) $q_{max} = 2$

(c) Invariant Manifold (d) $q_{max} = 2$

Fig. 3.16 Invariant manifolds for the Duffing oscillator: (a) $q(t)$-$\dot{q}(t)$ plot; (b) $q(t)$-t plot when $q_{max} = 2$ (Case A in Fig.3.15); (c) Invariant Manifold; (d) $\ddot{q}(t)$-$q(t)$-$\dot{q}(t)$ plot when $q_{max} = 2$(Case A in Fig.3.15)



(a) $\gamma = 0.1$ (b) $\gamma = 0.2$ (c) $\gamma = 0.3$

Fig. 3.17 Using nonlinear forced response to validate ω_0-q_{max} plot and γ-q_{max} plot for the Duffing oscillator: (a) $\gamma = 0.1$; (b) $\gamma = 0.2$; (c) $\gamma = 0.3$; Left: γ-q_{max} plot (Black curve); Right: ω_0-q_{max} (Black curve) and three nonlinear forced response in different colours

calculated using three different values of γ (0.1, 0.2 and 0.3) are shown in Fig.3.10. For a given value of γ, the resonant frequency ω_0 and vibrational amplitude q_{max} can be predicted using the dNNM. From figures, the predicted resonant amplitude and resonant frequency show a great agreement with the one calculated from nonlinear forced response. This shows that the methods can also provide accurate prediction for systems with conservative nonlinearities.

3.5.4 Summary

Two different numerical approaches for the computation of the dNNM are described in this chapter, which are CNM, EPMC approaches (two different damping assumptions: viscous damping and hysteretic damping). Generally, all approaches can be used for the computation of dNNMs of systems with non-conservative nonlinearities. The E-EBM can be used for both approaches and can provide accurate predictions for resonances. The benefits and limitations of each method are critically discussed.

For systems with non-conservative nonlinearities, the solutions in CNM are assumed to be sinusoidal with an exponential decay. In AFT procedure, the solutions are assumed to be periodic solutions. The aperiodicity of the solution and the periodic assumption make the solutions of dNNMs from CNM less accurate. For systems with large damping, the accuracy of the CNM can be even worse. In conservative nonlinear systems, the solutions are periodic and the inaccuracy of the CNM approach will not exist anymore.

An artificial hysteretic damping is introduced to balance the energy exchanged in EPMC-H. Unlike the viscous damping, the hysteretic damping is independent to the resonant frequency. Therefore, for displacement dependent nonlinearities, the evolution of modal damping ratio obtained from the EPMC-H follows the same trend of energy dissipation curve with respect to the vibration displacement.

In second test case, the accuracy of these numerical methods drops significantly. In EPMC approach, an assumed linear damping term is enforced to balance the nonlinear damping effect. Using a linear damping ratio (either viscous or hysteretic) is difficult to represent and quantify the damping effect of a higher order nonlinear damping. It is not rigorous to conclude that EPMC cannot work under the presence of higher order nonlinear damping. But the use of these numerical methods in such systems should be carefully considered.

A classic Duffing oscillator is studied as an example of a system with a conservative nonlinearity. In a conservative nonlinear autonomous system, the solutions are undamped and in the form of a periodic orbit. The damping assumptions in three numerical methods do

not show any impact on the results. In summary, the use of these numerical methods is also possible in a system with a conservative nonlinearity.

3.6 Concluding Remarks

In this chapter, two different existing numerical methods and one novel method used to compute dNNMs for systems with nonlinear damping have been described and compared. These three methods are tested by three simplistic test cases: a one DoF system with frictional contact, a one DoF system with quadratic nonlinear damping and a Duffing oscillator.

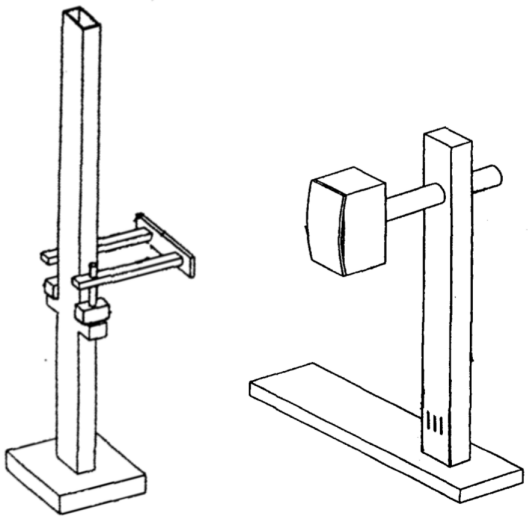
By comparing the dNNMs from three different methods, several useful suggestions can be concluded. Firstly, for a system with a large modal damping, CNM cannot provide accurate prediction because of the periodic assumption used in the AFT process. Secondly, for EPMC, the assumption of the linear artificial damping (viscous or hysteretic damping) to represent the nonlinear damping is also very important. If there is no significant variation of the resonant frequency, both damping assumptions can give similar results. For systems with displacement dependent nonlinear force, the hysteretic damping assumption can provide a better representation of the energy dissipation. For systems with a higher order nonlinear damping (i.e. $q^2\dot{q}$), the dNNMs computed from these numerical methods show a significant difference with the reference solutions. Therefore, the use of these numerical methods is not suggested for systems with a high order nonlinear damping. Finally, all three methods are also applicable for systems with conservative nonlinearities.

The numerical formulations of E-EBM coupled with the three methods have been derived in detail. This method can be simply adopted with these numerical methods to construct the force amplitude plot as a by-product of the computation of the damped nonlinear normal mode. The EPMC approach coupled with E-EBM is considered as a numerical tool and used in the rest of thesis to study the nonlinear dynamic response of structures with friction dampers. In the next chapter, these numerical methods will be validated by comparing with existing experimental results.

Chapter 4

Numerical Validation and Parametric Study of Frictional Dampers

In this chapter, the numerical methods described in the previous chapter are validated using the reference results from Berthillier *et al.* in 1998 [13]. Then, a parametric study of UnderPlatform Damper (UPD) is achieved using the validated numerical methods. A simplified beam model is used to represent the blade for the preliminary design stage. This parametric study will provide some useful guidance to design a novel experimental test rig in the near future. The frictional damper is numerically analysed based on two parameters, the contact angle and vertical position of the platform. Using nonlinear modal analysis, the modal damping ratio, the resonant amplitude and the resonant frequency are directly and efficiently computed for a range of design parameters. Monte Carlo Simulations (MCS) together with Latin Hypercube Sampling (LHS) is then used to assess the robustness of the frictional damper, whose contact parameters involve uncertainties due to manufacturing tolerances and wear effects. The influence of those two parameters is obtained and the best performance of the frictional damper can be achieved when the contact angle is around 25°-30°. The vertical position of the platform is highly mode-dependent and other design considerations need to be accounted for. The results have been proved that the uncertainties of the contact surfaces do not have significant effects on the performance of the frictional damper. The second part of this chapter has already been published in Sun *et al* . [165].



(a) (b)

Fig. 4.1 Experimental setups [13]: (a) Overview of the beam and dampers; (b) Friction dampers

4.1 Validation of Numerical Methods

4.1.1 Experimental setup for validation

A beam with a rigid platform is used for the validation of the numerical methods. This beam model has the same dimension of the experimental test rig in [13]. As shown in Fig.4.1 and Fig.4.2, the beam is a 1.33 m long vertical steel tube with a rectangular cross section of a 0.08 m by 0.04 m and 0.002 m thickness. There is a rigid platform located at 0.318 m from the clamped end of the beam. A stiff friction damper is applied to both sides of the platform for the sake of symmetry. A horizontal excitation force is applied by an electrodynamic shaker at 1.28 m from the root of beam. An accelerometer is horizontally placed on the beam at the shaker position.

4.1.2 Mechanical model for validation

The beam is modelled by a two-dimensional Euler-Bernoulli beam model with 665 elements. According work of Berthillier *et al.* [13], the lumped parameters are added to the beam model to represent the platform and shaker. A mass of 2 kg and inertia of 8.5×10^{-4} $kg\,m^2$ is used to model the platform, whereas a moving mass of 0.133 kg is used to model the shaker. The material properties used for the beam model are: density 7800 kg/m^3; Poisson ratio 0.3; Young's modulus 2.0×10^{11} Pa. The natural frequency of the first bending mode (without

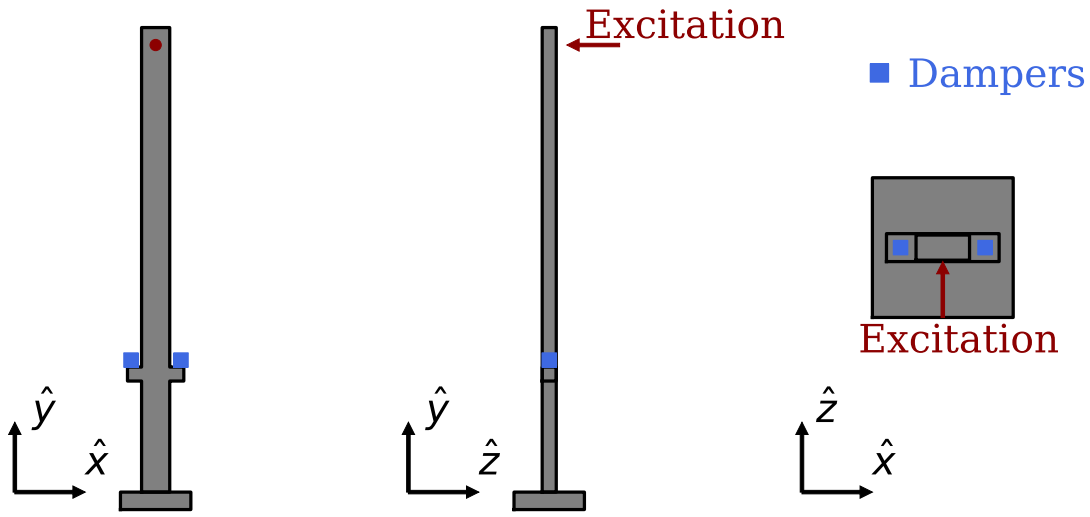


Fig. 4.2 Reference mechanical model: Two dimensional views of beam and dampers

the damper) is 25.4 Hz or 160 rad/s. When the damper is fully stuck, the resonant frequency is 35.2 Hz or 221 rad/s. The natural frequencies are almost identical with the ones obtained experimentally [13]. The response u_1 is taken from the Z-displacement of the node where the shaker is placed. The normal load applied to the friction damper is 372.8 N. To match the experimental forced response at low excitation force ($f_{ex} = 0.938\ N$), the linear damping ratio is assumed to be 2.2%.

A classic Jenkins element is used to model the friction force, which has been described in Section 2.3.3. In the experimental work from Berthillier *et al.* [13], the friction coefficient and the contact stiffness have not been properly measured. The friction coefficient and contact stiffness depend on many factors, i.e. the material, the temperature and the normal load [41]. Therefore, the determination of the contact parameters in the numerical simulation is a complicated task. In this work, the contact parameters are determined by tuning the numerical results with the experimental results. The contact stiffness can be simply tuned by matching the resonant frequency at the fully stuck case. The friction coefficient is obtained by matching the forced response at the fully sliding case. After this process, a tangential contact stiffness $1.4 \times 10^7\ N/m$ and a friction coefficient 0.66 are used in the Jenkins element to simulate the frictional contact.

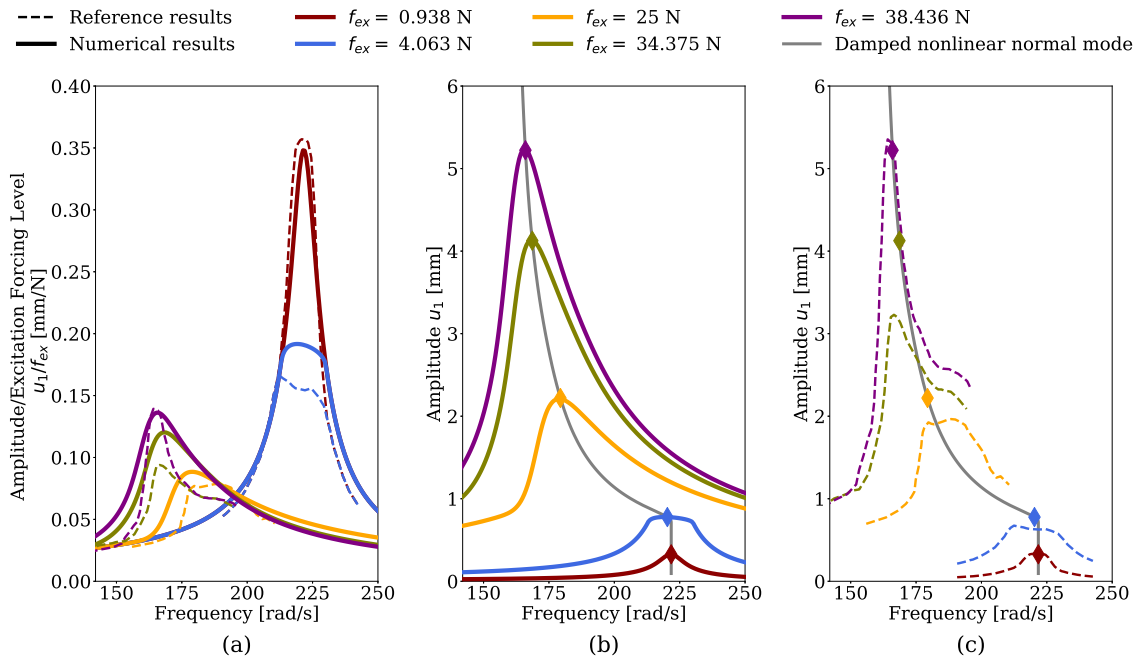


Fig. 4.3 Experimental results and numerical results: (a) Comparison of forced responses from experiments (dashed curves) and numerical simulations (solid); (b) Forced responses (from numerical simulation) and damped nonlinear normal mode (grey curve); (c) Forced responses (from experiments) and damped nonlinear normal mode (grey curve)

4.1.3 Numerical results and experimental results

The experimental results from [13] are considered as the reference results to validate the numerical methods described in Chapter 3. The forced responses with different excitation forcing levels f_{ex} are shown in Fig.4.3(a): the dashed curves represents the experimental results and the solid curves come from the numerical simulations. At low excitation forcing level $f_{ex} = 0.938\ N$ (red curves), the friction damper is almost fully stuck and there is no energy dissipated. An increase in excitation forcing level leads to a lower resonant frequency and lower u_1/f_{ex} value because of the energy dissipation caused by the frictional contact. The results from numerical simulations can capture the main features of nonlinear dynamic behaviour of such a beam model with a friction damper by comparing with the reference results.

To validate the results obtained from the nonlinear modal analysis, in Fig.4.3(b), the frequency amplitude plot (grey curve) obtained from the damped Nonlinear Normal Mode (dNNM) using Extended Periodic Motion Concept (EPMC) are shown in together with several numerical forced responses. From the figure, the frequency amplitude plot can accurately predict the resonance in the numerical forced response. In Fig.4.3(c), the reference

results are shown together with the frequency amplitude plot. At high excitation forcing level (i.e. $f_{ex} = 34.375\ N$ and $f_{ex} = 38.436\ N$), the reference resonant frequency is slightly lower than the one computed from dNNM. However, the friction coefficient used in numerical simulations is tuned by matching numerical results to reference results, instead of measured by experiments. This can be a possible reason for a small difference in resonant frequency for larger excitation forcing levels. Wear effects of the contact interface and the normal load has significant effect on both the friction coefficient and the contact stiffness [41]. These effects are not considered in numerical simulations and result in a small discrepancy between the numerical results and the reference results.

4.1.4 Summary

In summary, we can safely conclude that the numerical simulations can capture the main features of nonlinear dynamic behaviour of such a structure with an acceptable accuracy. The determination of the contact parameters has significant importance on the accuracy of the numerical simulations. The reference experimental results were measured in 1998 [13]. The quality of experimental results might be improved with the use of modern laboratory techniques. Therefore, the objective of rest of this chapter is to demonstrate a preliminary design of a test rig and investigate the two important factors that can influence the performance of the friction damper.

4.2 Parametric Study of Frictional Dampers

4.2.1 Model description

The objective of the rest of this chapter is to investigate the influence of the position of the damper and the contact angle of the UPD in terms of its capacity to dissipate energy. The mechanical model and contact model used in this work is described in the first place.

Mechanical model

The model is based on a simple two-dimensional model represented as Fig.4.4(a). The blade is modelled with a beam of length L_b, on which one platform is fixed at the height H, where $H/L_b \in (0,1]$. The latter is modelled with a beam of length L_p. This modelling choice has been widely used in the numerical and experimental analysis in the literature [120]. Firstly, several simplifications were made about the model shown in Fig.4.4(a) and listed below.

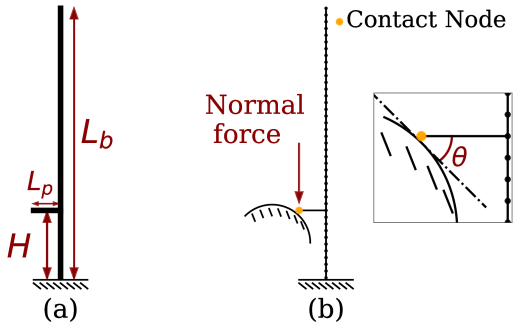


Fig. 4.4 Mechanical model: (a) Two dimensional view X-Y Plane; (b) Two dimension finite element model

1. *Blade and platform:* The properties of the blade and platform are assumed to be constant along the axis of rotation. Therefore, the blade structure is considered as a two-dimensional Finite Element (FE) model. In addition, turbine blades in turbomachinery are rigid enough to avoid the kinematic nonlinearities. Therefore, a linear Euler-Bernoulli beam element with a bar element is used to model the flexural and axial vibration of the blade-platform. To understand the influence of the contact angle, only one side of the damper is modelled (usually UPDs are placed underside of the adjacent blades) .

2. *Cyclic symmetry:* Cyclic symmetry boundary condition is usually required for the actual design of UPDs. However, to investigate the impact of these factors (vertical position of the damper and contact angle), the cyclic symmetric framework is not considered so that each blade is isolated.

3. *Damper:* A cylindrical damper is considered, because it is inexpensive to test for different contact angles in the future experimental work as shown in Fig4.4(b). The damper is assumed as a rigid body and completely fixed to the ground, so the contact force is introduced between the tip of the platform and ground. Therefore, the influence of the contact angle can be obtained independently.

4. *Frictional contact:* Only one contact node is taken into account, which is used to model the line contact for the cylindrical damper. The normal force applied to the contact surface is used to simulate the centrifugal force for real bladed disks.

A simplified model is shown in Fig.4.4(b). The platform can be located between the bottom and the tip of the blade to test the different vertical positions of the UPD. The contact interface between the damper and the blade is modelled with a contact point at the tip of

the platform. The angle θ between the damper and the platform is taken in the range of $[0, \pi/2]$. If $\theta = 0$, then the local contact force is purely friction, whereas if $\theta = \pi/2$ there is only impact between the contact points. A constant vertically downwards normal force N is applied at contact node to represent the reaction force from the centrifugal effect due to the rotation of the bladed disk. This force is always positive and N_0 is set to be 50 N.

For two-dimensional FE beam model, each node has three Degrees of Freedom (DoFs) which are the translational DoFs in X-Y plane and a rotational one. The beams have the following dimensions: a length of 200 *mm*, a width of 40 *mm* and a thickness of 3 *mm*, which is the same beam used in [82]. The mass and stiffness matrices of each element can be obtained as in [131]. A fixed interface component mode synthesis method, namely the Craig Bampton method [28, 66], is used to reduce the computational cost.

Contact model

In the present study, a two-dimensional cylindrical damper with a point contact is modelled. A simplistic contact model is used to calculate the nonlinear dynamic response in a fast time scale [191] and is represented in Fig.4.5. This contact model consists of a Jenkins element and a unilateral spring. In the normal direction, a unilateral-elastic behaviour with a stiffness k_n and a preload N_0 is considered. Whereas, in the tangential direction, the elastic dry Coulomb friction with the coefficient μ and a stiffness k_t is considered. $w(t)$ is the internal variable representing the sliding position during a vibration cycle. The value of the friction coefficient μ is chosen as 0.5. The dynamic friction coefficient is assumed to be identical to the static one. The values of contact stiffness is selected as the same value in [82]. The numerical formulations used to calculate the frictional force are described in Section 2.3.3.

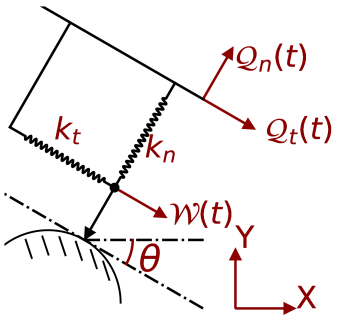


Fig. 4.5 Two dimensional contact model

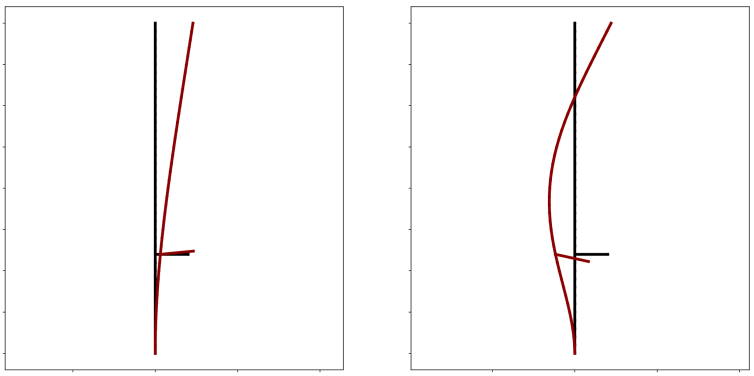


Fig. 4.6 Linear mode shape for beam model: (a) 1^{st} Bending mode $\omega_0 = 391.8\ rad/s$; (b) 2^{nd} Bending mode $\omega_0 = 2333.1\ rad/s$

4.2.2 Numerical results

This section is devoted to the discussion of the results. Firstly, a specific configuration of the system is presented to characterize the performance of the damper and to illustrate the results obtained based on the methodology presented previously. Then the performance of the frictional damper is analysed for all the possible configurations of the system.

Nonlinear modal analysis

In this part, a specific configuration of the system is considered where the position of the platform is characterized by $H/L_b = 0.3$ and the contact angle θ is set to 25°. At the first place, the first two linear modes are determined, as shown in Fig.4.6. They correspond to the first two bending modes at 391.8 rad/s and 2333.1 rad/s. The 1^{st} bending mode is chosen to illustrate the damping performance. The methodology presented in the previous section is applied and for a range of modal amplitude α. The dNNMs $\underline{Q}(t)$ and the modal properties, including the resonant frequency ω_0 and the modal damping ratio ζ, are computed. The modal properties are illustrated with respect to kinetic energy. Since the total kinetic energy varies during the oscillation, the mean kinetic energy per period E_{kin} is calculated based on Parseval's theorem [82]. Results are shown Fig.4.7, where the evolution of the resonant frequency ω_0 and the modal damping ration ζ are given versus the kinetic energy E_{kin}. The resonant frequency ω_0 is constant and equal to 394.2 rad/s when the kinetic energy E_{kin} is inferior to 8, and then it decreases and stabilizes at 392.6 rad/s when the higher level of kinetic energy is achieved. The natural frequency of the 1^{st} bending mode is also shown as the green dotted line in Fig.4.7(a). This variation of the resonant frequency with respect to

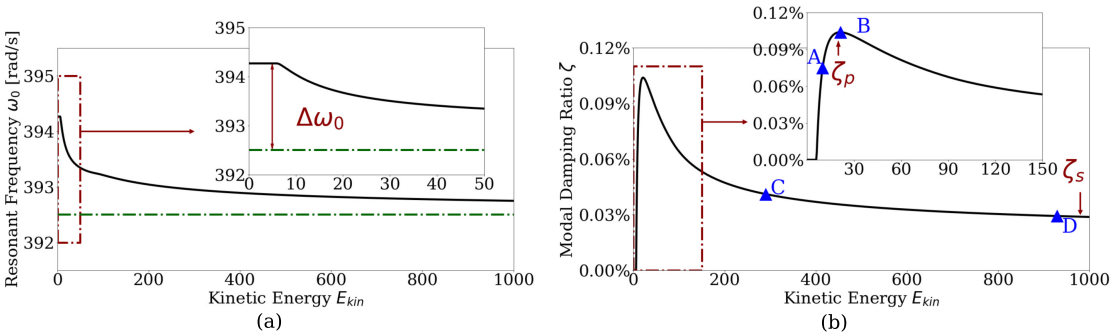


Fig. 4.7 Modal characteristics against kinetic energy ($H/L_b = 0.3$ and $\theta = 25°$): (a) Resonant frequency; (b) Modal damping ratio

the kinetic energy is typical to a structure with frictional contact. Looking at the evolution of modal damping ratio ζ (see Fig.4.7(b)), important variations are also observable. Principally, when kinetic energy E_{kin} is lower than 8, the modal damping ratio is zero. Then it increases to reach a maximum value of ζ_p equal to 0.1% when the kinetic energy E_{kin} reaches around 20. Finally, it decreases and tends to 0.025%.

When the kinetic energy E_{kin} is smaller than 8, the contact mode is sticking and the whole system is purely linear, so the resonant frequency ω_0 of the system remains constant and there is no energy loss due to the friction. The contact points start to slide when kinetic energy E_{kin} is 8. The resonant frequency decreases due to the softening effect caused by the friction (sliding). The total change of the resonant frequency is named as $\Delta\omega_0$, which indicates the shift in resonant frequency compared to the baseline configuration (no damper).

The performance of the damper can be directly assessed through Fig.4.7(b). The maximum modal damping ratio ζ_p can be directly obtained in the figure. However, when modal damping ratio at its maximum value ζ_p, a small change in kinetic energy results in a dramatic decrease of the modal damping ratio. Whereas, the analysis demonstrates the presence of steady region when the kinematic energy is larger (i.e. $E_{kin} > 600$). Indeed, the damping is not very sensitive to a variation of the kinetic energy and reaches a non-zero asymptotic value when kinetic energy E_{kin} is further increased. This asymptotic value of the modal damping ratio is named as ζ_s, which is approximated from the simulation. To further demonstrate the energy dissipated, four normalised hysteresis loops for different levels of kinetic energy are given Fig.4.8. The corresponding levels of amplitude are represented Fig.4.7(b) with the blue points. Thus, Fig.4.8(a) shows the normalised hysteresis loop before the maximum modal damping ratio ζ_p is achieved (example A). The normalised hysteresis loop at ζ_p (example B) is given in Fig.4.8(b). The other two hysteresis loops (example C and D) in Fig.4.8 correspond to higher values of the kinetic energy where the damping reach its asymptotic

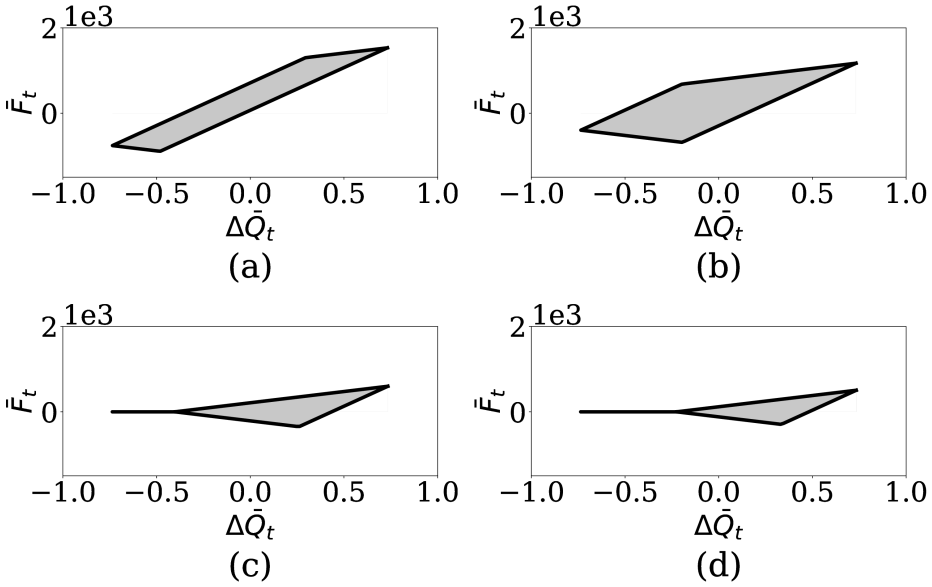


Fig. 4.8 Normalised hysteresis loops for example point in Fig4.7(b): (a) Example A; (b) Example B: maximum modal damping ratio ζ_p; (c) Example C; (d) Example D: asymptotic value of modal damping ratio ζ_s

value. Before the maximum damping is reached, the hysteresis loop is a quadrilateral, so the damper and the platform are always in contact and friction occurs. Whereas after the maximum damping ratio, the loss of contact occurs.

Design space exploration

In the previous part, a specific case was presented to illustrate the nonlinear dynamic behaviour of the blade with cylindrical frictional damper. In addition, parameters of interest for damper design are also defined. In the present part, the performance of the damper is determined for all possible positions H/L_b of the platform and all possible contact angles θ. Hence, the three performance indicators, namely ζ_p, ζ_s and $\Delta\omega_0$ (see Fig.4.7), are determined for the 1^{st} and the 2^{nd} bending modes of the system. The linear mode shape of the baseline configuration (no damper) for first two bending modes are displayed Fig.4.6.

The results are shown Fig.4.9. The figures in the left column correspond to the results associated to the 1^{st} bending mode, and the right column to the 2^{nd} bending mode. For each mode, the maximum modal damping ratio ζ_p, the asymptotic value of modal damping ratio ζ_s and the shift of resonant frequency $\Delta\omega_0$ are given. The first obvious observation is that the three parameters are highly related to both design parameters, namely the vertical position of the platform and the contact angle.

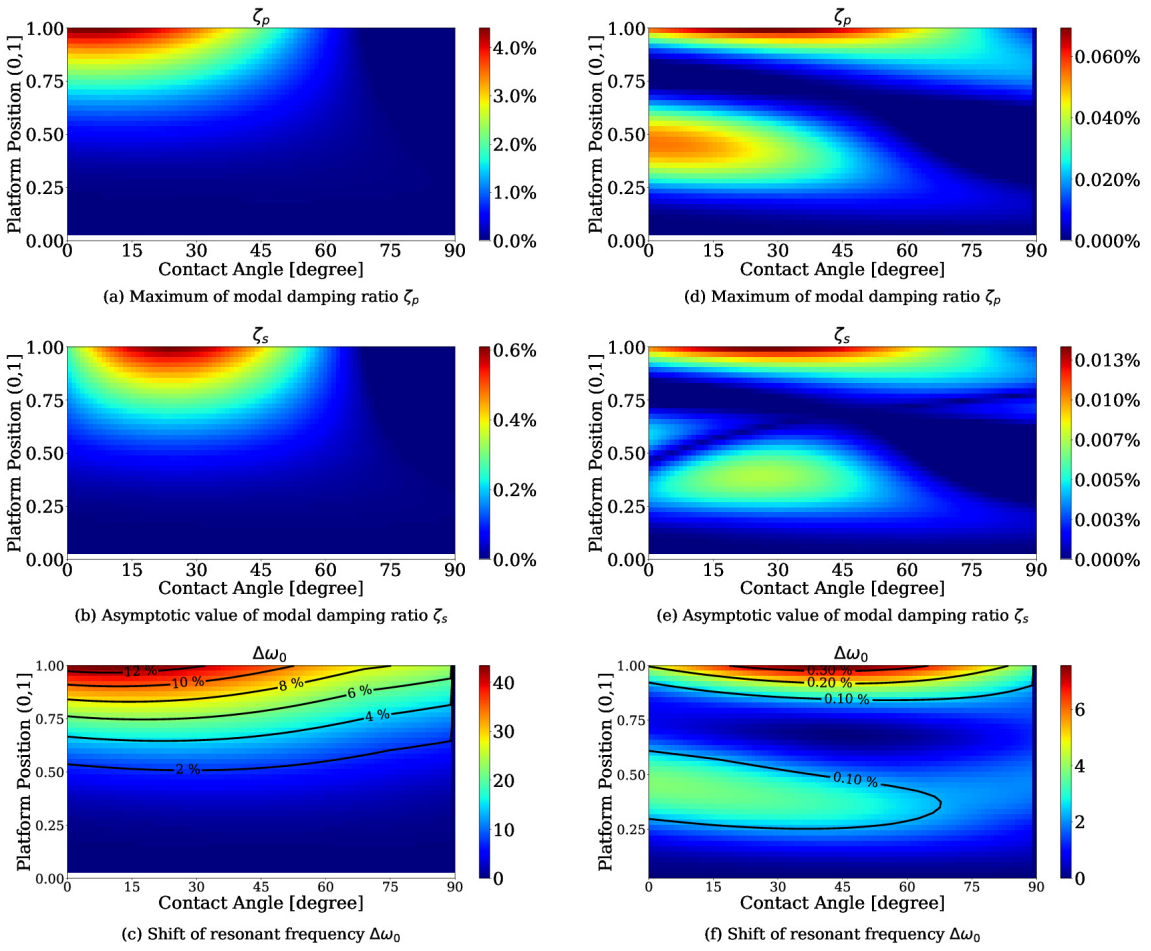


Fig. 4.9 Three design objectives (ζ_p, ζ_s and $\Delta\omega_0$): (a, b , c) 1^{st} Bending mode; (d, e, f) 2^{nd} Bending mode

By looking at the evolution of the modal damping ratios (see Fig.4.9(a,b,d,e)), it appears that the maximum is always achieved when the platform is close to the top of the blade. This can be explained by the fact that if the platform is located at the bottom of the blade, where the relative displacement between contact nodes is small, it will be more difficult to initiate sliding and so less energy is dissipated by the contact leading to lower modal damping ratio. This is confirmed by the evolution of the modal damping ratios for the 2^{nd} bending mode. Larger displacement can be achieved at an intermediary position of the platform, and so an increase of the damping ratios is also observable when the platform is located around the middle of the blade.

The contact angle θ has also a crucial impact on the damping performance. It appears that the damping ratios and the frequency shift have higher values when the angle is smaller. To illustrate the influence of the contact angle, the hysteresis loop for different contact angles

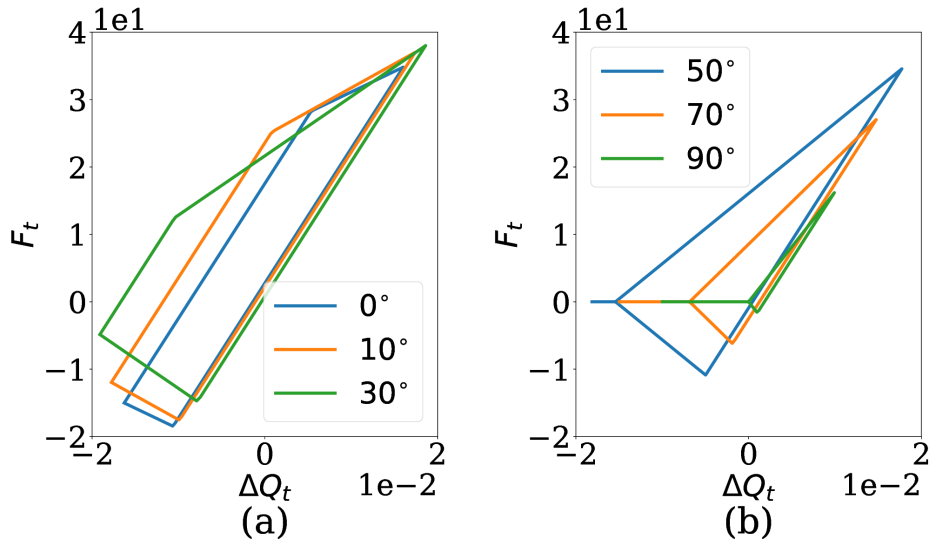


Fig. 4.10 Hysteresis loop for different contact angles θ: (a) $\theta = 0°$, $10°$ and $30°$; (b) $\theta = 50°$, $70°$ and $90°$

and when $H/L_b = 0.3$ is plotted in Fig.4.10. The area enclosed by a closed hysteresis loop represents the total energy dissipated due to friction. For values of θ inferior to $30°$, the peak-to-peak value of F_t decreases but the displacement variations increase, which leads to an increase of the enclosed area (see Fig.4.10(a)). When θ is superior to $50°$ (see Fig.4.10(b)), then loss of contact occurs and the enclosed area decreases. For further increase of θ, the energy dissipated by friction decreases. In the case of $\theta = 90°$, the contact mode is separating-sticking and there is no energy loss due to sliding, so the three objectives tend to zero. From Fig.4.9(b), the maximum case of the ζ_s for the 1^{st} bending mode is achieved while the contact angle θ is around $25°$-$30°$. From Fig.4.9(d,e), the best performance of the damper is also obtained when the contact angle is within $25°$-$30°$ for the 2^{nd} bending mode.

The shift of the resonant frequency for both modes are shown in Fig.4.9(c) and Fig.4.9(f). The evolution of the resonant frequency shift is similar to the evolution of the modal damping ratios, which leads to similar analysis. The contour plots in Fig.4.9(c) and Fig.4.9(f) show the percentage of variation of frequency ($\Delta\omega_0/\omega_0$). The maximum shift of resonant frequency for the 1^{st} and the 2^{nd} bending modes are 12% and 0.3% respectively. It is obvious that the frequency shift for the 2^{nd} bending mode is smaller than for the 1^{st} mode in term of both actual shift of resonant frequency and percentage. The shift of resonant frequency is caused by softening effects due to the sliding contact condition. For different modes and different H/L_b, the natural frequency sensitivities with regards to contact stiffness ($\partial\omega_0/\partial k$, $k = k_n = k_t$) are different. Therefore, a sensitivity analysis is used to investigate the effect of

the contact stiffness on the natural frequency. Natural frequency sensitivities are calculated. The sensitivity for the first three natural frequencies for different platform positions are shown in Fig.4.11. It is easy to see that the natural frequency of the 1^{st} bending mode is more sensitive to the contact stiffness. In addition, the sensitivities are also increased with the value of H/L_b. The shift of resonant frequency is an important factor for the design of the damper. Indeed, the damper is designed to get a certain resonance frequency shift, but a significant change in frequency can cause interaction with other modes.

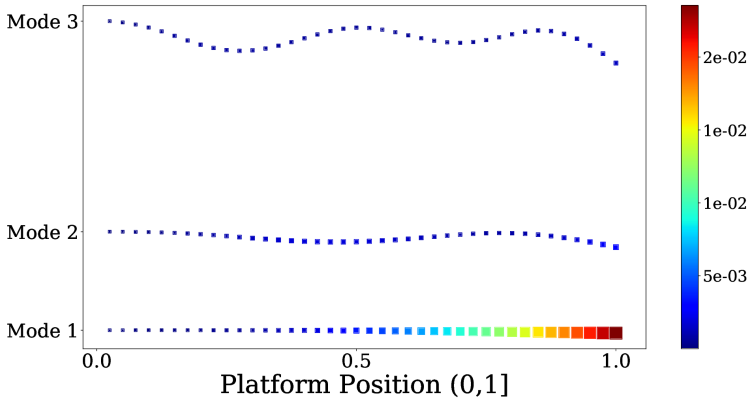


Fig. 4.11 Natural frequency sensitivity

Damping performance is very sensitive to the mode shape and the displacement at the contact node. The best configuration for the damper depends on the considered mode. By considering the 1^{st} bending mode, the best configuration would be a vertical position of $H/L_b = 1$, whereas for the second mode $H/L_b = 0.3$ is the optimal position. Besides the damping performance, other design considerations also need to be accounted for, e.g. placing the damper at mid-span would have detrimental effect on aerodynamic performance. For this reason, designers give their priority to placing the UPD at the lower position, which is regarded as the most efficient damping technique to reduce the vibrational stress of bladed disks structure [120].

4.2.3 Uncertainty quantification

The previous section was devoted to the analysis of the damping performance for different configurations of the system. This study has been performed in a deterministic case where all the parameters are supposed to be known and constant. However, some parameters within the contact surfaces might be uncertain and have a non-negligible impact on the damper performance. So the objective of this section is to investigate the impact from those uncertainties on the performance of the damper.

Table 4.1 Uncertain Parameters

	Mean	Standard deviation
Friction coefficient μ	0.5	0.05
Contact stiffness k	2 N/mm	0.1 N/mm

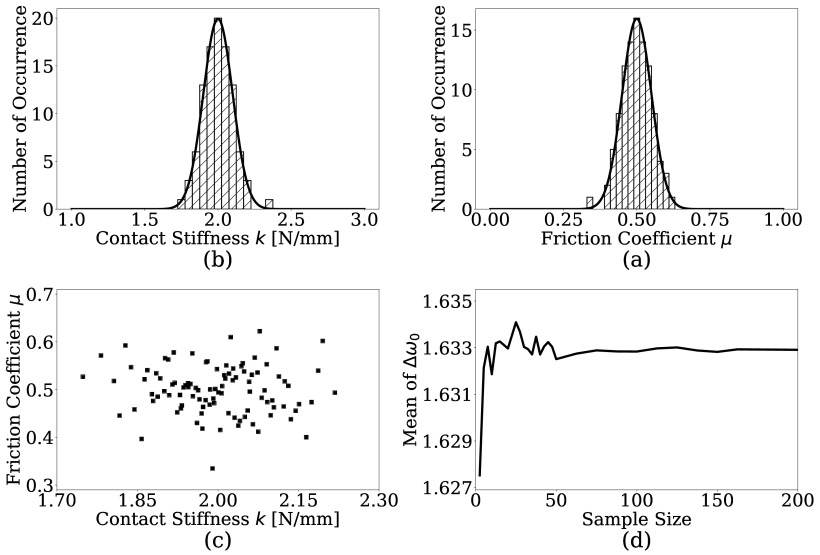


Fig. 4.12 Uncertainty quantification: (a) Number of occurrence for contact stiffness; (b) Number of occurrence for friction coefficient; (c) Samples from LHS; (d) Example of convergence study

Thus, the two parameters that define the contact are considered as uncertain and MCS are performed. This choice is motivated by the fact that the roughness of contact surfaces cannot be assumed as a constant due to manufacturing tolerances and wear effects caused during operation. The two contact parameters considered are the friction coefficient μ and the contact stiffness k ($k = k_n = k_t$). A normal distribution law is assumed for both uncertain parameters [124, 80]. The nominal value and the standard deviation of the uncertain parameters are given in Tab. 4.1.

The methodology adopted here to propagate the uncertainty is the classic MCS method. To ensure a quicker convergence, the samplings are generated based on LHS [105] with an open source library OpenTURNS [11]. A set of 100 samples is selected after a convergence study as shown in Fig.4.12(d). The distributions and the repartition of the input points are given Fig.4.12.

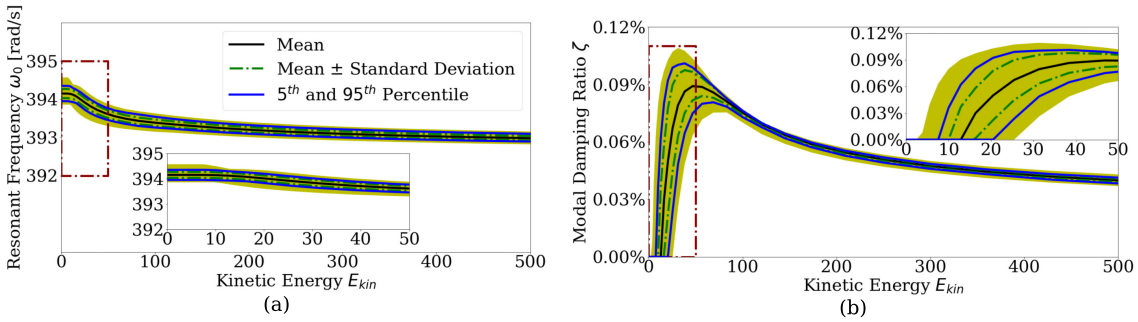
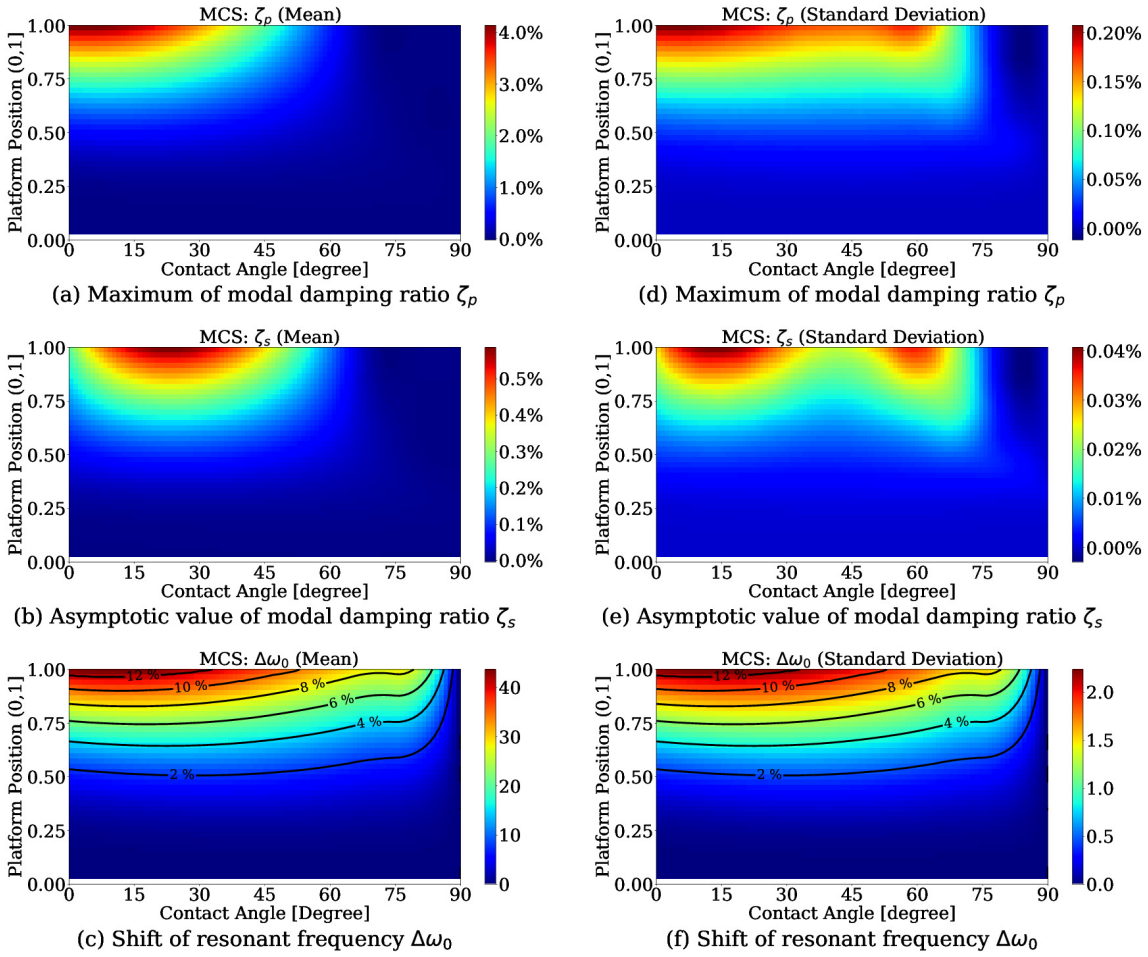


Fig. 4.13 MCS: Stochastic modal characteristics against kinetic energy ($H/L_b = 0.3$, $\theta = 25°$): (a) Resonance frequency; (b) Modal damping ratio

For a sake of consistency and according to previous results, only the 1^{st} bending mode is considered for this study. A first case where $H/L_b = 0.3$ and $\theta = 25°$ is considered as an illustration. For all the couples (μ, k) generated based on a LHS by OpenTURNS, the evolution of the stochastic resonant frequency and the modal damping ratio with the kinetic energy E_{kin} are given Fig.4.13. The mean of each parameter as well as the 5^{th} and 95^{th} percentile are given. For the resonant frequency, a wider band is obtained before the sliding occurs. In this case, the friction force only depends on the contact stiffness. When the kinetic energy E_{kin} is greater than 8, the resonant frequency starts to decrease and the band becomes thinner. The friction force is dominated by the friction coefficient instead of the contact stiffness. So the contact stiffness has a higher influence on the resonant frequency at low levels of kinetic energy, whereas the influence of the friction coefficient is important at higher levels of kinetic energy.

Considering the evolution of the modal damping ratio, the two contact parameters have an impact as soon as sliding occurs and change the threshold at which sliding appears (between 3 and 25). They also have an impact on the maximum of the modal damping ratio (0.11% versus 0.07%) and on the kinetic energy E_{kin} at which it appears (30 versus 80). However, the influence on modal damping ratio is small once loss of contact appears. So performance of the damper is affected by the uncertainties associated to the contact parameters.

To study the impact of these uncertain parameters, the procedure is performed for all the positions of the damper and all the contact angles. The mean and the standard deviation of the modal damping ratios ζ_p, ζ_s and the shift of resonant frequency $\Delta\omega_0$ are determined. Results are given in Fig.4.14. By comparison with the deterministic results (see Fig.4.9), the evolution of the mean of the different parameters does not give a significant difference. Indeed, the configuration which gives the optimal damping and the variations of the three performance indicators are very similar. For area where no sliding occurs in the dynamics



(a) Maximum of modal damping ratio ζ_p
(d) Maximum of modal damping ratio ζ_p
(b) Asymptotic value of modal damping ratio ζ_s
(e) Asymptotic value of modal damping ratio ζ_s
(c) Shift of resonant frequency $\Delta\omega_0$
(f) Shift of resonant frequency $\Delta\omega_0$

Fig. 4.14 MCS: Three design objectives (ζ_p, ζ_s and $\Delta\omega_0$): (a, b, c) Mean; (d, e, f) Standard deviation

of the system (i.e. $\zeta_p = 0$), this is justified by the fact that those uncertain parameters have no significant influence on ζ (see Fig.4.13(b)). So in the area where $\zeta_p = 0$, no variation is expected and so the variance remains close to zero. In the areas, where ζ_p and ζ_s are non-zero, larger variances are observed. As seen in Fig.4.13(b), the value of the maximum modal damping ratio ζ_p is highly influenced by the uncertain parameters, which is confirmed by the high variances. Similarly, the modal damping ratio ζ_s is influenced by the variation of the uncertain parameters, but less variation is observed than for ζ_p (see the wider band for ζ_p than ζ_s on Fig.4.13(b)), which is in concordance with the lower level of variance observed for ζ_s compared to those of ζ_p (0.2% versus 0.04%). As for the shift of resonant frequency, the maximum standard deviation for $\Delta\omega_0$ is around 2 rad/s as shown in Fig.4.14(f). By considering the standard deviation of the three design objectives (ζ_p, ζ_s and $\Delta\omega_0$), it has been proved that the uncertainties involved in the contact surfaces do not have significant effects on the performance of the frictional damper.

4.3 Concluding Remarks

In the first part of this chapter, the numerical methods for nonlinear modal analysis described in the previous chapter has been validated based on the reference results from an experimental work. Then, a preliminary parametric design of the friction damper for aero-engine turbine blades has been effectively explored using the nonlinear modal analysis. A two-dimensional beam model was used to represent the blade and platform as a case study. Two design parameters, namely the contact interface angle and the vertical position of the platform on the blade, have been considered for the parametric study of the friction damper design. With such a definition of design parameters, the model is able to simulate the dynamic behaviour of different configurations for underplatform dampers.

The performance of the frictional damper has been assessed based on three objectives: the maximum modal damping ratio, asymptotic limit of the modal damping ratio and the shift of the resonant frequency. The results showed an optimal configuration of the frictional damper can be achieved when contact angle is around 25°-30°. The vertical position of the platform is highly mode-dependent and other design considerations need to be addressed. In the nonlinear modal analysis, it is important to notice that there is a non-zero asymptotic limit of the modal damping ratio, which indicates that the frictional damper is able to dissipate energy at higher levels of kinetic energy. Frictional dampers are usually designed to mitigate resonance with higher modes and the first several modes are commonly avoided. Since this work is considered as preliminary study for future experimental work. Only the first

two bending modes are considered. An effective design of underplatform dampers can significantly reduce the maximum dynamic stress, which contributes to a higher fatigue safety factor and ensure the guaranteed high cycle fatigue life.

As the contact parameters on the frictional interface involve many uncertainties due to the manufacturing tolerances and the wear effects on their contact surfaces, they would significantly change the dynamics of the friction damper. To evaluate the robustness of the friction damper subjected to these uncertainties, Monte Carlo simulations together with Latin hypercube sampling is used to quantify the effects of these uncertainties on the modal characteristics of the friction damper. By considering the mean value and standard deviation from the uncertainty quantification process, the uncertainties involved contact surfaces do not have significant influence on the performance of the friction damper.

In the next chapter, these numerical methods will be applied to an engineering structure, a blisk with a friction ring damper.

Chapter 5

Application of Nonlinear Modal Analysis to Blisks with Ring Dampers

In the previous chapter, the numerical methods for nonlinear modal analyses have been validated against a set of experimental results. In this chapter, the nonlinear modal analysis is applied to study the nonlinear dynamics of the compressor blisks with friction ring dampers. Two different models are used to represent a blisk with a ring damper, which are an illustrative lumped parameter model and a 3D full-scale Finite Element (FE) model. The lumped parameter model is used to provide a qualitative study of such a system for giving some fundamental understandings of the dynamic response of blisks with friction ring dampers. The three-dimensional full-scale model aims to provide a realistic dynamic analysis for blisks with friction ring dampers. To obtain a high fidelity analysis, several steps of the pre-processing are completed before the nonlinear modal analysis, including a classic linear modal analysis, a rotor dynamic analysis and a nonlinear static analysis. The damping performance of the ring damper is evaluated and critically discussed. The first part of this chapter has already been published in Sun *et al* [166], and the second part of this chapter has already been published in Sun *et al*. [164].

5.1 Lumped parameter model

The lumped model used in the present thesis to model the blisk with a friction ring damper is referred to the existing research by Laxalde *et al* [94], as shown in Fig. 5.1. There are a total eight Degree of Freedoms (DoFs) per sector, which are used to represent the blisk as given in Eqn.(5.1): two DOFs represent the motion of the blade ($\underline{q}_{b1}$ and $\underline{q}_{b2}$), three DoFs for the disk (internal one $\underline{q}_{di}$, right one $\underline{q}_{dr}$ and left one $\underline{q}_{dl}$) and the other three for the ring

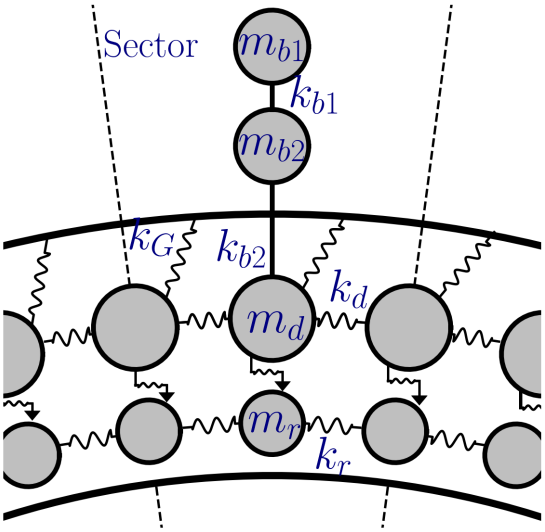


Fig. 5.1 Demonstration of lumped parameter model

damper (internal one $\underline{q}_{ri}$, right one $\underline{q}_{rr}$ and left one $\underline{q}_{rl}$). There are overall 24 sectors within this cyclic symmetric structure, $N_s = 24$. The blisk and ring are assumed to be identical for each sectors and the cyclic symmetry boundary condition described in Section 2.1 is applied. The model parameters are listed in Tab. 5.1. The formulation used to assemble the stiffness and mass matrices for a sector is provided in Eqn.(5.2-5.3). Mead's approach [106, 107] is used to apply the cyclic boundary condition, as mentioned in Section 2.5. The detailed formulations for Mead's approach will be provided in Section 5.2.3 together with the model reduction for the full-scale FE model. After applying Mead's approach, the DoFs associated with the right boundaries (q_{dr} and q_{rr}) are eliminated.

Table 5.1 Lumped Model Parameter

Symbols	Values	Units
m_{b1}	0.2	kg
m_{b2}	0.3	kg
m_d	0.4	kg
m_r	0.01	kg
k_{b1}	2×10^6	N/m
k_{b2}	10^6	N/m
k_d	5×10^7	N/m
k_G	6×10^5	N/m
k_r	2×10^7	N/m

$$\underline{Q} = [\underline{q}_{b1}, \underline{q}_{b2}, \underline{q}_{di}, \underline{q}_{dr}, \underline{q}_{dl}, \underline{q}_{ri}, \underline{q}_{rr}, \underline{q}_{rl}]^{\mathrm{T}} \tag{5.1}$$

$$\underline{\underline{\mathbf{K}}} = \begin{bmatrix} k_{b1} & -k_{b1} & 0 & 0 & 0 & 0 & 0 & 0 \\ -k_{b1} & k_{b1}+k_{b2} & -k_{b2} & 0 & 0 & 0 & 0 & 0 \\ 0 & -k_{b2} & k_{b2}+k_G+2k_d & -k_d & -k_d & 0 & 0 & 0 \\ 0 & 0 & -k_d & k_d+k_G & 0 & 0 & 0 & 0 \\ 0 & 0 & -k_d & 0 & k_d+k_G & 0 & 0 & 0 \\ 0 & 0 & 0 & 0 & 0 & 2k_r & -k_r & -k_r \\ 0 & 0 & 0 & 0 & 0 & -k_r & k_r & 0 \\ 0 & 0 & 0 & 0 & 0 & -k_r & 0 & k_r \end{bmatrix} \tag{5.2}$$

$$\underline{\underline{\mathbf{M}}} = \begin{bmatrix} m_{b1} & 0 & 0 & 0 & 0 & 0 & 0 & 0 \\ 0 & m_{b2} & 0 & 0 & 0 & 0 & 0 & 0 \\ 0 & 0 & m_d & 0 & 0 & 0 & 0 & 0 \\ 0 & 0 & 0 & m_d & 0 & 0 & 0 & 0 \\ 0 & 0 & 0 & 0 & m_d & 0 & 0 & 0 \\ 0 & 0 & 0 & 0 & 0 & m_r & 0 & 0 \\ 0 & 0 & 0 & 0 & 0 & 0 & m_r & 0 \\ 0 & 0 & 0 & 0 & 0 & 0 & 0 & m_r \end{bmatrix} \tag{5.3}$$

The frictional contact between the blisk and ring damper is modelled by a one dimensional contact model as given in Section 2.3.3. The normal load applied between contact nodes is linearly proportional to the mass of ring damper m_r. The contact stiffness is assumed to be $5 \times 10^7\ N/m$ and the friction coefficient is assumed to be 0.5.

5.1.1 Natural frequency against nodal diameter

The natural frequencies of the lumped parameter model (without the ring damper) are plotted against the Nodal Diameter (ND) in Fig.5.2. There are four families of modes, two of them marked by circles and diamonds represent blade dominated modes. The natural frequencies of these two families are almost constant for all possible NDs. The families marked by squares and triangles are disk dominated modes. For these modes, the modal stiffness increases dramatically with a growing ND. Therefore, a higher natural frequency can be seen for large NDs. The disk dominated modes have a strong blade-disk coupling effect leading to a large slope of the curves as shown in Fig.5.2. The blade-disk coupling effect is important, because it gives an access for the communication of the vibration energy between blades and disks. There is a crossing between 2^{nd} and 3^{rd} family of mode near ND 3. In order to

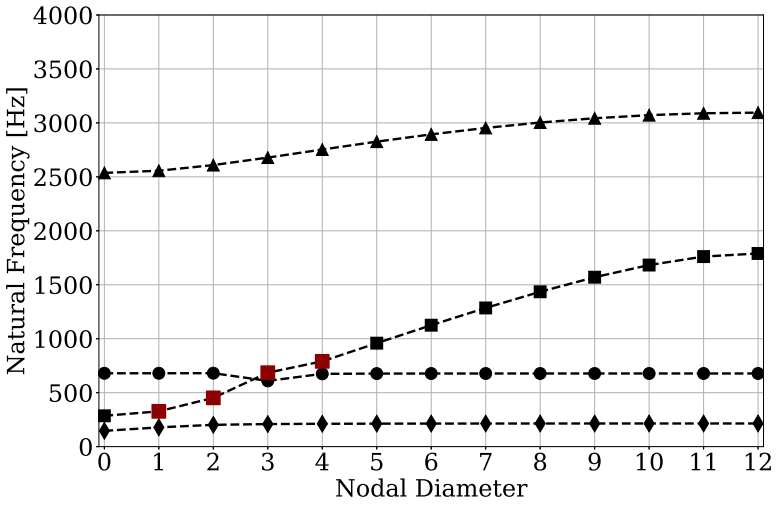


Fig. 5.2 Natural frequency against nodal diameter for lumped parameter model

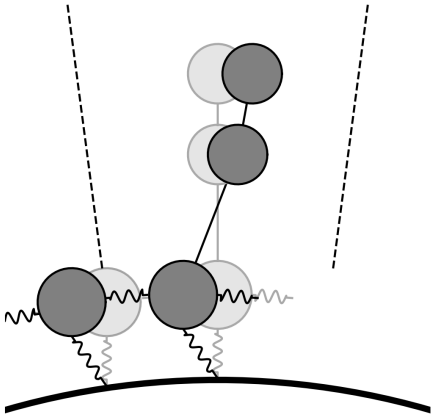


Fig. 5.3 Mode shape of 2^{nd} modal family (marked by squares in Fig.5.2)

evaluate the damping performance, the mode shape of 2^{nd} modal family is shown in Fig.5.3. By looking at the mode shape, the DoFs associated with the disk show a significant modal displacement. Ring dampers are designed to reduce the vibration amplitude for the mode with a large disk displacement. Therefore, the modes from 2^{nd} modal family are selected for the following study.

5.1.2 Effect of nodal diameter on damping performance

The influence of the ND on the damping performance of friction ring dampers has been demonstrated at the first place. To evaluate damping performance, the damped Nonlinear Normal Modes (dNNMs) for the 2^{nd} modal family are computed using the EPMC approach. The evolution of the modal damping ratio ζ is computed for a range of vibrational amplitude,

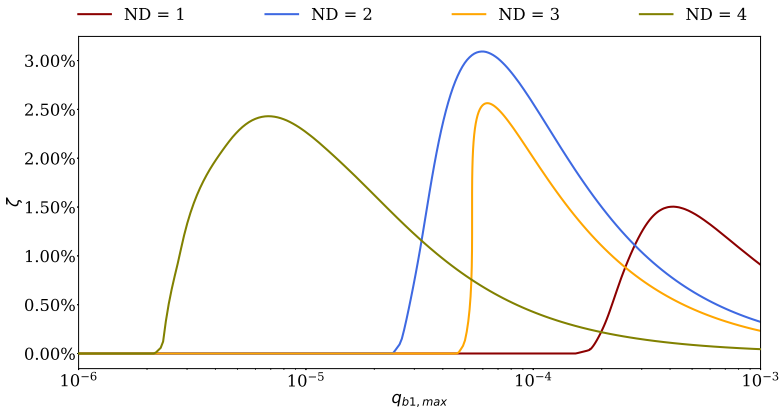


Fig. 5.4 Modal damping ratio ζ against the vibration amplitude $q_{b1,max}$ for 2^{nd} mode family with ND 1, 2, 3, 4

which is taken from the tip of the blade $q_{b1,max}$. Different NDs are tested for the selected modal family (1ND, 2ND, 3ND and 4ND). The results are given in Fig.5.4. The evolution of the modal damping ratio ζ against the vibration amplitude $q_{b1,max}$ follows a similar trend among these different NDs. When the structure vibrates at low amplitude, the friction ring is stuck to the blisk and the energy dissipation caused by friction is zero. An increase in the vibrational amplitude leads to a sliding contact condition and the total energy of system is reduced due to frictional contact. In this situation, a positive modal damping ratio can be obtained.

From Fig.5.4, the sliding contact condition occurs at the lowest vibration amplitude for the mode with ND 4, whereas the mode with ND 2 shows the greatest modal damping ratio (around 3%). Generally, a larger ND leads to a greater blade-disk coupling and a greater modal displacement on the disk. Therefore, the ring can slide at a lower vibrational amplitude for large NDs. However, as shown in Fig.5.2, the mode with ND 3 of the 2^{nd} modal family is very close to the 3^{rd} modal family which belongs to blade-dominated modes. Therefore, a lower blade-disk coupling can be seen for the mode with ND 3.

5.1.3 Effect of damper mass on damping performance

Then, the influences of the damper mass m_r on the damping performance are investigated. The mode from the 2^{nd} mode family with ND 2 is studied. The evolution of ζ against $q_{b1,max}$ is given in Fig.5.5. For an increasing vibrational amplitude, an earlier sliding contact condition can be seen for the ring with a smaller mass. As shown in Fig.5.5, the ring with $m_r = 0.005$ slides at the lowest amplitude at $1e-5$, whereas the ring with $m_r = 0.02$ slides at $5e-5$. The maximum modal damping ratio decreases with an increasing ring damper mass.

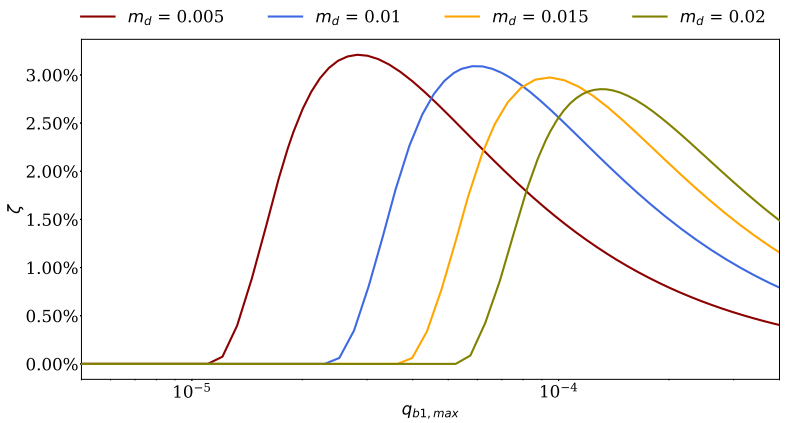


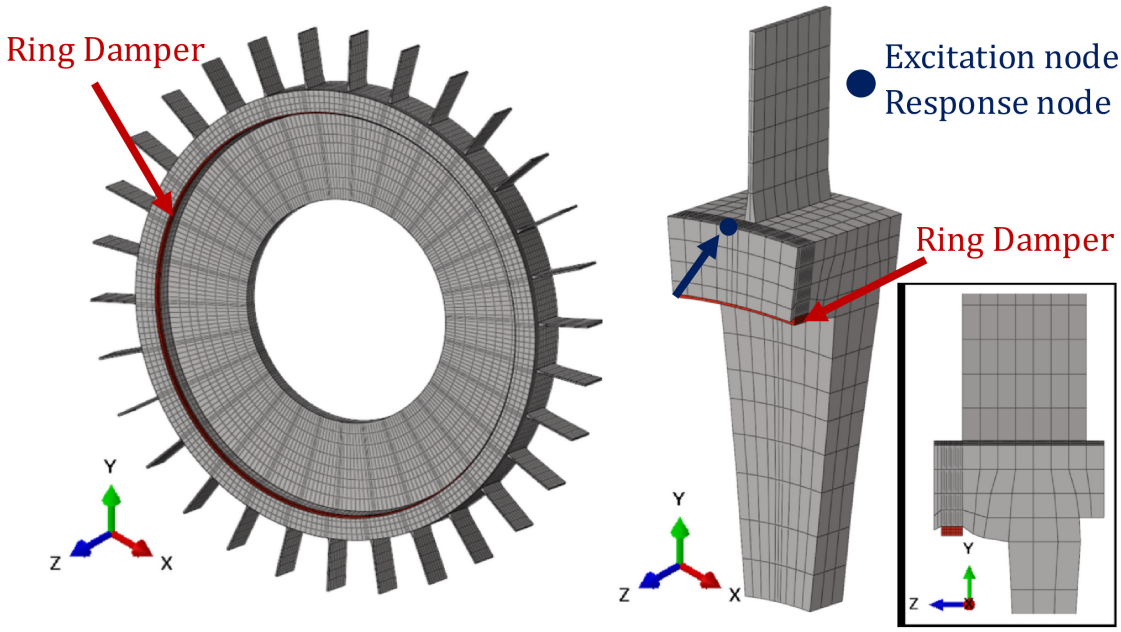
Fig. 5.5 Modal damping ratio ζ against vibration amplitude $q_{b1,max}$ for 2^{nd} mode family with ND 2 with different values of damper mass (0.005 kg, 0.01 kg, 0.015 kg, 0.02 kg)

For the same geometry of the ring damper and same rotational speed, the ring damper with a lower mass leads to a lower centrifugal force resulting in a small contact normal load. In addition, the mass of ring damper directly affects the inertia of the damper. For a lower contact normal load, the lighter damper is much easier to slide. And, for a given vibrational amplitude $q_{b1,max}$, different values of the ring damper mass contribute to a significantly different modal damping ratio.

5.1.4 Summary

In summary, a lumped parameter model with Jenkins elements is used to simulate the nonlinear dynamic behaviour of the blisk with friction ring damper. This system is analysed through its dNNMs and modal damping ratio. The numerical results provided a qualitative analysis for the blisk with a friction ring damper and its damping performance. The effects of the nodal diameter and the mass of ring damper are studied using this preliminary model. The efficiency of the friction ring damper has been approved by the initial results from this illustrative lumped parameter model. Conclusively, if the friction ring is well designed for a blisk, it can provide considerable damping to mitigate the vibration amplitude of the disk-dominated modes.

The use of the lumped parameter model can be only considered in the preliminary design phase and provide a qualitative analysis. In the present lumped model, only eight DoFs are used to represent one sector of the blisk with ring damper. The ring damper is assumed to be always in contact with the disk. However, this assumption will not be valid in a real blisk structure. Therefore, to provide a convincing analysis, a full-scale FE model is used



(a) Full Annulus (b) A Sector

Fig. 5.6 A three-dimensional blisk with ring damper: (a) A full annulus; (b) A sector

to represent the blisk with friction ring damper. The detailed work will be provided and discussed in the next section.

5.2 Full-scale Blisk with Friction Ring Damper

5.2.1 Finite element model

A full-scale FE model is used to represent the blisk with ring damper and considered as an academic testcase. The full annulus and a sector of the FE model are shown in Fig.5.6. There are 30 sectors in total. A sector of the blisk and ring damper (see Fig.5.6(b)) with cyclic symmetric boundary conditions is used to model the full annulus. Linear brick elements are used and the model is made by homogenous titanium material. There is one contact interface between the underneath of the blisk and upper surface of the ring damper. This FE model contains 1544 linear brick elements, where 1184 for the blisk sector and 360 for the ring sector. There are 143 contact nodes within the contact interface. To perform a dynamic analysis, the following assumptions are made:

1. *Cyclic Symmetry:* The blisk is assumed as a perfectly tuned structure which exhibits a cyclic symmetry. A split ring damper is usually considered for the actual design and

leads to a mistuning effect. The ring damper has been proved to be efficient for the mistuned case [94], therefore, this mistuning effect is ignored and the ring damper is assumed to be continuous and cyclic symmetric. The cross section of the ring is uniform along the circumferential axis.

2. *Kinematic Nonlinearity:* The blisk is assumed to be rigid enough to avoid any kinematic nonlinearities when it vibrates with a large amplitude. Hence, kinematic nonlinearities are ignored in the present study.

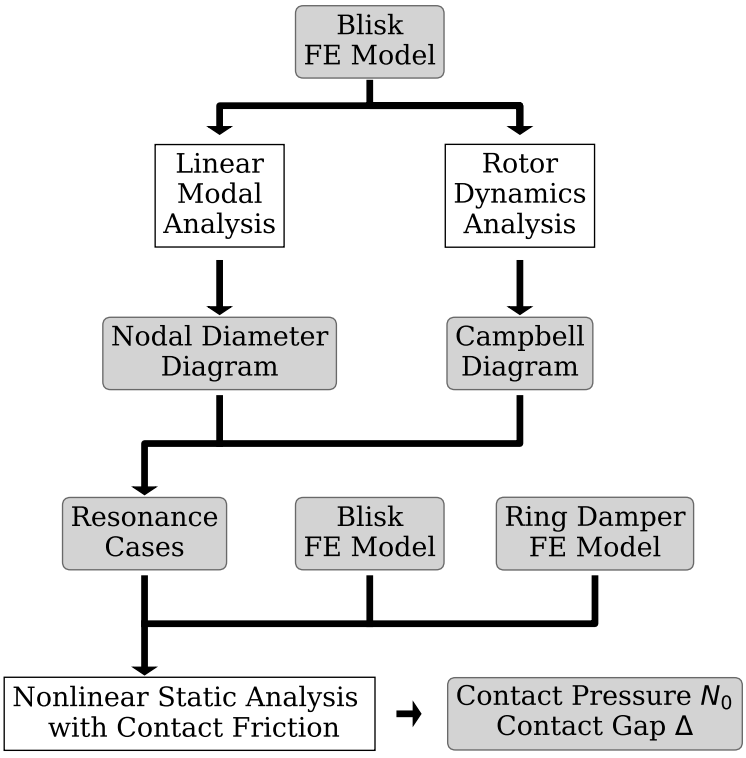


Fig. 5.7 Flow chart for pre-processing

5.2.2 Methodology for pre-processing

In this section, the methodology used for the pre-processing is explained in detail. The flow chart of the pre-processing is shown in Fig.5.7. The objective of the pre-processing is to identify the resonance cases for the nonlinear vibration analysis. A commercial FE solver ABAQUS is used for the pre-processing. In the first place, a linear modal analysis is used for the FE blisk model (see Fig.5.6) to obtain the ND diagram. Furthermore, a classic Campbell diagram is obtained through a rotor dynamics analysis to take the centrifugal stiffening

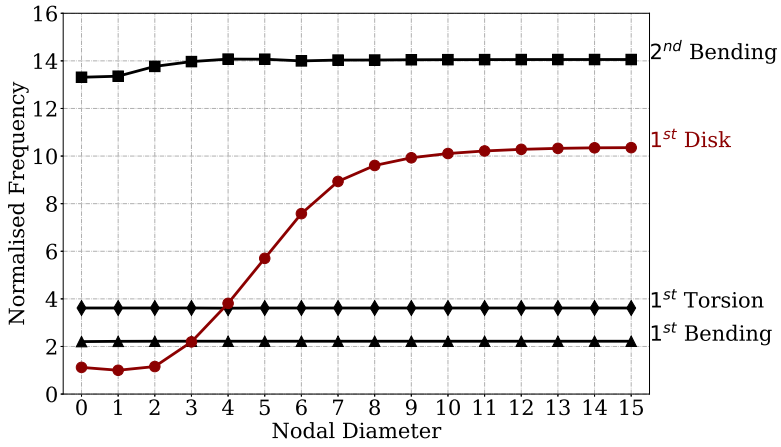


Fig. 5.8 Normalised natural frequency against nodal diameter: the 1^{st} In-plane bending, the 1^{st} torsion, the 2^{nd} In-plane bending and the 1^{st} Disk mode

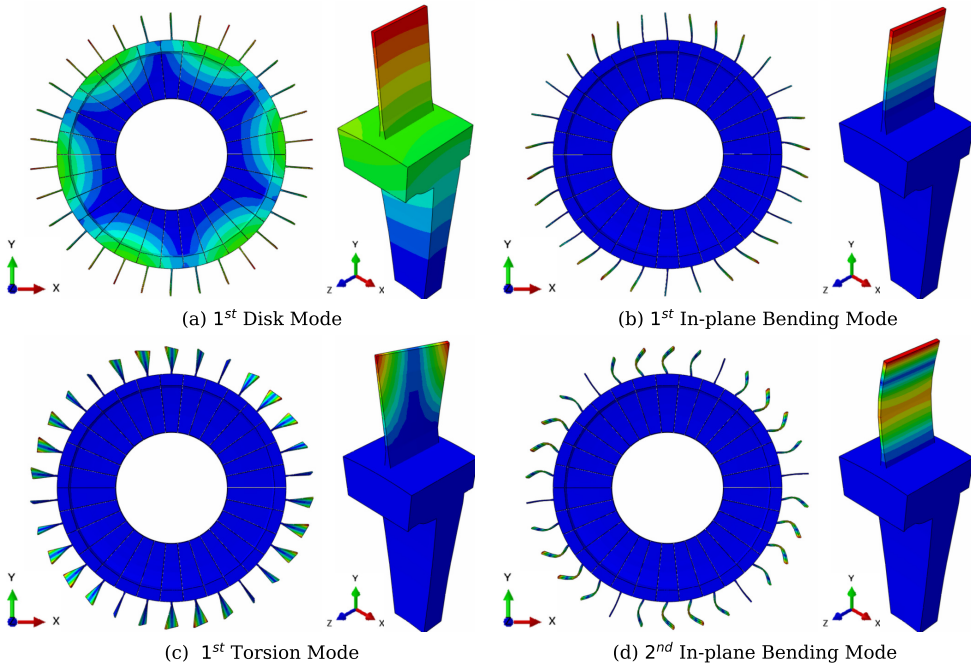
effect into consideration. Then, several resonance cases are identified through the Campbell diagram. After that, the blisk with friction ring damper is analysed with contact elements under the resonance case, and the contact pressure/gap distributions within contact interface are obtained in a nonlinear static analysis.

Nodal diameter diagram

The ND diagram is shown in Fig.5.8, which indicates the first four families of modes for this FE blisk model. The natural frequencies of the 1^{st} disk mode (1D), the 1^{st} in-plane bending mode (1B), the 1^{st} torsion mode (1T) and the 2^{nd} in-plane bending mode (2B) are provided in Fig.5.8 and the mode shapes are shown in Fig.5.9. From the Fig.5.8, the modal families dominated by blade motion do not significantly change with ND, e.g. 1B, 2B and 1T. Whereas, for those disk dominated modes (1D), the natural frequencies show a great difference among different NDs, especially at low NDs. However, for higher NDs, the natural frequencies can be considered as a constant for disk dominated modes (within same modal family). The friction ring damper aims to reduce the vibration amplitude for those disk dominated modes [94]. Therefore, the mode 1D with ND 3 is selected and used for following study. The normalised natural frequency of this selected mode is 2.192.

Campbell diagram

The main source of the excitation of the blisks comes from the aerodynamic loading leading to a synchronous vibration, which relates to the Engine Order (EO). This is known as the EO excitation. This aerodynamic unsteadiness of EO excitation can be linked with the rotor stator



(a) 1^{st} Disk Mode (b) 1^{st} In-plane Bending Mode

(c) 1^{st} Torsion Mode (d) 2^{nd} In-plane Bending Mode

Fig. 5.9 Mode shapes of the first four modes with nodal diameter 3: (a) The 1^{st} disk dominated mode; (b) The 1^{st} in-plane bending Mode; (c) The 1^{st} torsion mode; (d) The 2^{nd} in-plane bending mode

interaction. In the case of fan blades, the intake distortion can be considered as the unsteady aerodynamic loading. To identify resonances caused by EO excitation, the Campbell diagram of this blisk model is shown in Fig.5.10. The change of natural frequencies of modal family 1D with respect to the engine rotational speed is demonstrated by the red curves. The EO excitation are represented by the grey (unexcited) and the black curves (excited). All possible resonance cases are highlighted by the blue markers. When the engine rotational speed is 2081 rpm and the 27^{th} EO excitation is applied, the selected mode with resonant frequency 2.195 is excited. This resonance case is marked by a blue star in Fig.5.10 and will be used for the following analyses. Finally, a nonlinear static analysis is applied to obtain the contact pressure/gap distributions within the contact interface, which define the initial contact status and will be used in the contact model described later.

Nonlinear static analysis

Through the Campbell diagram, the resonances caused by the EO excitations are identified and one resonance case is retained for the present study. Then, the blisk and ring damper with frictional contact under resonance case are investigated by a nonlinear static analysis. A surface-to-surface contact model is used and the contact conditions within the contact

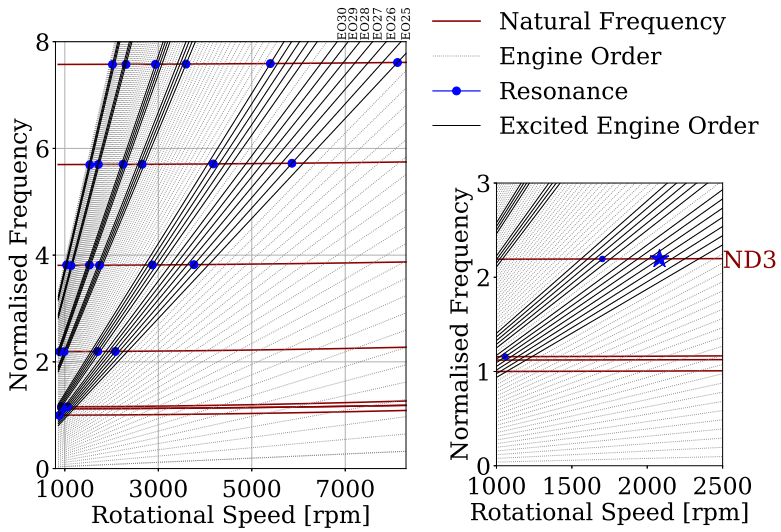


Fig. 5.10 Campbell diagram: Natural frequencies against the engine rotational speed (red curves); Engine order excitation (grey curves); Excited engine order excitation (black curves); Resonances (blue circle); Selected resonance (blue star)

interface are computed for a nonlinear static equilibrium status. A contact pressure distribution and a contact gap distribution are used to represent the contact conditions as shown in Fig.5.11. These static contact conditions are considered as the preloading for the nonlinear vibration analysis.

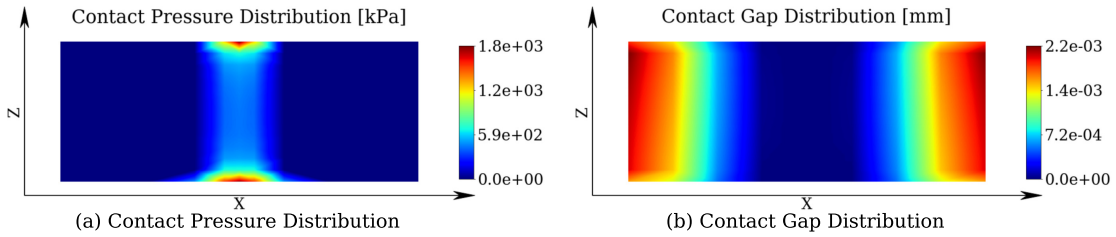


Fig. 5.11 Contact status from the nonlinear static analysis: (a) Contact pressure distribution; (b) Contact gap distribution

5.2.3 Nonlinear vibration solver

The FE model of the blisk and ring damper as well as the methodology for pre-processing have been presented in the previous sections. The nonlinear vibration solver is introduced in this section. The flow chart of the nonlinear vibration solver is shown in Fig.5.12. Firstly, model reduction methods applied are introduced. Then, the contact model used in vibration analysis is described.

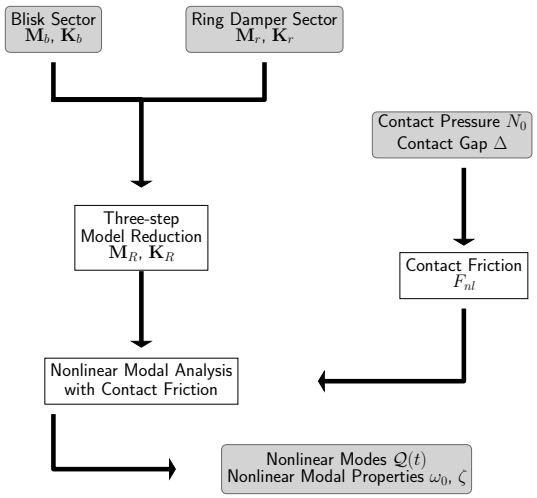


Fig. 5.12 Flow chart for nonlinear vibration solver

Three-step model reduction

For the three-dimensional FE model, the Reduced Order Modelling (ROM) is important to reduce the size of the system and achieve a better computational efficiency. Generally, blisks are assumed to be perfectly tuned structures. Therefore, the full annulus of the blisk and the ring damper can be modelled using a sector with cyclic symmetric boundary conditions. The mass and stiffness matrices of the blisk sector and the sector of ring damper are calculated using the commercial FE solver ABAQUS. Then, the mass and stiffness matrices of a generic sector are reduced in three steps. At the first place, the internal DoFs are eliminated using the well-known Craig-Bampton method (CB)[28]. Then, Mead's approach is applied to project the DoFs corresponding to the left cyclic symmetric boundaries onto the DoFs related to the right cyclic symmetric boundaries [106]. In the last step, the retained DoFs related to cyclic symmetric boundaries are further reduced using Partial Interface Mode (PIM) method [177]. A similar reduction process is applied on both the sector of blisk and ring respectively.

$$\underline{u}_{sector} = [\underline{u}_i^{\mathrm{T}}, \underline{u}_c^{\mathrm{T}}, \underline{u}_{rc}^{\mathrm{T}}, \underline{u}_r^{\mathrm{T}}, \underline{u}_{lc}^{\mathrm{T}}, \underline{u}_l^{\mathrm{T}}]^{\mathrm{T}} \tag{5.4}$$

The partition for DoFs of a generic isolated sector is given in Fig.5.13 and Eqn.(5.4), $\underline{u}_{sector}$ is a collection of all DoFs of this generic isolated sector, including DoFs related to the contact interface $\underline{u}_c$, DoFs corresponding to the left cyclic boundary $\underline{u}_l$, DoFs associated to the right cyclic boundary $\underline{u}_r$, DoFs related to the cyclic boundaries and contact interface $\underline{u}_{lc}$ and $\underline{u}_{rc}$, the remaining belongs to the internal DoFs $\underline{u}_i$.

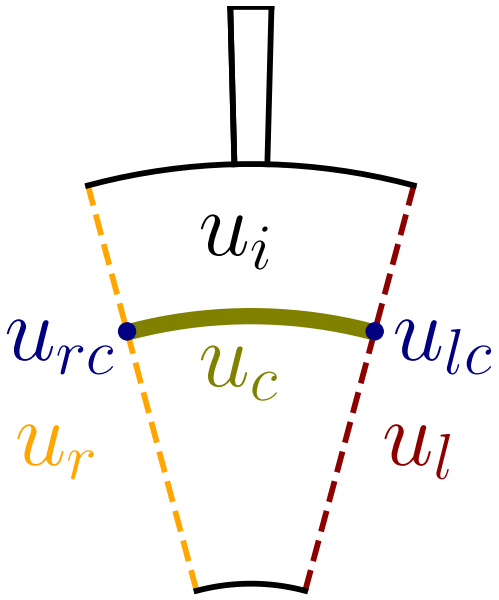


Fig. 5.13 Demonstration of the partition for DoFs of a generic isolated sector

1. Craig-Bampton reduction

The first step of the model reduction consists of a standard CB method retaining the boundary DoFs as master coordinates and eliminating the internal DoFs. The master DoFs $\underline{u}_{m1}$ includes $\underline{u}_c$, $\underline{u}_l$, $\underline{u}_r$, $\underline{u}_{lc}$ and $\underline{u}_{rc}$, whereas the internal DoFs are treated as the slave DoFs $\underline{u}_{s1}$. Then, a coherent partition can be applied for $\underline{\underline{\mathbf{M}}}_{sector}$, $\underline{\underline{\mathbf{K}}}_{sector}$ and $\underline{u}_{sector}$, as shown in Eqn.(5.5-5.6).

$$\begin{aligned} \underline{u}_{m1} &= [\underline{u}_c^{\mathrm{T}}, \underline{u}_{rc}^{\mathrm{T}}, \underline{u}_r^{\mathrm{T}}, \underline{u}_{lc}^{\mathrm{T}}, \underline{u}_l^{\mathrm{T}}]^{\mathrm{T}} \\ \underline{u}_{s1} &= \underline{u}_i \end{aligned} \tag{5.5}$$

$$\underline{\underline{\mathbf{K}}}_{sector} = \begin{bmatrix} \underline{\underline{\mathbf{K}}}_{s1,s1} & \underline{\underline{\mathbf{K}}}_{s1,m1} \\ \underline{\underline{\mathbf{K}}}_{m1,s1} & \underline{\underline{\mathbf{K}}}_{m1,m1} \end{bmatrix}; \quad \underline{\underline{\mathbf{M}}}_{sector} = \begin{bmatrix} \underline{\underline{\mathbf{M}}}_{s1,s1} & \underline{\underline{\mathbf{M}}}_{s1,m1} \\ \underline{\underline{\mathbf{M}}}_{m1,s1} & \underline{\underline{\mathbf{M}}}_{s1,s1} \end{bmatrix} \tag{5.6}$$

The reduction basis of CB method consists of the normal modes $\underline{\underline{\Phi}}_{s1}$ obtained by restraining all master DoFs, and the constraint modes $\underline{\underline{\Psi}}_c$ which is defined as static deformation when unit displacement is applied to constraint coordinate (master DoFs). Only a certain number of the normal modes N_{m1} are kept. The CB reduction basis $\underline{\underline{\mathbf{R}}}_{CB}$, the reduced stiffness matrix $\underline{\underline{\mathbf{K}}}_{CB}$ and the reduced mass matrix $\underline{\underline{\mathbf{M}}}_{CB}$ are calculated as follows:

$$(\underline{\underline{\mathbf{K}}}_{s1,s1} - \omega^2 \underline{\underline{\mathbf{M}}}_{s1,s1}) \underline{\underline{\Phi}}_{s1,s1} = \underline{\underline{\mathbf{0}}}_{s1,s1} \tag{5.7}$$

$$\underline{\underline{\Phi}}_{s1} = \begin{bmatrix} \underline{\underline{\Phi}}_{s1,N_{m1}} \\ \underline{\underline{\mathbf{0}}}_{m1,N_{m1}} \end{bmatrix} \tag{5.8}$$

$$\underline{\underline{\Psi}}_{s1,m1} = -\underline{\underline{\mathbf{K}}}_{s1,s1}^{-1}\underline{\underline{\mathbf{K}}}_{s1,m1}; \quad \underline{\underline{\Psi}}_{c} = \begin{bmatrix} \underline{\underline{\Psi}}_{s1,m1} \\ \underline{\underline{\mathbf{I}}}_{m1,m1} \end{bmatrix} \tag{5.9}$$

$$\underline{\underline{\mathbf{R}}}_{CB} = \begin{bmatrix} \underline{\underline{\Phi}}_{s1} & \underline{\underline{\Psi}}_{c} \end{bmatrix} \tag{5.10}$$

$$\underline{\underline{\mathbf{K}}}_{CB} = \underline{\underline{\mathbf{R}}}_{CB}^{\mathrm{T}}\underline{\underline{\mathbf{K}}}_{sector}\underline{\underline{\mathbf{R}}}_{CB}; \quad \underline{\underline{\mathbf{M}}}_{CB} = \underline{\underline{\mathbf{R}}}_{CB}^{\mathrm{T}}\underline{\underline{\mathbf{M}}}_{sector}\underline{\underline{\mathbf{R}}}_{CB} \tag{5.11}$$

Then, the reduced coordinates $\underline{u}_{CB}$ consists of N_{m1} modal coordinates $\underline{\xi}_{N_{m1}}$ and the master DoFs $\underline{u}_{m1}$.

$$[\underline{\xi}_{N_{m1}}^{\mathrm{T}}, \underline{u}_{c}^{\mathrm{T}}, \underline{u}_{rc}^{\mathrm{T}}, \underline{u}_{r}^{\mathrm{T}}, \underline{u}_{lc}^{\mathrm{T}}, \underline{u}_{l}^{\mathrm{T}}]^{\mathrm{T}} = \underline{u}_{CB} = \underline{\underline{\mathbf{R}}}_{CB}^{\mathrm{T}}\underline{u}_{sector} \tag{5.12}$$

2.Cyclic symmetric reduction

After the classic CB reduction, the number of the internal DoFs has been reduced significantly to N_{m1}. Then, Mead's approach is used to further reduce the DoFs related to the left cyclic boundary by projecting these DoFs onto the right cyclic boundary with a certain phase angle $\phi_p = 2\pi p/N_s$, p is the order of harmonics indicating the periodicity of the mode, N_s is the total number of sectors. The CB reduced stiffness $\underline{\underline{\mathbf{K}}}_{CB}$ and mass matrices $\underline{\underline{\mathbf{M}}}_{CB}$, as well as the coordinates $\underline{u}_{CB}$, are partitioned using Eqn.(5.13-5.14). The master DoFs $\underline{u}_{m2}$ contains all the CB reduced DoFs excluding the DoFs related to cyclic symmetric boundary ($\underline{u}_{rr}$ and $\underline{u}_{ll}$).

$$\begin{aligned} \underline{u}_{CB} &= [\underline{u}_{m2}^{\mathrm{T}}, \underline{u}_{R}^{\mathrm{T}}, \underline{u}_{L}^{\mathrm{T}}]^{\mathrm{T}}; \quad \underline{u}_{m2} = [\underline{\xi}_{N_{m1}}^{\mathrm{T}}, \underline{u}_{c}^{\mathrm{T}}]^{\mathrm{T}} \\ \underline{u}_{rr} &= [\underline{u}_{rc}^{\mathrm{T}}, \underline{u}_{r}^{\mathrm{T}}]^{\mathrm{T}}; \qquad \underline{u}_{ll} = [\underline{u}_{lc}^{\mathrm{T}}, \underline{u}_{l}^{\mathrm{T}}]^{\mathrm{T}} \end{aligned} \tag{5.13}$$

$$\underline{\underline{\mathbf{K}}}_{CB} = \begin{bmatrix} \underline{\underline{\mathbf{K}}}_{m2,m2} & \underline{\underline{\mathbf{K}}}_{m2,rr} & \underline{\underline{\mathbf{K}}}_{m2,ll} \\ \underline{\underline{\mathbf{K}}}_{rr,m2} & \underline{\underline{\mathbf{K}}}_{rr,rr} & \underline{\underline{\mathbf{K}}}_{rr,ll} \\ \underline{\underline{\mathbf{K}}}_{ll,m2} & \underline{\underline{\mathbf{K}}}_{ll,rr} & \underline{\underline{\mathbf{K}}}_{ll,ll} \end{bmatrix}; \quad \underline{\underline{\mathbf{M}}}_{CB} = \begin{bmatrix} \underline{\underline{\mathbf{M}}}_{m2,m2} & \underline{\underline{\mathbf{M}}}_{m2,rr} & \underline{\underline{\mathbf{M}}}_{m2,ll} \\ \underline{\underline{\mathbf{M}}}_{rr,m2} & \underline{\underline{\mathbf{M}}}_{rr,rr} & \underline{\underline{\mathbf{M}}}_{rr,ll} \\ \underline{\underline{\mathbf{M}}}_{ll,m2} & \underline{\underline{\mathbf{M}}}_{ll,rr} & \underline{\underline{\mathbf{M}}}_{ll,ll} \end{bmatrix} \tag{5.14}$$

By representing the left frontier using the right frontier, as shown in Eqn.(5.15). The transformation matrix $\mathrm{R}_{cyc,p}$ is obtained. Then, the cyclic reduced stiffness and mass matrices corresponding to the p^{th} order of periodicity can be obtained. $*^{\mathrm{H}}$ represents the Hermitian

transpose of the matrix. The reduced coordinates $\underline{u}_{cyc,p}$ equals $[\underline{u}_{m2}^{\mathrm{T}}, \underline{u}_{R}^{\mathrm{T}}]^{\mathrm{T}}$.

$$\underline{u}_{CB} = \begin{bmatrix} \underline{u}_{m2} \\ \underline{u}_{rr} \\ \underline{u}_{ll} \end{bmatrix} = \begin{bmatrix} \underline{\underline{\mathbf{I}}} & \underline{\underline{\mathbf{0}}} \\ \underline{\underline{\mathbf{0}}} & \underline{\underline{\mathbf{I}}} \\ \underline{\underline{\mathbf{0}}} & \underline{\underline{\mathbf{I}}} e^{i\phi_p} \end{bmatrix} \begin{bmatrix} \underline{u}_{m2} \\ \underline{u}_{rr} \end{bmatrix} = \mathrm{R}_{cyc,p} \begin{bmatrix} \underline{u}_{m2} \\ \underline{u}_{rr} \end{bmatrix} \tag{5.15}$$

$$\underline{\underline{\mathbf{K}}}_{cyc,p} = \underline{\underline{\mathbf{R}}}^{\mathrm{H}}_{cyc,p} \underline{\underline{\mathbf{K}}}_{CB} \underline{\underline{\mathbf{R}}}_{cyc,p}; \quad \underline{\underline{\mathbf{M}}}_{cyc,p} = \underline{\underline{\mathbf{R}}}^{\mathrm{H}}_{cyc,p} \underline{\underline{\mathbf{M}}}_{CB} \underline{\underline{\mathbf{R}}}_{cyc,p} \tag{5.16}$$

$$[\underline{\xi}_{N_{m1}}^{\mathrm{T}}, \underline{u}_{c}^{\mathrm{T}}, \underline{u}_{rc}^{\mathrm{T}}, \underline{u}_{r}^{\mathrm{T}}]^{\mathrm{T}} = [\underline{u}_{m2}^{\mathrm{T}}, \underline{u}_{rr}^{\mathrm{T}}]^{\mathrm{T}} = \underline{u}_{cyc,p} = \underline{\underline{\mathbf{R}}}^{\mathrm{H}}_{cyc,p} \underline{u}_{CB} \tag{5.17}$$

3. Partial interface mode reduction

In the third reduction step, the PIM reduction method proposed by Tran [177] is applied to further reduce the retained coordinates related to right cyclic boundaries. In PIM method, instead of using the interface modes, a second level CB approach is applied on a Guyan reduced system, which is obtained from a static condensation of whole structure onto the interface (including the contact interface and the cyclic interface). The reduced stiffness $\underline{\underline{\mathbf{K}}}_{cyc,p}$ and mass matrices $\underline{\underline{\mathbf{M}}}_{cyc,p}$, as well as the reduced coordinates $\underline{u}_{cyc,p}$ after the cyclic symmetric reduction are used. The first step of the PIM reduction is a classic Guyan reduction, the reduced system is partitioned into two parts: the master DoFs $\underline{u}_{m3}$ and the slave DoFs $\underline{u}_{s3}$, as given in Eqn.(5.18-5.19).

$$\underline{u}_{cyc,p} = [\underline{u}_{m3}^{\mathrm{T}}, \underline{u}_{s3}^{\mathrm{T}}]^{\mathrm{T}}; \quad \underline{u}_{m3} = \underline{\xi}_{N_{m1}}^{\mathrm{T}}; \quad \underline{u}_{s3} = [\underline{u}_{c}^{\mathrm{T}}, \underline{u}_{rc}^{\mathrm{T}}, \underline{u}_{r}^{\mathrm{T}}]^{\mathrm{T}} \tag{5.18}$$

$$\underline{\underline{\mathbf{K}}}_{cyc,p} = \begin{bmatrix} \underline{\underline{\mathbf{K}}}_{m3,m3} & \underline{\underline{\mathbf{K}}}_{m3,s3} \\ \underline{\underline{\mathbf{K}}}_{s3,m3} & \underline{\underline{\mathbf{K}}}_{s3,s3} \end{bmatrix}; \quad \underline{\underline{\mathbf{M}}}_{cyc,p} = \begin{bmatrix} \underline{\underline{\mathbf{M}}}_{m3,m3} & \underline{\underline{\mathbf{M}}}_{m3,s3} \\ \underline{\underline{\mathbf{M}}}_{s3,m3} & \underline{\underline{\mathbf{M}}}_{s3,s3} \end{bmatrix} \tag{5.19}$$

Then, a static condensation is applied and a Guyan's reduced system is obtained as follows:

$$\underline{\underline{\mathbf{R}}}_{G,p} = \begin{bmatrix} -\underline{\underline{\mathbf{K}}}^{-1}_{m3,m3} \underline{\underline{\mathbf{K}}}_{m3,s3} \\ \underline{\underline{\mathbf{I}}}_{s3,s3} \end{bmatrix} \tag{5.20}$$

$$\underline{\underline{\mathbf{K}}}_{G,p} = \underline{\underline{\mathbf{R}}}^{\mathrm{T}}_{G,p} \underline{\underline{\mathbf{K}}}_{p} \underline{\underline{\mathbf{R}}}_{G,p}; \quad \underline{\underline{\mathbf{M}}}_{G,p} = \underline{\underline{\mathbf{R}}}^{\mathrm{T}}_{G,p} \underline{\underline{\mathbf{M}}}_{p} \underline{\underline{\mathbf{R}}}_{G,p} \tag{5.21}$$

$$\underline{u}_{G,p} = [\underline{u}_{c}^{\mathrm{T}}, \underline{u}_{rc}^{\mathrm{T}}, \underline{u}_{r}^{\mathrm{T}}]^{\mathrm{T}} \tag{5.22}$$

A second level CB approach is applied onto this Guyan's reduced system. The DoFs related to the contact interface are kept as the master DoFs $\underline{u}_{m4} = [\underline{u}_{c}^{\mathrm{T}}, \underline{u}_{rc}^{\mathrm{T}}]^{\mathrm{T}}$ and $\underline{u}_{r}$ is treated as the slave DoFs $\underline{u}_{s4}$. Then, this Guyan's reduced system is further reduced by a CB method

following the similar process described above. N_{m2} number of the normal modes are retained.

$$\underline{\underline{\mathbf{K}}}_{G,p} = \begin{bmatrix} \underline{\underline{\mathbf{K}}}_{s4,s4} & \underline{\underline{\mathbf{K}}}_{s4,m4} \\ \underline{\underline{\mathbf{K}}}_{m4,s4} & \underline{\underline{\mathbf{K}}}_{m4,m4} \end{bmatrix}; \quad \underline{\underline{\mathbf{M}}}_{G,p} = \begin{bmatrix} \underline{\underline{\mathbf{M}}}_{s4,s4} & \underline{\underline{\mathbf{M}}}_{s4,m4} \\ \underline{\underline{\mathbf{M}}}_{m4,s4} & \underline{\underline{\mathbf{M}}}_{m4,m4} \end{bmatrix} \tag{5.23}$$

$$(\underline{\underline{\mathbf{K}}}_{s4,s4} - \omega^2 \underline{\underline{\mathbf{M}}}_{s4,s4}) \underline{\underline{\Phi}}_{s4,s4} = \underline{\underline{\mathbf{0}}}_{s4,s4} \tag{5.24}$$

$$\underline{\underline{\mathbf{R}}}_{PIM,p} = \begin{bmatrix} \underline{\underline{\Phi}}_{s4,N_{m2}} & -\underline{\underline{\mathbf{K}}}^{-1}_{m4,m4} \underline{\underline{\mathbf{K}}}_{m4,s4} \\ \underline{\underline{\mathbf{0}}}_{m4,N_{m2}} & \underline{\underline{\mathbf{I}}}_{m4,m4} \end{bmatrix} \tag{5.25}$$

The final reduced basis after this three-step reduction is represented by Eqn.(5.26). The final reduced system is given in Eqn.(5.26-5.28), where $\underline{\xi}_{N_{m2}}$ are the modal coordinates kept in the PIM method. Using a multi-harmonic formulation of the dynamic equation, this three-step reduction has to be repeated for each order of the periodicity of the mode p.

$$\underline{\underline{\mathbf{R}}}_p = \underline{\underline{\mathbf{R}}}_{CB} \underline{\underline{\mathbf{R}}}_{cyc,p} \underline{\underline{\mathbf{R}}}_{G,p} \underline{\underline{\mathbf{R}}}_{PIM,p} \tag{5.26}$$

$$\begin{aligned} \underline{\underline{\mathbf{K}}}_{R,p} &= \underline{\underline{\mathbf{R}}}^{\mathrm{H}}_p \underline{\underline{\mathbf{K}}}_{sector} \underline{\underline{\mathbf{R}}}_p \\ \underline{\underline{\mathbf{M}}}_{R,p} &= \underline{\underline{\mathbf{R}}}^{\mathrm{H}}_p \underline{\underline{\mathbf{M}}}_{sector} \underline{\underline{\mathbf{R}}}_p \end{aligned} \tag{5.27}$$

$$[\underline{\xi}^{\mathrm{T}}_{N_{m1}}, \underline{\xi}^{\mathrm{T}}_{N_{m2}}, \underline{u}^{\mathrm{T}}_c, \underline{u}^{\mathrm{T}}_{rc}]^{\mathrm{T}} = \underline{u}_{R,p} = \underline{\underline{\mathbf{R}}}^{\mathrm{T}}_p \underline{u}_{sector} \tag{5.28}$$

4. Efficiency and accuracy three-step model reduction

A convergence study for the number of the modes ($N_{m1} = N_{m2}$) retained in the model reduction process is given in Fig.5.14. After the convergence study, 15 normal modes are selected, which gives the maximum error 0.08% for the first four modes.

After the application of this three-step model reduction strategy, the size of system can be significantly reduced. There are 5085 DoFs for a blisk sector and 1716 DoFs for a ring sector. After this model reduction strategy, the reduced system contain 420 DoFs for both blisk and ring respectively, as shown in Tab.5.2.

Contact model

A three-dimensional node to node contact element, which is made of two Jenkins elements in the tangential plane and a unilateral spring in the normal direction, is used to simulate the friction force within the contact interface as shown in Fig.2.12(c). The detailed descriptions and the numerical formulations are given in Section 2.3.3. There are 143 contact pairs in total

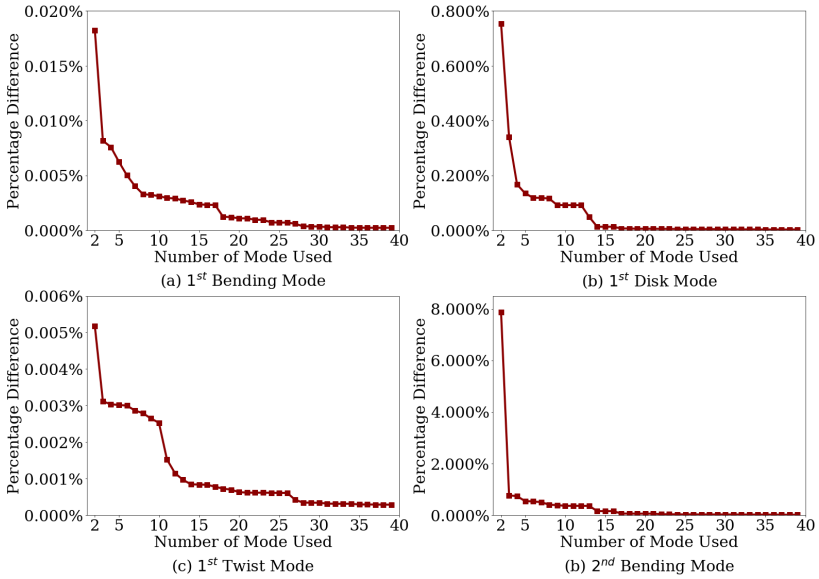


Fig. 5.14 Convergence study for the number of modes used in the model reduction porcess

within the contact interface. There are three basic contact conditions, including separation, sticking and sliding.

In the actual design process, the contact parameters, including the contact stiffness and the friction coefficient, are expected to be measured from the experiments. The measurement of the contact parameters is clearly out of the scope of the present thesis. Therefore, the friction coefficient is used as a value of 0.6 from [120]. The contact stiffness depends on several important factors, such as the material roughness, the normal load and so on [41]. It is difficult to find a proper reference value from the literature. Therefore, a value of $6 \times 10^6 N/m$ is estimated based on the experimental measurement [120].

In the equation of motion (EoM), the physical displacements $(\underline{q}_x, \underline{q}_y, \underline{q}_z)$ are in a global cartesian coordinate system. Whereas, in the computation of contact forces using the present contact element, the displacement in a global cartesian coordinate system needs to be transformed into a local normal-tangent coordinate system $(\underline{q}_n, \underline{q}_{t1}, \underline{q}_{t2})$. After the computation of the contact forces in the local normal-tangent coordinate system, the contact forces and their Jacobian matrices are transformed back to the global cartesian coordinate system.

Table 5.2 Number of DoFs for each model reduction step

Step	Model	Total $\underline{u}_{total}$	Internal $\underline{u}_i$	Modal $\underline{\xi}$	Contact Only $\underline{u}_c$	Right Only $\underline{u}_r$	Left Only $\underline{u}_l$	Right Contact $\underline{u}_{rc}$	Left Contact $\underline{u}_{lc}$
	Blisk	5085	3966	0	351	345	345	39	39
First	Blisk	1134	0	15	351	345	345	39	39
Second	Blisk	750	0	15	351	345	0	39	0
Third	Blisk	420	0	30	351	0	0	39	0
	Ring	1716	1053	0	351	117	117	39	39
First	Ring	678	0	15	351	117	117	39	39
Second	Ring	522	0	15	351	117	0	39	0
Third	Ring	420	0	30	351	0	0	39	0

5.2.4 Nonlinear modal analysis

Damped nonlinear normal mode

The EoM for the nonlinear modal analysis is given as Eqn.(5.29), where $\underline{\underline{\mathbf{M}}}_R$ and $\underline{\underline{\mathbf{K}}}_R$ are the reduced mass and stiffness matrices obtained from the three-step model reduction method described in Section 5.2.3. $\underline{F}_{nl}$ is the contact force in the global cartesian coordinate system calculated using the contact element described in Section 2.3.3. $\underline{Q}$ is the collection of displacements, including the modal displacements (e.g. $\underline{\xi}_1$), the physical displacement of response DoF ($\underline{q}_{rsps}$) and the contact nodes (e.g. $\underline{q}_{nl1,x}$, $\underline{q}_{nl1,y}$ and $\underline{q}_{nl1,z}$).

$$\underline{\underline{\mathbf{M}}}_R \ddot{\underline{Q}} + \underline{\underline{\mathbf{K}}}_R \underline{Q} + \underline{F}_{nl}(\underline{Q}) = 0 \tag{5.29}$$

$$\underline{Q} = [\underline{\xi}_1, \underline{\xi}_2, \underline{\xi}_3, \cdots, \underline{q}_{rsps}, \underline{q}_{nl1,x}, \underline{q}_{nl1,y}, \underline{q}_{nl1,z}, \cdots]^{\mathrm{T}} \tag{5.30}$$

The numerical results from the nonlinear modal analysis are shown in Fig.5.15. The modal properties, the resonant frequency ω_0, the modal damping ratio ζ and the excitation forcing level γ, are plotted against the vibrational amplitude of response DoF $q_{rsps,max}$. It has been verified that the results for all three methods show a very high similarity, so that only the results from EPMC-H method is shown in the following. The normalised natural frequency of the studied mode for the blisk is 2.195. At low amplitude, the contact nodes within the contact interface are either separated or sticking depending on the initial contact condition from the nonlinear static analysis (see Fig.5.11). The resonant frequency is around 2.201 at a

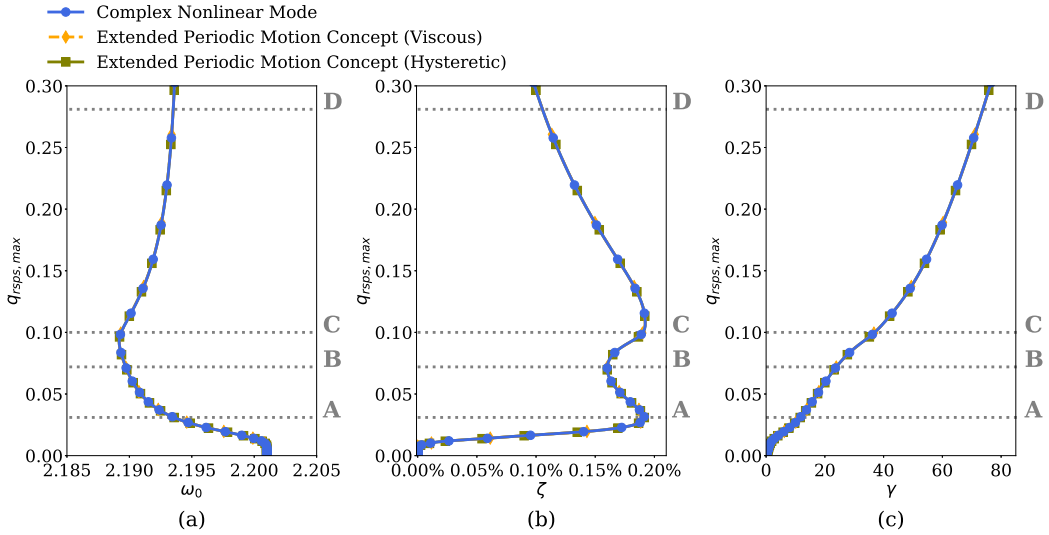


Fig. 5.15 Numerical results from the damped nonlinear normal mode within a range of modal amplitude for the blisk with ring damper: (a) ω_0-$q_{rsps,max}$ plot; (b) ζ-$q_{rsps,max}$ plot; (c) γ-$q_{rsps,max}$ plot using the extended energy balance method

low amplitude. When the structure is vibrating with a large amplitude, some contact nodes start to slide and energy is dissipated by those sliding nodes leading to a decreasing resonant frequency. When the amplitude exceeds 0.1 *mm*, those separated nodes are in-contact and lead to a higher stiffness of the structure resulting in an increase in resonant frequency.

In Fig.5.15(b), a zero modal damping can be observed at low amplitude, when the contact nodes are either separated or sticking. When sliding contact condition occurs at some contact nodes, the modal damping ratio becomes positive. The maximum modal damping ratio achieved is around 0.192%. To explain the evolution of modal damping ratio, four cases with different values of amplitude are selected as shown in Fig.5.15(b), where Case C has the maximum damping 0.192%. The normalised energy dissipated distributions for these four cases are shown in Fig.5.16. From the figures, it is obvious to notice that the energy dissipated in Case B is less than Case A and Case C. In the design point of view, if the ring damper can be designed around Case B (within the "valley" between Case A and Case C), the efficiency and robustness of the damper can be guaranteed.

Numerical validation for computed force amplitude plot

The γ-$q_{disk,max}$ computed from the dNNM coupled with E-EBM has shown in Fig.5.15(c). To validate that, the nonlinear forced response of the system is applied with several values of γ (10, 20, 40, 60 and 70, see Fig.5.17). The excitation force is applied on same DoF

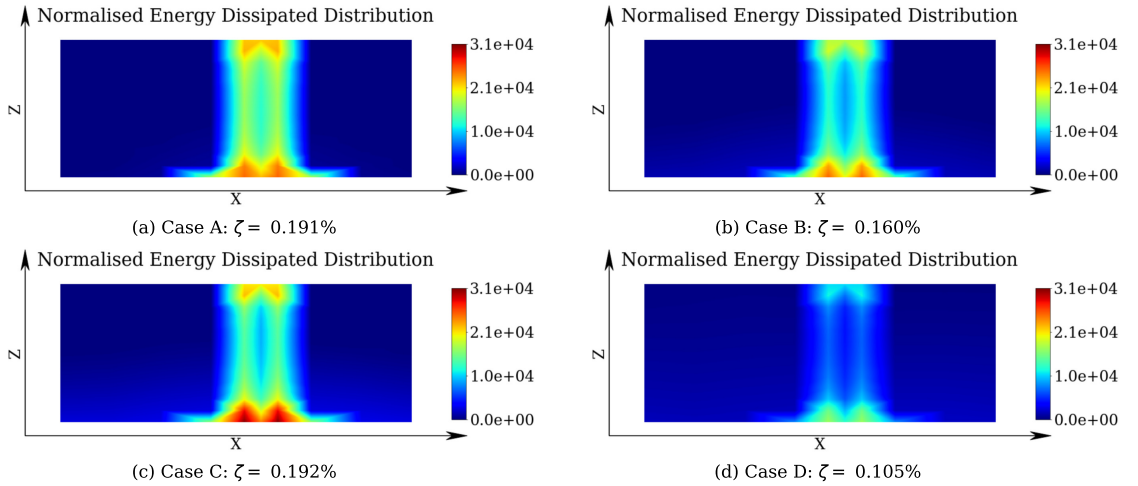


Fig. 5.16 Normalised energy dissipated distribution for the four cases (A, B, C, D) in Fig.5.15 obtained from EPMC-H

where the vibrational response is taken. The nonlinear forced responses are calculated using Eqn.(5.31, 5.32). To further demonstrate the accuracy in the prediction of the resonance, the energy dissipated distributions within the contact interface are shown in Fig.5.18. The upper row shows the distributions under resonance from the forced responses with γ value (10, 40 and 70), whereas distributions calculated from the EPMC-H are given in the lower row. The total energy dissipated is also given in the figure: which are 0.53 J, 8.77 J and 29.79 J for the forced responses; 0.53 J, 8.77 J and 29.78 J using the dNNM. By comparing the energy dissipated distributions (Fig.5.18) and the resonant amplitudes (Fig.5.17), the results show an excellent agreement between the predicted resonances using the E-EBM coupled with the dNNM and resonant solutions in the nonlinear forced response.

$$\underline{\underline{\mathbf{M}}}_R \ddot{\underline{Q}} + \underline{\underline{\mathbf{C}}}_R \dot{\underline{Q}} + \underline{\underline{\mathbf{K}}}_R \underline{Q} + \underline{F}_{nl}(\underline{Q}) = \underline{F}_{ex} \tag{5.31}$$

$$\underline{F}_{ex} = [0,0,0,\cdots,\gamma e^{j(\Omega_e t+\varphi)},0,0,0,\cdots]^{\mathrm{T}} \tag{5.32}$$

In the case with large γ values (60 and 70), the accuracy of predictions is lower than cases with $\gamma = 10$. This discrepancy is mainly due to the numerical method. The classic HBM is applied to solve the nonlinear equation of motion for both nonlinear modal analysis and nonlinear forced response. In HBM, periodic solutions in the time domain are decomposed into Fourier series truncated to a certain order of harmonics. Only zeroth and first harmonics are used in the numerical computation. A simple sinusoidal external excitation force is

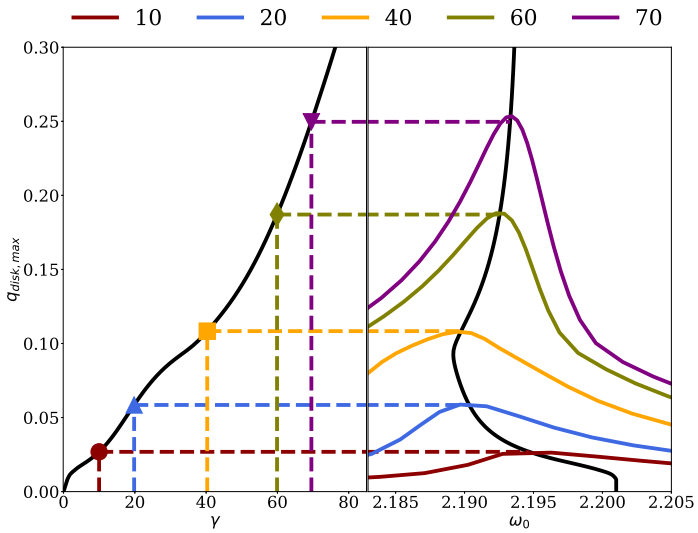
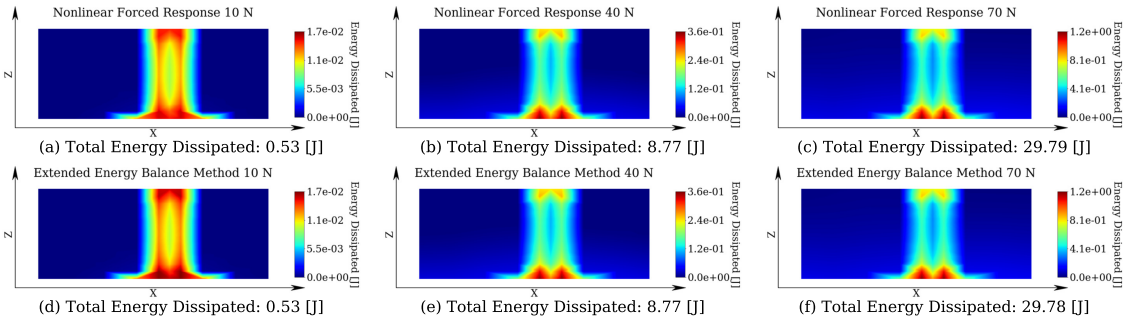


Fig. 5.17 Using nonlinear forced responses with different γ values (10, 20, 40, 60 and 70) to validate the predicted excitation forcing for the blisk with ring damper: Left: γ-q_{max} plot (Black curve); Right: ω_0-q_{max} (Black curve) and five nonlinear forced response in different colours

applied to the blisk. In E-EBM, a balance of energy transferred between the damping terms and forcing term ensures an accurate prediction of resonance. When the damping terms are mathematically equal to the forcing term, the E-EBM is expected to predict the resonance with zero error. However, in this work, when some of contact nodes show partial separation, a non-zero zeroth harmonic can be obtained. In the case with a non-zero zeroth harmonic coefficient, the contact nodes experience a constant shift in their displacements. The existence of the non-zero zeroth harmonic coefficient indicates that the nodes are vibrating around a non-zero equilibrium position. The energy dissipated is calculated based on the oscillating displacement within one vibration period instead of the actual displacement (including the constant shift). Thus, the energy stored by this constant shift in their displacements cannot be captured in the computation of the energy dissipated. Therefore, the prediction of the resonance is not completely accurate leading to a discrepancy in the resonant amplitude as shown in Fig.5.17.

Computational efficiency

The elapsed time used for the computation of the dNNMs by the three methods are given in Tab.5.3. Comparing all three methods, the differences in elapsed time can be ignored. The extra computational time for E-EBM is less than 3 s, which can be ignored compared to time used for the computation of the dNNMs. In forced response analysis, the computation of the



(a) Total Energy Dissipated: 0.53 [J] (b) Total Energy Dissipated: 8.77 [J] (c) Total Energy Dissipated: 29.79 [J]

(d) Total Energy Dissipated: 0.53 [J] (e) Total Energy Dissipated: 8.77 [J] (f) Total Energy Dissipated: 29.78 [J]

Fig. 5.18 Comparison of the energy dissipated distributions under resonance: (a, b) $\gamma = 10$; (b, c) $\gamma = 40$; (e, f) $\gamma = 70$; (a, c, e) From the nonlinear forced response; (b, d, f) From the damped nonlinear normal mode (EPMC-H) with the extended energy balance method

forced response has to be repeated for different values of excitation forcing level γ resulting in a heavy computational burden. Using the same configuration in the continuation method, the time used for nonlinear forced response is given in the Tab.5.4. The minimum computational time is 5458 s for case of $\gamma = 10$. The computational time increases with the value of γ. In summary, the E-EBM coupled with dNNM has shown an excellent accuracy with a much lower computational cost to investigate the resonance, especially for large structures.

Table 5.3 Comparison of computational time among three methods

Method	CNM	EPMC-V	EPMC-H
Elapsed Time	5578 s	5469 s	5443 s

Table 5.4 Comparison of computational time for nonlinear forced responses

γ	10	20	40	60	70
Elapsed Time	5458 s	5844 s	6285 s	6958 s	7809 s

5.2.5 Summary

A three-dimensional FE model is used in this section to represent the blisk with ring damper. The extended energy balance method coupled with the damped nonlinear normal mode is described to predict the resonance for this full-scale structure. The nonlinear modal properties and the classic force amplitude curves are computed using these methods. Several

forced responses are calculated to validate the results from the nonlinear modal analysis. From the numerical results, these methods can efficiently predict the resonance of structures with friction dampers without the computation of nonlinear forced responses. To obtain information for systems under resonance, comparing to forced response analyses, using the damped nonlinear normal mode coupled with the extended energy balance method can significantly reduce the computational cost. This extended energy balance method coupled with the damped nonlinear normal mode can be used for an engineering design problem with a lower computational cost and an accurate prediction in the future.

5.3 Concluding Remarks

In this Chapter, the numerical methods described in the present thesis are applied to an engineering application, a blisk with friction ring damper. In the first part, a lumped parameter model is used to unmask the dynamic response and damping ability of the friction ring damper. Then, the influences of the nodal diameter and damper mass are investigated using such a lumped parameter model. In the second part of this chapter, a full-scale finite element model is used to obtain a more realistic analyses of the blisk with friction ring damper. From the investigation of this full-scale structure, the friction ring damper has been proven to be efficient for disk dominated modes. Furthermore, the influences of the initial contact status on the damping ability have been identified. In the next chapter, a geometric exploration of the ring damper will be provided using this full-scale FE model.

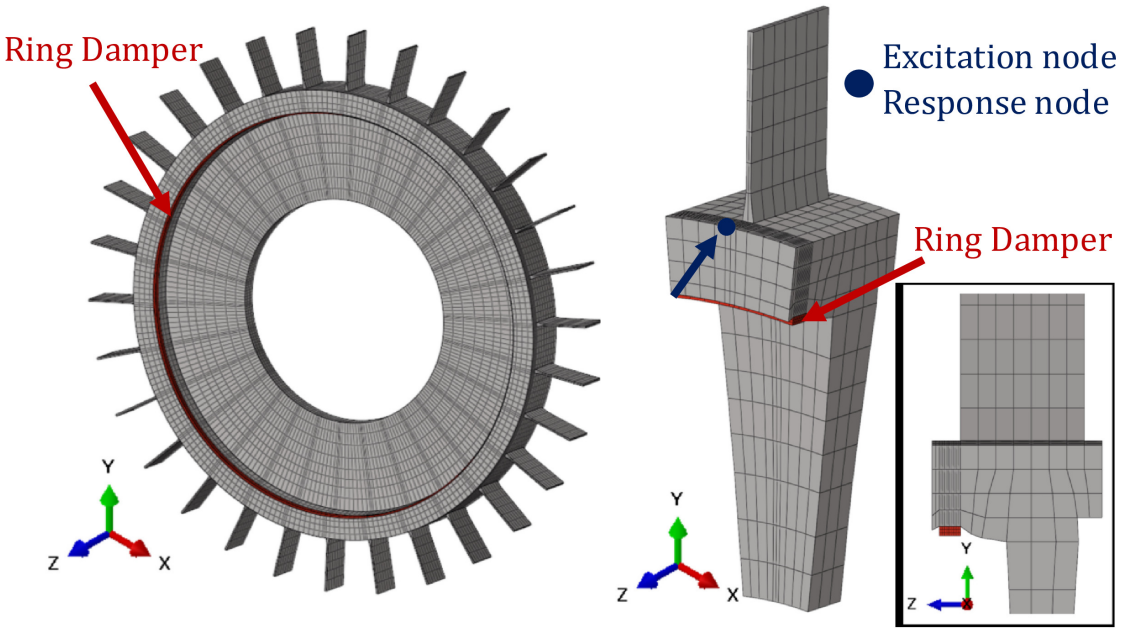
Chapter 6

Geometric Study of a Frictional Ring Damper in a Blisk

In this chapter, the influence of the damper geometry on the nonlinear dynamic responses of a full-scale blisk with frictional ring damper is studied. This full-scale model has been investigated in the previous chapter. The damped Nonlinear Normal Mode (dNNM) coupled with the Extended Energy Balance Method (E-EBM) is considered as the numerical method to study nonlinear dynamic response for such a structure. Three design parameters are considered to modify the geometry of the ring damper. To reduce the computational costs, Kriging meta-models are used to explore the whole design space. The sensitivity of each design parameter is investigated using Sobol indices. The importance of designing damper geometry and some design guidelines are provided. The ring damper geometry is first parameterized using three design parameters. Because of the high computational time associated with the computation of the dynamic responses (it takes about 3 hours for one simulation), a parametric study cannot be considered. To cope with this issue a strategy based on meta-modelling, and more precisely on Kriging, is employed. In this section, first, the damper geometry parameterisation is introduced. Second, a brief summary on Kriging and its use are presented. Finally, the impacts of the damper geometry on the blisk are assessed.

6.1 Damper Geometry Parametrisation

The blisks are considered as the structures with a cylindrical shape. Therefore, it is better to parameterize the ring damper in a cylindrical coordinate system ($\hat{r}$-$\hat{t}$-Z) instead of the global Cartesian coordinate system (X-Y-Z). $\hat{r}$-axis is the radial direction, whereas $\hat{t}$-axis represents the circumferential direction. To change the damper geometry, a parametrisation



(a) Full Annulus (b) A Sector

Fig. 6.1 A three dimensional blisk with ring damper: (a) A full annulus; (b) A sector

in the cylindrical $\hat{r}-\hat{t}$ plane is considered. The dimension in the radial direction of the ring damper can vary (in $\hat{r}$-axis), but the coordinates in the rotational axis (in Z-axis) and circumferential direction (in $\hat{t}$-axis) are unchanged (see Fig.6.1 and Fig.6.2 for axis names). The geometric modification of the ring damper comes from several considerations:

- *Modifying the initial contact status*: From the results in the Section 5.2, one can notice that the initial contact status (either normal load or initial gap) has a significant influence on the damping ability. Thus, the aim of the geometric design of the ring damper is to improve the damping performance through a modification of the initial contact status.

- *Modifying the geometry in the circumferential direction*: From Fig.5.18, the contact nodes in the middle under the blade show a higher energy dissipation than the other nodes. To improve the dissipative ability of the other contact nodes (the contact nodes are not in the middle under the blade), changing the shape of the ring damper in the circumferential direction ($\hat{r}$ axis) is considered instead of in the Z-axis.

- *Modifying the upper surface*: From the results in Section 4.2, different contact angles can lead to a distinctive damping performance. The modification of the upper surface of the ring damper is considered, because it can lead to different local contact angles.

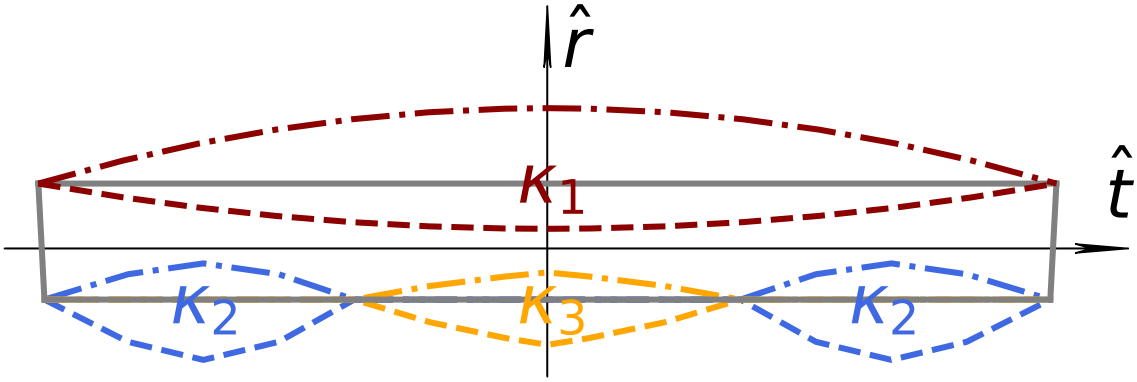


Fig. 6.2 Demonstration of damper geometry parametrisation

- *Modifying the lower surface*: In the study of the lumped parameter model in Section 5.1, different mass of the ring damper can result in a different normal load leading to a different damping ability. To change the mass of the ring damper, the geometric modification of the lower surface of the ring damper is included.

- *Adding bumps or concaves*: A continuous and smooth upper surface of the ring damper is desired based on the consideration of easy fabrication. Therefore, only one bump or a concave shape is considered for the upper surface. Whereas for the lower surface, the idea is to have a wavelet shape of the ring damper. A wavelet shape of the ring damper has a great potential to further improve the damping ability by treating the additional mass (bump) as a tune vibration damper [100, 101]. In this work, only three bumps/concaves are included to illustrate the potential of this idea.

The damper geometry is parametrized with three different parameters, κ_1, κ_2 and κ_3. The first one describes the upper surface, when the two others describe the lower surface. The damper is supposed to be symmetric in its centre about the Y-axis. The demonstration of the three design parameters are provided in Fig.6.2. Each parameter corresponds to the height of a bump (or a concave for a negative height) in different locations of the damper. For the upper surface, only one bump is considered, whereas three different bumps can be considered for the lower surface: one in the middle and one on each side, these outer two are similar to ensure the symmetry of the damper. Each parameter varies between -1 and 1, and the default geometry corresponds to the set $[0,0,0]$ which is represented by Fig.6.3(a). Different damper geometries when varying these three parameters are illustrated by Fig.6.3. To go into more details:

- κ_1 controls the upper surface (i.e. contact interface) of the ring damper using a spline function. A bump in the centre can be obtained when $\kappa_1 > 0$ (see Case A Fig.6.3(b)),

whereas a negative κ_1 leads to a "concave" surface (Case B Fig.6.3(c)). When κ_1 varies, the mass of the damper as well as the local coordinates at the contact interface are impacted. It is worth emphasizing that the contact interface underneath the blisk changes with the ring damper geometry to ensure that the contact points are always overlapped.

- κ_2 controls the two outer bumps of the lower surface, similarly to κ_1 it controls the geometry with a spline function and positive values lead to two concaves, when negative values lead to two bumps (one on each side). See Case C and D in Fig.6.3(d, e) for graphical illustrations. Deforming the lower surface can change the flexibility of the ring and the mass distribution along the circular-wise direction but has no impact on the local coordinate within contact interface.

- κ_3 controls the middle bump of the lower surface, it controls the geometry with a spline function and positive values lead to a concave, when negative values lead to a bump. See Case E and F in Fig.6.3(f, g) for graphical illustrations. Effects on the structure are similar to those for κ_2.

Table 6.1 Parameters that describe the damper geometry

Parameter	Normalized values	Physical values δy
κ_1	$[-1,0,1]$	$[-1.5,0,2.5]$
κ_2	$[-1,0,1]$	$[-2,0,1.5]$
κ_3	$[-1,0,1]$	$[-1.5,0,1]$

When one of the parameters κ_i with $i \in \{1,2,3\}$ is modified, the location of the geometrical points of the mesh are modified as well. Each parameter is normalized to an interval $[-1,1]$. The physical values δr for each normalized parameters are given in Tab.6.1. The physical values δr represent the change of radial coordinate ($\hat{r}$-axis), leading to a bump or a concave. The geometry of the upper surface and the lower surface is defined using a quadratic spline function by fixing the radial coordinate of the central node with its given physical value δr. To keep a consistent mesh quality, the number of nodes and elements of the ring damper are unchanged when the ring damper is deformed. During this process, the physical coordinates of each node for the ring damper are automatically updated according to the defined upper and lower surface.

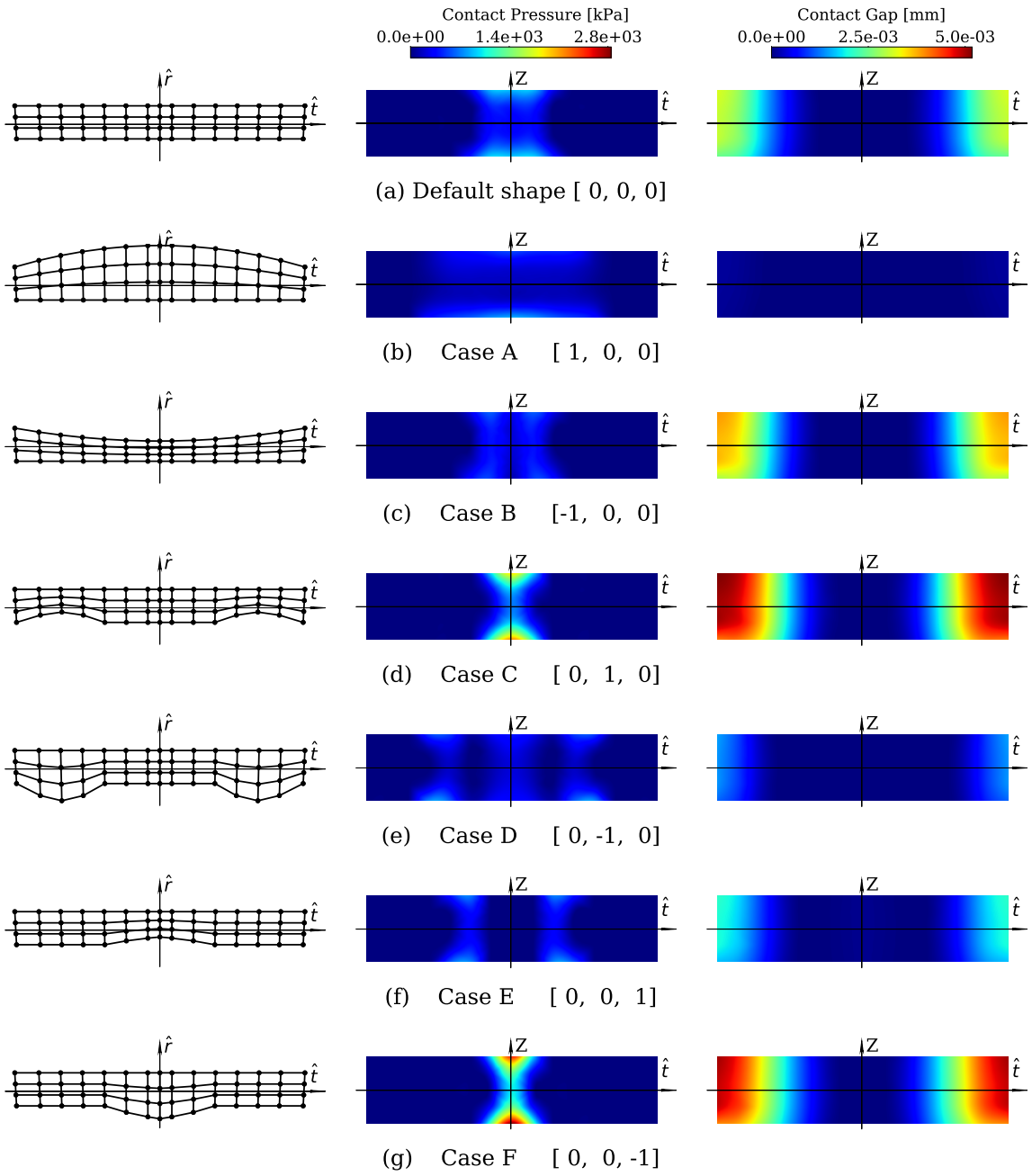


Fig. 6.3 Different geometries of a sector of ring damper: (a) Default shape; (b-g) Other six geometries when varying one the parameter; Left: $\hat{r}-\hat{t}$ view of geometries; Middle: Contact pressure distribution; Right: Contact gap distribution

For each geometry, before computing the system dynamic response, the contact pressure distribution as well as the gaps must be determined to initialize the different contact properties. This is done through a nonlinear static analysis where centrifugal effects are considered using the commercial FE solver ABAQUS. In order to illustrate the impact of the damper geometry on such contact properties, the contact pressure and gap for each geometry are given in Fig.6.3.

For the default shape, the nodes in the centre have a greater normal load, whereas nodes near boundaries show a larger gap (see Fig.6.3(a)). When κ_1 is positive, an increasing number of inner nodes are in contact and less outer nodes are separated (see Case A in Fig.6.3(b)). Whereas when κ_1 is negative, it leads to more separated nodes with larger gaps (see Case B in Fig.6.3(c)). The values of the contact pressure stay nevertheless similar. When κ_2 equals 1, the contact pressure is concentrated in the middle under the blade with higher values (up to $2e3\ kPa$, see Case C in Fig.6.3(d)). It also brings the largest gap near boundaries among all seven geometries. A more dispersive pressure distribution can be seen when κ_2 is -1. The highest contact pressure is observed when κ_3 is -1 and, the contact pressure located under the blade, it also brings large gaps for the outer nodes. From these different cases, one can see that by changing of three parameters, a large variety of contact pressure/gap distributions can be reached.

6.2 Nonlinear Modal Analysis

To get a quick overview on the impact of the damper geometry on the system dynamic, the dNNMs and the force amplitude plots are computed for the seven geometries using the nonlinear modal analysis and the E-EBM. The evolution of the resonant frequency ω_0, the modal damping ratio ζ and the predicted excitation forcing level γ are shown with respect to the vibration amplitude in Fig.6.4. The vibration amplitude is taken from the displacement in the Z direction from the response node (see Fig.6.1). The results for the default geometry are represented by the black curves. When the blisk vibrates at a low amplitude, the contact nodes are either sticking or separated resulting in a constant resonant frequency and a zero modal damping ratio. The predicted excitation forcing level increases linearly with the vibration amplitude. By continuing to increase the vibration amplitude, more and more contact nodes experience sliding. A softening effect is observed and so the resonant frequency decreases. The total energy of the blisk is dissipated due to the rubbing motion of those sliding nodes. Therefore, a positive modal damping ratio is obtained. The predicted excitation forcing level is no longer linearly proportional to the vibration amplitude. For the default geometry, the

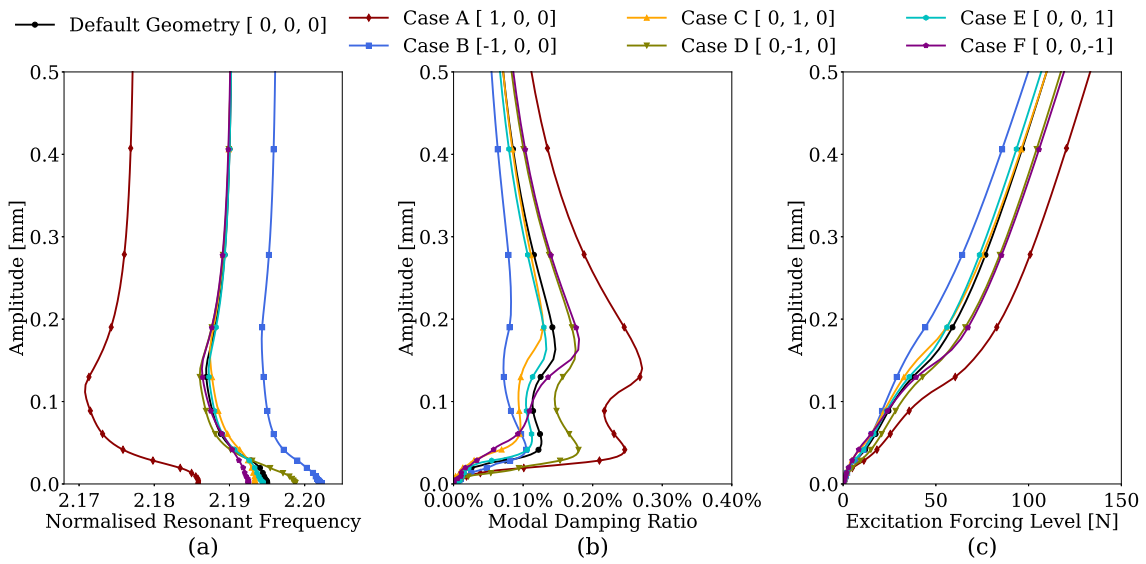


Fig. 6.4 Damped nonlinear normal mode and force amplitude plot for all seven geometries (Fig.6.3): (a) Normalised resonant frequency-amplitude plot; (b) Modal damping ratio-amplitude plot; (c) Force-amplitude plot using extended energy balance method

resonant frequency at zero amplitude is 2.195, which can be seen as a linear sticking natural frequency. This linear sticking natural frequency is obtained by considering the contact pairs in either sticking or separation condition based on the pre-loading (normal load or gap), i.e. sticking contact pairs (with normal load) connected by the linear springs in three dimensions. This can be explained by the fact that the nonlinear dynamic response lies on the linear sticking response before the sliding condition occurs. The maximum modal damping ratio 0.15% occurs when the excitation forcing level is 52.5 N with a vibration amplitude of 0.164 mm and a resonant frequency of 2.187.

Comparing the results for the different geometries, it appears that the resonant frequency, the modal damping ratio and the predicted excitation forcing level are very sensitive to κ_1. Since, the largest variation in the dynamic response is observed by comparing Case A and Case B with default case. As described above, a positive κ_1 leads to a more dispersive contact pressure distribution and less separated contact nodes. In nonlinear modal analysis, a lower resonant frequency and a better damping performance are observed. Indeed, the resonant frequency equals 2.185 at a low level of amplitude and the damping ratio reaches 0.28%. Moreover, for the same level of excitation, the vibration amplitude are always lower for Case A. Less variation is observed for κ_2 and κ_3, especially on the resonant frequency and the amplitude of vibration. However, a large variation can be observed on the modal damping ratio. Conclusively, changing κ_1 can improve the damping performance greatly

with a significant shift of the resonant frequency, and it allows for a large variation of the dynamic response. Whereas, different κ_2 and κ_3 can ensure a better damping performance with a negligible shift in the resonant frequency.

6.3 Kriging Meta-Modelling

Considering the high computational cost associated to the computation of the nonlinear dynamic response, the use of a surrogate model is considered here. From a set of inputs and outputs of the nonlinear analysis, a surrogate model is built and then used to predict the dNNM. This approach has the main advantage to be non-intrusive. Kriging is used here as it is the best linear unbiased estimator and proved to be efficient for the prediction of the stability of nonlinear systems when a large variation of design parameters is observed [32]. From the knowledge of the author, it has never been used yet for the prediction of the dNNMs.

In the present study, the input parameters are the three design parameters, namely κ_1, κ_2 and κ_3. For each modal amplitude α, four Kriging meta-models are built: one for the vibration amplitude, one for the resonant frequency, one for the modal damping ratio and one for the excitation forcing level. In the following, $\underline{\mathbf{x}} = [\kappa_1, \kappa_2, \kappa_3]$ will denote the vector of inputs, and y will denote one of the considered output. A set $\left\{(\underline{\mathbf{x}}^{(i)}), y^{(i)}\right\}$ of N points are used to train the surrogate models. In the present study, the Kriging meta-models are build based on the ordinary Kriging using pyKriging which is an open source Python Kriging toolkit [116]. In the ordinary Kriging algorithm, the expectation and covariance within the design space are assumed to be unknown. The function $y(\underline{\mathbf{x}})$ is approximated by a linear Kriging meta-model $\widehat{y}$ as [73, 139]:

$$y(\underline{\mathbf{x}}) \approx \widehat{y}(\underline{\mathbf{x}}) = \mu + \mathscr{Z}(\underline{\mathbf{x}}) \tag{6.1}$$

where μ is the unknown process average and $\mathscr{Z}$ is a stationary Gaussian process of zero mean of variance σ^2 which is to be determined. Its covariance function is given by $C(\underline{\mathbf{x}}, \underline{\mathbf{x}}') = \sigma^2 \mathscr{R}(\underline{\mathbf{x}}, \underline{\mathbf{x}}')$ where $\mathscr{R}(\underline{\mathbf{x}}, \underline{\mathbf{x}}')$ is the correlation function, given by the user. It is often chosen as a kernel function parametrized by a hyperparameter $\underline{\theta}$ to be found. The Kriging prediction at a point $\underline{\mathbf{x}}_0$ is given by:

$$\widehat{y}(\underline{\mathbf{x}}_0) = \mu + \underline{\mathbf{r}}_0^T \underline{\underline{\mathbf{R}}}^{-1} (\underline{\mathbf{y}} - \underline{\mathbf{1}}\mu) \tag{6.2}$$

where $\underline{\underline{\mathbf{R}}}$ is the correlation matrix whose coefficients are $\underline{\underline{\mathbf{R}}}_{ij} = C(\underline{\mathbf{x}}^{(i)}, \underline{\mathbf{x}}^{(j)})$, $\underline{\mathbf{r}}_0$ as the vector of $C(\underline{\mathbf{x}}_0, \underline{\mathbf{x}}^{(i)})$ and $\underline{\mathbf{1}}$ a vector of ones. Three parameters have to be determined, namely the process average μ, the process variance σ^2 and the hyperparameter $\underline{\theta}$. It is done by

solving a likelihood optimisation problem. For more details about the theoretical background, the readers are invited to refer to [73, 78, 116, 139].

6.4 Construction and Validation of the Meta-models

100 points are generated for the construction of the Kriging meta-models. It means that 100 dNNM analyses have been realized for 100 different geometries. Then, the modal amplitude is discretized and for each value, four different Kriging surrogate models are created: for the vibration amplitude, for the resonant frequency, for the modal damping ratio and for the excitation force level. The number 100 has been chosen based on a convergence study, not shown here for the sake of consistency. This sample set includes 27 points located on the boundary of three-dimensional design space and 77 points generated using the Latin hypercube sampling through the pyKriging [116].

An additional set of 20 geometries has been used to validate of results predicted from Kriging meta-models. This comparison is done in Fig.6.5(a-d), where the predicted values are plotted versus the reference values from the numerical simulations (i.e. the points are expected to be on the line with gradient of 1). It is worth noticing that for each point, Kriging meta-models are constructed for each modal amplitude values, so it leads to a much larger number of points than 20. For the vibration amplitude and the excitation forcing level, the predictions are very accurate as shown in Fig.6.5(a, d), where all the predictions are very close to the reference values (i.e. points are on the line with gradient of 1). However, for the modal damping ratio, the accuracy of the Kriging model is slightly lower at a low modal damping ratio (see Fig.6.5(c)). By looking at Fig.6.5(b), the Kriging meta-models show less accurate predictions at a larger resonant frequency. For a deeper insight into the error, the predicted dNNMs and the reference dNNMs from the nonlinear modal analysis are compared in Fig.6.5(e-g). Three geometries with design parameters $[-0.85, 0.65, 0.39]$, $[-0.03, -0.41, 0.59]$ and $[0.25, 0.45, 0.89]$ are selected from the validation set as examples to show the accuracy of the prediction. The predicted results are shown by the orange dashed curves whereas the reference results are represented by the black solid curves. It can be seen, the predictions are very close to the reference results, which gives confidence in the Kriging meta-models and their validation. In conclusion, these surrogate models can provide an accurate prediction of dNNMs with given design parameters.

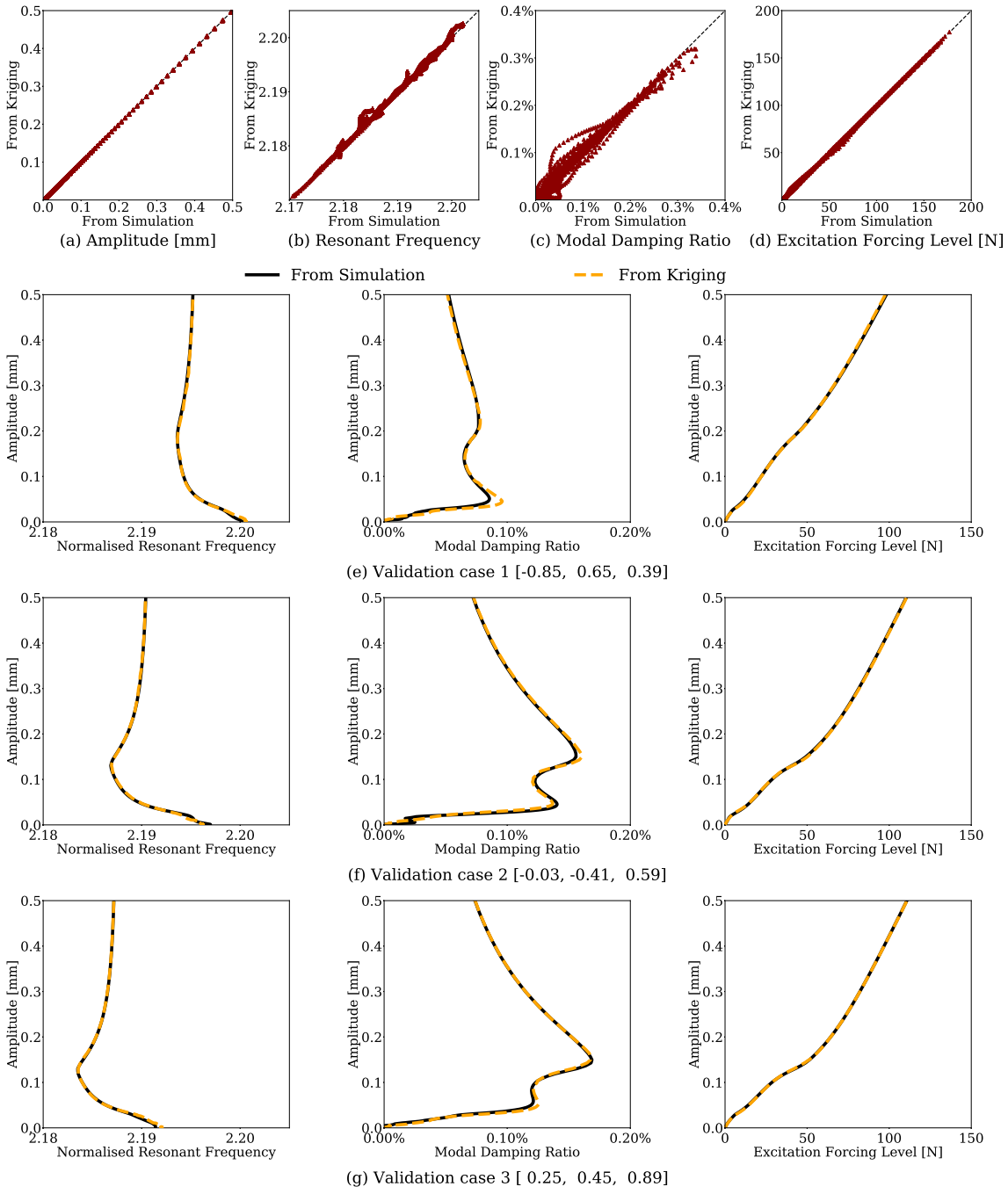


Fig. 6.5 Meta-models validation: (a-d) Comparison between the predicted values using Kriging against the values calculated from the nonlinear modal analysis from 20 validation cases: (a) physical vibration amplitude, (b) normalised resonant frequency, (c) modal damping ratio, (d) predicted excitation forcing level; (e-g) Comparison of the predicted results and actual results from the nonlinear modal analysis using three validation case as examples: (e) Validation case 1 $[-0.85, 0.65, 0.39]$, (f) Validation case 2 $[-0.03, -0.41, 0.59]$, (g) Validation case 3 $[0.25, 0.45, 0.89]$

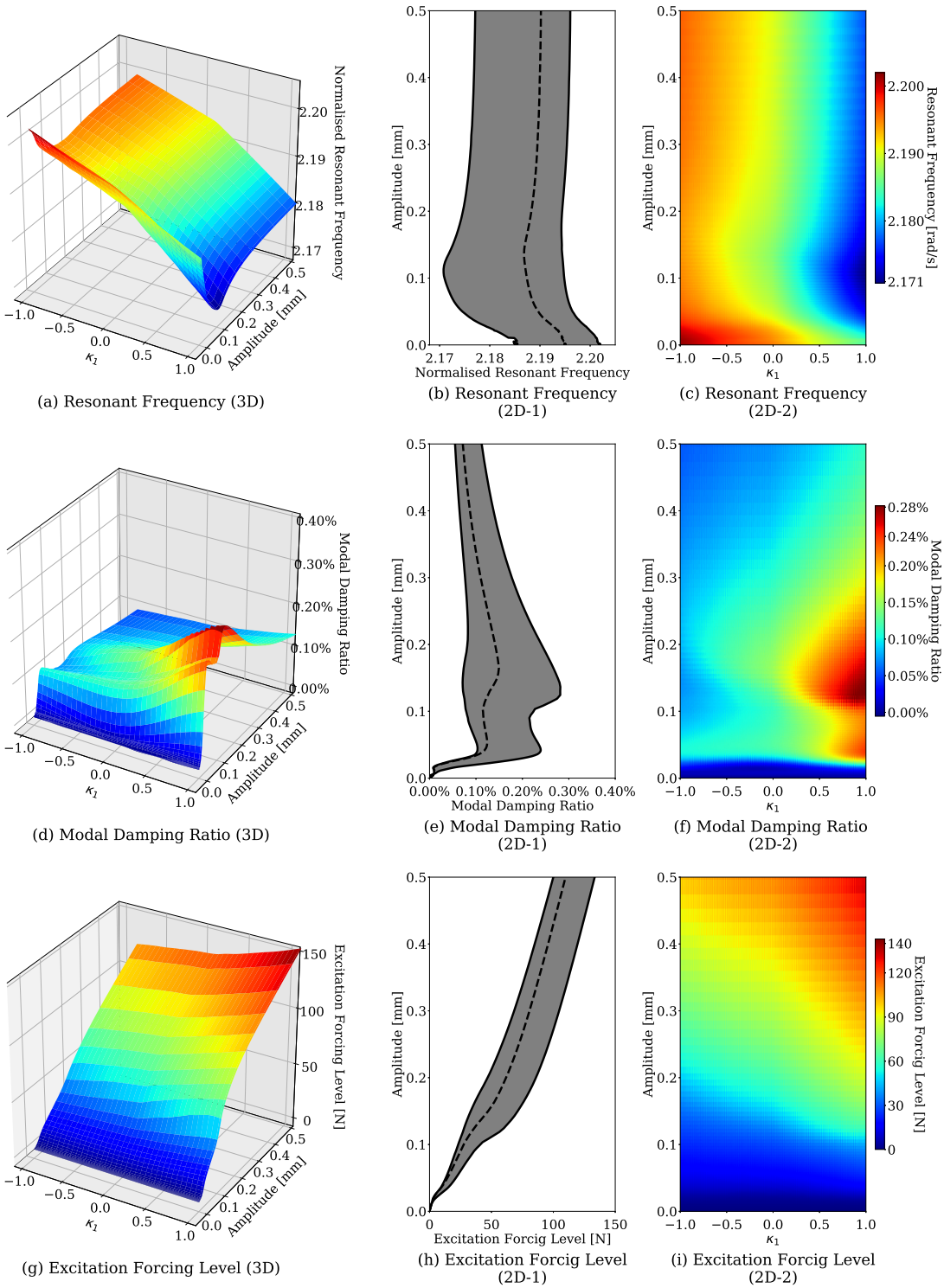
6.5 Design Space Exploration and Discussion

In this section, the surrogate models are exploited and analysed to assess the effect of each design parameter. This analysis is divided into two steps: first the influence of each parameter is studied when the two others are fixed to 0. Second, the whole design space is explored.

6.5.1 Influences of each design parameter

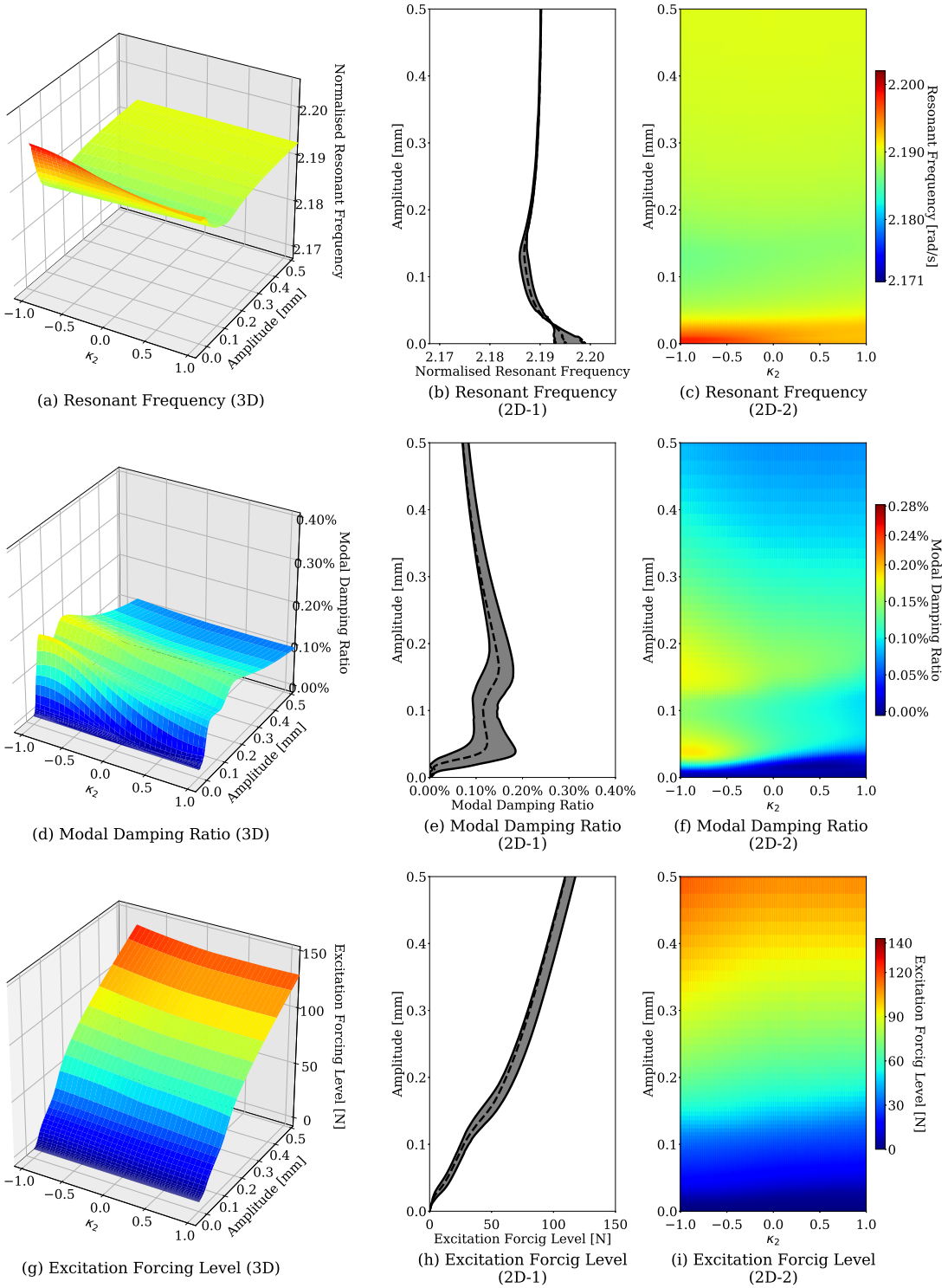
In this part, only one parameter can vary between -1 and 1 when the two others are fixed to 0. It allows to investigate the effects of each design parameter independently. Results are given in Fig.6.6 for κ_1 (upper surface modification), in Fig.6.7 for κ_2 and in Fig.6.8 for κ_3. In each case, the evolution of the normalized resonant frequency-amplitude curve, of the modal damping ratio-amplitude curve and of the excitation forcing level curves versus the vibration amplitude and the considered parameter are displayed in a three-dimensional plot (left column of the figures). For a better readability, two other views are also given: a side view that gives the envelopes of the dNNM properties versus the vibration amplitude (middle column in the figures) and the dNNM calculated from the default geometries $[0,0,0]$ is highlighted by black dashed curves, and a top view (right column).

- *Impact of* κ_1: From Fig.6.6, one can see that large variations of the dNNM properties are observed when κ_1 varies. Indeed, the normalized resonant frequency varies between 2.17 and 2.20 depending on the amplitude. The resonant frequency tends to decrease with an increasing value of κ_1. As a modification of the upper surface leads to a variation of the number of points in contact, a strong variation for the resonance frequency is expected as it modifies the stiffness of the global system. The modal amplitude ratio is also largely impacted by the variation of κ_1, and especially when κ_1 is positive. Indeed, the modal damping ratio tends to have similar evolution for negative κ_1 with one peak at an amplitude of 0.05 *mm* and a greater second one at 0.15 *mm*. But when κ_1 is positive, a large increase of the modal damping ratio for amplitudes between 0.05 *mm* and 0.25 *mm* is observed (see Fig.6.6(d)). The maximum modal damping ratio achieved is around 0.29% when κ_1 equals 1, with an amplitude of 0.13 *mm*. By looking at the contact pressure distribution (See Case A in Fig.6.3(b)), a more dispersive pressure distribution is obtained when $\kappa_1 = 1$ and more nodes are in-contact. The excitation forcing level follows the same trend as the modal damping ratio when the κ_1 is varying. Because, the total energy injected into the system by excitation is expected to balance the total energy dissipated by the damping terms,



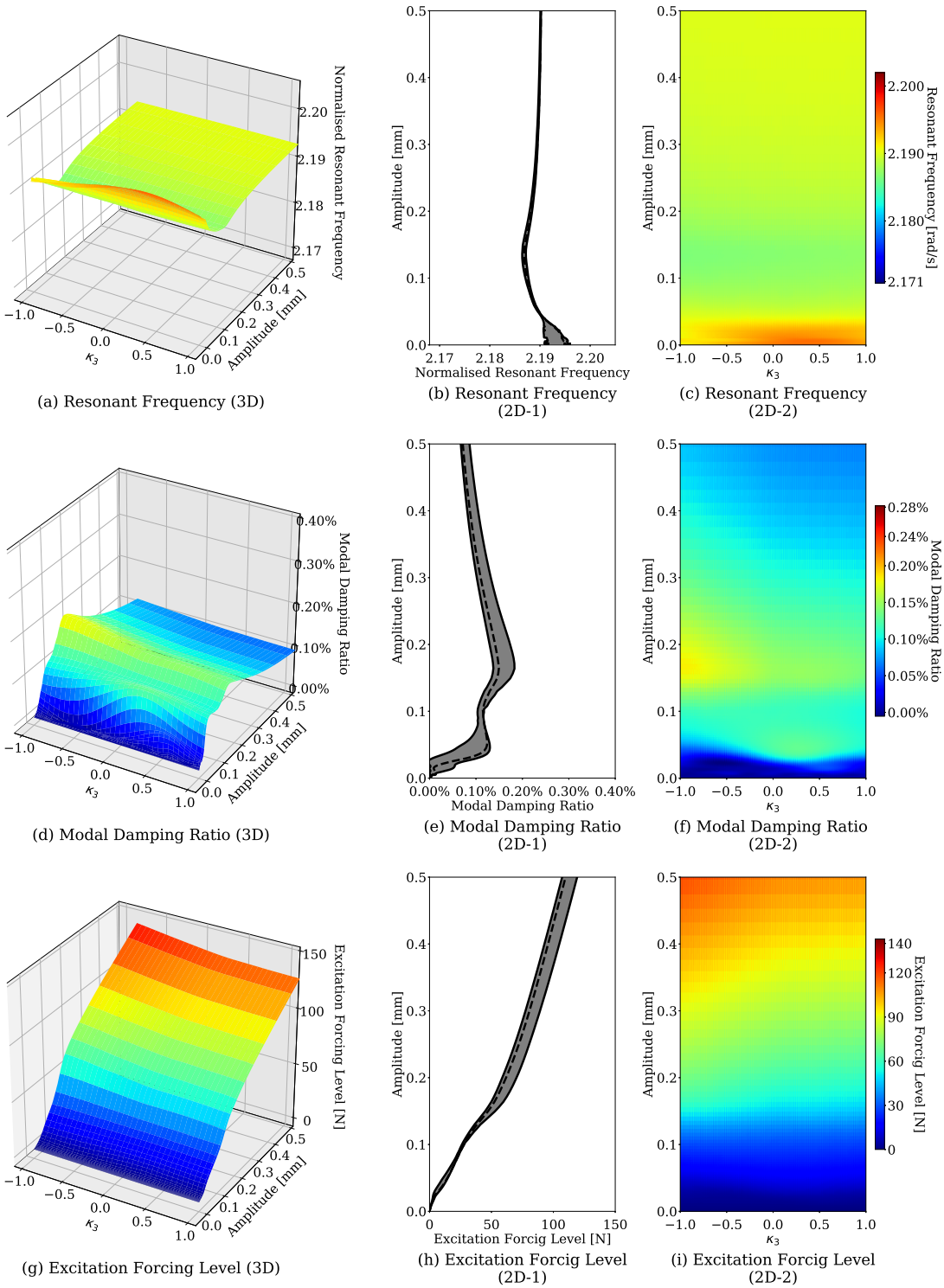
(a) Resonant Frequency (3D)
(b) Resonant Frequency (2D-1)
(c) Resonant Frequency (2D-2)
(d) Modal Damping Ratio (3D)
(e) Modal Damping Ratio (2D-1)
(f) Modal Damping Ratio (2D-2)
(g) Excitation Forcing Level (3D)
(h) Excitation Forcig Level (2D-1)
(i) Excitation Forcig Level (2D-2)

Fig. 6.6 Effect of κ_1 ($-1 \leq \kappa_1 \leq 1$) on the damped nonlinear normal mode $[\kappa_1, 0, 0]$: (a-c) Normalised resonant frequency; (d-f) Modal damping ratio; (g-i) Excitation forcing level; Black dashed curve: default geometry $[0, 0, 0]$



(a) Resonant Frequency (3D)
(b) Resonant Frequency (2D-1)
(c) Resonant Frequency (2D-2)
(d) Modal Damping Ratio (3D)
(e) Modal Damping Ratio (2D-1)
(f) Modal Damping Ratio (2D-2)
(g) Excitation Forcing Level (3D)
(h) Excitation Forcig Level (2D-1)
(i) Excitation Forcig Level (2D-2)

Fig. 6.7 Effect of κ_2 ($-1 \leq \kappa_2 \leq 1$) on the damped nonlinear normal mode $[0, \kappa_2, 0]$: (a-c) Normalised resonant frequency; (d-f) Modal damping ratio; (g-i) Excitation forcing level; Black dashed curve: default geometry $[0,0,0]$



(a) Resonant Frequency (3D)
(b) Resonant Frequency (2D-1)
(c) Resonant Frequency (2D-2)
(d) Modal Damping Ratio (3D)
(e) Modal Damping Ratio (2D-1)
(f) Modal Damping Ratio (2D-2)
(g) Excitation Forcing Level (3D)
(h) Excitation Forcig Level (2D-1)
(i) Excitation Forcig Level (2D-2)

Fig. 6.8 Effect of κ_3 ($-1 \leq \kappa_3 \leq 1$) on the damped nonlinear normal mode $[0,0,\kappa_3]$: (a-c) Normalised resonant frequency; (d-f) Modal damping ratio; (g-i) Excitation forcing level; Black dashed curve: default geometry $[0,0,0]$

including both the friction damping and viscous damping. Higher modal damping ratio leads to more dissipated energy due to the friction force. Therefore, an excitation with a large forcing level is required to balance the energy dissipated due to the friction damping and viscous damping.

- *Impact of* κ_2: From Fig.6.7, the resonant frequency at low amplitude (linearized sticking frequency) decreases with an increasing value of κ_2. However, the resonant frequency at large amplitude is almost constant. The two outer bumps on the lower surface do not have a significant effect on the resonant frequency. For the damping performance (see Fig.6.7(d-f)), the maximum modal damping ratio 0.19% is achieved when $\kappa_2 = -1$, at a vibration amplitude of 0.03 *mm*. By looking at the contact pressure distribution (See Case D in Fig.6.3(e)), a more dispersive pressure distribution is obtained when $\kappa_2 = -1$ and more nodes are in-contact with a relatively smaller contact pressure. The excitation forcing level follows a similar trend with the modal damping ratio.

- *Impact of* κ_3: By looking at Fig.6.8, the variation of κ_3 does not have a remarkable impact on the modal properties. However, it is worth emphasizing that a lower peak can be noticed when $\kappa_3 = 0.3$ for both the resonant frequency (at lower amplitude) and the modal damping ratio (see Fig.6.8(c, f)). In more details, the modal damping ratio-amplitude curve shows two peaks around an amplitude of 0.03 *mm* (the first peak) and 0.15 *mm* (the second peak). An increasing value of κ_3 leads to a higher first peak and a lower second peak. The maximum modal damping ratio 0.19% is obtained when $\kappa_3 = -1$, with an amplitude of 0.17 *mm*.

In summary, all nonlinear modal properties are very sensitive to the design parameter κ_1. For κ_2 and κ_3, the impact on the resonant frequency and the excitation forcing level are negligible. In other words, damping performance can be significantly improved by varying κ_1, resulting in a remarkable change in the resonant frequency. Whereas, by varying κ_2 and κ_3, the damping ability can be improved in a certain amount with a negligible variation of the resonant frequency. Furthermore, a dispersive contact pressure distribution and an increasing number of the contact nodes can lead to a larger modal damping ratio.

6.5.2 All design space exploration

Finally, the surrogate models are used to explore the whole design space. It is done by evaluating the different meta-models on a grid of $50 \times 50 \times 50$ points. The dNNMs for all

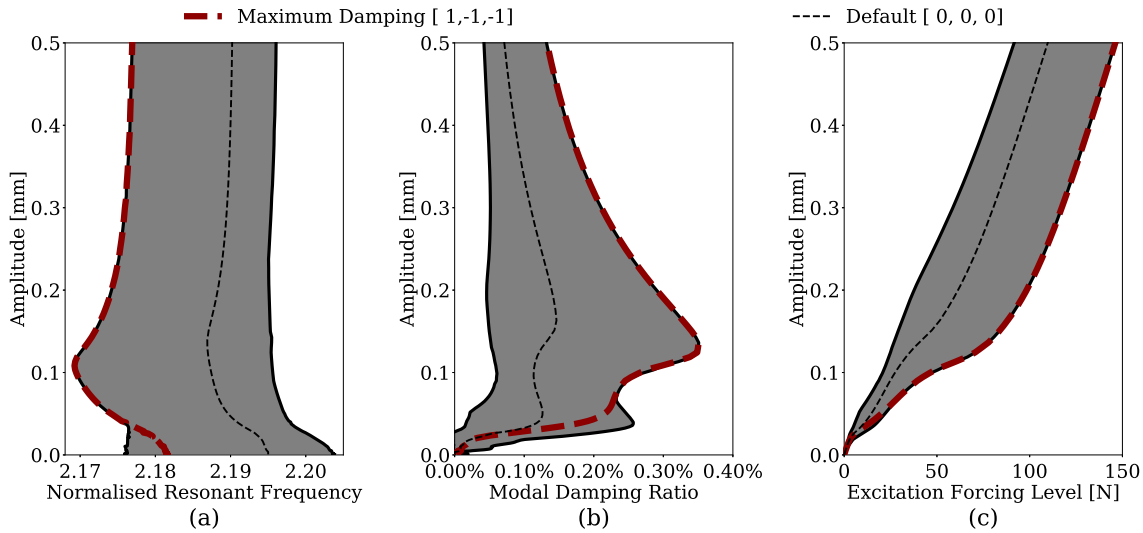


Fig. 6.9 Design space exploration of the damped nonlinear normal mode: (a) Normalised resonant frequency; (b) Modal damping ratio; (c) Excitation forcing level; Black dashed curve: default geometry $[0,0,0]$; Red dashed curve: geometry with the maximum modal damping ratio $[1,-1,-1]$

possible geometries are given in Fig.6.9 where the envelopes of variation are given. The black dashed line represents the dNNM of the default geometry $[0,0,0]$.

Compared to the previous cases (Fig.6.6- Fig.6.8), larger variations of all nonlinear modal properties are obtained as shown in Fig.6.9. Within the whole design space, the resonant frequency falls in a range of 2.168-2.203 and in a percentage of -1.3% to 0.3% of the natural frequency. For the modal damping ratio, the maximum is always reached at vibration amplitudes that are smaller than 0.2 *mm*. The highest modal damping ratio is around 0.35% and this geometry is defined as the optimum geometry in the following. The dNNM that corresponds to the optimum geometry is represented by the red dash line. The design parameters for this optimum geometry are $[1,-1,-1]$. The latter is represented in Fig.6.10 with the associated contact pressure and gap distribution. The optimum geometry shows an upper bump and three lower bumps. By comparing the contact pressure distribution between the optimum geometry (Fig.6.10(c)) and the default geometry (Fig.6.3(a)), more nodes are in-contact with a higher contact pressure. Apart from the effect of the contact pressure, the optimum geometry is less flexible in the Y direction leading to less separation within the contact interface.

Compared to the default initial geometry, the normalized resonant frequency of the optimized one is reduced from 2.195 to 2.182 (0.6% of reduction). For a given excitation forcing level, the optimum geometry shows always the lowest resonant amplitude compared

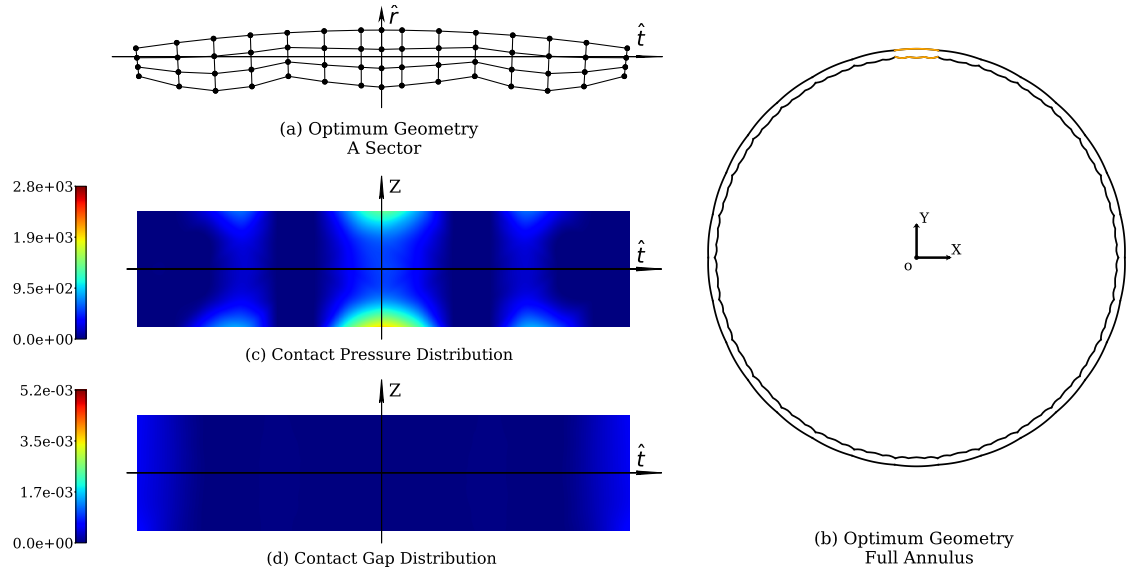


Fig. 6.10 The optimal geometry $[1,-1,-1]$:(a) Geometry (A sector); (b) Geometry (Full annulus); (c) Contact pressure distribution; (d) Contact gap distribution

to the whole design space, but also has the lowest resonant frequency when the amplitude is superior to 0.05 *mm*. Moreover, this geometry always has the highest modal damping ratio when the amplitude is superior to 0.07 *mm*. The properties of this optimum geometry are compared to those of the default geometry in Tab.6.2, values are given when the maximum of the modal amplitude is reached. For the default geometry, the maximum damping ratio equals 0.15% and is reached when the resonant amplitude is 0.16 *mm*. Whereas for the optimum geometry, the maximum damping ratio is 0.35%, which improved more than 100% compared to the default geometry.

Table 6.2 Comparison of maximum modal damping using surrogate models

	Default	Optimum
Amplitude [mm]	0.164	0.137
Resonant Frequency	2.187	2.171
Modal Damping Ratio	0.15%	0.35%
Excitation Forcing Level [N]	52.5	77.8

6.6 Variance Based Sensitivity Analysis

A sensitivity analysis is achieved using a variance based approach using Sobol indices. The sensitivity of the three design parameters have been investigated in both global design space and local design space (around the optimal geometry). The fundamental knowledge of Sobol indices is given at the beginning of this section. Then, the global sensitivity and local sensitivity are discussed.

6.6.1 Sobol indices

Sobol indices can be considered as a type of the variance based sensitivity analysis [159, 158]. This method is a form of global sensitivity analysis and can be used for nonlinear responses. The sensitivity indices are obtained by the decomposition of the output variance into fractions due to a single input parameter or an interaction effect of more than one input parameters.

In the present study, the input parameters are the three design parameters, namely κ_1, κ_2 and κ_3. All three design parameters are assumed to be uniformly distributed within the design space. The output parameters are the values of the resonant frequency, the modal damping ratio and the excitation forcing level at specific vibration amplitude level. In the following, $\kappa = [\kappa_1, \kappa_2, \kappa_3]$ represents the vector of inputs, and y denotes one of the considered outputs. The output can be seen as a function of inputs $y = f([\kappa_1, \kappa_2, \kappa_3])$. Sobol indices are used to investigate the direct influence of the different input parameters $\kappa_i, i \in [1,2,3]$, as well as their coupling effects on the output variance. Therefore, the output variance $\mathrm{V}(y)$ can be decomposed in:

$$\mathrm{Var}(y) = \sum_{i=1}^{3} \mathrm{Var}_i + \sum_{i<j}^{3} \mathrm{Var}_{i,j} + \mathrm{Var}_{1,2,3} \tag{6.3}$$

where Var denotes the variance [145, 146], and where the other terms are defined as:

$$\begin{aligned} \mathrm{Var}_i &= \mathrm{Var}(\mathrm{E}(y|\kappa_i)) \\ \mathrm{Var}_{i,j} &= \mathrm{Var}(\mathrm{E}(y|\kappa_i, \kappa_j)) - \mathrm{Var}_i - \mathrm{Var}_j \\ \mathrm{Var}_{1,2,3} &= \mathrm{Var}(\mathrm{E}(y|\kappa_1, \kappa_2, \kappa_3)) - \textstyle\sum_{i=1}^{3} \mathrm{Var}_i - \sum_{i<j}^{3} \mathrm{Var}_{i,j} \end{aligned} \tag{6.4}$$

where E represents the expectation. Then, the first three orders Sobol indices are defined as:

$$\begin{aligned} \mathrm{S}_i &= \mathrm{Var}_i/\mathrm{Var}(y) \\ \mathrm{S}_{i,j} &= \mathrm{Var}_{i,j}/\mathrm{Var}(y) \\ \mathrm{S}_{1,2,3} &= \mathrm{Var}_{1,2,3}/\mathrm{Var}(y) \end{aligned} \tag{6.5}$$

The total order of Sobol indices ST_i can be calculated as below where $\mathrm{Var}(\mathrm{E}(y|-\kappa_i))$ is the total contribution to the variance of y due to non-κ_i.

$$\mathrm{ST}_i = 1 - \mathrm{Var}(\mathrm{E}(y|-\kappa_i))/\mathrm{Var}(y) \tag{6.6}$$

The Sobol index is considered as a very useful tool to describe the sensitivity of a function to its input parameters and their coupling effects. If the Sobol index S_i of an input variable κ_i is high (i.e. close to 1), then the input variable κ_i has a strong effect on the output y. If the Sobol index S_i of an input variable κ_i is low (i.e. close to 0), the influence of κ_i on output y is limited. For the first order indices, the direct effect of the input parameter is described. Whereas for higher order indices, the coupling effect of a set of parameters are indicated. The total order index measures the contribution of a single input parameter to the output variance considering all the possible interactions with the other parameters.

6.6.2 Sensitivity analysis

In the present sensitivity study, there are three output parameters, which are the resonant frequency, the modal damping ratio and the excitation forcing level. Four sets of Sobol indices are computed at different levels of vibration amplitude, 0.05 *mm*, 0.1 *mm*, 0.2 *mm* and 0.4 *mm* (refer to Fig.6.9). The Sobol indices are calculated using an open source library, OpenTURNS [11].

Sensitivity analysis in global design space

The Sobol indices are computed within the whole design space and given in Fig.6.11(a, c, e, g), where circles represent the first order Sobol indices and squares represent the total order indices. The orange markers show the Sobol indices of the resonant frequency. Generally, the first order index of κ_1 for the resonant frequency almost reaches 1. Therefore, κ_1 has the most important influence on the resonant frequency regardless the level of amplitude. The

interaction of κ_1 with the other input parameters can be ignored, since the total indices are very close to the first order index. This is in agreement with the observations in Fig.6.6-6.8.

The blue markers describe the Sobol indices for the modal damping ratio and green for the excitation forcing level. As discussed in Section 6.5, the variation of the excitation forcing level always shows a similar trend to the modal damping ratio. By looking at the indices for the modal damping ratio (blue), it is easy to notice that the contributions for each input parameter are distinguishable for different levels of the vibrational amplitude. At low amplitude (see Fig.6.11(a)), the total order indices for three inputs are 0.46, 0.39 and 0.33 and the first order indices are 0.41, 0.27 and 0.21 respectively. The three input parameters have a similar influence on the modal damping ratio and the excitation forcing level, and interactions between the parameters is small, since the first order and the total order Sobol indices are close for each parameter.

Therefore, from the global sensitivity analysis, one can come up with a few points. First, the direct effect of κ_1 is the most important factor for the variance three targeting outputs. The interaction of κ_1 with the two other inputs is almost negligible. κ_2 and κ_3 have a very limited effect on the resonant frequency regardless the vibrational amplitude. For low amplitude, the influence of the three input parameters on the modal damping ratio and excitation forcing level are almost similar. For higher amplitude, the direct contribution of κ_2 and κ_3 decreases and interaction effect vanished.

Sensitivity analysis around local optimum geometry

The optimum geometry is identified as shown in Fig.6.10 in Section 6.5. To investigate the sensitivity around the optimal geometry, the Sobol indices are calculated in a similar way. The three input parameters for the optimum design are $[\kappa_1, \kappa_2, \kappa_3] = [1, -1, -1]$. Therefore, the range for each input parameter is chosen as: $\kappa_1 \in [0.9, 1])$, $\kappa_2 \in [-1, -0.9])$ and $\kappa_3 \in [-1, -0.9]$. The local Sobol indices are shown in Fig.6.11(b, d, f, h). The local Sobol indices do not show a significant difference compared to the global ones.

As a conclusion, the upper surface of the damper has a high influence on the damper characteristics, whereas the lower surface geometry has a very limited impact. But if the damper is aimed to be used at low amplitude level, the modal damping ratio can be tuned with κ_2 and κ_3. The coupling effect between κ_2 and κ_3 cannot be ignored in this case. Moreover, it appears that the three parameters do not have significant coupling effect at large amplitude, which means that they can be treated independently in a design process.

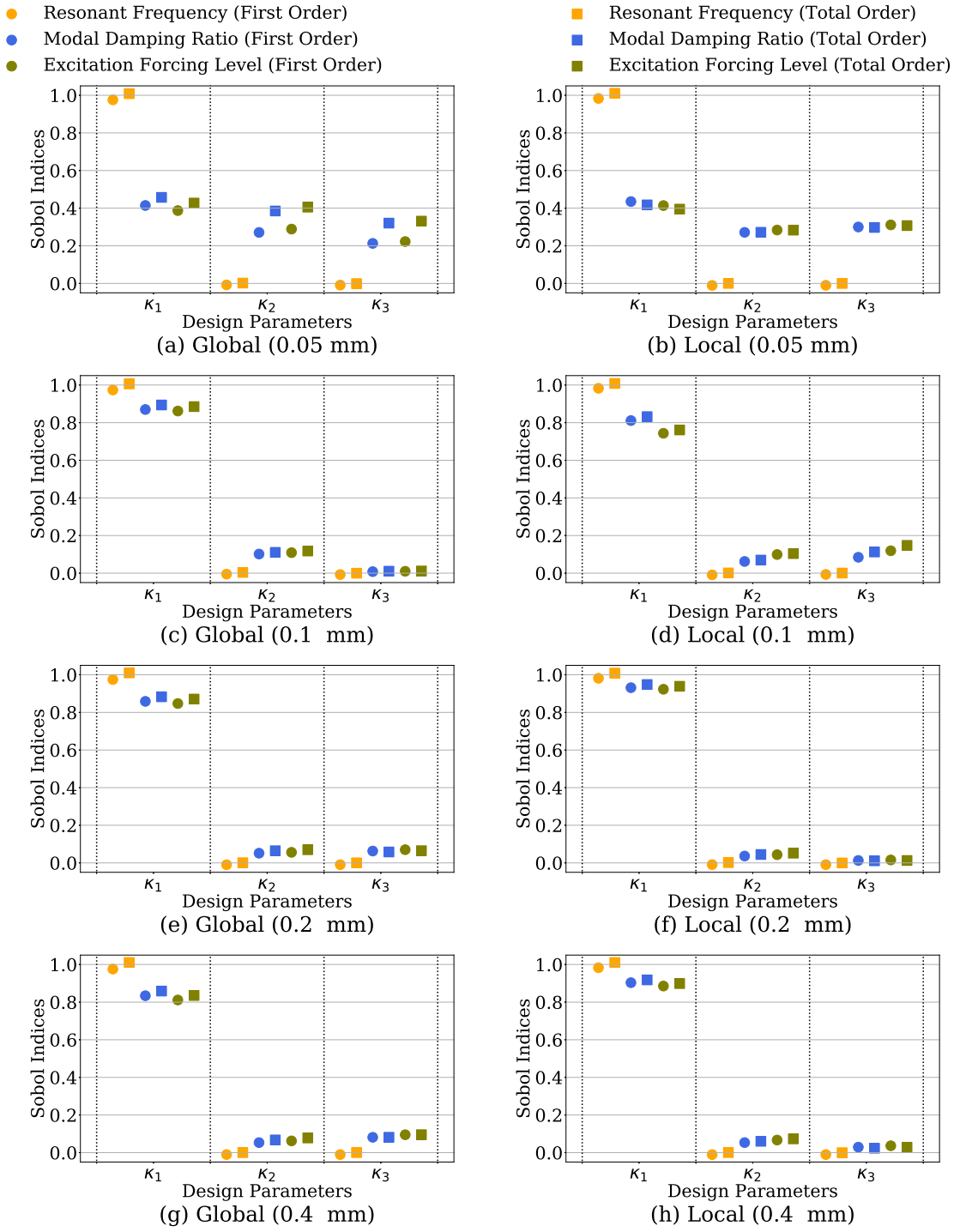


Fig. 6.11 Sobol indices for different levels of the vibrational amplitude within the whole design space ($\kappa_{1,2,3} \in [-1,1]$):(a, b) 0.05 *mm*; (c, d) 0.1 *mm*; (e, f) 0.2 *mm*; (g, h) 0.4 *mm*; (a, c, e, g) Global Sobol indices; (b, d, f, h) Local Sobol indice

6.7 Concluding Remarks

In this chapter, the geometry of the ring damper is modified using three design parameters. With these parameters, the lower and upper surfaces of the ring damper can be modified. It implies the modification in the contact pressure distribution, but also in the stiffness and mass of the damper. The effect of these parameters on the blisk dynamics is studied based on a parametric study using surrogate models. These Kriging meta-models are used to explore the design space and assess the impact of the different geometrical modifications of the damper on the blisk dynamic. Sobol indices are used to describe the sensitivity of the three design parameters to resonant frequency, modal damping ratio and excitation forcing level.

Different geometries of ring damper can lead to a change of its mass, its flexibility, of the local coordinates within the contact interface, of the contact pressure and gap distribution, resulting in a change in the resonant frequency and the modal damping ratio. The largest impact on the nonlinear modal properties is obtained from the modification of the upper surface. In contrast, the impact of the lower surface on the resonant frequency can be neglected and the effect on the modal damping ratio is limited. As for contact pressure distribution, a dispersive one can lead to more sliding nodes and so more energy dissipation and better damping performance. This work demonstrates the importance of designing damper geometry for a better performance and shape or topological optimisation should be considered. Furthermore, thanks to Kriging meta-models, the exploration of whole design space is achievable with acceptable computational costs. The validated Kriging meta-models can be considered as efficient tools to predict nonlinear responses of complicated system.

Chapter 7

Conclusions and Future Work

7.1 Conclusions of the Research Work

The research motivation of the present thesis originated from the demands of higher modelling efficiency for an industrial structure with non-conservative nonlinearities, such as an industrial bladed disk or blisk with friction dampers. The construction of classic forced response of such a complicated structure results in heavy computational costs. Repeated computations are required to obtain an evolution of resonant response with respect to excitation forcing level, leading to an even heavier computational burden. To improve the modelling efficiency, a numerical methodology based on nonlinear modes is described, validated and applied. Using such a modelling methodology, the computational cost can be significantly reduced.

7.1.1 Conclusions on nonlinear modal analysis

Nonlinear modal analysis is a numerical tool to investigate the dynamic response of a nonlinear system by only considering its resonant solutions. The nonlinear modes can be seen as a collection of the resonant solutions in a series of the forced responses. From the nonlinear modal analysis, the evolution of the nonlinear modes and other modal properties with respect to the vibration amplitude can be easily obtained with a lower computational cost. Furthermore, some complicated phenomena in the regime of nonlinear dynamics can be intuitively understood, such as modal interactions, bifurcations, stiffening/hardenings effects and so on. Nonlinear modal analysis has become a popular modelling methodology in the research field.

To solve an engineering problem, the forced response of a complicated structure is usually the prime interest. The relation between the nonlinear mode and the resonant solution in

forced response is complicated, and it is difficult to derive in a straightforward way. In the literature, the whole forced response can be reconstructed using a nonlinear modal synthesis based on single nonlinear resonant mode theory. The energy balance method is a numerical tool to predict the resonant solution in the forced response using nonlinear modes. This method provides a direct link between the nonlinear modes and resonant solutions. Nonlinear modal analysis coupled with the energy balance method can be seen as an efficient method to study the nonlinear dynamic response of a complicated structure with various nonlinearities in the future.

7.1.2 Conclusions on existing numerical approaches

Numerical approaches for the computation of the damped Nonlinear Normal Modes (dNNMs) were recently developed in last two decades. Specifically, there are two existing proven numerical approaches: Complex Nonlinear Mode (CNM) and Extended Periodic Motion Concept (EPMC). An increasing number of researchers have started to use these numerical approaches to investigate the nonlinear dynamic response for structures with non-conservative nonlinearities. However, uncertainties definitely exist and more research work is expected to serve the overall purpose of the development of a reliable numerical approach.

For structures with non-conservative nonlinearities, the dNNMs are damped and non-periodic. In CNM, the actual damped solutions are represented in a harmonic expression with an exponential decay. CNM can capture the damped feature of the dNNMs and initial assumptions are not required. Whereas, if the classic harmonic balance method with alternating frequency/time transformation is used to solve the nonlinear dynamic equations, damped solutions cannot be directly applied. In detail, the discrete Fourier transformation and the inverse discrete Fourier transformation are used to obtain the nonlinear force iteratively. In this process, the exponential terms that represent damping features are ignored. Thus, it raises inaccuracy if the dNNM shows large damping.

In contrast, the EPMC approach, a periodic concept is assumed beforehand: an artificial linear damping is applied to balance the energy dissipation caused by non-conservative nonlinearities leading to periodic dNNMs. In original EPMC approach, an artificial viscous damping is added into the dynamic equation and makes the dNNM periodic. For the sake of clarity, this method is called as EPMC-V. However, there is no firm statement explaining the choice of the viscous damping. Therefore, in the present thesis, EPMC with artificial hysteretic damping (EPMC-H) is firstly developed and compared with original EPMC (EPMC-V). Hysteretic damping and viscous damping are two different types of

linear damping models in the context of physics and mathematics. Hysteretic damping is independent of the resonant frequency. From the present thesis, EPMC-H can provide better representation of energy dissipation of nonlinearities that only depends on displacement, i.e. systems with frictional contact.

7.1.3 Conclusions on the extended energy balance method

The Extended Energy Balance Method (E-EBM) is a numerical method that can predict the resonance for a given excitation force without the computation of the nonlinear forced response. E-EBM is based on the assumption that, under small enough damping, the solution of dNNM and resonant solutions share great similarities. The energy exchanged by the summation of non-conservative nonlinearities and the given damping equals to the energy injected by excitation force. Therefore, the classic force amplitude plot can be constructed during the computation of the dNNM. E-EBM can be simply adopted for both CNM and EPMC. In addition, the main features of the isolated branches for a forced response can be directly detected and tracked using the method. However, the accuracy of the method is limited by the contribution of the other modes in the forced response, especially in the case of internal resonance. The accuracy of the method is also affected by the numerical method used to solve the nonlinear dynamic problem. The E-EBM coupled with dNNMs can be used for engineering design problems to dramatically reduce the computational cost while ensuring an accurate prediction of the resonance.

7.1.4 Conclusions on friction ring dampers

The friction ring damper is considered as one of the emerging solutions for improving of the damping level in a blisk structure. It usually consists of a ring with an open gap located within the groove of blisk. The ring damper is held in contact with the blisk by centrifugal force. This damping device is analysed in the present thesis using a lumped model and a full-scale FE model. Furthermore, the geometric effects of the ring damper are explored. The damping ability of the friction ring damper is evaluated and critically discussed.

Effect of blade disk coupling

The mechanism of the friction damping is based on the relative rubbing motion between two bodies. In the case of the friction ring damper, it is efficient only if the relative displacements within the contact interface are significant. In an actual working environment of the blisk, the

engine order excitation is one of the most common excitations and is mainly applied on the blade. The ring dampers are not directly in-contact with the blade. Therefore, the damping performance of ring dampers is governed by the blade disk coupling effect, which controls the energy transfer between the blades and the disk. For those modes with a large blade disk coupling effect, a ring damper can be considered as a very efficient device to mitigate the vibration amplitude.

Effect of initial contact status

The initial contact status is obtained from a static analysis, which takes the frictional contact into consideration. Within the whole contact interface, the contact pairs can be either in-contact (with a contact pressure) or separated (with an initial gap). For nodes with a lower contact pressure, the sliding contact condition occurs at low amplitude. As for nodes with a higher contact pressure, it is very difficult to initiate sliding contact conditions (very large relative displacement is required). For nodes with a small initial gap, these nodes pair can become partial separation and partial sliding with a large enough displacement. The existence of separation can lead a significant reduction in the damping performance. Therefore, the initial gap should be avoided as much as possible.

Effect of ring damper geometry

The choice of the material for the ring damper is very limited because of its extreme working environment. Geometric design of the ring dampers seems to be one of the potential ways to improve the damping performance. Changing the geometry of ring damper can result in a change of its mass, its flexibility, the local coordinates within the contact interface, the contact pressure and gap distributions. The resonant frequency and the modal damping ratio can also be changed as a consequence.

The last chapter of the present thesis provides an illustrative example of a geometric design of a ring damper based on only three design parameters. From this study, the geometric modification of the upper surface of the ring damper leads to a significant impact on the resonant frequency and the damping performance. In contrast, the influence of the lower surface of the ring damper is limited. The maximum damping ratio achieved is almost doubled. Therefore, designing damper geometry has been proven to be a very efficient way to obtain a better damping performance.

7.2 Scientific Contribution

- The first important contribution of the present thesis on the field of nonlinear dynamics is the description of EPMC-H method and demonstration of the limitations of existing numerical method. EPMC-H is able provide better prediction of the energy dissipation for structures with friction damping than the original EPMC-V.
- Development of E-EBM is the most important scientific contribution of the present thesis. E-EBM is a numerical tool that can accurately predict the resonance using the dNNM. It provides a direct link between the dNNM and the resonant solutions in forced responses. E-EBM can be simply adopted in all existing numerical approaches (CNM and EPMC). The use of E-EBM in a full-scale FE structure with friction damper is possible.
- The present thesis also contributes to dynamic analysis of the friction ring damper. A geometric study of a friction ring damper is achieved. Some design guidelines of ring dampers are highlighted.

7.3 Future Work

Here is a list of topics that author finds interesting and would like to suggest pursuing further:

- In Chapter 4, a parametric study of nonlinear modal properties for the test rig are completed. A test rig with an adjustable platform will be designed, manufactured and tested in the near future. This novel test rig will be used to validate the results from the numerical simulations.
- The dynamic response of a bladed disk or blisk with a friction damper has been widely studied in the literature. In reality, other types of nonlinearities might also exist in turbomachinery. For example, an assembled fan has both frictional contact (at the root joints) and geometric nonlinearity under large deformation. The coupling effects between the frictional contact and large deformation would be a very interesting topic.
- Friction ring dampers are one of the potential damping devices for blisks. The application of a piezoelectric patch can be seen as another possible damping device. Using piezoelectric material to achieve an active or passive control of normal contact force within the contact interface might improve the damping performance of ring damper.

- In the present thesis, the friction ring damper is assumed as a cyclic symmetric structure. Whereas in reality, there is a small open gap within the ring damper and this small open gap breaks the cyclic symmetry leading to mistuning effects. Taking mistuning effects into the consideration while designing the ring dampers would be very useful in the design of the friction ring damper.
- The geometric effect of ring damper has already been explored in the present thesis. A shape or topological optimisation can be considered as the future work to achieve an optimal design of the friction ring damper.

7.4 Publications

7.4.1 Journal publications

- **Sun, Y.**, Yuan, J., Pesaresi, L., Denimal, E. and Salles, L., (2020), "Parametric study and uncertainty quantification of the nonlinear modal properties of frictional dampers", *Journal of Vibration and Acoustics*, 142(5):051102.
- **Sun, Y.**, Vizzaccaro, A., Yuan, J., and Salles, L., (2020), "An extended energy balance method for resonance prediction in forced response of systems with non-conservative nonlinearities using damped nonlinear normal mode", *Nonlinear Dynamics*.
- **Sun, Y.**, Yuan, J., Denimal, E., and Salles, L., (2021) "Nonlinear modal analysis of frictional ring damper for compressor blisk", *Journal of Engineering for Gas Turbines and Power*, 143(3):031008.
- **Sun, Y.**, Denimal, E., Yuan, J., and Salles, L., (2021), "Influence of the geometry of friction ring dampers in blisks using nonlinear modal analysis and kriging surrogate model", *Structural and Multidisciplinary Optimization* [Submitted].
- **Sun, Y.**, Yuan, J., Vizzaccaro, A., and Salles, L., (2021), "Comparison of numerical approaches for computation of damped nonlinear normal mode in a nonlinear system with non-conservative nonlinearties", *Nonlinear Dynamics* [Submitted].
- Yuan, J., **Sun, Y.**, Schwingshackl, C. W., and Salles, L., (2021), "Computation of damped nonlinear normal modes for large scale nonlinear systems in a self-adaptive modal subspace", *Mechanical Systems and Signal Processing* [Submitted].

7.4.2 Conference publications

- **Sun, Y.**, Yuan, J., Pesaresi, L., and Salles, L., (2018), "Nonlinear vibrational analysis for integrally bladed disk using frictional ring damper", *Journal of Physics: Conference Series*, 1106:012026.

- **Sun, Y.**, Yuan, J., Denimal, E., and Salles, L., (2021) "Nonlinear modal analysis of frictional ring damper for compressor blisk", *ASME Paper GT2020-14277*.

- **Sun, Y.**, Yuan, J., Denimal, E., and Salles, L., (2021), "A Study of the Contact Interface for Compressor Blisks with Ring Dampers Using Nonlinear Modal Analysis", *IOP Conference Series: Materials Science and Engineering*, 1081:012041.

- Lasen, M., **Sun, Y.**, Schwingshackl, C. W., and Dini, D., (2020), "Analysis of an actuated frictional interface for improved dynamic performance", In: Kerschen G., Brake M.R., Renson L. (eds) *Nonlinear Structures & Systems, Volume 1*. Conference Proceedings of the Society for Experimental Mechanics Series. Springer, Cham..

References

[1] AL-Qassab, M. and Nair, S. (2003). Wavelet-galerkin method for free vibrations of elastic cable. *Journal of Engineering Mechanics*, 129(3):350–357.

[2] Aleshin, V. and Abeele, K. V. D. (2009). Fundamental consequences of a new intrinsic time measure: Plasticity as a limit of the endochronic theory. *Journal of the Mechanics and Physics of Solids*, 57(4):657–672.

[3] Allgower, E. L. and Georg, K. (2003). Introduction to Numerical Continuation Methods. *Classics in Applied Mathematics*, 45:xxvi–388.

[4] Amabili, M. (2008). *Nonlinear Vibrations and Stability of Shells and Plates*. Cambridge University Press.

[5] Amontons, G. (1732). *Sur les frottements des machines*. Académie Royale des Sciences, Paris, France, Troiséme (1732) edition,.

[6] Anandavel, K. and Prakash, R. V. (2011). Effect of three-dimensional loading on macroscopic fretting aspects of an aero-engine blade-disc dovetail interface. *Tribology International*, 44(11):1544–1555.

[7] Armand, J., Pesaresi, L., Salles, L., and Schwingshackl, C. W. (2016). A multiscale approach for nonlinear dynamic response predictions with fretting wear. *ASME. Paper GT2016-56201*.

[8] Ascher, U., Christiansen, J., and Russell, R. D. (1979). A collocation solver for mixed order systems of boundary value problems. *Mathematics of Computation*, pages 659–679.

[9] Baek, S. and Epureanu, B. (2017). Reduced-order modeling of bladed disks with friction ring dampers. *Journal of Vibration and Acoustics*, 139(6):061011.

[10] Battiato, G., Firrone, C., Berruti, T., and Epureanu, B. (2018). Reduction and coupling of substructures via gram-schmidt interface modes. *Computer Methods in Applied Mechanics and Engineering*, 336:187–212.

[11] Baudin, M., Dutfoy, A., Iooss, B., and Popelin, A.-L. (2015). Openturns: An industrial software for uncertainty quantification in simulation.

[12] Becker, J. and Gaul, L. (2008). Cms methods for efficient damping prediction for structures with friction. *Proceedings of the IMAC-XXVI, Orlando*.

[13] Berthillier, M., Dupont, C., Mondal, R., and Barrau, J. J. (1998). Blades forced response analysis with friction dampers. *Journal of Vibration and Acoustics*, 120(2):468–474.

[14] Bhatnagar, S., Yuan, J., Fantetti, A., Denimal, E., and Salles, L. (2020). Quantification of uncertainties in nonlinear vibrations of turbine blades with underplatform dampers. In *ISMA International Conference on Noise and Vibration Engineering 2020*, Leuven, Belgium.

[15] Bouc, R. (1971). A mathematical model for hysteresis. *Acustica*, 24(1):16–25.

[16] Bourquin, F. (1992). Component mode synthesis and eigenvalues of second-order operators: discretization and algorithm. *Mathematical modelling AND numerical analysis*, 26(3):385–423.

[17] Brake, M. R. W. (2018). *An Overview of Constitutive Models*, pages 207–221. Springer International Publishing, Cham.

[18] Cameron, T. M. and Griffin, J. H. (1989). An alternating frequency/time domain method for calculating the steady-state response of nonlinear dynamic systems. *Journal of Applied Mechanics*, 56(1):149–154.

[19] Canudas de Wit, C., Olsson, H., and Astrom, K.and Lischinsky, P. (1995). A new model for control of systems with friction. *IEEE Transactions on Automatic Control*, 40(3):419–425.

[20] Cardona, A., Lerusse, A., and Géradin, M. (1998). Fast fourier nonlinear vibration analysis. *Computational Mechanics*, 22:128–142.

[21] Castanier, M. P. and Pierre, C. (2006). Modeling and analysis of mistuned bladed disk vibration: Current status and emerging directions. *Journal of Propulsion and Power*, 22(2):384–396.

[22] Cenedese, M. and Haller, G. (2020). How do conservative backbone curves perturb into forced responses?: A Melnikov function analysis. *Proceedings of the Royal Society A: Mathematical, Physical and Engineering Sciences*, 476(2234):20190494.

[23] Cheung, Y. K., Chen, S. H., and Lau, S. L. (1990). Application of the incremental harmonic balance method to cubic non-linearity systems. *Journal of Sound and Vibration*, 140(2):273–286.

[24] Chung, J. and Hulbert, G. M. (1993). A time integration algorithm for structural dynamics with improved numerical dissipation: The generalized-alpha method. *Journal of Applied Mechanics*, 60(2):371–375.

[25] Cochelin, B., Damil, N., and Potier-Ferry, M. (1994). Asymptotic–numerical methods and pade approximants for non-linear elastic structures. *International Journal for Numerical Methods in Engineering*, 37(7):1187–1213.

[26] Cochelin, B. and Vergez, C. (2009). A high order purely frequency-based harmonic balance formulation for continuation of periodic solutions. *Journal of Sound and Vibration*, 324(1):243–262.

[27] Coulomb, C. A. (1821). *Theorie des machines simple*. Bachelier, Paris, France.

[28] Craig, JR., R. R. and Bampton, M. C. C. (1968). Coupling of substructures for dynamic analyses. *AIAA Journal*, 6(7):1313–1319.

[29] Crisfield, M. (1981). A fast incremental/iterative solution procedure that handles "snap-through". *Computers & Structures*, 13(1):55–62.

[30] Dahl, P. R. (1976). Solid friction damping of mechanical vibrations. *AIAA Journal*, 14(12):1675–1682.

[31] Dankowicz, H. and Schilder, F. (2011). An extended continuation problem for bifurcation analysis in the presence of constraints. *Journal of Computational and Nonlinear Dynamics*, 6(3).

[32] Denimal, E., Sinou, J.-J., and Nacivet, S. (2019). Influence of structural modifications of automotive brake systems for squeal events with kriging meta-modelling method. *Journal of Sound and Vibration*, 463:114938.

[33] Dhooge, A., Govaerts, W., and Kuznetsov, Y. A. (2003). Matcont: a matlab package for numerical bifurcation analysis of odes. *ACM Transactions on Mathematical Software*, 29(2):141–164.

[34] Doedel, E., Champneys, A., Fairgrieve, T., Kuznetsov, Y., Sandstede, B., and Wang, X. (1999). Auto 97: Continuation and bifurcation software for ordinary differential equations (with homcont).

[35] Dokainish, M. A. and Subbaraj, K. (1989). A survey of direct time-integration methods in computational structural dynamics–i. explicit methods. *Computers & Structures*, 32(6):1371–1386.

[36] Dye, R. C. F. and Henry, T. A. (1969). Vibration amplitudes of compressor blades resulting from scatter in blade natural frequencies. *Journal of Engineering for Power*, 91(3):182–187.

[37] Ewins, D. J. (1969). The effects of detuning upon the forced vibrations of bladed disks. *Journal of Sound and Vibration*, 9(1):65–79.

[38] Ewins, D. J. (1970). A study of resonance coincidence in bladed discs. *Journal of Mechanical Engineering Science*, 12(5):305–312.

[39] Ewins, D. J. (1973). Vibration characteristics of bladed disc assemblies. *Journal of Mechanical Engineering Science*, 15(3):165–186.

[40] Ewins, D. J. (1976). Vibration modes of mistuned bladed disks. *Journal of Engineering for Power*, 98(3):349–355.

[41] Fantetti, A., Tamatam, L., Volvert, M., Lawal, I., Liu, L., Salles, L., Brake, M., Schwingshackl, C., and Nowell, D. (2019). The impact of fretting wear on structural dynamics: Experiment and simulation. *Tribology International*, 138:111–124.

[42] Fontanela, F., Grolet, A., Salles, L., and Hoffmann, N. (2019). Computation of quasi-periodic localised vibrations in nonlinear cyclic and symmetric structures using harmonic balance methods. *Journal of Sound and Vibration*, 438:54–65.

[43] Gastaldi, C., Berruti, T. M., and Gola, M. M. (2018a). Best practices for underplatform damper designers. *Proceedings of the Institution of Mechanical Engineers, Part C: Journal of Mechanical Engineering Science*, 232(7):1221–1235.

[44] Gastaldi, C., Berruti, T. M., and Gola, M. M. (2018b). The relevance of damper pre-optimization and its effectiveness on the forced response of blades. *Journal of Engineering for Gas Turbines and Power*, 140(6):062505.

[45] Gastaldi, C. and Gola, M. M. (2016). Pre-optimization of asymmetrical underplatform dampers. *Journal of Engineering for Gas Turbines and Power*, 139(1):012504.

[46] Gaul, L. and Nitsche, R. (2001). The role of friction in mechanical joints. *Applied Mechanics Reviews*, 54(2):93–106.

[47] Gendelman, O., Manevitch, L., Vakakis, A., and Bergman, L. (2003). A degenerate bifurcation structure in the dynamics of coupled oscillators with essential stiffness nonlinearities. *Nonlinear Dynamics*, 33(1):1–10.

[48] Giuseppe, B. (2017). *Vibrations Prediction and Measurement of Multi-Stage Bladed Disks with non Linear Behavior due to Friction Contacts*. PhD thesis, Politecnico di Torino.

[49] Goldman, R. L. (1969). Vibration analysis by dynamic partitioning. *AIAA Journal*, 7(6):1152–1154.

[50] Gopinath, A. and Jameson, A. (2005). Time spectral method for periodic unsteady computations over two- and three- dimensional bodies. *AIAA. Paper 2005-1220*.

[51] Grenat, C. (2018). *Nonlinear Normal Modes and multi-parametric continuation of bifurcations : Application to vibration absorbers and architectured MEMS sensors for mass detection*. PhD thesis, Ecole Centrale de Lyon.

[52] Grenat, C., Baguet, S., Dufour, R., and Lamarque, C.-H. (2018). Generalization of conservative nonlinear normal modes to the non-conservative equation of motion. *ASME. Paper DETC2018-85799*.

[53] Griffin, J. H. (1980). Friction damping of resonant stresses in gas turbine engine airfoils. *Journal of Engineering for Power*, 102(2):329–333.

[54] Grolet, A. and Thouverez, F. (2012). On a new harmonic selection technique for harmonic balance method. *Mechanical Systems and Signal Processing*, 30:43–60.

[55] Gross, J. and Krack, M. (2020). Multi-wave vibration caused by flutter instability and nonlinear tip shroud friction. *Journal of Engineering for Gas Turbines and Power*, 142(2):021013.

[56] Guskov, M., Sinou, J.-J., and Thouverez, F. (2008). Multi-dimensional harmonic balance applied to rotor dynamics. *Mechanics Research Communications*, 35(8):537–545.

[57] Guyan, R. J. (1965). Reduction of stiffness and mass matrices. *AIAA Journal*, 3(2):380–380.

[58] Hall, K. C., Thomas, J. P., and Clark, W. S. (2002). Computation of unsteady nonlinear flows in cascades using a harmonic balance technique. *AIAA Journal*, 40(5):879–886.

[59] Haller, G. and Ponsioen, S. (2016). Nonlinear normal modes and spectral submanifolds: existence, uniqueness and use in model reduction. *Nonlinear Dynamics*, 86(3):1493–1534.

[60] Hill, T., Cammarano, A., Neild, S., and Wagg, D. (2015). Interpreting the forced responses of a two-degree-of-freedom nonlinear oscillator using backbone curves. *Journal of Sound and Vibration*, 349:276–288.

[61] Hill, T., Neild, S., and Cammarano, A. (2016). An analytical approach for detecting isolated periodic solution branches in weakly nonlinear structures. *Journal of Sound and Vibration*, 379:150–165.

[62] Hintz, R. M. (1975). Analytical methods in component modal synthesis. *AIAA Journal*, 13(8):1007–1016.

[63] Hoffmann, N., Fischer, M., Allgaier, R., and Gaul, L. (2002). A minimal model for studying properties of the mode-coupling type instability in friction induced oscillations. *Mechanics Research Communications*, 29(4):197–205.

[64] Hoffmann, T., Panning-von Scheidt, L., and Wallaschek, J. (2019). Analysis of contacts in friction damped turbine blades using dimensionless numbers. *Journal of Engineering for Gas Turbines and Power*, 141(12):121023.

[65] Hsu, C. S. (1974). On approximating a general linear periodic system. *Journal of Mathematical Analysis and Applications*, 45:234–251.

[66] Hurty, W. C. (1960). Vibrations of structural systems by component mode synthesis. *Journal of the Engineering Mechanics Division*, 86(4):51–70.

[67] Hurty, W. C. (1965). Dynamic analysis of structural systems using component modes. *AIAA Journal*, 3(4):678–685.

[68] Idelsohn, S. R. and Cardona, A. (1985). A reduction method for nonlinear structural dynamic analysis. *Computer Methods in Applied Mechanics and Engineering*, 49(3):253–279.

[69] Iwan, W. D. (1966). A distributed-element model for hysteresis and its steady-state dynamic response. *Journal of Applied Mechanics*, 33(4):893.

[70] Jahn, M., Tatzko, S., Panning-von Scheidt, L., and Wallaschek, J. (2019). Comparison of different harmonic balance based methodologies for computation of nonlinear modes of non-conservative mechanical systems. *Mechanical Systems and Signal Processing*, 127:159–171.

[71] Jenkins, G. (1962). Analysis of the stress-strain relationships in reactor grade graphite. *British Journal of Applied Physics*, 13:8–10.

[72] Jezequel, L. and Lamarque, C. (1991). Analysis of non-linear dynamical systems by the normal form theory. *Journal of Sound and Vibration*, 149(3):429–459.

[73] Jones, D. R., Schonlau, M., and Welch, W. J. (1998). Efficient global optimization of expensive black-box functions. *Journal of Global optimization*, 13(4):455–492.

[74] Kartal, M., Mulvihill, D., Nowell, D., and Hills, D. (2011). Measurements of pressure and area dependent tangential contact stiffness between rough surfaces using digital image correlation. *Tribology International*, 44(10):1188–1198.

[75] Kelley, A. (1967). On the liapounov subcenter manifold. *Journal of Mathematical Analysis and Applications*, 18(3):472–478.

[76] Kerschen, G., Kowtko, J. J., Mcfarland, D. M., Bergman, L. A., and Vakakis, A. (2007). Theoretical and experimental study of multimodal targeted energy transfer in a system of coupled oscillators. *Nonlinear Dynamics*, 47:285–309. Special Issue: Non-linear Structural Dynamics.

[77] Kerschen, G., Peeters, M., Golinval, J., and Vakakis, A. (2009). Nonlinear normal modes, part i: A useful framework for the structural dynamicist. *Mechanical Systems and Signal Processing*, 23(1):170–194. Special Issue: Non-linear Structural Dynamics.

[78] Kleijnen, J. P. (2017). Regression and kriging metamodels with their experimental designs in simulation: a review. *European Journal of Operational Research*, 256(1):1–16.

[79] Krack, M. (2015). Nonlinear modal analysis of nonconservative systems: Extension of the periodic motion concept. *Computers & Structures*, 154:59–71.

[80] Krack, M., Panning, L., Wallaschek, J., Siewert, C., and Hartung, A. (2012). Robust design of friction interfaces of bladed disks with respect to parameter uncertainties. *ASME. Paper No.GT2012-68578*.

[81] Krack, M., Panning-von Scheidt, L., and Wallaschek, J. (2013a). A high-order harmonic balance method for systems with distinct states. *Journal of Sound and Vibration*, 332(21):5476–5488.

[82] Krack, M., Panning-von Scheidt, L., and Wallaschek, J. (2013b). A method for nonlinear modal analysis and synthesis: Application to harmonically forced and self-excited mechanical systems. *Journal of Sound and Vibration*, 332(25):6798–6814.

[83] Krack, M., Salles, L., and Thouverez, F. (2016). Vibration prediction of bladed disks coupled by friction joints. *Archives of Computational Methods in Engineering*, 24:589–636.

[84] Krack, M., Tatzko, S., Panning-von Scheidt, L., and Wallaschek, J. (2014). Reliability optimization of friction-damped systems using nonlinear modes. *Journal of Sound and Vibration*, 333(13):2699–2712.

[85] Krylov, N. and Bogoliubov, N. (1943). *Introduction to Non-linear Mechanics*. Annals of mathematics studies. no.11. Princeton University Press.

[86] Kumar, B. R. (2013). A review on blisk technology. *International Journal of Innovative Research in Science, Engineering and Technology*, 2(5).

[87] Kuznetsov, Y. A.and Levitin, V. V. (1995). Content: A multiplatform environment for analyzing dynamical systems. *User's Guide, Dynamical Systems Laboratory, CWI, Amsterdam, Netherlands*.

[88] LaBryer, A. and Attar, P. (2009). High dimensional harmonic balance dealiasing techniques for a duffing oscillator. *Journal of Sound and Vibration*, 324(3):1016–1038.

[89] Lavella, M., Botto, D., and Gola, M. (2013). Design of a high-precision, flat-on-flat fretting test apparatus with high temperature capability. *Wear*, 302(1):1073–1081.

[90] Laxalde, D., Gibert, C., and Thouverez, F. (2008a). Experimental and numerical investigations of friction rings damping of blisks. *ASME. Paper No.GT2008-50862*.

[91] Laxalde, D., Salles, L., Blanc, L., and Thouverez, F. (2008b). Non-linear modal analysis for bladed disks with friction contact interfaces. *ASME. Paper No. GT2008-50860*.

[92] Laxalde, D. and Thouverez, F. (2009). Complex non-linear modal analysis for mechanical systems: Application to turbomachinery bladings with friction interfaces. *Journal of Sound and Vibration*, 322(4):1009–1025.

[93] Laxalde, D., Thouverez, F., and Lombard, J.-P. (2010). Forced response analysis of integrally bladed disks with friction ring dampers. *Journal of Vibration and Acoustics*, 132(1):011013.

[94] Laxalde, D., Thouverez, F., Sinou, J.-J., and Lombard, J.-P. (2007). Qualitative analysis of forced response of blisks with friction ring dampers. *European Journal of Mechanics A/Solids*, 26(4):676–687.

[95] Ling, F. (1991). Quasi-periodic solutions calculated with the simple shooting technique. *Journal of Sound and Vibration*, 144(2):293–304.

[96] Liu, J., Li, L., and Fan, Y. (2018). A comparison between the friction and piezoelectric synchronized switch dampers for blisks. *Journal of Intelligent Material Systems and Structures*, 29(12):2693–2705.

[97] Liu, L., Dowell, E., and Thomas, J. (2007). A high dimensional harmonic balance approach for an aeroelastic airfoil with cubic restoring forces. *Journal of Fluids and Structures*, 23(3):351–363.

[98] Liu, L., Thomas, J., Dowell, E., Attar, P., and Hall, K. (2006). A comparison of classical and high dimensional harmonic balance approaches for a duffing oscillator. *Journal of Computational Physics*, 215(1):298–320.

[99] Lufthansa (1999). *Training Manual: A319 / A320 / A321*. Lufthansa Technical Training.

[100] Lupini, A. and Epureanu, B. I. (2020). A friction-enhanced tuned ring damper for bladed disks. *Journal of Engineering for Gas Turbines and Power*. [Accepted].

[101] Lupini, A., Mitra, M., and Epureanu, B. I. (2019). Application of tuned vibration absorber concept to blisk ring dampers: A nonlinear study. *Journal of Engineering for Gas Turbines and Power*, 141(10):101016.

[102] Lyapunov, A. M. (1992). The general problem of the stability of motion. *International Journal of Control*, 55(3):531–534.

[103] MacNeal, R. H. (1971). A hybrid method of component mode synthesis. *Computers & Structures*, 1(4):581–601.

[104] Marquina, F. J., Coro, A., Gutie´rrez, A., Alonso, R., Ewins, D. J., and Girini, G. (2008). Friction damping modeling in high stress contact areas using microslip friction model. *ASME. Paper GT2008-50359*.

[105] McKay, M. D., Beckman, R. J., and Conover, W. J. (1979). A comparison of three methods for selecting values of input variables in the analysis of output from a computer code. *Technometrics*, 21(2):239–245.

[106] Mead, D. J. (1975a). Wave propagation and natural modes in periodic systems: I. mono-coupled systems. *Journal of Sound and Vibration*, 40(1):1–18.

[107] Mead, D. J. (1975b). Wave propagation and natural modes in periodic systems: Ii. multi-coupled systems, with and without damping. *Journal of Sound and Vibration*, 40(1):19–39.

[108] Mikhlin, Y. V. and Avramov., K. V. (2010). Nonlinears normal modes for vibrating mechanical systems: review of theoretical developments. *Applied Mechanics Reviews*, 63(6):060802.

[109] Morin, A. (1833). New friction experiments carried out at metz in 1831– 1833. *Proceedings of French Royal Academy of Sciences*, 4(1):1–128.

[110] Nacivet, S., Pierre, C., Thouverez, F., and Jezequel, L. (2003). A dynamic lagrangian frequency–time method for the vibration of dry-friction-damped systems. *Journal of Sound and Vibration*, 265(1):201–219.

[111] Nayfeh, A. H. (1995). On direct methods for constructing nonlinear normal modes of continuous systems. *Journal of Vibration and Control*, 1(4):389–430.

[112] Newmark, N. M. (1959). A method of computation for structural dynamics.

[113] Niemotka, M. A. and Ziegert, J. C. (1995). Optimal design of split ring dampers for gas turbine engines. *Journal of Engineering for Gas Turbines and Power*, 117(3):569–575.

[114] Panning, L., Sextro, W., and Popp, K. (2000). Optimization of interblade friction damper design. *ASME. Paper No.2000-GT-0541*.

[115] Panning, L., Sextro, W., and Popp, K. (2002). Optimization of the contact geometry between turbine blades and underplatform dampers with respect to friction damping. *ASME. Paper No.GT-2002-30429*.

[116] Paulson, C. and Ragkousis, G. (2015). pykriging: A python kriging toolkit.

[117] Peeters, M., Viguié, R., Sérandour, G., Kerschen, G., and Golinval, J.-C. (2009). Nonlinear normal modes, part ii: Toward a practical computation using numerical continuation techniques. *Mechanical Systems and Signal Processing*, 23(1):195–216. Special Issue: Non-linear Structural Dynamics.

[118] Pesaresi, L., Armand, J., Schwingshackl, C., Salles, L., and Wong, C. (2018). An advanced underplatform damper modelling approach based on a microslip contact model. *Journal of Sound and Vibration*, 436:327–340.

[119] Pesaresi, L., Fantetti, A., Cegla, F., Salles, L., and Schwingshackl, C. (2020). On the use of ultrasound waves to monitor the local dynamics of friction joints. *Experimental Mechanics*, 60(1):129–141.

[120] Pesaresi, L., Salles, L., Jones, A., Green, J., and Schwingshackl, C. (2017). Modelling the nonlinear behaviour of an underplatform damper test rig for turbine applications. *Mechanical Systems and Signal Processing*, 85:662–679.

[121] Petrov, E. (2011). A high-accuracy model reduction for analysis of nonlinear vibrations in structures with contact interfaces. *Journal of Engineering for Gas Turbines and Power*, 133(10):102503.

[122] Petrov, E. P. (2004). A method for use of cyclic symmetry properties in analysis of nonlinear multiharmonic vibrations of bladed disks. *Journal of Turbomachinery*, 126(1):175–183.

[123] Petrov, E. P. (2006). Direct parametric analysis of resonance regimes for nonlinear vibrations of bladed disks. *Journal of Turbomachinery*, 129(3):495–502.

[124] Petrov, E. P. (2007). A sensitivity-based method for direct stochastic analysis of nonlinear forced response for bladed discs with friction interfaces. *ASME. Paper No.GT2007-27981*.

[125] Petrov, E. P. (2008). Explicit finite element models of friction dampers in forced response analysis of bladed disks. *Journal of Engineering for Gas Turbines and Power*, 130(2).

[126] Petrov, E. P. and Ewins, D. J. (2003). Analytical formulation of friction interface elements for analysis of nonlinear multi-harmonic vibrations of bladed disks. *Journal of Turbomachinery*, 125(2):364–371.

[127] Petrov, E. P. and Ewins, D. J. (2005). Effects of damping and varying contact area at blade-disk joints in forced response analysis of bladed disk assemblies. *Journal of Turbomachinery*, 128(2):403–410.

[128] Ponsioen, S., Pedergnana, T., and Haller, G. (2018). Automated computation of autonomous spectral submanifolds for nonlinear modal analysis. *Journal of Sound and Vibration*, 420:269–295.

[129] Popova, E. and Popov, V. L. (2015). The research works of coulomb and amontons and generalized laws of friction. *Friction*, 3(2):183–190.

[130] Preisach, F. (1935). Uber die magnetische nachwirkung. *Annalen der Physik*, 94:277–302.

[131] Przemieniecki, J. (1985). *Theory of Matrix Structural Analysis*. Dover Civil and Mechanical Engineering. Dover.

[132] Rand, R. H. (1971). A higher order approximation for non-linear normal modes in two degree of freedom systems. *International Journal of Non-Linear Mechanics*, 6(4):545–547.

[133] Rand, R. H. (1973). The geometrical stability of non-linear normal modes in two degree of freedom systems. *International Journal of Non-Linear Mechanics*, 8(2):161–168.

[134] Rand, R. H. (1974). A direct method for non-linear normal modes. *International Journal of Non-Linear Mechanics*, 9(5):363–368.

[135] Renson, L., Kerschen, G., and Cochelin, B. (2016). Numerical computation of nonlinear normal modes in mechanical engineering. *Journal of Sound and Vibration*, 364:177–206.

[136] Riks, E. (1979). An incremental approach to the solution of snapping and buckling problems. *International Journal of Solids and Structures*, 15(7):529–551.

[137] Rosenberg, R. M. (1960). Normal modes of nonlinear dual-mode systems. *Journal of Applied Mechanics*, 27(2):263–268.

[138] Rubin, S. (1975). Improved component-mode representation for structural dynamic analysis. *AIAA Journal*, 13(8):995–1006.

[139] Sacks, J., Welch, W. J., Mitchell, T. J., and Wynn, H. P. (1989). Design and analysis of computer experiments. *Statistical science*, pages 409–423.

[140] Salles, L. (2010). *Etude de l'usure par fretting sous chargements dynamiques dans les interfaces frottantes : application aux pieds d'aubes de turbomachines*. PhD thesis, Ecole Centrale de Lyon ; Universite Technique d'Etat Bauman de Mosco.

[141] Salles, L., Blanc, L., Thouverez, F., and Gouskov, A. (2011). Dynamic analysis of fretting-wear in friction contact interfaces. *International Journal of Solids and Structures*, 48(10):1513–1524.

[142] Salles, L., Blanc, L., Thouverez, F., and Gouskov, A. M. (2009). Dynamic analysis of fretting-wear in friction contact interfaces. *Journal of Engineering for Gas Turbines and Power*, 132(1):012503.

[143] Salles, L., Blanc, L., Thouverez, F., Gouskov, A. M., and Jean, P. (2012). Dual time stepping algorithms with the high order harmonic balance method for contact interfaces with fretting-wear. *Journal of Engineering for Gas Turbines and Power*, 134(3):032503.

[144] Salles, L., Staples, B., Hoffmann, N., and Schwingshackl W., C. (2016). Continuation techniques for analysis of whole aeroengine dynamics with imperfect bifurcations and isolated solutions. *Nonlinear Dynamics*, 86(3):1897–1911.

[145] Saltelli, A., Tarantola, S., and Chan, K. (1999). A quantitative, model independent method for global sensitivity analysis of model output. *Technometrics*, 41(1):39–56.

[146] Saltelli, A., Tarantola, S., and Chan, K. (2002). A. making best use of model evaluations to compute sensitivity indices. *Computer Physics Communication*, 145:280–297.

[147] Sanliturk, K. Y., Ewins, D. J., and Stanbridge, A. B. (1998). Underplatform dampers for turbine blades: Theoretical modeling, analysis, and comparison with experimental data. *Journal of Engineering for Gas Turbines and Power*, 123(4):919–929.

[148] Sarrouy, E. (2019). Phase driven modal synthesis for forced response evaluation. In *7 th International Conference on Nonlinear Vibrations, Localization and Energy Transfer*, Marseille, France.

[149] Sarrouy, E. and Sinou, J.-J. (2011). Non-linear periodic and quasi-periodic vibrations in mechanical systems-on the use of the harmonic balance methods. In Ebrahimi, F., editor, *Advances in Vibration Analysis Research*, chapter 21. InTech, Rijeka.

[150] Schilder, F., Vogt, W., Schreiber, S., and Osinga, H. M. (2006). Fourier methods for quasi-periodic oscillations. *International Journal for Numerical Methods in Engineering*, 67(5):629–671.

[151] Schwarz, S., Kohlmann, L., Hartung, A., Gross, J., Scheel, M., and Krack, M. (2019). Validation of a turbine blade component test with frictional contacts by phase-locked-loop and force-controlled measurements. *Journal of Engineering for Gas Turbines and Power*, 142(5):051006.

[152] Schwingshackl, C. W., Petrov, E., and Ewins, D. J. (2012). Effects of contact interface parameters on vibration of turbine bladed disks with underplatform dampers. *Journal of Engineering for Gas Turbines and Power*, 134(3):032507.

[153] Segalman, D. J. (2005). A four-parameter iwan model for lap-type joints. *Journal of Applied Mechanics*, 72(5):752.

[154] Shaw, S. W. and Pierre, C. (1991). Non-linear normal modes and invariant manifolds. *Journal of Sound and Vibration*, 150(1):170–173.

[155] Shaw, S. W. and Pierre, C. (1993). Normal modes for non-linear vibratory systems. *Journal of Sound and Vibration*, 150:40.

[156] Sicot, F., Puigt, G., and Montagnac, M. (2008). Block-jacobi implicit algorithms for the time spectral method. *AIAA Journal*, 46:3080–3089.

[157] Siewert, C., Panning, L., Wallaschek, J., and Richter, C. (2010). Multiharmonic forced response analysis of a turbine blading coupled by nonlinear contact forces. *Journal of Engineering for Gas Turbines and Power*, 132(8):082501.

[158] Sobol, I., Tarantola, S., Gatelli, D., Kucherenko, S., and Mauntz, W. (2007). Estimating the approximation errors when fixing unessential factors in global sensitivity analysis. *Reliability Engineering and System Safety*, 92:957–960.

[159] Sobol, I. M. (1993). Sensitivity analysis for nonlinear mathematical model math. *Mathematical models and computer experiment*, 1(4):407–414.

[160] Srinivasan, A. V. (1984). Vibrations of bladed-disk assemblies–a selected survey (survey paper). *Journal of Vibration, Acoustics, Stress, and Reliability in Design*, 106(2):165–168.

[161] Srinivasan, A. V. (1997). Flutter and resonant vibration characteristics of engine blades. *Journal of Engineering for Gas Turbines and Power*, 119(4):742–775.

[162] Stribeck, R. (1902). Die wesentlichen eigenschaften der gleit- und rollenlager (characteristics of plain and roller bearings). *Zeit. des VDI 46*.

[163] Sun, Y., Vizzaccaro, A., Yuan, J., and Salles, L. (2020a). An extended energy balance method for resonance prediction in forced response of systems with non-conservative nonlinearities using damped nonlinear normal mode. *Nonlinear Dynamics*.

[164] Sun, Y., Yuan, J., Denimal, E., and Salles, L. (2020b). Nonlinear modal analysis of frictional ring damper for compressor blisk. *ASME. Paper GT2020-14277*.

[165] Sun, Y., Yuan, J., Pesaresi, L., Denimal, E., and Salles, L. (2020c). Parametric study and uncertainty quantification of the nonlinear modal properties of frictional dampers. *Journal of Vibration and Acoustics*, 142(5):051102.

[166] Sun, Y., Yuan, J., Pesaresi, L., and Salles, L. (2018). Nonlinear vibrational analysis for integrally bladed disk using frictional ring damper. *Journal of Physics: Conference Series*, 1106:012026.

[167] Szemplinska-Stupnicka, W. (1983). Non-linear normal modes and the generalized ritz method in the problems of vibrations of non-linear elastic continuous systems. *International Journal of Non-Linear Mechanics*, 18(2):149–165.

[168] Szemplińska-Stupnicka, W. (1979). The modified single mode method in the investigations of the resonant vibrations of non-linear systems. *Journal of Sound and Vibration*, 63(4):475–489.

[169] Szwedowicz, J., Gibert, C., Sommer, T., and Kellerer, R. (2006). Numerical and experimental damping assessment of a thin-walled friction damper in the rotating setup with high pressure turbine blades. *Journal of Engineering for Gas Turbines and Power*, 130:012502.

[170] Szwedowicz, J., Kissel, M., Ravindra, B., and Kellerer, R. (2005a). Estimation of contact stiffness and its role in the design of a friction damper. *ASME. Paper 2001-GT-0290*.

[171] Szwedowicz, J., Slowik, S., Mahler, A., and Hulme, C. (2005b). Nonlinear dynamic analyses of a gas turbine blade for attainment of reliable shroud coupling. *ASME. Paper GT2005-69062*.

[172] Tang, W. and Epureanu, B. I. (2017). Nonlinear dynamics of mistuned bladed disks with ring dampers. *International Journal of Non-Linear Mechanics*, 97:30–40.

[173] Tang, W. and Epureanu, B. I. (2019). Geometric optimization of dry friction ring dampers. *International Journal of Non-Linear Mechanics*, 109:40–49.

[174] Thomas, D. L. (1974). Standing waves in rotationally periodic structures. *Journal of Sound and Vibration*, 37(2):288–290.

[175] Touzé, C. (2014). Normal form theory and nonlinear normal modes: theoretical settings and applications. In Kerschen, G., editor, *Modal Analysis of nonlinear Mechanical Systems*, pages 75–160, New York, NY. Springer Series CISM courses and lectures, vol. 555.

[176] Tran, D.-M. (2001). Component mode synthesis methods using interface modes. application to structures with cyclic symmetry. *Computers & Structures*, 79(2):209–222.

[177] Tran, D.-M. (2009). Component mode synthesis methods using partial interface modes: Application to tuned and mistuned structures with cyclic symmetry. *Computers & Structures*, 87(17):1141–1153.

[178] Trujillo, D. M. (1977). An unconditionally stable explicit algorithm for structural dynamics. *International Journal for Numerical Methods in Engineering*, 11(10):1579–1592.

[179] Urabe, M. (1965). Galerkin's procedure for nonlinear periodic systems. *Archive for Rational Mechanics and Analysis*, 20(2):120–152.

[180] Vakakis, A. F. (1997). Non-linear normal modes (nnms) and their applications in vibration theory: An overview. *Mechanical Systems and Signal Processing*, 11(1):3–22.

[181] Vakakis, A. F. (2001). Inducing passive nonlinear energy sinks in vibrating systems. *Journal of Vibration and Acoustics*, 123(3):324–332.

[182] Valanis, K. C. (1980). Fundamental consequences of a new intrinsic time measure: Plasticity as a limit of the endochronic theory. *Archives of Mechanics*, 32:171–191.

[183] Wagner, J. T. (1967). Coupling of turbomachine blade vibrations through the rotor. *Journal of Engineering for Power*, 89(4):502–512.

[184] Wang, Y., Ye, H., Jiang, X., and Tian, A. (2018). A prediction method for the damping effect of ring dampers applied to thin-walled gears based on energy method. *Symmetry*, 10(12):677.

[185] Wen, Y.-K. (1976). Method for random vibration of hysteretic systems. *Journal of the Engineering Mechanics Division*, 102(2):249–263.

[186] Whitehead, D. S. (1966). Effect of mistuning on the vibration of turbo-machine blades induced by wakes. *Journal of Mechanical Engineering Science*, 8(1):15–21.

[187] Witteveen, W. and Irschik, H. (2009). Efficient mode based computational approach for jointed structures: joint interface modes. *AIAA Journal*, 47(1):252–263.

[188] Witteveen, W. and Pichler, F. (2014). Efficient model order reduction for the dynamics of nonlinear multilayer sheet structures with trial vector derivatives. *Shock and Vibration*, 2014.

[189] Woiwode, L., Balaji, N. N., Kappauf, J., Tubita, F., Guillot, L., Vergez, C., Cochelin, B., Grolet, A., and Krack, M. (2020). Comparison of two algorithms for harmonic balance and path continuation. *Mechanical Systems and Signal Processing*, 136:106503.

[190] Wu, Y., Li, L., Fan, Y., Zucca, S., Gastaldi, C., and Ma, H. (2020). Design of dry friction and piezoelectric hybrid ring dampers for integrally bladed disks based on complex nonlinear modes. *Computers & Structures*, 233:106237.

[191] Yang, B. D., Chu, M. L., and Menq, C. H. (1998). Stick-slip-separation analysis and non-linear stiffness and damping characterization of friction contacts having variable normal load. *Journal of Sound and Vibration*, 210(4):461–481.

[192] Yang, B. D. and Menq, C. H. (1998). Characterization of 3d contact kinematics and prediction of resonant response of structures having 3d frictional constraint. *Journal of Sound and Vibration*, 217(5):909–925.

[193] Yuan, J., Allegri, G., Scarpa, F., Rajasekaran, R., and Patsias, S. (2015). Novel parametric reduced order model for aeroengine blade dynamics. *Mechanical Systems and Signal Processing*, 62:235–253.

[194] Yuan, J., Salles, L., Haddad, F. E., and Wong, C. (2020a). An adaptive component mode synthesis method for dynamic analysis of jointed structure with contact friction interfaces. *Computers & Structures*, 229:106177.

[195] Yuan, Y., Jones, A., Setchfield, R., and Schwingshackl, C. (2020b). Robust design optimisation of underplatform dampers for turbine applications using a surrogate model. *Journal of Sound and Vibration*, page 115528.

[196] Zhang, J., Perez, R. J., and Lavernia, E. J. (1993). Documentation of damping capacity of metallic, ceramic and metal-matrix composite materials. *Journal of Materials Science*, 28(9):2395–2404.

[197] Zucca, S., Firrone, C. M., and Facchini, M. (2010). A method for the design of ring dampers for gears in aeronautical applications. *ASME. Paper No.IMECE2010-38788*.

[198] Zucca, S., Firrone, C. M., and Gola, M. M. (2012). Numerical assessment of friction damping at turbine blade root joints by simultaneous calculation of the static and dynamic contact loads. *Nonlinear Dynamics*, 67(3):1943–1955.

Appendix A

Numerical Formulations for Contact Models

The numerical formulations used to computation of friction force are provided for all three contact models. The computation of friction force is completed in time domain in an iterative way because of history dependency of friction law. The demonstration of the contact elements are provided in Fig.A.1.

A.1 One Dimensional Contact Element

This one dimensional contact element is shown in Fig.A.1(a). For a current time step i, relative displacement $x(t_i)$ and displacement of contact point $w(t_i)$, the friction force $F_x(t_i)$ is calculated using equations below. The tangential friction forces is predicted in the first place using Eqn.(A.1), then corrected using Eqn.(A.2).

$$f_{pre} = k_t(x(t_i) - w(t_{i-1})) \tag{A.1}$$

$$F_x(t_i) = \begin{cases} f_{pre} & \text{if} \quad f_{pre} < \mu N_0 \quad \text{Sticking} \\ \mu N_0 \cdot f_{pre} / \left| f_{pre} \right| & \text{if} \quad f_{pre} \geq \mu N_0 \quad \text{Sliding} \end{cases} \tag{A.2}$$

$$w(t_i) = \begin{cases} w(t_{i-1}) & \text{if} \quad f_{pre} < \mu N_0 \quad \text{Sticking} \\ x(t_i) - F_x(t_i)/k_t & \text{if} \quad f_{pre} \geq \mu N_0 \quad \text{Sliding} \end{cases} \tag{A.3}$$

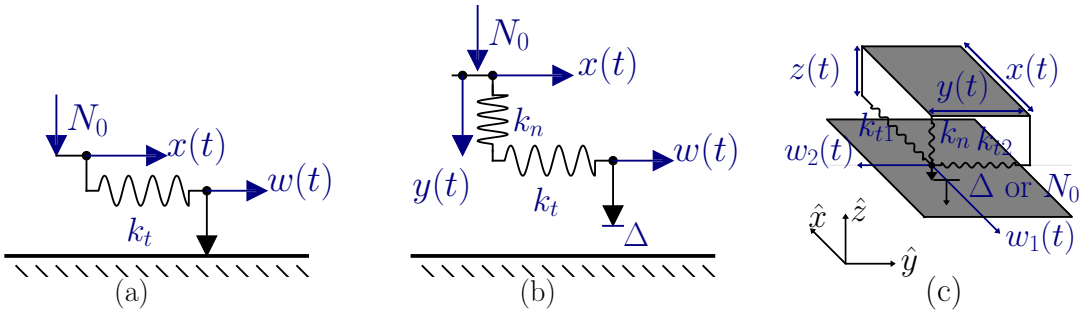


Fig. A.1 Three contact elements: (a) One dimensional contact element (A Jenkins element in tangential direction with a constant normal load); (b) Two dimensional contact element (A Jenkins element in tangential direction with a unilateral spring); (c) Three dimensional contact element (Two Jenkins elements in tangential plane with a unilateral spring)

A.2 Two Dimensional Contact Element

This two dimensional contact element is shown in Fig.A.1(b). For a current time step i, relative displacement $x(t_i)$, $y(t_i)$ and displacement of contact point $w(t_i)$ the friction force can be predicted in Eqn.(A.4), then corrected using Eqn.(A.6). A positive N_0 is used if two nodes are in-contact, or a negative $N_0 = -k_n\Delta$ when two nodes are separated with an initial gap Δ.

$$f_{pre} = k_t(x(t_i) - w(t_{i-1})); \tag{A.4}$$

$$F_y(t_i) = \begin{cases} 0 & \text{if} \quad N_0 + k_n y(t_i) < 0 \quad \text{Separation} \\ N_0 + k_n y(t_i) & \text{if} \quad N_0 + k_n y(t_i) \geq 0 \quad \text{In-contact} \end{cases} \tag{A.5}$$

$$F_x(t_i) = \begin{cases} 0 & \text{if} \quad F_y(t_i) = 0 & & & \text{Separation} \\ f & \text{if} \quad F_y(t_i) > 0 & \text{and} & f_{pre} < \mu F_y(t_i) & \text{Sticking} \\ \mu F_y(t_i) \cdot f_{pre}/|f| & \text{if} \quad F_y(t_i) > 0 & \text{and} & f_{pre} \geq \mu F_y(t_i) & \text{Sliding} \end{cases} \tag{A.6}$$

In the case of sticking contact condition, the displacement of contact point $w(t_i)$ equals to the value on previous time step $w(t_{i-1})$. Whereas, when separation occurs, the displacement of contact point $w(t_i)$ is null. If sliding contact condition happens, $w(t_i)$ can be calculated using Eqn.(A.7).

$$w(t_i) = \begin{cases} x(t_i) & \text{if} \quad F_y(t_i) = 0 & \text{Separation} \\ w(t_{i-1}) & \text{if} \quad f_{pre} < \mu F_y(t_i) & \text{Sticking} \\ x(t_i) - F_x(t_i)/k_{t1} & \text{if} \quad f_{pre} \geq \mu F_y(t_i) & \text{Sliding} \end{cases} \tag{A.7}$$

A.3 Three Dimensional Contact Element

This three dimensional contact element is shown in Fig.A.1(c). For a current time step i the normal contact force $F_z(t_i)$ is calculated at the first to define the contact status whether is separation or in-contact. If two contact nodes are fully separated and a null tangential friction force can be obtained. A positive N_0 is used if two nodes are in-contact, or a negative $N_0 = -k_n\Delta$ when two nodes are separated with an initial gap Δ.

$$F_z(t_i) = \begin{cases} 0 & \text{if} \quad N_0 + k_n z(t_i) < 0 \quad \text{Separation} \\ N_0 + k_n z(t_i) & \text{if} \quad N_0 + k_n z(t_i) \geq 0 \quad \text{In-contact} \end{cases} \tag{A.8}$$

In the case of in-contact, the tangential friction forces in the contact plane are predicted in the first place using Eqn.(A.9) to obtain the components of the predicted friction force in two orthogonal directions ($f_{pre,x}$ and $f_{pre,y}$). Then, the modulus $\left|f_{pre}\right|$ and direction $D(t_i)$ of the predicted friction force are calculated using Eqn.(A.10). When $\left|f_{pre}\right|$ exceeds the sliding limit $\mu F_z(t_i)$, friction forces are oriented along circumference radius $\left|f_{pre}\right|$.

$$f_{pre,x} = k_{t1}(x(t_i) - w_1(t_{i-1})); \quad f_{pre,y} = k_{t2}(y(t_i) - w_2(t_{i-1})) \tag{A.9}$$

$$\begin{aligned} \left|f_{pre}\right| &= \sqrt{f_{pre,x}^2 + f_{pre,y}^2} \\ D(t_i) &= \sqrt{(x(t_i) - w_1(t_{i-1}))^2 + (y(t_i) - w_2(t_{i-1}))^2} \end{aligned} \tag{A.10}$$

Then, the friction force in tangential contact plane can be corrected using Eqn.(A.11-A.12), and the displacements of contact point ($w_1(t_i)$ and $w_2(t_i)$) can be computed using Eqn.(A.13-A.14).

$$F_x(t_i) = \begin{cases} 0 & \text{if} \quad F_z(t_i) = 0 & & \text{Separation} \\ f_{pre,x} & \text{if} \quad F_z(t_i) > 0 & \text{and} \quad \left|f_{pre}\right| < \mu F_z(t_i) & \text{Sticking} \\ \mu F_z(t_i) \cdot (x(t_i) - w_1(t_i))/D(t_i) & \text{if} \quad F_z(t_i) > 0 & \text{and} \quad \left|f_{pre}\right| \geq \mu F_z(t_i) & \text{Sliding} \end{cases} \tag{A.11}$$

$$F_y(t_i) = \begin{cases} 0 & \text{if} \quad F_z(t_i) = 0 & & \text{Separation} \\ f_{pre,y} & \text{if} \quad F_z(t_i) > 0 & \text{and} \quad \left|f_{pre}\right| < \mu F_z(t_i) & \text{Sticking} \\ \mu F_z(t_i) \cdot (y(t_i) - w_2(t_i))/D(t_i) & \text{if} \quad F_z(t_i) > 0 & \text{and} \quad \left|f_{pre}\right| \geq \mu F_z(t_i) & \text{Sliding} \end{cases} \tag{A.12}$$

$$w_1(t_i) = \begin{cases} x(t_i) & \text{if} \quad F_z(t_i) = 0 & & \text{Separation} \\ w_1(t_{i-1}) & \text{if} \quad F_z(t_i) > 0 & \text{and} \quad \left|f_{pre}\right| < \mu F_z(t_i) & \text{Sticking} \\ x(t_i) - F_x(t_i)/k_{t1} & \text{if} \quad F_z(t_i) > 0 & \text{and} \quad \left|f_{pre}\right| \geq \mu F_z(t_i) & \text{Sliding} \end{cases} \tag{A.13}$$

$$w_2(t_i) = \begin{cases} y(t_i) & \text{if} \quad F_z(t_i) = 0 & & & \text{Separation} \\ w_2(t_{i-1}) & \text{if} \quad F_z(t_i) > 0 & \text{and} & \left|f_{pre}\right| < \mu F_z(t_i) & \text{Sticking} \\ y(t_i) - F_y(t_i)/k_{t2} & \text{if} \quad F_z(t_i) > 0 & \text{and} & \left|f_{pre}\right| \geq \mu F_z(t_i) & \text{Sliding} \end{cases} \tag{A.14}$$